The Mechanics of Active Faulting and Mountain Building

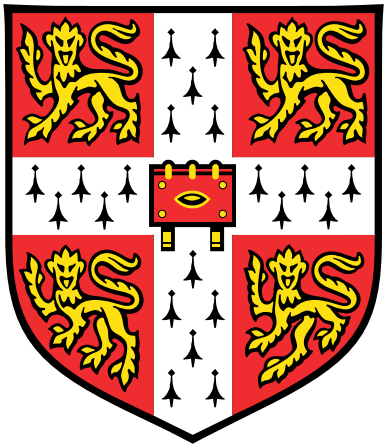

Samuel E. Wimpenny

Department of Earth Sciences
University of Cambridge

This dissertation is submitted for the degree of
Doctor of Philosophy

Corpus Christi College

June 2019

To my family ...

Declaration

I hereby declare that except where specific reference is made to the work of others, the contents of this dissertation are original and have not been submitted in whole or in part for consideration for any other degree or qualification in this, or any other university. This dissertation is my own work and contains nothing which is the outcome of work done in collaboration with others, except as specified in the text by sections highlighted in *italics* and the Acknowledgements. This dissertation contains fewer than 275 pages including appendices, bibliography, footnotes, tables and equations and has fewer than 150 figures.

Samuel E. Wimpenny
June 2019

Acknowledgements

A massive thanks go to my supervisor, Alex Copley, for making researching and writing this thesis a thoroughly enjoyable experience. In addition, I would like to thank the whole faculty and studentship at the Bullard Laboratories for their inspiration and shared enthusiasm in Earth Sciences. I extend particular thanks to Lindsey Walters, Thomassina Ball and Aisling O'Kane for proof-reading sections of this thesis.

I wish to thank Carlos Benavente, Briant Garcia, Lorena Rossell, Enoch Aguirre and Fabrizio Delgado for their hospitality and help during my fieldwork visit to Peru.

I thank my family wholeheartedly for their support over the last 24 years. None of them know what a PhD is, and they consider Geology to be pretty boring. Nonetheless, their encouragement has been unwavering, and for that I am truly grateful.

Last but certainly not least I want to acknowledge my partner, Lindsey. Her support and tolerance is infallible — never has somebody believed in me so much. Hopefully this thesis is as good as you.

Abstract

The aims of this thesis are to place new constraints on the rheological properties of active faults, and to investigate the influence of fault rheology on mountain building.

The first chapter studies the postseismic deformation following the 2003 Bam earthquake in south-eastern Iran, with the intention of probing the material properties of the fault zone. Measurements of ground deformation following the earthquake made using InSAR suggest there was an unusually small amount of postseismic afterslip at Bam compared to similar earthquakes. I use numerical calculations of stress-driven afterslip to show that, in order to account for the limited postseismic afterslip at Bam, most of the fault zone must remain frictionally locked. I also find that, to explain the postseismic InSAR measurements and the long-term growth of topography at Bam, there must be either an E-W deviatoric stress of 2-10 MPa acting across the fault zone, or some component of fabric on the fault zone controlling the rake of fault slip.

The second chapter expands in scope, investigating the orogen-scale deformation of the high Andes in south Peru. First I present a source model for a M_w 6.1 normal-faulting earthquake that occurred in the shallow crust of the south Peruvian Altiplano, which indicates that the Andes are extending parallel to the direction of shortening in the adjacent sub-Andean forelands. I then discuss a compilation of earthquake source models from across the Andes, using the earthquake depth distribution and slip vectors to infer that buoyancy forces are important in controlling the pattern of deformation. Calculations of the buoyancy forces indicate that faults cutting through the foreland support forces $\sim$4-8 TN/m and have effective coefficients of static friction $\lesssim$0.2. Finally, I speculate that the recent normal faulting in the Andes is a result of a reduction in the shear stresses transmitted across faults on the eastern margin of the range, causing the high plateau to extend and thrust eastwards over the adjacent South American foreland.

The final chapter remains focused on the normal faulting in south Peru. I use field observations and remote sensing to show that a 20 km-wide band of normal faults between Cusco and Lake Titicaca are extending $\sim$NNE-SSW to NE-SW at $\sim$1-3 mm/yr. The normal faults became active in the past $\sim$5 Myrs and re-activate pre-existing reverse faults. To account for the extension rates across the normal faults, I calculate that the average shear stresses transmitted across the sub-Andean detachment may have decreased by $\sim$0.02-3 MPa, which is $\sim$0.1-30% of their absolute value. I conclude that within most mountain belts the rate and style of faulting is sensitive to small spatial and temporal variations in the material properties of faults in their forelands.

Table of contents

List of figures

List of tables

Chapter 1

Introduction

Since the mid-20th century two fields of investigation in Earth Sciences have developed in parallel but often in isolation. The study of large-scale continental tectonics focuses on understanding the kinematics of continental deformation resulting from motion on a distributed network of faults [Jackson and McKenzie, 1984; Molnar, 1988]. Constraints from observations of deformation are then used to develop dynamical models of how the continental lithosphere deforms as a product of its rheology and the forces acting on the lithosphere, over 10^5-10^7 year time-scales [Bird, 1978; England and McKenzie, 1982]. Studies of fault mechanics, on the other hand, aim to explain features of the earthquake cycle on individual faults lasting 10^2-10^4 years [Scholz et al., 1969; Avouac et al., 2015]. This field involves developing rheological formulations for the forces that faults support [Byerlee, 1978; Copley, 2017] and the range of fault slip styles, including aseismic creep and seismogenic rupture [Dieterich, 1978].

A long-term goal of both fields should be to build a physical theory of how the continental lithosphere deforms, which explicitly includes the effects of earthquake cycle behaviour. Properly defining the stress boundary conditions acting to load and break faults in earthquakes requires coupling the theory of large-scale continental dynamics with fault-scale mechanics. In this thesis I aim to combine these two approaches into a coherent view of continental mechanics and dynamics from the fault to orogen-scale, using a wide-range of observations from interferometric synthetic aperture radar (InSAR), Global Positioning Systems (GPS), seismology, satellite remote sensing, field studies, Quaternary dating and high-resolution digital elevation models (DEMs).

In the following sections I outline a number of major themes of current research in continental dynamics and fault mechanics, and discuss how the results from this thesis shed new light on these topics.

1.1 The Stresses Acting on Faults

There has been significant debate surrounding the stresses acting on faults, and in particular the magnitude of the stresses required to break faults in earthquakes [e.g. Copley, 2017]. Within the forelands of mountain belts, stresses on faults contribute the majority of the integrated strength of the lithosphere [Maggi et al., 2000a; Jackson et al., 2002], and therefore play a key role in the dynamics of mountain building. In addition, estimates of the shear stress that faults can support are fundamental

to assessing seismic hazard. If, for example, earthquake stress drops are a fraction of the absolute shear stress on a fault, the fault could rupture in multiple earthquakes in quick succession [Fukushima et al., 2018]. In contrast, if the stress drop in earthquakes is equivalent to the total shear stress on a fault [Copley et al., 2011a], then a long period of reloading may be required before the next earthquake can occur.

Until recently the canonical view derived from rock mechanics experiments was that the shear resistance to fault slip could be described by a single static coefficient of friction μ between 0.6 and 0.85, irrespective of the fault rock type (apart from certain phyllosilicate minerals) [Byerlee, 1978]. Based upon these experimental results, the differential stresses ($\sigma_{xx} - \sigma_{zz}$) required to rupture a reverse fault in a ∼20 km-thick seismogenic layer under hydrostatic conditions would be at least ∼400 MPa, with average shear stresses on the fault equivalent to ∼100 MPa. Given that typical stress drops in earthquakes within the continents are ∼0.1-10 MPa [Allmann and Shearer, 2009], the results of Byerlee [1978] would imply faults have the capacity to rupture multiple times to relax the stresses acting upon them. However, simple force balance arguments imply that the differential stresses acting to break faults in mountain belt forelands and subduction zones are likely to be far smaller, on the order of 10's of megapascals, indicating the effective coefficient of friction on faults μ' may be on the order of ∼0.03-0.2 [Lamb, 2006; Copley et al., 2011a]. In addition, the clustering of fault dips around 45^o in dip-slip earthquakes indicates that the static coefficient of friction on faults is probably $\lesssim$0.3 [Middleton and Copley, 2014; Craig et al., 2014].

Within this thesis, I present new results from the forelands of the Andes that are consistent with the emerging view that the effective coefficient of friction on natural seismogenic faults is $\lesssim$0.2 and that these faults support average shear stresses $\lesssim$90 MPa (Chapter 3). This work forms an important new finding, as it expands the range of geological environments in which weak faults have been recognised.

Despite the evidence that some seismogenic faults are weak, the reasons behind their low frictional resistance to slip relative to the experiments of Byerlee [1978] remain enigmatic. One possibility is that foliated phyllosilicates with intrinsically low friction within the cores of natural faults may reduce the stresses they can support [Holdsworth, 2004; Collettini et al., 2009]. Alternatively, high pore-fluid pressures generated by compaction or dehydration reactions from alteration of fault-zone constituents may reduce the effective coefficient of friction on faults [Sibson, 2004]. Paradoxically, both the presence of foliated phyllosilicates and high pore-fluid pressures in fault cores have also been inferred to cause creeping behaviour, inhibiting the occurrence of earthquakes [Ikari et al., 2011; Thomas et al., 2014b]. Differentiating the conditions that reduce the strength of seismogenic faults from the conditions that favour fault creep therefore forms a logical extension of this research.

Unlike seismogenic faults, where the shear stresses are limited by static friction, creeping[1] faults provide velocity-dependent resistance to slip [e.g. Jolivet et al., 2013]. There remains significant debate regarding whether, when averaged over multiple earthquake cycles, creeping faults provide less resistance to slip than seismogenic faults. For example, Gao and Wang [2014] used heat-flow data and a model of the frictional heat dissipation above subduction-zone forearcs to argue that creeping megathrusts have larger apparent[2] effective friction μ'_{app} than seismogenic megathrusts. However, the conclusion of Gao

[1] Creep in this context simply refers to aseismic deformation, and does not imply any rheology.

[2] The friction is apparent because it is non-linearly dependent on the fault slip velocity [Copley and Jolivet, 2016].

and Wang [2014] is at odds with simple force-balance arguments. Both the Peru-Chile megathrust and the Main Himalayan Thrust support significant shear stresses (∼10-40 MPa) due to the horizontal buoyancy forces generated by the Andes and Tibet, and probably have the highest frictional strength of any megathrusts [Lamb, 2006]. Both of these faults also host M_w 8-9 earthquakes and are frictionally locked [Chlieh et al., 2011; Stevens and Avouac, 2015]. In addition, a more recent study using the same heat flow data as Gao and Wang [2014], but a different model linking shear heating on the megathrust to surface heat flow, found that there is no significant difference in the apparent effective friction between megathrusts, irrespective of whether they are creeping or locked [England, 2018].

A novel contribution from this thesis is a new estimate of the deviatoric stresses ($\sigma_{xx} - \sigma_m$) acting on a creeping fault near Bam in south-eastern Iran, which does not rely on the ambiguous interpretation of heat-flow data that is sensitive to fluid flow in the forearc and along the megathrust. Using geomorphology, observations of postseismic fault creep and stress-driven afterslip calculations, I demonstrate that the deviatoric stresses supported by the creeping fault in the top 5 km of crust are likely to be ∼2-10 MPa, This result is similar to estimates of the strength of seismogenic faults in the shallow crust with $\mu'_{app} < 0.1$ (Chapter 2).

1.2 Controls on Fault Creep versus Seismogenic Slip

One of the major contrasts between active faults, thought to be related to their rheological properties, is whether they can creep aseismically, or whether they remain locked, accumulate elastic strain and rupture in earthquakes. Being able to determine whether a fault is locked or creeping is key to building constitutive relationships that accurately describe the rheology of faults, and for estimating the seismic hazard they pose [e.g. Avouac et al., 2015].

With modern geodetic measurements it is now possible to map the creeping and locked areas on fast-moving faults throughout the earthquake cycle [e.g. Konca et al., 2008; Chlieh et al., 2011]. A key observation to emerge from these kinematic analyses of fault slip is that following an earthquake on a predominantly creeping fault, there is typically large amounts of postseismic slip [e.g. Heki et al., 1997; Thomas et al., 2014a; Howell et al., 2016]. One of the best-recorded examples of this behaviour is the 2003 Parkfield earthquake, where GPS measurements captured postseismic slip with an equivalent moment release >170% of the coseismic moment release [Barbot et al., 2009]. The equivalent moment released by postseismic slip is consistently far higher than the moment released by aftershocks, suggesting the vast majority of the slip is aseismic [Perfettini, 2004]. Therefore, the ratio of postseismic to coseismic moment release is a potential metric for the fraction of locking or creep on a fault. However, few examples have been found where the converse is true — where the amount of postseismic slip is small on predominantly locked faults — which reflects the significant bias in the literature towards earthquakes with large postseismic transients. Within this thesis I present a study of postseismic deformation that partly addresses this bias, using a novel application of stress-driven afterslip modelling to argue that the limited postseismic slip following an earthquake at Bam in south-eastern Iran is a product of frictional locking on the fault (Chapter 2).

Creeping sections of faults are often inferred to form persistent barriers to seismogenic rupture, limiting the potential magnitude of earthquakes [Perfettini et al., 2010]. However, dynamical models of earthquakes that use empirical descriptions of fault rheology imply that creeping regions can fail seismically if the dynamic weakening through thermal pressurisation of pore fluids is large enough [Noda and Lapusta, 2013]. There are few robust observations of seismogenic rupture on the creeping sections of faults to test these competing models, as kinematic inversions of surface deformation for fault slip are highly underdetermined, requiring regularisation that smooths the resulting slip distributions [e.g. Funning et al., 2005b]. Stress-driven afterslip models offer one way to mitigate these issues by physically coupling postseismic slip to the distribution of coseismic slip. An interesting conclusion from the stress-driven afterslip models developed in this thesis is that ∼10-15 cm of postseismic slip in the top 5 km of the fault zone at Bam overlapped with a region that experienced $\lesssim$1 m of coseismic slip (Chapter 2). As a result, it appears sections of faults that can creep postseismically may also be able to break in earthquakes.

1.3 Fault Rheology and Continental Mountain Building

Mountain belts and their margins remain a key testing ground for models of continental dynamics and fault rheology, as they are one of a few places where it is possible to estimate the forces acting through the lithosphere [Dalmayrac and Molnar, 1981]. The margins of mountain belts are also amongst the most rapidly-deforming parts of the continental lithosphere, generating the largest continental earthquakes and landslides due to the precipitous terrain, and are therefore amongst the most hazardous regions globally [Bilham, 2019]. A major theme of this thesis is the relationship between the rheology of faults on the margins of mountain belts and the mechanics of continental mountain building.

There remains significant debate regarding the contribution of fault rheology to the long-term integrated strength of the continental lithosphere in mountain belt forelands. One view states that a single brittle layer cut by faults supports the vast majority of the forces acting through the foreland lithosphere in regions where the whole lower crust is cold, anhydrous and seismogenic [Maggi et al., 2000a; Jackson et al., 2002]. It is thought that the top few kilometres of lithospheric mantle can also be brittle and strong, but only if it is $< 600°C$ [McKenzie et al., 2005], which typically requires it to be underlain by a thick lithospheric root insulating it from the convecting mantle [Sloan and Jackson, 2012]. If this view is correct, it is the thickness of the seismogenic layer and the frictional resistance to slip along faults within it that controls the strength of the continental lithosphere and how deformable the foreland is. An alternative school of thought is that the continental lithospheric mantle contributes a significant fraction of the integrated strength of the lithosphere along the margins of most mountain belts [Burov and Watts, 2006; Hammer et al., 2013]. If this view is correct, resistance to ductile creep in the lithospheric mantle is the modulating factor for the strength of the continental lithosphere, not necessarily just the frictional strength of faults.

The observations surrounding these competing models of continental rheology have typically focused on the Alpine-Himalayan belt. Within this thesis, I discuss observations of earthquake centroid depths and gravity anomalies along the eastern margin of the Andes to test these different models of continental rheology, and to study the importance of fault rheology on the mechanics mountain building. I find that

nowhere do earthquakes occur unambiguously in the upper mantle, though the whole crust of South America is seismogenic down to near the Moho (Appendix B.5). The effective elastic thickness of the lithosphere is poorly constrained, but is feasibly less than the seismogenic thickness (<45 km) and does not appear to vary along-strike the mountain belt (Appendix B.5). In the Llanos Basin of Colombia, I find a rare example of a normal-faulting earthquake associated with flexure in the foreland at ∼13-22 km depth, overlying reverse faulting at depths of ∼28-40 km (Chapter 3). The depth-distribution of seismicity and the curvature of the bending foreland indicates that the shear stresses acting to rupture these faults in earthquakes must be $\lesssim$90-130 MPa (Chapter 3). Over the depth of the seismogenic layer, shear stresses on faults could feasibly support all of the horizontal force acting through the foreland due to contrasts in the gravitational potential energy between the Andes and South America (4-8 TN/m; Chapter 3). None of these results require any long-term strength to be present within the upper mantle of the South American foreland, and imply that a single seismogenic layer may contain the majority of the integrated strength of the lithosphere.

Despite these new constraints on the rheology of the foreland lithosphere, it remains unclear what controls the structural style of shortening along the margins of mountain belts, principally whether they are thin- or thick-skinned. Watts et al. [1995] and Mouthereau et al. [2013] proposed that in regions of thin-skinned shortening the lower crust and lithospheric mantle is too strong to deform, whilst in areas of thick-skinned deformation the lower crust and lithospheric mantle is hot and thin, so can deform through grain-scale creep at low differential stresses. Alternatively, Kley et al. [1999] argued that the correlation between segments of the Andean foreland that experienced pre-Andean rifting and the segments that are currently undergoing thick-skinned shortening indicates that the lower crust can deform because of pre-existing normal faults that have been re-activated on shortening. Using earthquake centroid depths in the eastern Andes, I demonstrate that the lower crust in regions undergoing thick-skinned shortening is seismogenic, therefore is not deforming predominantly through grain-scale creep (Appendix B.5). Earthquakes near the Moho in the Colombian and Argentinian foreland imply the lower crust is cold, but able to deform due to the presence of frictionally weak faults.

The strength of faults on the margins of mountain belts also play a key role in modulating the forces transmitted between the forelands and the mountain range interior. In particular, where there is rigid lithosphere being underthrust beneath the margin of a mountain belt, the local force balance is controlled by the shear stresses on the contact between the overriding and underthrusting material [Lamb, 2006; Copley and McKenzie, 2007]. The resistance to shear on the mountain-foreland contact is not only important for controlling the instantaneous deformation within mountain belts [Copley, 2008] but will also modulate the temporal and geometrical evolution of deformation and crustal thickening along their margins [Reynolds et al., 2015]. The widely-used thin-viscous sheet approximation for studying mountain belt dynamics ignores the influence of shear stresses, therefore misses some of the key physics controlling the evolution of mountain ranges [e.g. England and McKenzie, 1982; Lamb, 2000; Flesch and Kreemer, 2010].

A major contribution from this thesis is that a decrease in the shear stresses supported by faults along the margin of the Andes (the sub-Andes) is likely to have caused the onset of extension at ∼5-9 Ma within the mountains of south Peru and the rapid jump in the locus and rate of deformation in the sub-Andean fold-thrust belt (Chapter 3, 4). I present the first estimates of the slip rates on the normal

faults perched high in the south Peruvian Altiplano (∼1-3 mm/yr), and use a novel force balance model to infer that only small changes in the average shear stresses transmitted across the margin of the mountain belt (∼0.02-3 MPa) is required to explain the recent deformation. I conclude that the faulting within mountain belts like the Andes and Tibet is highly sensitive to small temporal and spatial changes in the strength of faults along their margins (Chapter 4). In part, this sensitivity is a product of the extremely hot and weak crust that forms within mountain belt interiors [McKenzie et al., 2019].

The new insights into the dynamics of mountain building discussed above focus on the long-term (i.e. million year) evolution of deformation. Within this thesis I also present evidence that the force balance in the Andes changes over a few hundred years due to the accumulation and release of elastic strain in earthquakes on the faults bounding the margins of the mountain belt. The normal faults in south Peru were compressed prior to the 2001 Arequipa earthquake, temporarily suppressing slip on them. Immediately following the megathrust earthquake, the normal faults were unclamped and the moment release from normal-faulting earthquakes in the high Andes increased, suggesting the majority of the permanent strain in south Peru occurs during the co- and postseismic period of the megathrust earthquake cycle.

1.4 Thesis Overview

The aims of this thesis are to place new constraints on the stresses acting on faults, and to study the influence of fault rheology on the evolution of mountain building. The chapters progress as follows:

Chapter 2: This chapter focuses on the difference between creeping and locked faults. I study the postseismic deformation following the 2003 Bam (Iran) earthquake using InSAR time-series analysis and numerical models of fault mechanics. I find that, to account for the limited postseismic deformation, the fault zone must have remained predominantly locked following the 2003 earthquake. In order to explain the short-term postseismic deformation, and the long-term growth of the local topography, I find that an E-W deviatoric compression between 2 and 10 MPa is likely to be acting on the fault zone.

Chapter 3: This chapter is focused on the forces controlling deformation in the Andes of south Peru. I begin by deriving a detailed source model for a M_w 6.1 normal-faulting earthquake in the high Andes between Cusco and Lake Titicaca to place new constraints on the kinematics of deformation in the mountains. Using this source model, in conjunction with seismological source models of other moderate-magnitude earthquakes in the surrounding area, I discuss the kinematics of deformation across the Andes. I then present calculations for the forces controlling the deformation. Finally, I speculate on the possible causes for the onset of extension in the high Andes of south Peru, suggesting that the shear stresses transmitted across the margin of the Eastern Andes may have decreased at ∼5-9 Ma.

Chapter 4: In this chapter I study the rate and kinematics of faulting in the south Peruvian Altiplano using field studies, Quaternary dating and satellite remote sensing. I discuss the factors controlling the preservation of the active normal faults. I use the rates of slip on the normal faults to calculate the decrease in the shear stresses transmitted across the sub-Andes required to account for the rate and pattern of recent deformation in the south Peru. Finally, I discuss evidence that transient shortening

across the fault system related to the offshore megathrust earthquake cycle may temporarily suppress normal-faulting earthquakes.

Chapter 2

Fault Mechanics and Postseismic Deformation at Bam [1]

Overview

This chapter studies the postseismic deformation following the 2003 M_w 6.6 Bam earthquake. The motivation for focusing on this particular event is that the magnitude of the postseismic surface displacements following the Bam earthquake was unusually small. I investigate the possibility that the limited postseismic deformation is a product of frictional locking on the fault that resists fault creep — a phenomenon that has not previously been recognised in postseismic deformation signals. Using observations from interferometric synthetic aperture radar (InSAR), in conjunction with numerical models of stress-driven afterslip, I show that the faults at Bam remain predominantly locked throughout the seismogenic crust. As a result, the elastic strain stored down-dip and along-strike of the 2003 rupture patch may be released in a future $\sim M_w$ 6 earthquake.

The observations and models developed in this chapter also provide an opportunity to probe the growth of topography at Bam. A 4 km-wide topographic ridge underlain by a reverse fault outcrops near the Bam mainshock epicentre. Elsewhere in Iran, growth of similar topographic ridges has been seen to occur through fault creep initiated by stress changes from slip on nearby faults. I find that, for the afterslip distribution on the reverse fault at Bam to be consistent with forming the anticlinal ridge over repeated earthquake cycles, and also to be consistent with the postseismic InSAR observations, requires either: (1) a far-field tectonic compression equivalent to a 2-10 MPa deviatoric stress acting across the fault system, or (2) that the fault surface has some form of mechanical anisotropy, such as a corrugated fault plane, that controls the sense of slip.

[1] Material in this chapter is adapted from the publication: S. Wimpenny, A. Copley, T. Ingleby (2017). Fault mechanics and post-seismic deformation at Bam, SE Iran, *Geophysical Journal International* 209(2):1018–1035

2.1 Introduction

The M_w 6.6 Bam earthquake occurred on the 26th December 2003 in Kerman Province, south-east Iran, along a previously unknown strike-slip fault [Jackson et al., 2006; Berberian, 2014]. Seismological and geodetic source models proposed that slip in the earthquake was concentrated between 2 and 8 km depth [Fialko et al., 2005; Funning et al., 2005b; Stramondo et al., 2005; Motagh et al., 2006; Peyret et al., 2007]. However, the pattern of aftershocks extended well beneath the coseismic slip patch, to nearly 20 km depth [Tatar et al., 2005], suggesting the bottom ∼10 km of the fault zone remained unruptured and is able to generate earthquakes. This observation raised serious concerns regarding whether the bottom half of the fault at Bam could produce another damaging earthquake in the near future by releasing accumulated elastic strain in response to coseismic loading [Jackson et al., 2006]. Postseismic deformation may relax some of the coseismic stress changes, either through aseismic fault creep (afterslip) or viscous flow.

To date, mapping the parts of faults that can creep aseismically, and the parts that are frictionally locked, has only been possible on fast-moving continental strike-slip faults and megathrusts [e.g. Jolivet et al., 2012; Thomas et al., 2014a; Stevens and Avouac, 2015]. An intriguing pattern has emerged from these studies — faults that creep extensively during the interseismic period also experience large amounts of postseismic afterslip [Heki et al., 1997; Furuya and Satyabala, 2008; Barbot et al., 2009; Thomas et al., 2014a; Howell et al., 2016]. This observation implies that the amount of afterslip is related to the frictional locking of the fault zone around the coseismic rupture, and the magnitude of the coseismic stress changes. Therefore, postseismic deformation measurements may provide insight into the frictional locking on active faults. A previous study of Bam revealed that the postseismic deformation between 2004 and 2007 is consistent with limited afterslip following the 2003 earthquake [Fielding et al., 2009]. Therefore, the fault zone surrounding the Bam rupture may remain predominantly locked, in which case the deformation caused by the earthquake will remain stored as elastic strains around the coseismic rupture.

In this chapter I develop a new InSAR time-series of ground deformation between 2004 and 2009 at Bam, with the intention of investigating the rheology of the fault zone. I present forward calculations of postseismic afterslip and visco-elastic deformation that are consistent with the InSAR observations, and quantify the maximum possible relaxation of coseismic loading on the deep portion of the fault, between 10 and 20 km depth. Subsequently, I investigate the postseismic afterslip and frictional properties on the shallow fault zone (0-10 km) using forward models of stress-driven afterslip [e.g. Barbot et al., 2009].

Four kilometres east of Bam is a 4 km-wide anticlinal ridge formed by motion along an underlying reverse fault [Jackson et al., 2006]. In the final section of this chapter, I use models of stress-driven afterslip, geomorphology and observations from the postseismic InSAR time-series to investigate the growth of the anticlinal ridge. In particular, I test under what conditions stress-driven afterslip following the Bam earthquake can explain both the short-term InSAR observations and long-term growth of the local topography.

2.2 Tectonic Setting

2.2.1 Regional Tectonics

The regional tectonic framework in south-eastern Iran is dominated by the transition from ocean-continent subduction east of 57^o beneath the Makran Range, to continental collision between Arabia and Eurasia west of 57^o in central and western Iran (Fig. 2.1). Convergence between Arabia and Eurasia occurs at 20-30 mm/yr [Reilinger et al., 2006], with 10-15 mm/yr of this motion accommodated by shortening within the Zagros Mountains [Vernant et al., 2004]. In eastern Iran and Afghanistan the majority of the convergence is accommodated by slip along the subduction interface beneath the Makran [Vernant et al., 2004]. As a result, there is differential motion between Afghanistan and central Iran equivalent to ∼15 mm/yr of right-lateral shear on N-S orientated planes (Fig. 2.1b).

The seismicity and the geomorphology across this transition region delineates a number of N-S trending strike-slip faults that accommodate right-lateral shear around the eastern and western edges of the Dasht-e-Lut (Fig. 2.1c). Faults on the west of the Dasht-e-Lut have slip rates between 2 and 5 mm/yr [Walker et al., 2011; Walpersdorf et al., 2014] and have ruptured in a series of earthquakes over the instrumental period, including four $M_w > 5$ earthquakes along the Gowk Fault Zone alone in the past 40 years [Berberian, 2005, 2014] (Fig. 2.1c). The deformation around Bam is consistent with this regional strain field, with interseismic GPS measurements capturing a step of ∼1-3 mm/yr in the northward component of the GPS velocities across the Bam faults [Walpersdorf et al., 2014] (Fig. 2.1b). Interseismic measurements of ground deformation between 1992 and 1999 from InSAR identified no resolvable displacements projected into the satellite line-of-sight (LOS) [Fialko et al., 2005], which requires surface creep rates on the faults at Bam to be $\lesssim$4 mm/yr.

2.2.2 Local Geomorphology and Faulting

Prior to 2003 the only active fault identified at Bam was inferred based on the presence of a 15 km-long, N-S trending escarpment that lies 15-30 m above the surrounding desert plains, known as the Bam-Baravat Ridge [Berberian, 1976] (Fig. 2.2). The topographic asymmetry of the escarpment, presence of an uplifted water table, incised drainage in its western limb, sharp topographic step (Fig. 2.2b) and folded bedding [Hessami et al., 2005] suggest the ridge was formed by motion on a west-dipping reverse fault [Jackson et al., 2006]. Deflected streams around its southern tip are indicative of the southward propagating growth of the ridge [Jackson et al., 2006], but the lack of reliably offset rivers crossing the ridge, or offset qanat tunnels, suggests there is no significant long-term strike-slip motion.

The topography of the ridge decreases over a distance of ∼4 km perpendicular to the ridge crest (Fig. 2.2d). Growth of the ridge is therefore sensitive to slip along the top ∼4 km of the underlying fault, as any fault motion at depths $\gtrsim$5 km would lead to a broader pattern of uplift. The sharp step in elevation across the escarpment requires that dip-slip fault motion extends to the near surface. Similar structures have been recognised elsewhere in Iran, such as at Tabas-e-Golshan [Walker et al., 2003], Ferdows [Walker et al., 2003], Sefidabeh [Berberian et al., 2000], Rigan [Walker et al., 2013] and Shahdad [Berberian et al., 2001].

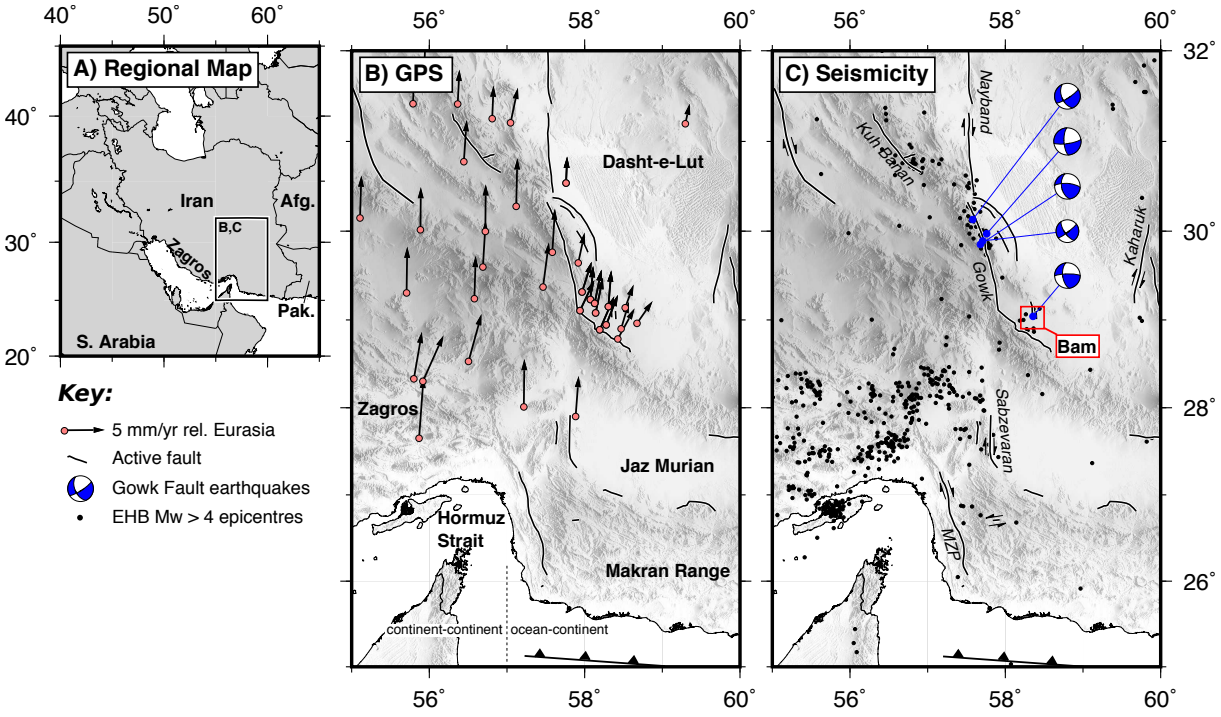

Figure 2.1 Overview of the active tectonics of south-east Iran. (a) Regional map showing the study area. Pak = Pakistan and Afg = Afghanistan. (b) GPS velocities of Walpersdorf et al. [2014] relative to stable Eurasia, omitting the error ellipses for clarity (errors in the horizontal components are typically ∼1-2 mm/yr). (c) The distribution of earthquake hypocentres from the EHB catalogue [Engdahl et al., 2006] highlighting the concentration of events around the western edge of the Dasht-e-Lut. Also plotted in (b) and (c) are the locations of active faults from Walker and Jackson [2004] and Penney et al. [2015]. MZP is the Minab-Zendan-Palami Fault. Body-waveform modelled earthquakes along the Gowk Fault in (c) are taken from Berberian [2014].

2.2.3 Observations of Coseismic Slip: 2003 Bam Earthquake

The fault geometry and slip distribution in the Bam earthquake has been studied using a combination of teleseismic body-waveform modelling [Talebian, 2004; Jackson et al., 2006; Poiata et al., 2012], InSAR [Talebian, 2004; Fialko et al., 2005; Funning et al., 2005b; Stramondo et al., 2005], optical-image pixel tracking [Fu et al., 2004; Binet and Bollinger, 2005; Peyret et al., 2007; de Michele et al., 2008] and levelling measurements [Motagh et al., 2006]. These independent studies consistently found a N-S trending, right-lateral strike-slip fault that dips ∼85^o to the east beneath the western set of surface ruptures can account for the majority of the observations (Fig. 2.2a). This strike-slip fault, which I refer to as the Arg-e-Bam Fault (AEBF), moved with up to 2.7 m of slip concentrated between ∼2 and 8 km depth. There is also evidence for oblique slip on a steep (∼ 60^o), west-dipping reverse fault beneath the Bam-Baravat Ridge, which I refer to as the Bam-Baravat Fault (BBF). Slip on the Bam-Baravat Fault can account for the eastern set of surface ruptures (Fig. 2.2a) and, when included in the coseismic slip inversions, leads to a significant improvement in the fit of the InSAR measurements [Jackson et al., 2006]. Throughout the modelling in this chapter, I use the two-fault coseismic slip distribution and fault geometry of Funning et al. [2005b].

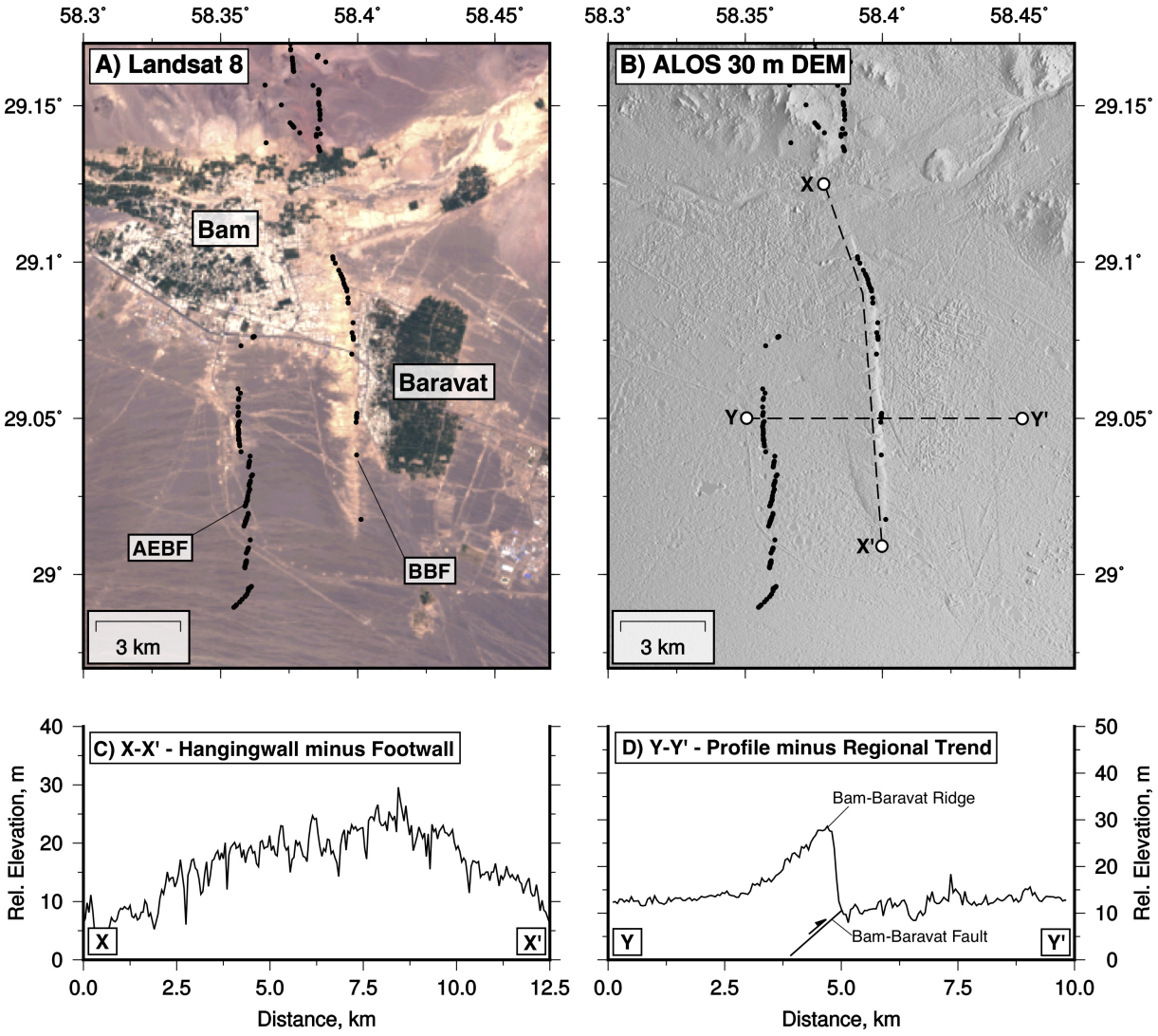

Figure 2.2 Geomorphology and surface ruptures at Bam. (a) Landsat 8 image (bands 4,3,2) of Bam and the surrounding region. Black dots mark the locations of the coseismic surface ruptures from the 2003 earthquake [Jackson et al., 2006]. Those in the west have an en-echelon left-stepping pattern, consistent with right-lateral motion on the Arg-e-Bam Fault. The ruptures in the east occur along the front of the Bam-Baravat Ridge, and are associated with thrust motion on the Bam-Baravat Fault. (b) ALOS 30 m digital elevation model highlighting the location and morphology of the Bam-Baravat Ridge. (c) The variation in the along-strike elevation of the ridge's crest relative to the adjacent plains to the east. (d) A topographic profile perpendicular to the ridge, with the regional trend removed.

2.2.4 Limited Postseismic Moment Release at Bam

Fielding et al. [2009] used InSAR to study the postseismic deformation immediately after the Bam earthquake, between 2004 and 2007. They performed an inversion for the afterslip distribution on the faults at Bam required to match the InSAR observations, and found there had been only 10-15 cm of shallow afterslip above 5 km depth on the Arg-e-Bam Fault, and 10-15 cm of afterslip along the base of the Bam-Baravat Fault. The afterslip model of Fielding et al. [2009] accounts for a postseismic moment release of 1-3$\times 10^{17}$ Nm, corresponding to 1-3% of the coseismic geodetic moment release [Funning et al., 2005b].

The ratio of postseismic to coseismic moment release M_p/M_c in the Bam earthquake (1-3%) lies well below that of other earthquakes that have been studied using similar techniques (Fig. 2.3). The compilation in Fig. 2.3 includes large-magnitude subduction zone earthquakes that cause significant viscous flow in the lower crust and upper mantle, with the associated surface deformation potentially being mapped into moment release through afterslip, leading to an over-estimate of M_p/M_c. However, this effect will be limited for smaller magnitude, shallow earthquakes, which induce far less viscous flow in the lower crust. As the difference in M_p/M_c between Bam and the other earthquakes is consistent across both subduction zone events and smaller intra-continental events, the inference that M_p/M_c at Bam is anomalously low appears robust.

There are a number of possible reasons for the low M_p/M_c at Bam. Firstly, the InSAR time-series of Fielding et al. [2009] may not have fully sampled the postseismic transient, missing some component of afterslip that contributed to the postseismic moment release. Secondly, there may be extensive afterslip below the coseismic rupture that was not captured by in the InSAR time-series, as surface deformation measurements are relatively insensitive to slip at depth due to the filtering effects of the overlying elastic crust. Finally, the low M_p/M_c could be a product of the frictional properties of the fault. Fault zones that show the opposite behaviour to Bam, in which M_p/M_c is $\gtrsim$80%, are consistently located near parts of the fault surface that have interseismic creep rates similar to the far-field loading rate. Examples include the Parkfield section of the San Andreas Fault [Barbot et al., 2009] and the Longitudinal Valley Fault in Taiwan [Thomas et al., 2014a]. On these faults there is limited frictional locking around the asperities that ruptured coseismically, therefore afterslip was free to occur without any elastic resistance caused by adjacent locked zones. The opposite may be the case at Bam.

The remainder of this chapter is focused on investigating why there has been limited postseismic deformation at Bam. In the next section, I develop a new, extended postseismic InSAR time-series to place constraints on the deformation mechanisms following the Bam earthquake and to probe the rheological properties of the fault zone.

2.3 Observations: Postseismic InSAR

Fielding et al. [2009] produced an InSAR time-series of the ground deformation between 2004 and 2007 at Bam to study the postseismic deformation on the top two kilometres of the Arg-e-Bam Fault. However, across both the northern tip of the Arg-e-Bam Fault, and across the surface outcrop of the

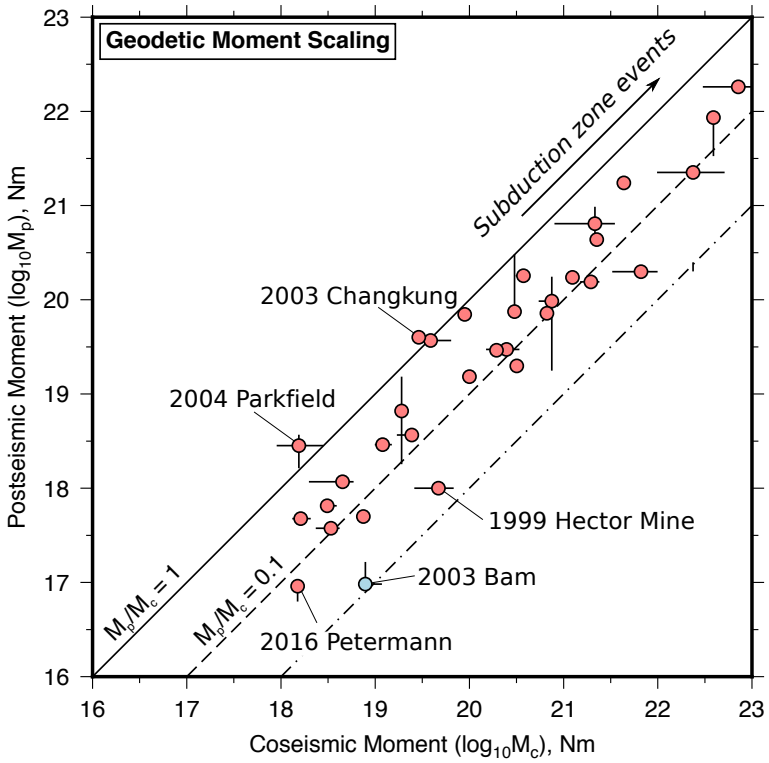

Figure 2.3 Compilation of the postseismic and coseismic geodetically-derived moment release estimates from published studies of earthquakes (see Appendix A). Uncertainties are estimated from the spread in moment release estimates from different published inversions. Points without uncertainty bars represent earthquakes with only one published inversion with no formal uncertainty estimates.

Bam-Baravat Fault, Fielding et al. [2009] did not recover any ground deformation measurements. This shortcoming was predominantly due to the small-baselines processing flow used to construct their time series, which only selects pixels that pass a particular coherence threshold [e.g. Berardino et al., 2002]. As coherence is a measure of the stability of a pixel's phase in relation to the pixels surrounding it, then areas that contain large numbers of decorrelated pixels but a few stable pixels, such as the vegetated areas next to buildings in Bam and Baravat, were not included in Fielding et al. [2009]'s time-series. In this chapter, my focus is on the ground displacements associated with afterslip around the tips of Arg-e-Bam Fault and across the Bam-Baravat Fault, which requires resolving ground deformation that is not present in the study of Fielding et al. [2009]. To address this limitation, I produced a new, extended time-series of postseismic deformation using SAR data collected by Envisat between 2004 and 2009, from ascending track 156 and descending track 120.

The SAR data was processed using a combined persistent-scatter and small-baselines approach implemented in the software StaMPS [Hooper et al., 2004, 2007]. Combined processing optimizes the coherent pixel density in the radar scene by selecting pixels that have stable phase characteristics through time, such as pixels that contain buildings and walls, irrespective of the phase characteristics of surrounding pixels (unlike small-baselines processing). Single-look complex images were focused using ROI_PAC [Rosen et al., 2004] and interferograms generated using DORIS [Kampes and Usai, 1999], with Delft orbital ephemerides and topographic corrections performed using an SRTM 90 m elevation model [Farr et al., 2007]. Interferograms were then unwrapped using a statistical-cost network-flow algorithm [Chen

and Zebker, 2001]. I attempted to remove any relic orbital effects and a component of long-wavelength atmospheric noise by subtracting a linear ramp from each interferogram. The resulting data set consists of an ascending-track time series that includes 25 SAR acquisitions and a descending-track time series that includes 28 acquisitions (Fig. 2.4, 2.5).

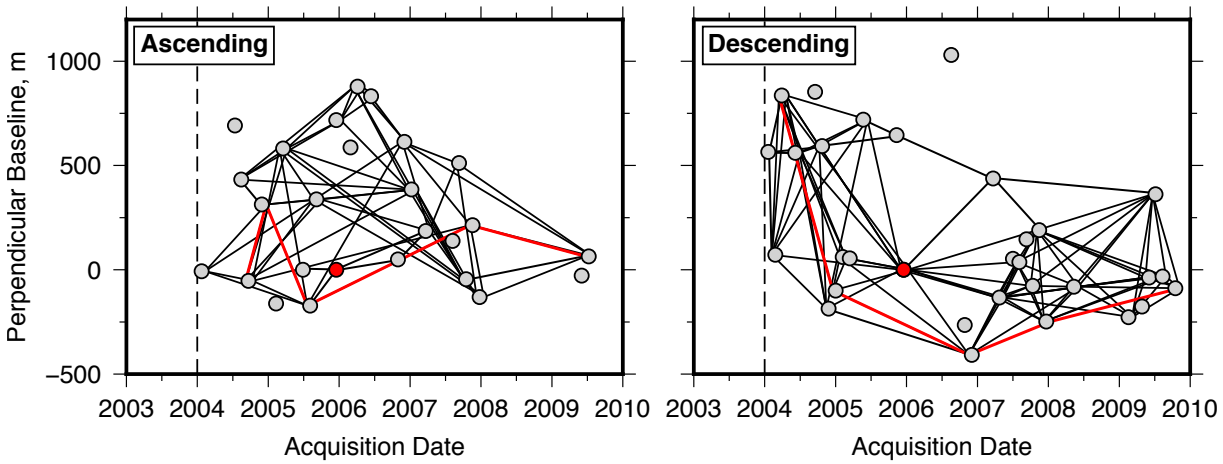

Figure 2.4 Baseline-time plot of the SAR acquisitions and interferograms used in creating the time series and the chain-stack interferograms. The grey circles correspond to individual SAR acquisitions, with the black lines representing an interferogram pair. Grey circles without any connecting lines are SAR acquisitions that contain significant atmospheric noise, so were not used in constructing the time series. The red circle is the reference frame used in the persistent-scatter processing. The black dashed line is the time of the 2003 Bam earthquake and the red lines represent interferogram pairs used in creating the chain stacks shown in Fig. 2.8.

The combined persistent-scatter and small-baselines time series only focuses on a small region surrounding the fault zone due to computational limitations (see Fig. 2.5). Therefore, to study the long-wavelength deformation tens of kilometres from the fault, I also produced 118 descending and 66 ascending track interferograms with perpendicular baselines <500 m processed with ROI_PAC [Rosen et al., 2004], using Delft orbital ephemerides and the SRTM 90 m elevation model to correct for the effect of topography on radar phase. These interferograms were unwrapped using the branch-cut algorithm [Goldstein and Werner, 1998] and a linear ramp was removed. I formed a series of chain-stacks by summing the phase in multiple interferograms with short temporal and perpendicular baselines that share a common reference image [e.g. Biggs et al., 2007]. The resulting chain-stacked interferograms contain the cumulative ground displacements over the time period 2004-2009, and have reduced noise levels compared to individual interferograms covering the same period with long temporal baselines. All the InSAR measurements use the convention that positive line-of-sight changes correspond to motion of the ground towards the satellite.

2.3.1 Results: Postseismic InSAR

The InSAR time-series of postseismic ground deformation is shown in Fig. 2.5 and Fig. 2.6. The spatial pattern of the signals around the tips of the Arg-e-Bam Fault (Fig. 2.5), and their temporal evolution (Fig. 2.6), are consistent with deformation caused by transient postseismic strike-slip motion around the

periphery of the coseismic rupture [Fielding et al., 2009]. The temporal evolution of ground deformation shows initial rapid motion in the first 2 years following the earthquake, after which deformation slows significantly, until the postseismic transient is complete at the end of the observation period (Fig. 2.6).

The time series indicate that the postseismic moment release in the shallow fault zone estimated from Fielding et al. [2009] is likely to be robust because: (1) the low M_p/M_c is not due to incomplete sampling of a long-lived postseismic transient, and (2) extrapolating each of the time-series back to the time of the earthquake using a logarithmic function of the form $u(t) = a\ln(1 + t/t_r)$ suggests that only minor (∼0.5-2 cm) line-of-sight (LOS) displacement may have been missed in the early postseismic period, where there is no SAR data. This unsampled deformation does not account for the order of magnitude difference between M_p/M_c observed at Bam and the majority of other studied earthquakes (Fig. 2.3).

Across the escarpment of the Bam-Baravat Ridge a negative ∼1 cm step change in LOS is visible from west to east in both the ascending and descending interferograms (Fig. 2.5, profile A-A'), which increases in amplitude monotonically through time. This signal is too short wavelength and temporally too consistent to be associated with atmospheric noise. The positive LOS displacement of the ridge relative to the adjacent plain is opposite to what would result from aquifer discharge through the qanat tunnels at Baravat, as this would cause subsidence of the ridge and therefore negative LOS change relative to the adjacent plains. In addition, the change in elevation across the ridge front (15-30 m) and digital elevation model errors are too small to account for the 1 cm step-change in LOS. I conclude that this signal is tectonic and represents shallow, thrust-orientated creep on the Bam-Baravat Fault underlying the ridge. As there was no resolvable interseismic LOS displacement across the ridge between 1992 and 1999 [Fialko et al., 2005], the shallow creep probably initiated following the 2003 Bam earthquake in response to coseismic stress changes.

I found no obvious tectonic deformation signals that occur on length-scales of 10-20 km in the InSAR data, suggesting any afterslip or visco-elastic deformation at depth must lead to surface displacements smaller than the amplitude of the noise in the InSAR measurements (∼1.5 cm at 10-20 km wavelength). In the following section, I use this limit on the amount of long-wavelength deformation in the interferograms, in addition to aftershock locations and forward modelling, to place constraints on the rheology of the deep fault zone at Bam, and the extent to which coseismic stress changes may have been relaxed by postseismic deformation.

2.4 Deep Postseismic Deformation

2.4.1 Aftershocks

Deep afterslip has primarily been found to be co-located with, and share the same temporal evolution as, deep aftershock sequences [Perfettini, 2004; Savage et al., 2005; Hsu et al., 2006; Peng and Zhao, 2009; D'Agostino et al., 2012; Mencin et al., 2016]. In addition, aftershock sequences are often localised around the edges of the coseismic rupture and share at least one nodal plane with the mainshock [Bodin and Horton, 2004; Tatar et al., 2005], indicating that some aftershocks represent failure on the

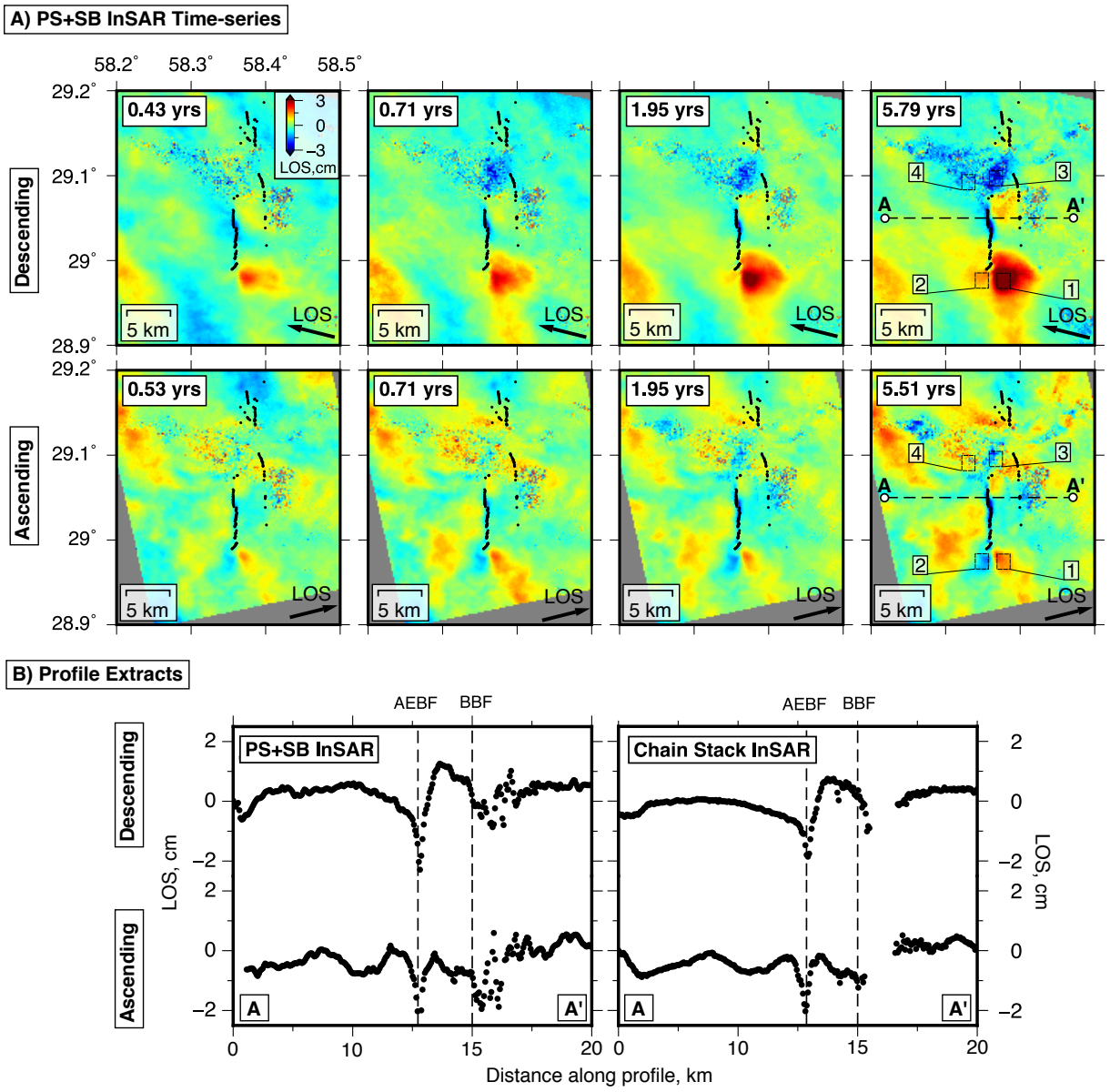

Figure 2.5 Time series of postseismic line-of-sight (LOS) displacements from the combined persistent-scatter and small-baselines InSAR processing (PS+SB). (a) Cumulative surface displacements through time, with time increasing from left to right. The time of each snapshot after the first SAR acquisition in January 2004 is shown in the top left corner. Black dots are the coseismic surface ruptures, and the satellite look vector projected into the horizontal plane is shown in the bottom right of each image (the incidence angle is ∼23°). I use the convention that positive LOS change is motion towards the satellite. (b) Profiles of LOS displacement extracted between A-A' from both the combined (PS+SB) time-series after 5.7 years, and the chain-stacked interferograms covering the same time period. The location of the profile's intersection with the faults are outlined with vertical dashed lines. The sharp negative LOS change over the Arg-e-Bam Fault was studied by Fielding et al. [2009] and has been interpreted to reflect poro-elastic compaction of the shallow fault zone.

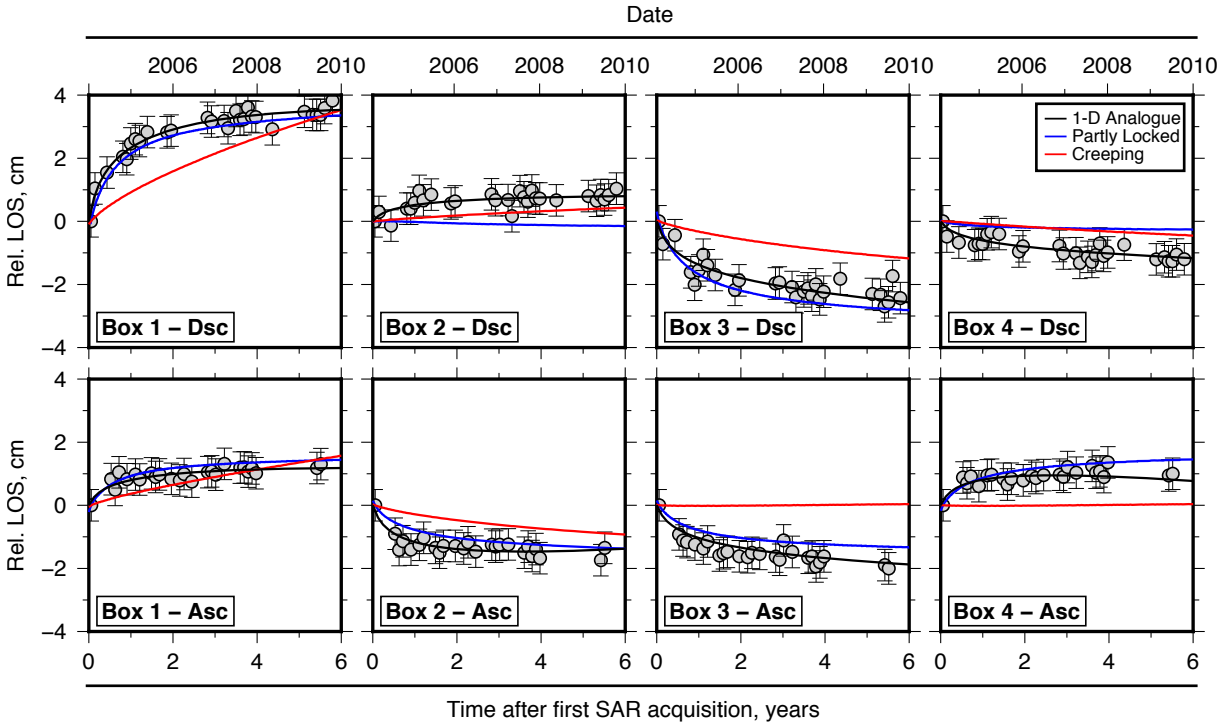

Figure 2.6 Relative line-of-sight (LOS) displacement time-series for the 4 small boxes highlighted in Fig. 2.5. The grey points represent the difference between the average LOS displacement within the box, and a collection of reference pixels (point 5 in Fig. 2.10a). The error bars are the combined standard deviation of the pixel LOS in the box and the reference pixels. The solid black lines are the best-fitting functions from a 1-D spring-slider analogue model [Perfettini, 2004]. The red line is the best-fitting stress-driven afterslip forward model when the Arg-e-Bam and Bam-Baravat Faults are allowed to creep (surface displacements shown in Fig. 2.10). The blue line is a stress-driven afterslip forward model in which only small patches around the edge of the coseismic rupture are allowed to creep, with the remainder of the fault zone remaining locked. The surface displacements associated with this 'partially-locked' fault model are shown in Fig. 2.11 and the distribution of the creeping patches in Fig. 2.12

same fault surface as the mainshock. Therefore local aftershock studies may provide some insight into whether deep afterslip is occurring at Bam.

The aftershock sequence recorded at Bam consists of two catalogues: one produced by a dense local array of 23 stations deployed throughout January 2004 [Tatar et al., 2005], and a smaller local array of 9 stations recording between February and March 2004 [Nakamura et al., 2005]. I only consider the catalogue of Tatar et al. [2005], as the 5 km station spacing used in their study is small enough to reliably estimate the depth of events with ±2 km uncertainty within the seismogenic layer (0-20 km).

The aftershock distribution from Tatar et al. [2005] indicates that seismicity was focused between 10 and 18 km depth, and almost absent from the region directly over, and along-strike from, the coseismic rupture (Fig. 2.7a). A similar pattern was also observed following the 2004 and 2009 Qeshm Island earthquakes in Iran [Nissen et al., 2010]. The aftershocks follow a decay in frequency as a function of time (Fig. 2.7b), but their locations do not change with time (Fig. 2.7c). Finally, the majority of the well-constrained aftershock mechanisms have at least one nodal plane compatible with right-lateral motion along N-S planes, the same mechanism as the mainshock [Tatar et al., 2005]. All three observations are consistent with the aftershocks being a product of transient afterslip loading and breaking small asperities along the down-dip edge of the coseismic slip patch.

The absence of aftershocks along-strike from the coseismic rupture indicates this region is either too strong to break in response to the coseismic stress changes, or that the region is creeping and contains no locked patches. I explore these two possibilities later in Section 2.5.

2.4.2 Forward Calculations of Deep Afterslip

The postseismic InSAR measurements contain no evidence of the long-wavelength deformation signals that might be associated with afterslip in the region of aftershocks on the Arg-e-Bam Fault (Fig. 2.8a,c). Therefore, afterslip at depth cannot lead to surface displacements greater than the noise levels in the InSAR measurements, placing a bound on the amount of deep fault creep that could relax the coseismic stress changes on the bottom 10-20 km of the Arg-e-Bam Fault.

I performed a set of calculations for the LOS motions that would result from afterslip in the region of the aftershock activity beneath the coseismic rupture, simulating afterslip as motion on a dislocation in an elastic half-space [Okada, 1985]. The crust was taken to have a shear modulus of 30 GPa and a Poisson's ratio of 0.25, which is consistent with the local 1-D velocity model determined by Tatar et al. [2005]. The along-strike length, dip and rake of the slipping fault were all fixed to the fault geometry determined by Funning et al. [2005b]. The top of the afterslip patch was fixed at 10 km depth, near the base of the coseismic rupture, and I varied the amount of afterslip and the down-dip width of the slipping patch. Surface displacements for each calculation were then converted into satellite LOS.

The afterslip signal should be visible if its amplitude is larger than the apparent LOS changes in the interferograms arising from noise sources (i.e. there is a signal-to-noise ratio >1). To estimate the amplitude of the signals unrelated to postseismic deformation, I calculated the standard deviation of the pixel phase within the interfergram, masking out areas that contain clear tectonic deformation signals. Typically the standard deviation of the far-field noise is equivalent to ∼1-1.5 cm of apparent

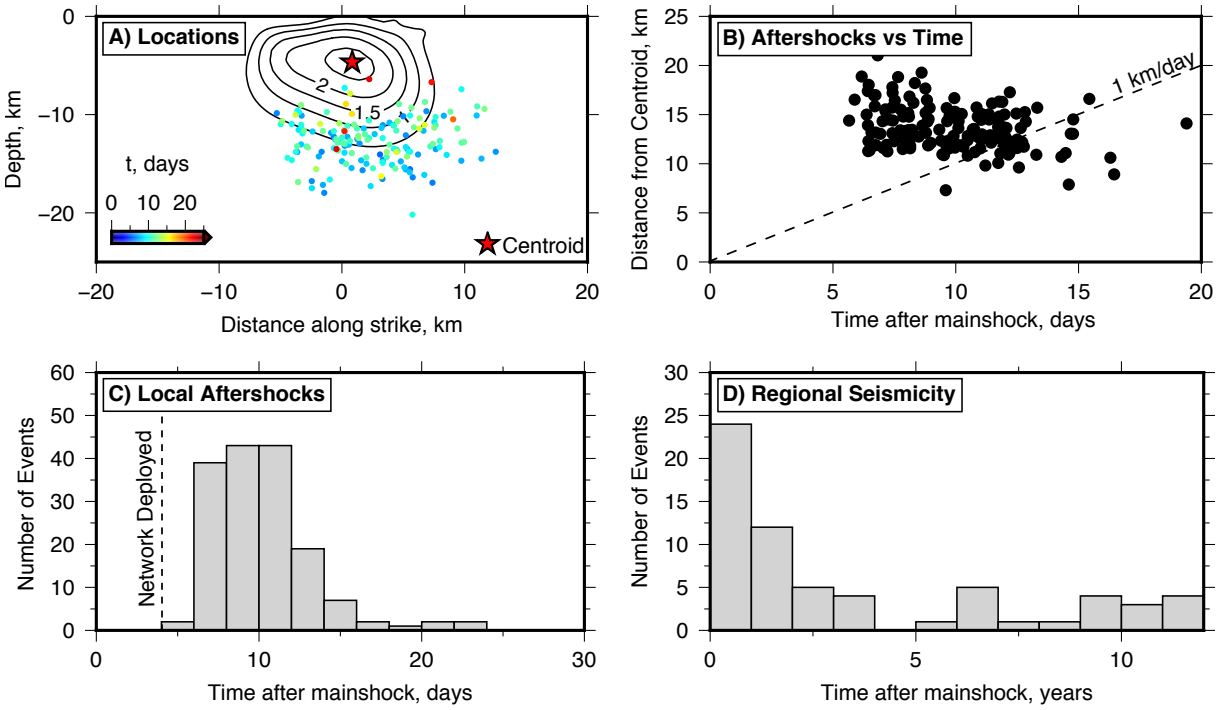

Figure 2.7 Characteristics of the Bam aftershock sequence. (a) Hypocentral location of each aftershock from the local survey of Tatar et al. [2005] projected onto the fault plane and colour coded by the time after the mainshock. Contours of slip are taken from Funning et al. [2005b]. (b) Temporal evolution of aftershock locations relative to the surface projection of the mainshock centroid. (c) Temporal decay in aftershock frequency as a function of time following the mainshock from the catalogue of Tatar et al. [2005]. (d) Temporal decay in regional seismicity as a function of time following the mainshock in the region between 58.2-58.5^{o}E and 28.9-29.2^{o}N from the catalogue of Karimiparidari et al. [2013]. Prior to the earthquake, there was no seismicity at Bam in the same area recorded in the catalogue of Karimiparidari et al. [2013].

LOS displacement. Therefore, if the signals generated by afterslip were >1.5 cm LOS motion in either the ascending or descending interferogram, they should be visible in the InSAR measurements.

If the region experiencing afterslip overlaps with the area of aftershock activity on the lower half of the Arg-e-Bam Fault between 10 and 18 km depth, there must be <50 cm of deep afterslip for the resulting surface displacements to remain invisible in the InSAR measurements (Fig. 2.9a). This corresponds to a maximum 'invisible' geodetic moment release of 1.5×10^{18} Nm by deep afterslip, which is equivalent to 10% of the coseismic moment release. Hence, it is possible that afterslip at depth could account for the difference in M_p/M_c between Bam and the lower end of other studied earthquakes' moment scaling (Fig. 2.3). However, it is not clear why there would be 50 cm of afterslip below the coseismic rupture, yet only 10-20 cm of afterslip around the rupture in the shallow fault zone [Fielding et al., 2009], unless there is significant vertical variability in the fault's frictional properties.

The lack of both co- and post-seismic fault slip (< 50 cm) between 10 and 18 km depth relative to the shallow coseismic slip (2.7 m) suggests that $\lesssim$ 20% of the coseismic shear stress changes on the bottom 10 km of the Arg-e-Bam fault zone have been released through postseismic afterslip.

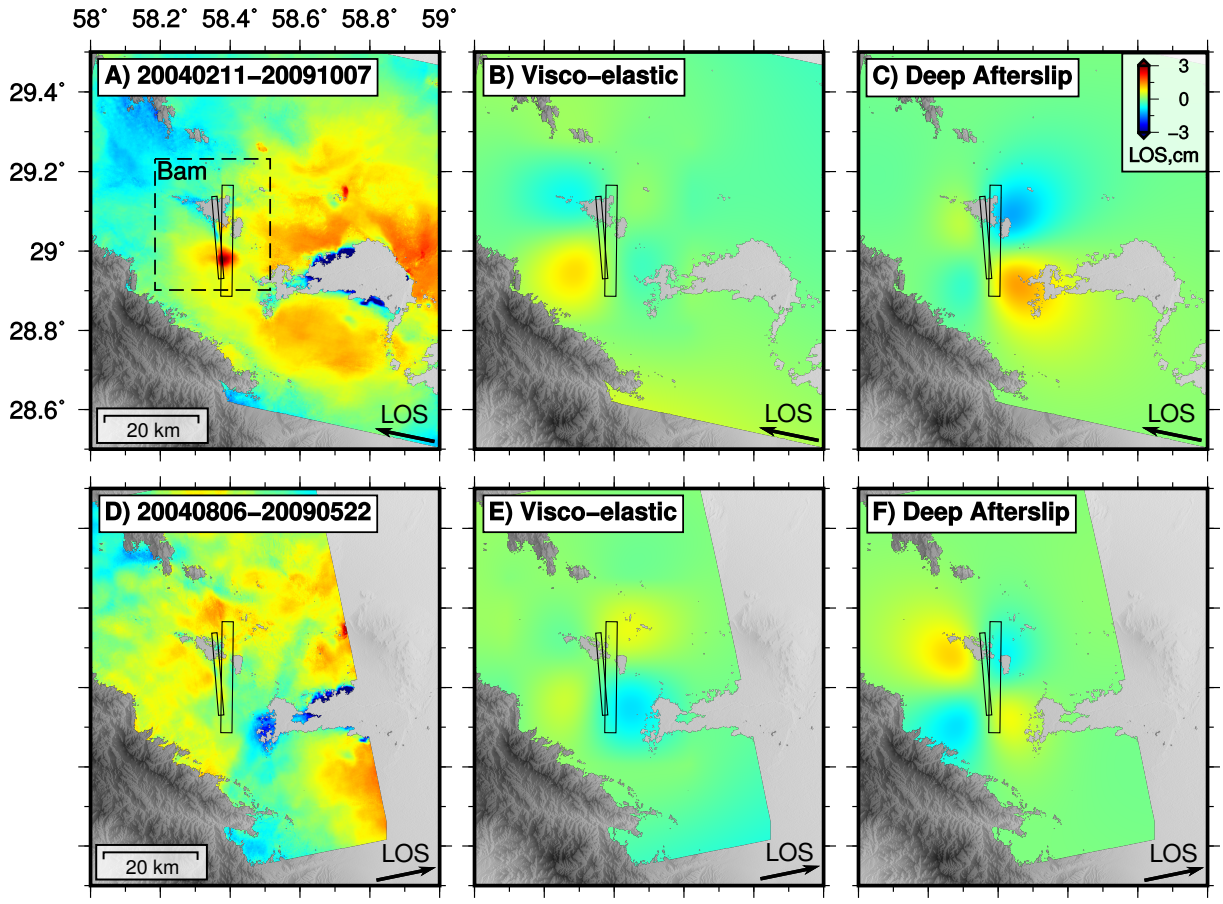

Figure 2.8 A comparison of line-of-sight (LOS) displacements in chain-stack interferograms with forward calculations of visco-elastic relaxation and deep afterslip following the Bam earthquake. (a,d) Descending and ascending chain-stack interferograms over the period displayed in the title with the format YYYYMMDD. The dashed box in (a) is the area shown in Fig. 2.5. (b,e) Calculated LOS displacements resulting from 5.7 years of visco-elastic relaxation due to stress changes in the Bam earthquake. The calculations were performed using a model with a 15 km thick elastic lid overlaying a linearly-viscous half-space with viscosity 1×10^{19} Pa s. (c,f) Calculated LOS displacements due to 50 cm of afterslip along the base of the Arg-e-Bam Fault between 10 and 18 km depth.

2.4.3 Forward Calculations of Visco-elastic Relaxation

An alternative mechanism for stress release beneath the Arg-e-Bam Fault zone is viscous flow in the lower crust [e.g. Freed and Bürgmann, 2004; Ryder et al., 2007]. At crustal temperatures $>350^oC$ the creep strength of hydrous, quartz-rich rocks becomes smaller than their frictional strength, meaning that deformation preferentially occurs via grain-scale creep as opposed to frictional sliding [e.g. Bürgmann and Dresen, 2008]. These conditions are probably satisfied at >15-20 km depth at Bam, as the aftershock seismicity was confined above this depth range.

To simulate the postseismic viscous flow beneath the Arg-e-Bam Fault, I constructed a simple model of an elastic layer, representing the brittle crust, overlying a homogeneous, linearly-viscous half-space, which represents the crust at high enough temperatures that diffusion creep can occur over the timescale of years. Including spatially heterogeneous viscosity structure associated with a weak sub-crustal shear zone [e.g. Yamasaki and Houseman, 2012] would lead to only second order effects, and will not be

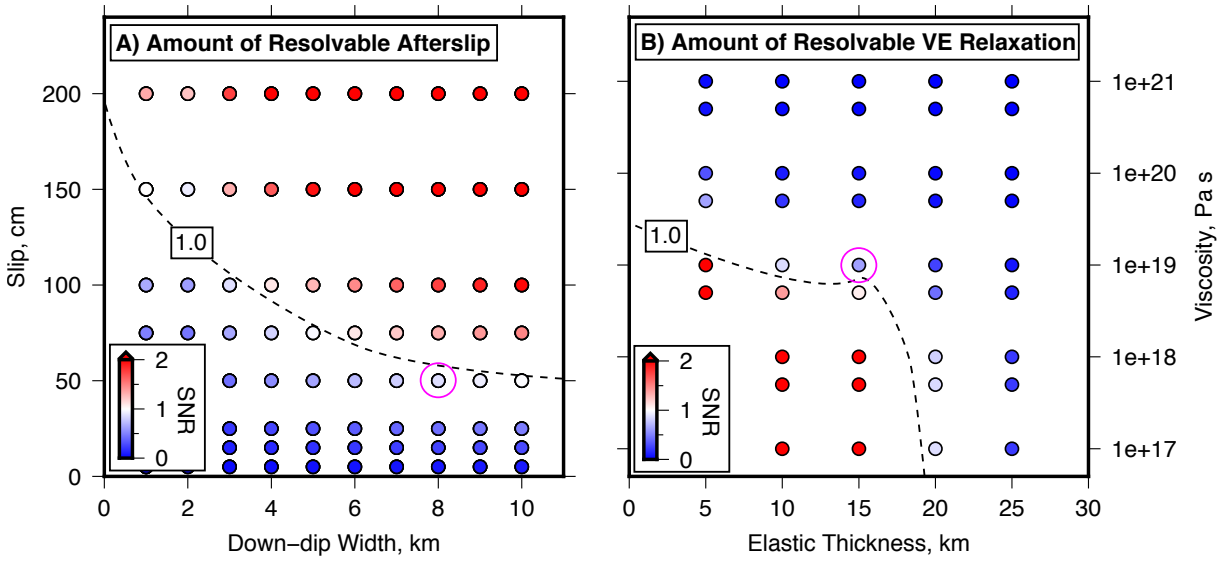

Figure 2.9 Calculations for the amplitude of the ground deformation resulting from deep afterslip and visco-elastic relaxation on the Arg-e-Bam Fault, converted into a signal-to-noise ratio (SNR). A SNR = 1 contour marks the upper bound on the amount of deep afterslip and visco-elastic relaxation that could occur without being visible in the interferograms. (a) The SNR for deep afterslip below the coseismic rupture over the period covered by the InSAR measurements. The purple circle corresponds to the model shown in Figs. 2.8c and f. (b) The SNR for visco-elastic relaxation with a variable elastic layer thickness and half-space viscosity. The purple circle corresponds to the model shown in Figs. 2.8b and e.

considered further. The system was perturbed by the stress changes from the Bam earthquake, leading to flow in the viscous lower crust that relaxes the coseismic stress changes, and deforms the overlying elastic upper crust. No slip is allowed on the Arg-e-Bam Fault. The polarity of the resulting surface deformation is opposite to that resulting from afterslip (Fig. 2.8b,c). I performed calculations for a range of elastic-layer thicknesses and half-space viscosities using the Computational Infrastructure for Geodynamics code RELAX [Barbot et al., 2009; Barbot and Fialko, 2010b,a]. To compare the model predictions with the InSAR observations, I projected the modelled surface displacements 5.7 years after the coseismic stress changes into the satellite LOS, and compared the amplitude of the modelled deformation with the noise levels in the interferograms.

It is not immediately clear what elastic layer thickness to use in these models. Aftershocks extending down to ∼18-20 km depth immediately after the Bam earthquake imply that, at the elevated strain rates in the early postseismic period, elastic strain can accumulate and be released in material at <20 km depth. Over the timescale of multiple earthquake cycles and longer, the seismogenic thickness of the crust is typically slightly larger than the effective elastic thickness of the lithosphere [Jackson et al., 2002, 2008], suggesting that earthquake depths slightly overestimate the depth to which the lithosphere holds longer-term elastic strength. Therefore, I consider a realistic estimate of the thickness of the elastic layer to use in these models is ∼15-20 km (i.e. slightly less than the seismogenic thickness).

If the elastic layer is 15 km thick, then the minimum possible viscosity of the underlying half-space would be $\sim 1 \times 10^{19}$ Pa s (Fig. 2.9b). If the viscosity were any lower, the surface deformation resulting from viscous flow in the lower crust should be visible in the interferograms. For higher elastic layer

thicknesses, the viscosity of the lower crust and upper mantle could be significantly lower and still the postseismic visco-elastic relaxation would not be visible in the interferograms (Fig. 2.9b).

Any viscous flow that occurs beneath the brittle crust in response to coseismic stress changes will begin to reload the overlying fault zone. The larger the viscous flow, the greater the reloading of the deep fault zone, particularly just above the brittle-ductile transition. The calculations suggest that, if the lower crust had a viscosity of $\sim 1 \times 10^{19}$ Pa s below 15 km depth, then 5.7 years after the earthquake viscous flow could increase the average shear stress on the bottom 10-15 km of the Arg-e-Bam Fault by a maximum of ∼15% of the coseismic stress changes on the same fault patch.

The calculations presented above are highly sensitive to the assumed rheology, particularly the thickness of the elastic layer (Fig. 2.9b) and the nature of the brittle-ductile transition region. Therefore the values for the stress changes are unlikely to be accurate. Nonetheless, they suggest that the lack of observed long-wavelength postseismic deformation reflects limited deep afterslip and limited viscous flow immediately beneath the coseismic rupture on the Arg-e-Bam Fault.

In contrast, the InSAR observations captured 3-4 cm of short-wavelength ground deformation focused around the tips of the coseismic surface ruptures, with the rate of the deformation decayed rapidly in the first two years after the earthquake (Fig. 2.5, 2.6). In the following section, I assess whether the shallow postseismic deformation is consistent with models of stress-driven afterslip on the faults at Bam, and determine the frictional properties of the shallow fault zone.

2.5 Shallow Postseismic Deformation

To relate the coseismic stress changes on the fault zone following the Bam earthquake to the resulting afterslip, I employ the rate-and-state friction parameterisation [Dieterich, 1978; Ruina, 1983; Scholz, 1998]. This empirical description of friction has been applied to both laboratory [Ruina, 1983; Marone, 2003] and natural faults [Perfettini and Avouac, 2007; Copley and Jolivet, 2016], and appears to be a good approximation of the constitutive relationship that governs steady-state fault slip in the upper crust. A preliminary test of the application of this formulation to the faults at Bam is to compare the observed deformation with simple analogue models of steady-state, rate-strengthening fault creep.

2.5.1 1-D Fault Analogue Models

The temporal evolution of the LOS displacements in Fig. 2.5 can be compared to a simple 1-D fault analogue. One such model treats the fault mechanics as a spring-slider block system with friction along its base governed by a simplified rate-strengthening friction law [Perfettini, 2004]. According to this model, ground deformation following a stress change $\Delta\tau$ will evolve as: $u(t) = \alpha V_0 t + \beta V_0 t_r \log\left[1 + d(\exp(t/t_r) - 1)\right]$, where α and β are geometric constants, V_0 is the interseismic creep rate, t_r is the relaxation time and $d = \exp(\Delta\tau / a\sigma'_n)$, where $a = \partial\mu_{ss}/\partial\log(V)$ gives the dependence of steady-state friction on sliding velocity, and σ'_n is the effective normal stress acting on the modelled fault.

I found this model provides a good fit to the observations with the same relaxation time ($t_r = 1.3$ years) and friction parameters for all LOS time-series extracted over areas of afterslip (Fig. 2.6), but the solutions were non-unique due to trade-offs between the geometric constants and friction parameters. Nonetheless, the consistent relaxation time for all time-series suggests that the postseismic deformation at Bam is compatible with creep on patches of the fault with uniform friction properties. The subsequent modelling builds on this suggestion by implementing a more geometrically realistic, quasi-static model of afterslip driven by coseismic stress changes.

2.5.2 Coseismic Stress-Driven Afterslip Models

Measurements of postseismic deformation record the effects of multiple superimposed mechanisms including afterslip, visco-elastic relaxation and poro-elastic rebound [Jónsson et al., 2003; Jónsson, 2008; Hsu et al., 2006]. In the previous section I showed that visco-elastic relaxation and deep afterslip have no resolvable effect on the short-wavelength (<10 km) surface deformation at Bam, hence can be ignored. I also calculated the deformation resulting from poro-elastic rebound by taking the difference between the coseismic deformation for an elastic model calculated with a drained and undrained Poisson's ratio ($\nu_d = 0.25$ and $\nu_{ud} = 0.28$, respectively) [e.g. Peltzer et al., 1998]. Deformation caused by poro-elastic rebound was found to correspond to a maximum of ∼1 cm LOS motion, which is small compared to the observed transient LOS motion (∼3-4 cm). As a result, I assume the InSAR measurements around the fault tips, on a wavelength of 2-10 km, are dominated by shallow afterslip.

To model the surface deformation caused by stress-driven afterslip at Bam, I performed a series of calculations using the fault mechanics code `RELAX` [Barbot et al., 2009; Barbot and Fialko, 2010b,a; Rousset et al., 2012], and compared the forward calculations to the InSAR time-series of ground deformation to determine the frictional properties of the fault zone.

The initial condition in the models is the fault geometry and coseismic slip distribution along the two faults taken from the source model of Funning et al. [2005b], which is used to calculate the stress changes driving afterslip. I assume that afterslip is occurring on the along-strike and down-dip extensions of the faults that ruptured coseismically.

The magnitude of the stress changes are a function of the input slip model and the elastic moduli of the shallow crust (computed from the velocity models of Tatar et al. [2005]). Following the approach of Barbot et al. [2009], I adapted the model of Funning et al. [2005b] by compacting the coseismic slip distribution to account for three effects: (1) the dynamic propagation of coseismic slip into regions that may otherwise creep [Noda and Lapusta, 2013], (2) the smoothing of the slip distribution introduced by the Laplacian regularisation in the coseismic slip inversion [e.g. Funning et al., 2005b], and (3) the possibility of afterslip overlapping with regions of reduced coseismic slip [e.g. Jacobs et al., 2002; Copley et al., 2012]. The slip distribution was compacted by removing areas in which slip is less than some factor ζ of the peak coseismic slip, with the remaining slip distribution re-scaled to maintain the same coseismic geodetic moment. In addition, near-surface coseismic slip under Bam city was removed, as this occurs beneath a region that is decorrelated in the coseismic interferograms [Funning et al., 2005b], therefore is not robust.

In the models the temporal evolution of afterslip driven by the coseismic stress changes is governed by a generalised rate-strengthening friction relationship: $V = V_0 \sinh(\Delta\tau / a\sigma_n)$, where V is the sliding velocity, $\Delta\tau$ is the shear stress change, and V_0 and $a\sigma_n$ are constitutive parameters that are varied to fit the observed time-series of ground deformation [e.g. Barbot et al., 2009]. As the two creeping faults at Bam are in close proximity and cut the same geology, both are assumed to have the same frictional properties.

Coseismic stress changes alone are assumed to be responsible for driving afterslip, with the contribution of any long-term creep presumed to be small (as seen in Fialko et al. [2005]). Once the pattern of afterslip has been calculated, the resulting surface deformation can be computed using Fourier domain Green's functions [Barbot and Fialko, 2010b], allowing comparison of the model with the InSAR time-series observations.

To find the best-fitting afterslip model and friction parameters I performed a grid search of forward calculations varying $a\sigma$, V_0 and ζ and found the model that minimized the reduced chi-square misfit between the InSAR time-series measurements and the corresponding stress-driven afterslip predictions. The model misfit is defined as:

$$\chi_r^2 = \frac{1}{N-P} \sum_{i=1}^{n} \sum_{j=1}^{k} \left[\frac{(\phi_{ij}^{mod} - \phi_{ij}^{obs})}{\sigma_i} \right]^2, \tag{2.1}$$

where N is the number of independent measurements (i.e. the number of pixels), P is the number of variables used in the models, ϕ_{ij}^{mod} is the modelled LOS displacement in the j'th pixel of the i'th interferogram, ϕ_{ij}^{obs} is the observed LOS displacement in the j'th pixel of the i'th interferogram and σ_i is an estimate of the standard deviation of the noise calculated in a non-deforming region of the i'th interferogram. A $\chi_r^2 = 1$ indicates that the model fits the data to within the uncertainties of the observations, but without over-fitting.

2.5.3 Results: Stress-Driven Afterslip Modelling

The best-fitting afterslip model is shown in Fig. 2.10 and corresponds to a $\chi_r^2 = 1.17$ with the associated fitting parameters being $a\sigma_n = 5.5$ MPa, $V_0 = 5$ mm/yr and $\zeta = 0.4$ (i.e. only fault patches with coseismic slip >1 m are included in the input slip model), although the models are relatively insensitive to variations in $a\sigma_n$ (Fig. 2.10c). Other studies have found similar values for the fault friction parameters with $a\sigma_n$ in the range 0.1-10 MPa [Hsu et al., 2006; Perfettini and Avouac, 2007; Barbot et al., 2009; Wei et al., 2015] and V_0 being on the order of the interseismic loading rate, which at Bam is ∼1-3 mm/yr [Walpersdorf et al., 2014].

The calculated afterslip distribution extends outwards from the edges of the compacted coseismic slip patch and reaches a peak slip of 20-30 cm (Fig. 2.10b), which is significantly smaller than the 60-90 cm of afterslip needed to fully relax the coseismic stress changes (see Fig. 2.11 and discussion in Section 2.5.4). On the Arg-e-Bam Fault, slip is almost completely right-lateral and occurs across the depth range of 0-15 km, whilst on the Bam-Baravat Fault the direction of the calculated slip vector is highly variable and afterslip >10 cm is constrained only to the lower half of the fault.

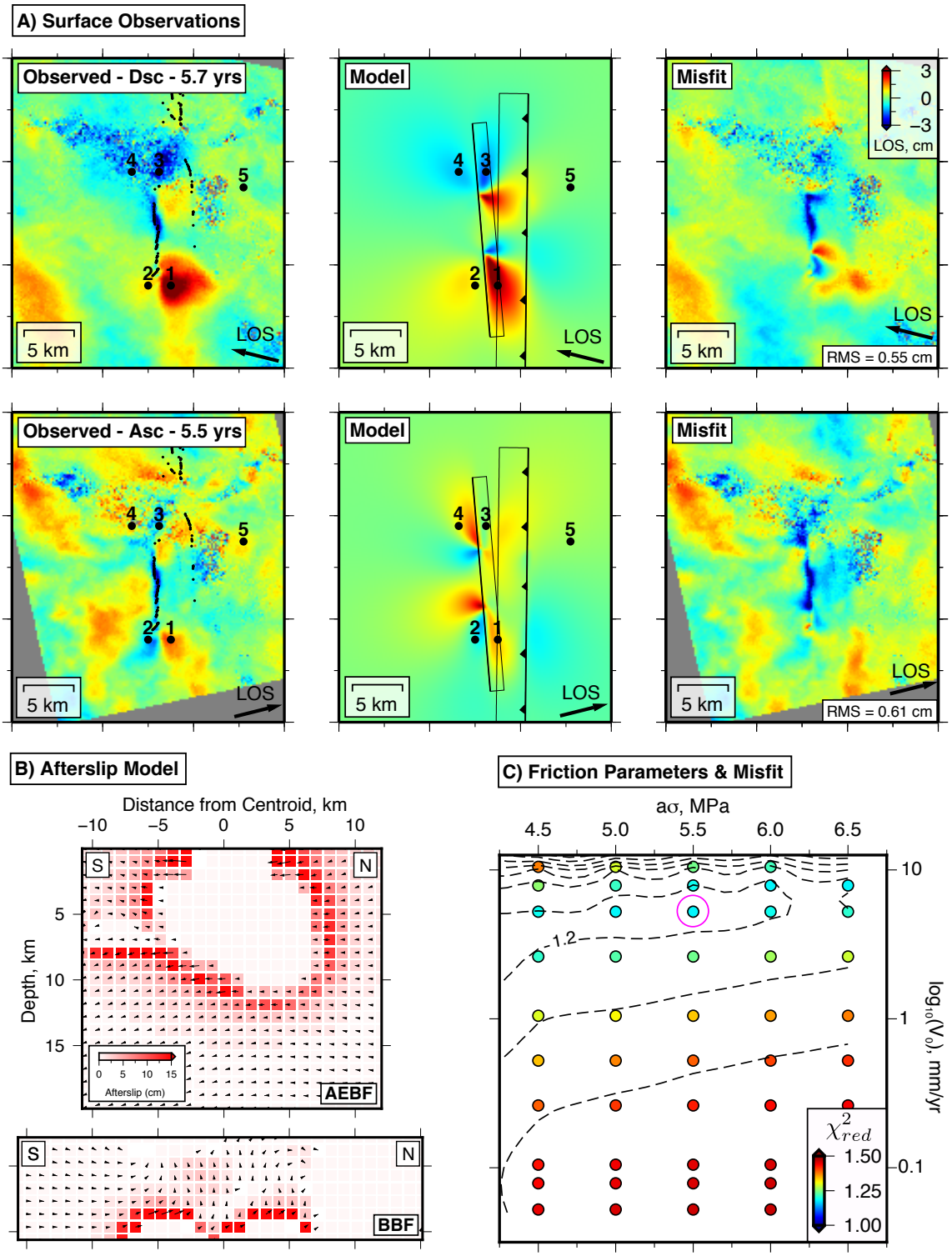

Figure 2.10 Best-fitting stress-driven afterslip model assuming the faults at Bam are both creeping. (a) Observed surface deformation at the end of the InSAR measurement period (left-hand column), the model predictions for the best-fitting stress-driven afterslip calculation (middle column), and the misfit between the models and the observations (right-hand column). Small black dots are the surface ruptures from the 2003 Bam earthquake, and the surface projection of the faults used in the models are shown in the modelled interferograms. Numbered dots represent locations in which a time-series of LOS displacements was extracted in Fig. 2.6. Point 5 is the location of the reference pixels. (b) Afterslip distribution that leads to the surface displacements in (a). Arrows show motion of the hangingwall relative to the footwall. Blank areas are patches of the fault with no afterslip. (c) Reduced chi-square misfit between a set of models with different friction parameters and the InSAR time-series, with the best-fitting model highlighted with a purple circle. The model shown has a geodetic moment release of 5.6×10^{17} Nm, which is 5% of the coseismic geodetic moment.

Misfits in the spatial distribution of ground deformation between the models and observations are on the order of the atmospheric noise within the interferograms (Fig. 2.10a), apart from the narrow strip of negative LOS motion in both tracks directly over the Arg-e-Bam Fault. This negative LOS motion is caused by poro-elastic compaction of the top 1-2 km of the fault zone [Fielding et al., 2009], and is not modelled here, as it is not associated with afterslip. Not accounting for the shallow poro-elastic compaction does not affect the estimate of the best-fitting model, as I do not allow afterslip in this area of the Arg-e-Bam Fault (see Fig. 2.10).

The temporal evolution of ground displacement is fit less well. The modelled LOS displacement time-series in the locations of box 1 and 3 are distinctly different to the observed displacements (box locations shown in Fig. 2.5 and the time-series shown in Fig. 2.6). The LOS changes in box 3 are extracted over the eastern edge of Bam city and are both equally negative in the ascending and descending track, suggesting the ground surface is subsiding in this area. It may be that the tectonic signal near box 3 has been contaminated by some anthropogenic effects, such as groundwater extraction from shallow aquifers in the Posht-e-Rud river. However, in box 1 the afterslip model predicts a much longer relaxation time of deformation than is observed, and the model cannot fit the period of rapid deformation in the first year after the earthquake, which is also a feature of the time-series in all areas of postseismic transient deformation. The best-fit model also predicts that afterslip will continue long after the observations end, which is not consistent with the InSAR measurements (Fig. 2.6).

The afterslip calculations described above cannot fit the observed postseismic surface displacements without either: (1) over-predicting the amplitude of deformation late in the postseismic period, or (2) under-predicting the amount of early, rapid postseismic deformation (see red lines in Fig. 2.6). This feature of the models suggests they over-predict the total amount of stress-driven afterslip following the 2003 Bam earthquake. In the next section, I investigate the possible causes of this over-prediction.

2.5.4 Locking on the Faults at Bam

Afterslip on a creeping fault will continue until the stresses that drive creep have been relaxed, or are balanced by resistance to creep. The postseismic time-series at Bam suggests that shallow afterslip has finished, therefore the stresses on the fault zone that were driving afterslip in the first two years after the Bam earthquake have either been relaxed, or are now balanced by some form of resistance. A calculation that simulates the complete relaxation of coseismic stress changes via afterslip surrounding the coseismic rupture over-predicts the surface deformation by a factor of 3-4 (Fig. 2.11). This suggests either: (1) the calculated coseismic stress changes that drive fault creep are too high, or (2) that creep is resisted by locked portions of the fault surface.

The coseismic stress changes that drive afterslip in the forward models are controlled in part by the input slip distribution. Forward calculations suggest the geodetic moment of the input slip model would have to be as little as $\sim$10% of the best-fitting coseismic moment of Funning et al. [2005b] in order for stress-driven afterslip on entirely creeping faults to cause surface deformation consistent with the postseismic InSAR measurements. Multiple independent slip inversions for the 2003 Bam earthquake [Fialko et al., 2005; Stramondo et al., 2005; Motagh et al., 2006] indicate the coseismic moment can be

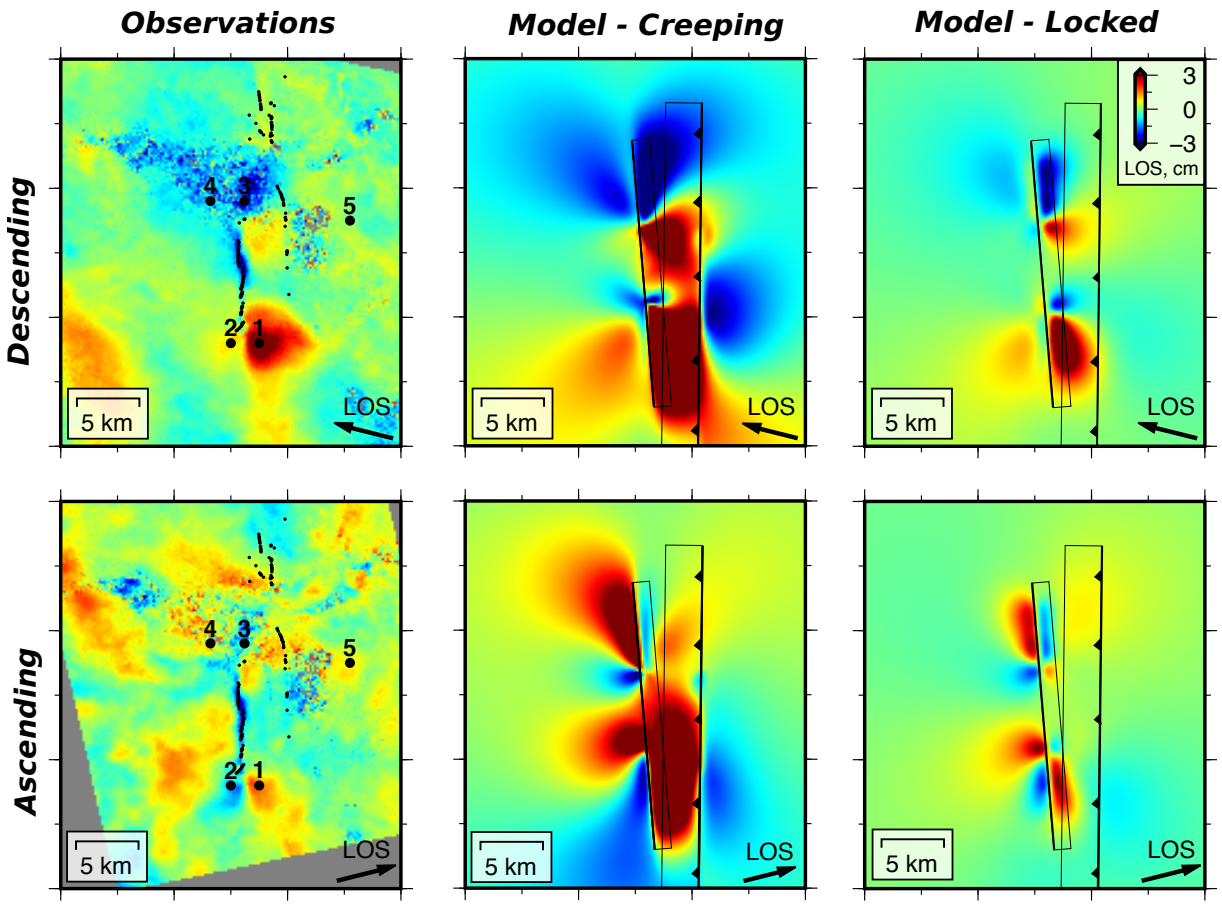

Figure 2.11 Surface deformation resulting from the complete relaxation of coseismic stress changes by postseismic afterslip on a fully-creeping and partially-locked fault. The distribution of creeping patches and locked patches is shown in Fig. 2.12, and the temporal evolution of deformation in the partially-locked model at points 1-4 is shown by the blue lines in Fig. 2.6.

a minimum of 60% of that suggested by Funning et al. [2005b]. Therefore uncertainties in the input coseismic slip model cannot account for the over-prediction of afterslip following the Bam earthquake.

The elastic moduli of the upper crust will scale the coseismic stress changes driving afterslip by making the region around the coseismic rupture more or less compliant. For the total amount of surface deformation predicted in the stress-driven afterslip calculations to be consistent with the observed postseismic deformation would require the elastic moduli of the crust at Bam to be only ∼10% of the best-fit values determined from the seismic velocity models of Tatar et al. [2005]. By combining the uncertainties from the velocity models with a realistic range of crustal densities (2500-2900 kg/m^3), the elastic moduli are likely within ∼75% of the best-fit values of Tatar et al. [2005]. Therefore uncertainties in the bulk elastic properties of the crust cannot account for the over-prediction of afterslip at Bam. Geodetic and seismological studies have also suggested that compliant fault damage zones can have elastic moduli some 50% less than the adjacent undamaged country rock [Fialko et al., 2002; Cochran et al., 2009]; even so, this still cannot reduce the elastic moduli enough to reconcile the model predictions with the InSAR observations.

Inelastic yielding of the near-surface during coseismic rupture has also been suggested to reduce the stress changes available for driving postseismic slip [Fialko et al., 2005; Kaneko and Fialko, 2011]. Although inelastic yielding models can account for some of the limited shallow postseismic afterslip, they cannot account for the lack of deeper (>5 km) postseismic afterslip along-strike and down-dip of the coseismic rupture, as the high confining pressures at depth reduce the inelastic response of the crust to the dynamic stress changes during the earthquake [Kaneko and Fialko, 2011]. Significant interseismic creep in the middle of the seismogenic layer is also unlikely, as this would prevent the accumulation of elastic strain at depths in which earthquakes nucleate at Bam. Inelastic yielding is therefore limited to possibly accounting for the lack of afterslip in the shallow fault zone only.

I present an alternative model to explain the limited postseismic afterslip at Bam that is related to lateral and vertical variations in the frictional properties of the fault surface. The models discussed above suggest that the amplitude and pattern of postseismic afterslip may be limited by locked areas of the fault. This scenario is consistent with recent observations in which earthquakes that show significant afterslip-related moment release compared to coseismic moment release are surrounded by creeping areas on the fault zone. In these cases, stress-driven afterslip can relax the majority of the coseismic stress changes on the fault zone, and large amounts of afterslip occurs. On the contrary, if at Bam the adjacent fault zone remains locked and provides elastic resistance to creep, it could limit the amount of afterslip. Locking would also be consistent with the lack of observed interseismic creep in the pre-earthquake InSAR and GPS measurements [Fialko et al., 2005; Walpersdorf et al., 2014]

To test this proposition I performed calculations in which the creeping area on both faults is restricted to small patches that are located around the edge of the coseismic rupture, with the rest of the fault zone remaining locked (Fig. 2.12). This geometry allows for the possibility that afterslip occurs on parts of the fault that also experience coseismic slip, similar to the patterns of slip observed following the 1999 Hector Mine and 2006 Mozambique earthquakes [Simons et al., 2002; Copley et al., 2012]. The small creeping patches experience initial rapid afterslip following the earthquake, but eventually stop creeping as the elastic resistance from the adjacent locked zones approaches the driving stress. The result is a more non-linear temporal evolution of ground deformation that is localised adjacent to the coseismic slip patch (see Fig. 2.11 for the spatial pattern of the surface displacements and Fig. 2.6 for the temporal evolution). The misfit between the predicted and observed deformation at the end of the postseismic transient as a result of afterslip along two predominantly locked faults is significantly smaller than for calculations with faults that can creep over their whole surface area (see Fig. 2.6 and 2.11). Therefore the InSAR measurements are better explained by a model in which the faults at Bam remain predominantly locked.

The stress-driven afterslip models I have described above simulate the postseismic slip distribution on the fault surfaces at Bam. In the following section, I use these predictions to test whether coseismic stress changes on the Bam-Baravat Fault would lead to an afterslip distribution consistent with growing the overlying topography over multiple earthquake cycles.

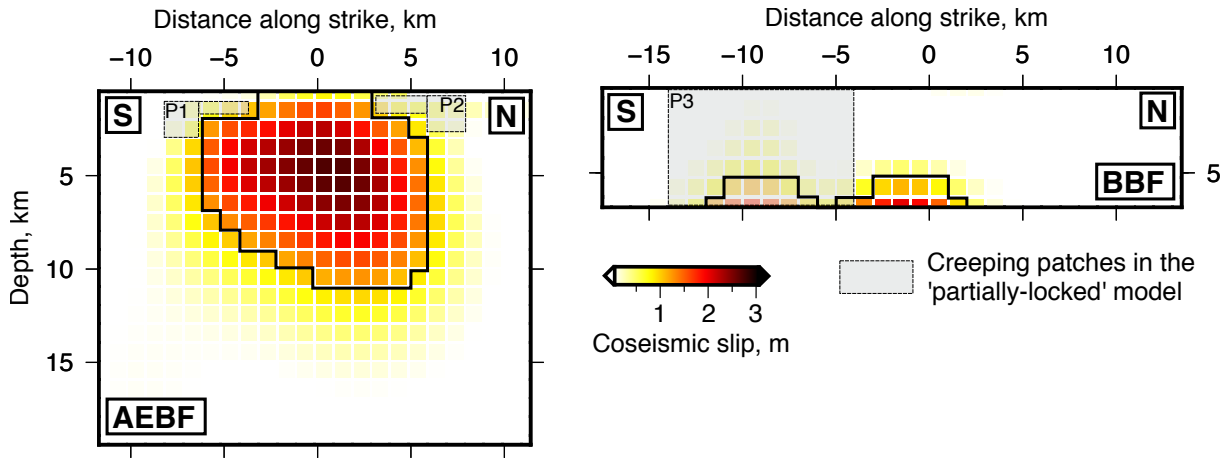

Figure 2.12 Coseismic slip distribution and the distribution of creeping patches (grey rectangles) used in the partially-locked fault models. The coseismic slip distribution comes from Funning et al. [2005b]. The distribution of the creeping patches were adjusted manually to fit the InSAR observations. The black line is the 1 m coseismic slip contour, and is the edge of the compacted slip distribution used in the forward models. AEBF = Arg-e-Bam Fault, BBF = Bam-Baravat Fault.

2.6 Growth of the Bam-Baravat Ridge

Short-wavelength topographic ridges, like the Bam-Baravat Ridge, often grow as a result of creep along shallow faults. These shallow faults typically creep in response to the stress changes caused by slip on adjacent faults [e.g. Nishimura et al., 2008; Copley and Reynolds, 2014; Fattahi et al., 2015; Copley and Jolivet, 2016]. The ∼1 cm step change in LOS motion across the Bam-Baravat Ridge indicates that the shallow part of the Bam-Baravat Fault began creeping after the 2003 earthquake (see Fig. 2.5), consistent with this mechanism of growth. The topography, and the lack of any geomorphic evidence for right-lateral motion along the front of the Bam-Baravat Ridge, suggest that the majority of the recent creep on the Bam-Baravar Fault is manifested as thrusting. However, the stress-driven afterslip calculations presented above predict little or no shallow thrust motion on the Bam-Baravat Fault (Fig. 2.10b). Therefore the current setup of the stress-driven afterslip models cannot account for the InSAR observations over the Bam-Baravat Fault, and would not lead to long-term growth of the Bam-Baravat Ridge through repeat earthquakes and the associated shallow postseismic creep.

The direction of the modelled slip vector on the Bam-Baravat Fault is parallel to the maximum shear stress resolved in the fault plane, and therefore is a function of both the coseismic stress changes and the regional tectonic stress acting through the lithosphere. As coseismic stress-driven afterslip alone is not consistent with forming the local topography, I investigated whether a component of far-field tectonic stress can modify the postseismic slip distribution on the Bam-Baravat Fault to reconcile the afterslip models with both short-term postseismic, and long-term geomorphic, observations.

2.6.1 Forward Calculations for Variable $\Delta\sigma$

Reverse-sense motion along the N-S trending Bam-Baravat Fault will occur if there is an E-W orientated compressive deviatoric stress $\Delta\sigma$ acting through the shallow crust. I simulated this effect by applying a

range of $\Delta\sigma$ as a pre-stress acting on the faults when performing stress-driven afterslip calculations as described above, then repeated the grid search to determine the best-fitting afterslip model and friction parameters in a χ^2_r sense. The upper bound on the value of $\Delta\sigma$ is then defined by the increase in the χ^2_r misfit with increasing $\Delta\sigma$.

The calculations were performed for the case of both fully-creeping and partially-locked faults. In the grid search the value of $a\sigma_n$ was fixed to be the nominal best fit of 5.5 MPa, because the misfit is relatively insensitive to this parameter (Fig. 2.10c). I calculated the average shallow rake direction on the top 4 km of the Bam-Baravat Fault to track the effect of increasing $\Delta\sigma$ on the rake of modelled postseismic slip.

2.6.2 Results: Forward Calculations for Variable $\Delta\sigma$

The forward calculations suggest that for values of $\Delta\sigma$ greater than 10 MPa, the misfit between the models and the InSAR observations is significant, irrespective of the friction properties of the faults (Fig. 2.13a). The large misfits are generated by two effects. Firstly, $\Delta\sigma$ resolves mainly as a normal stress on the near-vertical Arg-e-Bam Fault, clamping the fault and limiting strike-slip afterslip in the shallow fault zone. Secondly, $\Delta\sigma$ resolves mainly as a thrust-orientated shear stress that drives thrust-orientated fault creep on the Bam-Baravat Fault, over-predicting the observed LOS motions near the Bam-Baravat Ridge.

A trade-off exists between increasing $\Delta\sigma$ enough such that the postseismic slip vector along the Bam-Baravat Fault is predominantly thrust orientated, in agreement with the geomorphic evidence of recent motion on the fault, and increasing the misfit between the afterslip models and the postseismic InSAR observations. This trade-off can be used to place bounds on the magnitude of the deviatoric stresses acting across the faults at Bam. Slip on the shallow portion of the Bam-Baravat Fault becomes predominantly thrust orientated when $\Delta\sigma \gtrsim 2$ MPa (Fig. 2.13b). An approximate upper bound corresponds to $\Delta\sigma \lesssim 10$ MPa, above which there is a significant deterioration in the fit between modelled and observed LOS displacements (Fig. 2.13b). In particular, the models significantly over-predict the positive LOS displacements over the Bam-Baravat Ridge in the ascending track InSAR measurements.

Horizontal contrasts in gravitational potential energy between the ∼1500-2000 m-high Kerman Plateau and ∼500-800 m-high Dasht-e-Lut could plausibly account for the horizontal compressive stresses acting across the Bam faults (Fig. 2.1).

2.6.3 Mechanical Effects of Fault Surface Anisotropy

An alternative explanation for the misfit between predictions of afterslip and the growth of long-term topography is that slip along the Bam-Baravat Fault may not be free to occur along any rake direction, as assumed in the models. If the surface of the fault had some component of topography or fabric [Sagy et al., 2007; Candela et al., 2009; Sagy and Brodsky, 2009], such as corrugations aligned sub-parallel to dip [Jones et al., 2009], then slip would occur parallel to this fabric. If the fault were corrugated down dip then, irrespective of the irregularity of the maximum shear stress resolved onto the fault plane,

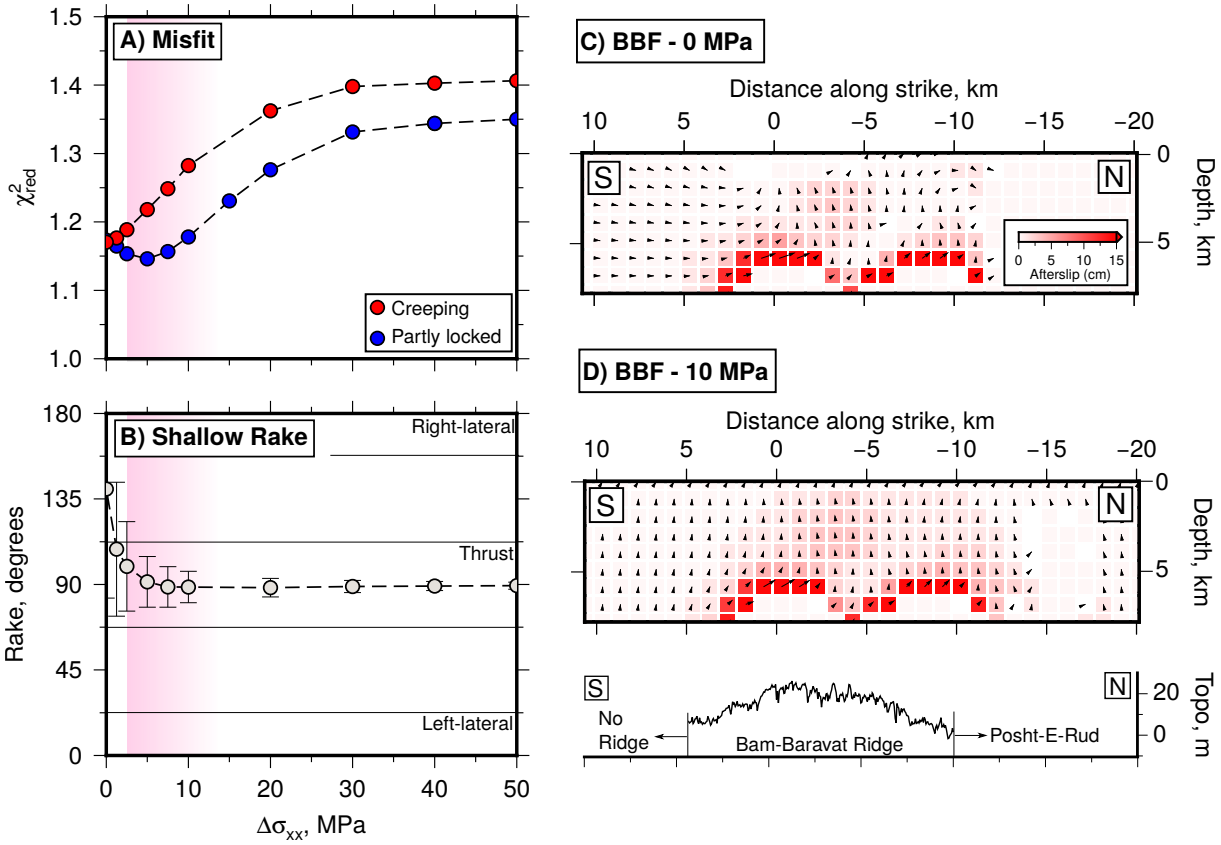

Figure 2.13 The effect of an E-W orientated deviatoric stress $\Delta\sigma$ on the fit between the stress-driven afterslip models and the InSAR measurements. (a) Change in the reduced chi-square misfit of the best-fitting model for a range of $\Delta\sigma$. (b) Evolution of the slip vector rake in the top 4 km of the fault zone for a range of $\Delta\sigma$, which is independent of the locking pattern on the fault. The purple shaded region corresponds to the proposed lower and upper bound on the E-W deviatoric stresses acting through the upper crust at Bam. (c,d) The postseismic afterslip distribution on the Bam-Baravat Fault 5.7 years after the Bam earthquake with $\Delta\sigma = 0$ and $\Delta\sigma = 10$ MPa, respectively. As in Fig. 2.10 the arrows correspond to the motion of the hangingwall relative to the footwall.

relative motion of the two fault surfaces would always be thrust-orientated and consistently lead to the growth of the overlying topography. Some corrugations may have formed during a previous tectonic regime, which could explain the mismatch between the predicted orientation of the slip vector from the forward models and the orientation of the proposed corrugations.

2.7 Discussion

2.7.1 Limited Afterslip and Future Seismic Hazard at Bam

Limited postseismic deformation on the coseismically stressed portion of the Arg-e-Bam Fault between 10 and 15 km depth, either through afterslip or viscous flow, indicates that significant elastic strain may remain stored in the fault zone. The lack of recorded historical seismicity at Bam [Ambraseys and Melville, 2005], despite the city being inhabited for over 2000 years [Berberian, 2005], suggests that there has not been recent seismogenic failure of the bottom portion Arg-e-Bam Fault. The estimated GPS loading rate of 1-3 mm/yr [Walpersdorf et al., 2014] would allow between 2 and 6 m of slip deficit to accumulate over this 2000 year time period, which is sufficient to critically stress the fault, as revealed by the 2.7 m of slip in the 2003 earthquake. Release of the elastic strain accumulated in the deep fault zone (10-20 km) could occur in future earthquakes that rupture the bottom part of the seismogenic layer, or via long-term aseismic creep that is currently invisible in the InSAR measurements.

The size of a single earthquake that could rupture the bottom of the Arg-e-Bam Fault, releasing the deep elastic strain, would be around M_w 6-6.5 (i.e. 15×5 km patch with 2 m of slip). Earthquakes that ruptured the top and bottom half of the seismogenic layer in separate events have been documented elsewhere [Berberian et al., 2001; Elliott et al., 2011] and can be explained by loading of the unruptured part of the fault following the earlier earthquake. Of these examples, the Qaidam earthquakes were separated by 10 months [Elliott et al., 2011], and the Golbaf-Sirch earthquakes by 17 years [Berberian et al., 2001], showing that failure of the loaded half of the seismogenic layer can occur on timescales much shorter than the usual recurrence interval for faults in central and eastern Iran, which is typically $\gg$100 years [e.g. Fattahi et al., 2006; Walker et al., 2010].

Alternatively, long-term creep on the bottom of the Arg-e-Bam Fault could release the elastic strain aseismically. As <50 cm of afterslip at depth may have occurred over the 5.7 years of InSAR measurements, and assuming the creep has a constant rate due to a long relaxation time, it would take $\gtrsim$30 years to release the full component of stored elastic strain on the lower half of the fault. This would also require the deep portion of the fault zone to have significantly different friction properties to the shallow fault zone, as transient creep on the top 5 km of the Arg-e-Bam Fault has a far shorter relaxation time of $\sim$1.3 years. It remains unclear whether significant vertical gradients in frictional properties do exist on natural faults [Blanpied et al., 1995; Johnson et al., 2006; Chang et al., 2013], and therefore whether this is a viable mechanism of strain release. Longer-term measurements (10's of years) of postseismic deformation within 10-20 km of the fault zone would be needed to detect any slow, deep creep at Bam, which may be possible by combining the Envisat and Sentinel-1A/B SAR data. Although, the near-polar orbital geometry of these SAR satellites makes them relatively insensitive to the N-S orientated fault slip.

Analysis of the short-wavelength InSAR measurements that are sensitive to deformation in the shallow crust indicates the fault zone remains predominantly locked along-strike of the Bam rupture. I found that the spatial and temporal evolution of postseismic ground deformation at Bam cannot be simulated by stress-driven afterslip on a fully-creeping fault zone, and requires a significant component of frictional locking on both faults to match the observed ground deformation.

In summary, it is likely that significant elastic strains remain around the fault zone at Bam both along-strike and down-dip, which could be released in future earthquakes of M_w 6, and therefore the future seismic hazard remains high.

2.7.2 Postseismic Afterslip on the Coseismic Rupture

In order to fit the postseismic InSAR measurements, the stress-driven afterslip models indicated that afterslip may overlap with areas of the fault that also moved with up to 1 m of coseismic slip (Fig. 2.12). As the InSAR measurements are sensitive to slip in the top 5 km of the fault zone, the spatial overlap appears robust. However, as the first post-event SAR data was collected 8 days after the earthquake, it is not possible to determine the exact ratio of coseismic to postseismic slip on the same patches of fault.

Superimposed coseismic and postseismic fault motions suggests that, if the creeping part of the fault is subject to dynamic stresses above a certain threshold, then the creeping regions may move at seismogenic slip rates. This conditional stability of frictional sliding has previously been recognised in laboratory experiments [e.g. Marone et al., 1991; Scholz, 1998], and suggests that creeping segments of faults do not necessarily form persistent barriers to fault rupture [Noda and Lapusta, 2013].

2.7.3 Postseismic Relaxation Time and Fault Friction

The postseismic deformation observed at Bam is consistent with afterslip along discrete fault surfaces. Similar observations have been made for other earthquakes in Iran, including at Tabas-e-Golshan [Copley, 2014; Zhou et al., 2016] and Sefidabeh [Copley and Reynolds, 2014]. However, both the Tabas and Sefidabeh earthquakes show unusually long-lived afterslip, with transient deformation still visible in postseismic interferograms 15-30 years after the earthquake. This observation is curious as, in most cases, the surface deformation due to afterslip decays on the timescale of months to a few years [Savage et al., 2005]. Copley [2014] proposed two possible explanations for the observation of long-lived postseismic transients at Sefidabeh and Tabas-e-Golshan: (1) low noise levels in the InSAR measurements acquired over Iran allow small signals to be recognised that may have been missed elsewhere, therefore the long relaxation times are potentially just a sampling bias, or (2) these faults, and others with long-lived afterslip, may have different frictional properties to those with shorter afterslip transients. The observation that the postseismic deformation at Bam is complete in less than 6 years, despite the quality of the InSAR measurements and low atmospheric noise levels, suggests that measurement bias is not to blame for the differences in the relaxation time of postseismic deformation. Instead, it seems that contrasts in the relaxation time between Bam, Sefidabeh and Tabas are a result of the differing frictional properties of the fault surfaces, though there is no obvious difference in the surface geology between these localities that could account for this.

2.7.4 Strength of the Bam-Baravat Fault

Section 2.6.2 argued that an E-W orientated, 2-10 MPa deviatoric stress is likely to be acting across the Bam-Baravat Fault. This result supports accumulating geophysical evidence that the deviatoric stresses in the seismogenic portion of the lithosphere are on the order of earthquake stress drops (∼1-30 MPa) [Lamb, 2006; Copley et al., 2009, 2011a]. If the Bam-Baravat Fault were supporting shear stresses consistent with Byerlee's laboratory-derived static friction range $\mu = 0.6$-0.85 [Byerlee, 1978], then the depth-averaged deviatoric stress acting on the fault, if critically stressed, would be ∼100 MPa. This is at least one order of magnitude greater than the results of my calculations. Therefore, it appears that the creeping patches of the Bam-Baravat Fault are 'weak' ($\mu'_{app} < 0.1$) compared to traditional views of static fault strength, which is in line with recent suggestions for both stick-slip and creeping faults [Lamb, 2006; Jolivet et al., 2013; Copley et al., 2018].

2.8 Conclusions

I have analysed the postseismic ground deformation following the 2003 Bam earthquake in Iran and find the observations are consistent with coseismic stress-driven afterslip on a predominantly locked fault zone interspersed with small creeping patches. Afterslip and visco-elastic deformation between 10 and 20 km depth that is 'invisible' to the InSAR measurements may relax <20% of the coseismic stress changes on the deep fault zone, whilst the shallow fault experiences limited afterslip and appears to remain mostly locked. As a result, the elastic strains stored in the fault zone at Bam could be released in a M_w 6 earthquake, hence the risk of future seismicity at Bam remains high.

To date, mapping the distribution of creeping and locked patches on faults has been performed solely using the pattern of interseismic strain around fast-slipping faults [e.g. Jolivet et al., 2012; Chlieh et al., 2011]. One of the key results from this chapter is that postseismic deformation can be used as a tool to probe the frictional locking on active faults, particularly ones where the rate of interseismic deformation is slow. Studying faults with little postseismic deformation like Bam fills an observation bias in the current literature, which heavily focuses on earthquakes with large postseismic transients. It is essential to study the full range of postseismic fault behaviour to determine why some faults are predominantly frictionally locked, whilst others can creep throughout the seismogenic crust.

In the final section, I found that the postseismic slip distribution resulting from coseismic stress changes along the creeping Bam-Baravat Fault was inconsistent with forming the overlying Bam-Baravat Ridge. This finding suggests that either: (1) a 2-10 MPa deviatoric stresses act through the shallow crust and compresses the fault system, leading to thrust-orientated creep that extends to the surface on the Bam-Baravat Fault, or (2) the Bam-Baravat Fault may have some component of surface fabric that controls the direction of the fault slip vector.

Chapter 3

Extension and Dynamics in the Andes Revealed by the 2016 Parina Earthquake [1]

Overview

The M_w 6.1 2016 Parina earthquake led to extension of the south Peruvian Andes along a normal fault with evidence of Holocene slip. This chapter uses interferometric synthetic aperture radar, seismology, and field mapping to determine a source model for this event and show that extension at Parina is orientated NE-SW, which is parallel to the shortening direction in the adjacent sub-Andean lowlands. In addition, using earthquake source models and GPS data, I demonstrate that shortening within the sub-Andes is parallel to topographic gradients. Both observations imply that forces resulting from spatial variations in gravitational potential energy are important in controlling the geometry of the deformation in the Andes. I calculate the horizontal forces per unit length acting between the Andes and South America due to these potential energy contrasts to be 4-8$\times 10^{12}$ N per metre along strike of the mountain range. Normal faulting at Parina implies that the Andes in south Peru have reached the maximum elevation that can be supported by the forces transmitted across the adjacent foreland, which requires that the foreland faults have an effective coefficient of friction $\mu' \lesssim 0.2$. Additionally, the onset of extension in parts of the Central Andes following orogen-wide compression in the late Miocene suggests that there has been a change in the force balance within the mountains. I propose that shortening on weak detachment faults within the Andean foreland since ∼5–9 Ma reduced the shear tractions acting along the base of the upper crust in the eastern Andes, leading to extension in the highest parts of the range.

[1] Material in this chapter is adapted from the publication: S. Wimpenny, A. Copley, C. Benavente, E. Aguirre (2018). Extension and Dynamics in the Andes Revealed by the 2016 Parina (Haurichancara) Earthquake, *Journal of Geophysical Research: Solid Earth* 123(9):8198-8228

3.1 Introduction

On the 1st December 2016 (22:40:26 UTC) a M_w 6.1 normal-faulting earthquake occurred ∼70 km west of Lake Titicaca in the south Peruvian Andes (Fig. 3.1a). This event marks the first $M_w > 6$ extensional earthquake to occur within the Andes for 70 years, and provides a rare opportunity to study crustal deformation, lithosphere rheology and the forces driving deformation in this region.

Observations of crustal deformation within the high Andes are sparse, but are fundamental to testing models of orogen dynamics [England and Houseman, 1989; Liu et al., 2002; Flesch and Kreemer, 2010]. One particular area of contention is whether extension in the high Andes is parallel [e.g. Dalmayrac and Molnar, 1981] or perpendicular [e.g. Sébrier et al., 1985; Mercier et al., 1992] to shortening in the adjacent sub-Andean lowlands. Extension in the Andes parallel to shortening in the sub-Andes can be explained by the balance between the buoyancy forces arising from differences in gravitational potential energy between the mountains and lowlands, and the forces acting through the foreland lithosphere [Dalmayrac and Molnar, 1981; Froidevaux and Isacks, 1984]. However, if extension in the Andes is perpendicular to sub-Andean shortening, shear tractions acting on the base of the Andean lithosphere are required to influence the stress state in the mountains [Liu et al., 2002].

Current observations of normal-faulting earthquakes in the Andes [Doser, 1987; Cabrera and Sebrier, 1998; Devlin et al., 2012; Jay et al., 2015] provide a limited constraint on the geometry of the extension, as the majority of the events are too small ($M_w < 5.5$) to break the full thickness of the seismogenic layer, so may not be representative of the dominant crustal strain [e.g. Brune, 1968; Jackson and Blenkinsop, 1997; Scholz, 2002]. To supplement the sparse earthquake data, a number of studies have inferred the direction of extension throughout the Andes to be N-S based on slip vectors along minor fault planes [Sébrier et al., 1985; Mercier et al., 1992; Cladouhos et al., 1994; Schoenbohm and Strecker, 2009; Daxberger and Riller, 2015; Tibaldi and Bonali, 2018]. However slip on minor faults also represents a small component of the total crustal strain, and may not accurately record the bulk orientation of extension [Riller et al., 2017].

There are also competing views regarding the orientation of shortening across the sub-Andean lowlands. Earthquake mechanisms suggest shortening in the sub-Andes is parallel to gradients in the topography [Assumpção, 1992; Assumpção and Araujo, 1993; Lamb, 2000]. Alternatively, some studies have argued that the GPS velocity field in the sub-Andes can be explained by a combination of elastic strain accumulation on the locked Peru-Chile subduction interface and slip along a detachment fault beneath the sub-Andes. These elastic models assume motion on the detachment fault beneath the sub-Andes has a slip vector parallel to relative plate motion between the Nazca plate and South America, rather than parallel to gradients in topography [Bevis et al., 2001; Chlieh et al., 2011].

In this chapter I use seismology, interferometric synthetic aperture radar (InSAR) and field observations to determine a detailed source model of the 2016 Parina earthquake, and relate the pattern of co- and post-seismic fault slip to the surface geomorphology. I then combine the source model for the Parina earthquake with additional seismological source models, and existing GPS data, to re-assess the pattern of crustal deformation in the high Andes, and its relationship with shortening in the adjacent sub-Andean lowlands. I use the pattern of deformation to test models of the forces driving deformation

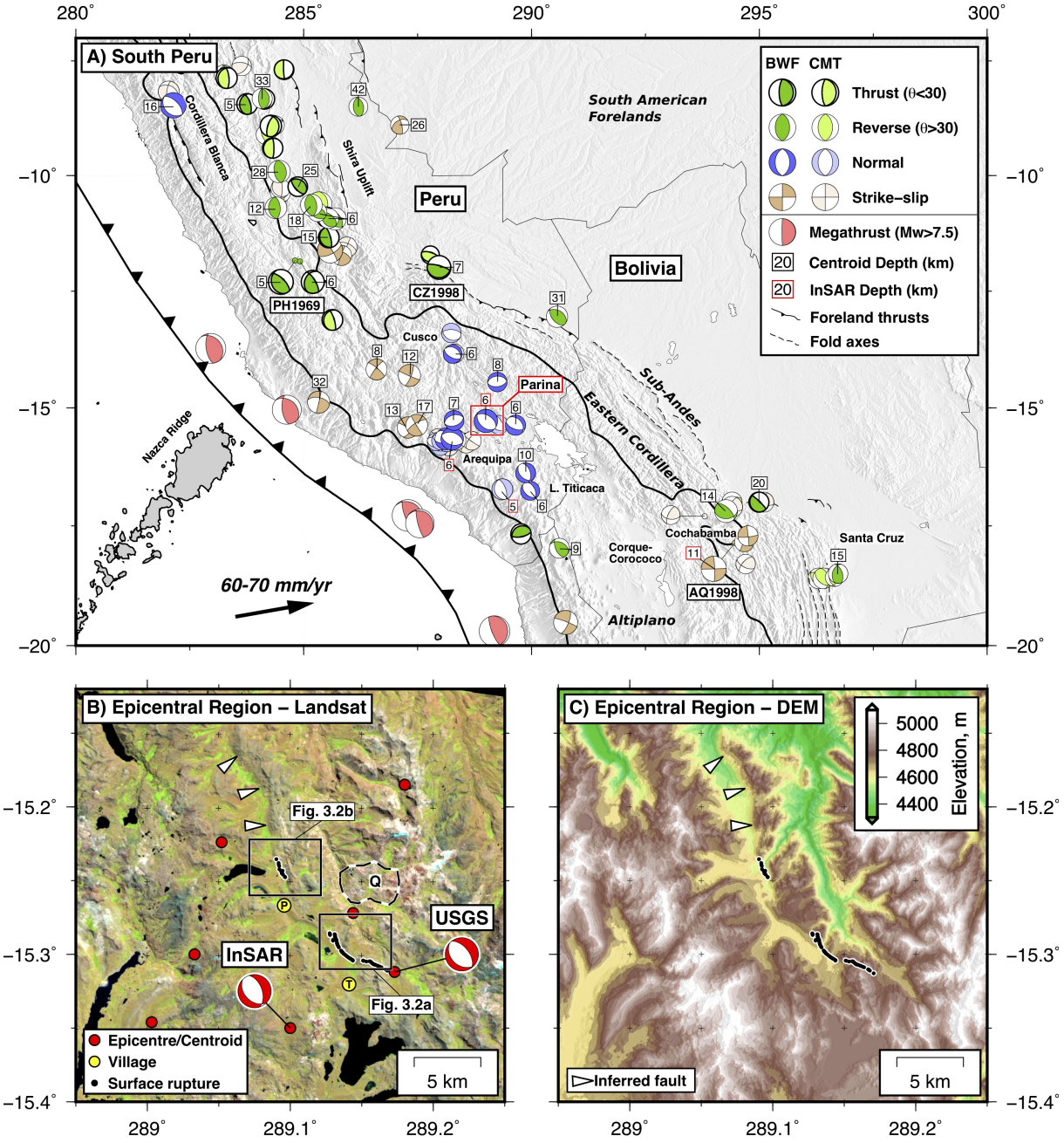

Figure 3.1 Overview of the Parina earthquake epicentral region. (a) Waveform modelled (BWF) and global CMT catalogue earthquakes [Ekström et al., 2012] with $M_w > 5$ in the overriding plate (see Table B.1 for sources). PH1969 are the 1969 Pariahuanca earthquakes [Philip and Megard, 1977], AQ1998 is the 1998 Aiquile earthquake [Funning et al., 2005a] and CZ1998 is the 1998 Cusco foreland earthquake [Emmerson, 2007]. The thick black line is the 3000 m contour from the 100 km Gaussian filtered topography. The red box marks the location of (b) and (c). (b) Landsat 8 (bands 4,3,2) image of the epicentral region. Black dots are the coseismic surface ruptures, and the white triangles mark the northern extension of the Parina Fault. P and T marks the villages of Parina and Togra. The centroid and mechanism of the best-fit InSAR fault plane, and the epicentre of the USGS source model, are shown along with the epicentres of $M_w > 4.0$ NEIC aftershocks (location error >5 km). Black boxes outline the locations of the satellite imagery in Figure 3.2, and the region marked 'Q' is an open cast quarry. (c) SRTM 30 m digital elevation model of the Parina Fault.

in the Andes, and investigate the rheology of the South American lithosphere. Finally, I discuss possible causes for the onset of normal faulting in the high Andes at ∼5-9 Ma, and suggest a general model for the support and evolution of mountain ranges based upon the strength of faults in their forelands.

3.2 1st December 2016 Parina Earthquake

The M_w 6.1 Parina earthquake occurred in a region of south Peru that has experienced a number of M_w 5-5.8 normal-faulting earthquakes in the past 50 years [Dziewonski et al., 1981; Cabrera and Sebrier, 1998; Ekström et al., 2012; Devlin et al., 2012; Jay et al., 2015] (Fig. 3.1a). Geomorphic evidence of Quaternary normal faulting in the epicentral region is scarce [e.g. Benavente et al., 2013], but has been documented further north near Cusco [Suarez et al., 1983; Sébrier et al., 1985; Mercier et al., 1992; Benavente et al., 2013], and to the south near Arequipa [Lavenu et al., 2000]. The limited geomorphic expression of normal faults in south Peru probably reflects the small amount of finite extensional strain in the high mountains ($< 1\%$; Sébrier et al. [1985]). In Chapter 4, I present new observations of the morphology and slip rates on the normal faults in south Peru.

3.2.1 Local Geomorphology and Surface Ruptures

The surface rupture observations discussed in this section were collected following the Parina earthquake by Enoch Aguirre and Fabrizio Delgado of the Instituto Geológico, Minero y Metalúrgico (INGEMMET), Lima, Perú. These observations were confirmed by my own fieldwork in October 2018.

Surface ruptures associated with the Parina earthquake were mapped within three days of the event, and consist of two NW-SE trending sections with an along-strike length of ∼12 km, a maximum height of ∼30 cm (downthrown to the south west), and maximum tensional opening of ∼30 cm (Fig. 3.1b). The ruptures coincide with a 150 m-high escarpment that extends an additional 10 km north west of Parina, and bounds a narrow hangingwall basin on its south-western side (Fig. 3.1c). Tensional opening across the ruptures was largest in areas where vertical offsets were also highest, which is a common feature of normal faults that steepen in the near-surface [e.g. Jackson et al., 1982].

Along the southern section of the fault the ruptures form a semi-continuous trace that coincides with a 10 m-high Holocene scarp incised by streams in its footwall (Fig. 3.2a). Offsets across the ruptures have both opening and vertical components up to 30 cm (Fig. 3.2c). Along the the northern section of the fault, the ruptures consist of discontinuous, overlapping splays that map onto NW-SE trending, metre-high scarps visible in pre-event satellite imagery (Fig. 3.2b). Both the tensional opening and vertical offsets across the ruptures in the northern section were typically <10 cm (Fig. 3.2d). Dammed ponds on the downthrown, south-western side of the scarps pre-date the Parina earthquake (Fig. 3.2a,b), and suggest there has probably been $\lesssim$10-20 m of slip on the Parina Fault since the last major glaciation event reset the landscape in the region at ∼10-45 ka [Clapperton, 1983; Smith et al., 2005b; D'Arcy et al., 2019]. The height and estimated age of the Holocene scarps indicates a slip rate $\lesssim$1 mm/yr on the Parina Fault. A more detailed overview of the morphology of the Parina Fault is presented in Section 4.2.4, including a high-resolution (1×1 m) digital elevation model of the Holocene scarps.

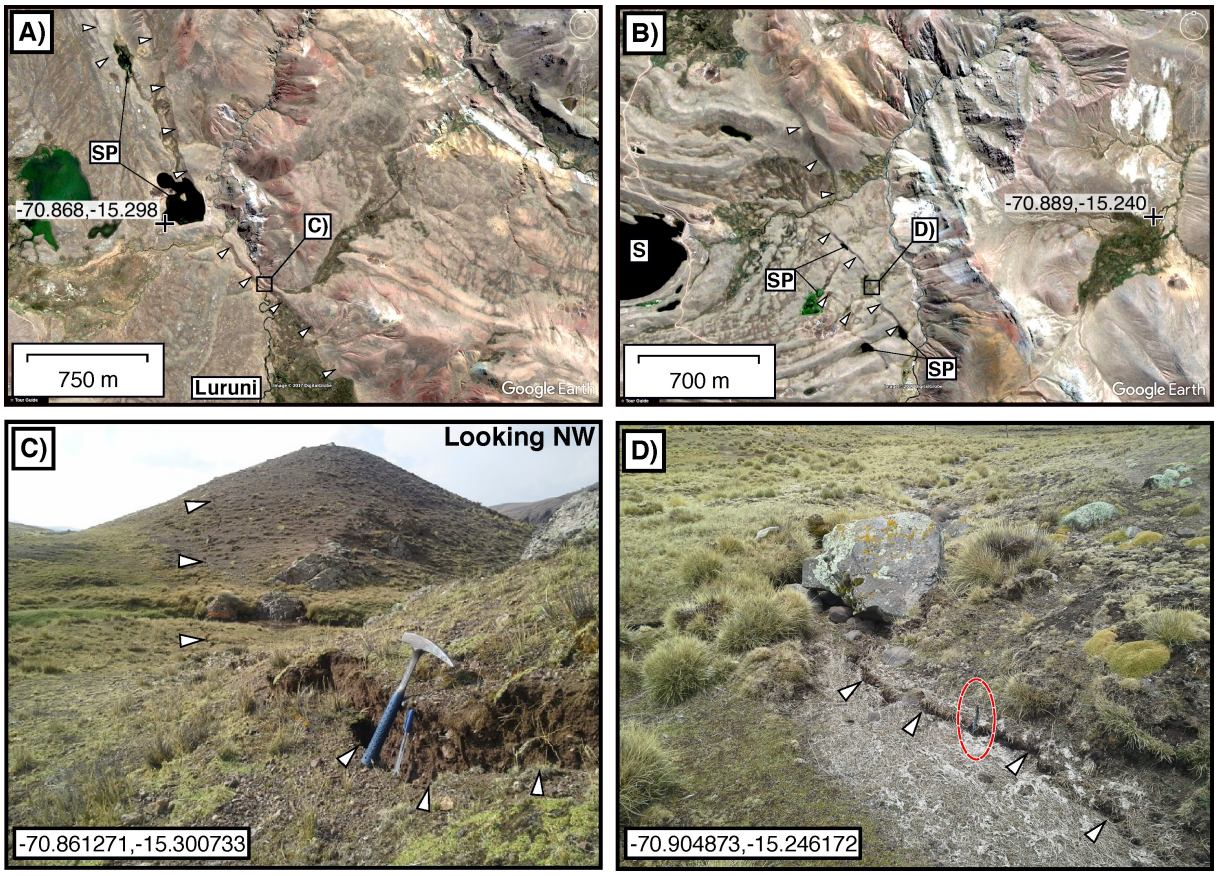

Figure 3.2 Geomorphology and surface ruptures of the 1st December 2016 Parina earthquake. (a) Digital Globe image from Google Earth (from 2015) of the southern section of the coseismic surface ruptures near Togra (Fig. 3.1b). White triangles pick out small scarps in the topography, and bodies of water marked SP are small ponds dammed against the footwall scarp of the Parina Fault. (b) Digital Globe imagery from Google Earth (from 2015) over the northern section of the ruptures near Lake Saguanani (marked S). In (a) and (b) the longitude and latitude refer to the location of the black cross. (c) Photograph of the 30 cm-high surface ruptures along the southern section of the fault in (a), hammer shown for scale. (d) Photograph of the <10 cm-high surface ruptures found along the northern section of the rupture in (b), pen circled for scale.

3.2.2 Teleseismic Body-Waveform Modelling

I determined the strike, dip, rake, centroid depth, source-time function and moment release of the Parina earthquake by modelling the event as a finite-duration rupture at a point source. I performed a joint inversion of long-period P and SH seismic waveforms recorded at teleseismic distances using the MT5 program of Zwick et al. [1994] (based on the algorithm of McCaffrey and Abers [1988] and McCaffrey et al. [1991]). The methodology behind this procedure has been described in detail elsewhere [see Taymaz et al., 1990], hence only a brief summary will be provided here.

Broadband seismograms recorded at stations within 30-90^o of the earthquake epicentre were selected from the IRIS data management centre, and were filtered to reproduce the response of a long-period WWSSN instrument (15-100 s). Long-period waveforms are insensitive to small-scale heterogeneity in the source region velocity structure [Taymaz et al., 1990], therefore I used a simple 1-D crustal velocity model with V_p = 6.5 km/s, V_s = 3.7 km/s and density 2800 kg/m^3 [Dorbath, 1996; Schurr et al., 1999]. Inaccuracies in the velocity model typically lead to uncertainties in the centroid depth estimate of ±4 km for shallow (<30 km) crustal events [Taymaz et al., 1990]. Geometrical spreading and attenuation were accounted for using a Futterman attenuation operator with t^* of 1.0 and 4.0 for the P and SH waves, respectively. Accurate arrival times of the P and SH phases were picked from the broadband seismograms. The starting model for the inversion was taken as the best double-couple gCMT solution [Ekström et al., 2012], and the final model is constrained to have a double-couple moment tensor.

The minimum-misfit solution consisted of a normal-fault source with a strike/dip/rake of 144/39/276, a centroid depth of 12 km, and a seismic moment of 1.1×10^{18} Nm (M_w 6.0) (Fig. 3.3). The mapped surface ruptures trend parallel to the minimum-misfit strike estimate, and the sense of motion across the ruptures indicates that the SW-dipping nodal plane is the fault plane.

Uncertainties in the source model were estimated using the standard procedure of fixing each parameter of interest at values away from their best fit, and performing inversions in which all other parameters were free to vary. I estimated the strike to be constrained between 110^o and 160^o by the deterioration in fit to the SH waveforms recorded at stations DBIC, COYC and EFI outside this range (Fig. 3.4). Within this range of possible strikes, the dip could not be lower than 35^o otherwise the stations MPOM and SJG would lie near the P-wave nodal plane, and the amplitude of the predicted P arrivals would be too low to fit the observations. Mechanisms with dips >55^o did not fit the observed waveforms as they predict the incorrect SH first motion at stations FFC and SSPA. The rake must be in the range 250-300^o to fit the SH first motions and amplitudes at stations DBIC, COYC, EFI and MESJ (Fig. 3.4). All of the models that fit the observed waveforms within the constraints described above have a slip vector azimuth between 211^o and 245^o (NE-SW). Centroid depths greater than 20 km cannot match the observed SH waveforms as the direct S and reflected sS phases would be separated, which is not observed (e.g. see clear waveform misfits at stations EFI and COYC in Fig. 3.4). For all inversion results with a good fit to the observed waveforms, the seismic moment is 0.9-1.4×10^{18} Nm (M_w 5.9-6.1).

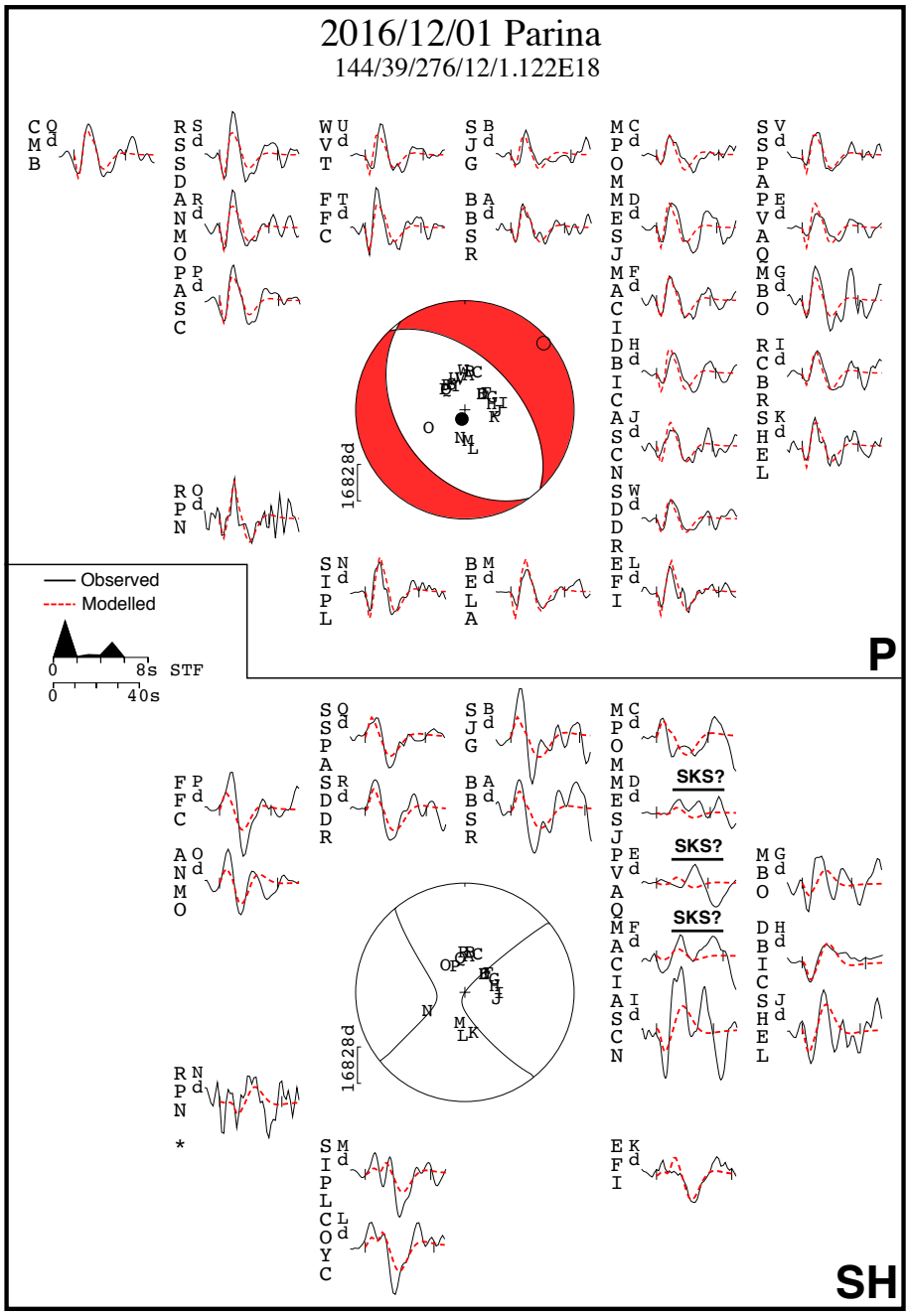

Figure 3.3 Minimum-misfit teleseismic body-waveform solution for the 1st December 2016 Parina earthquake. Details of the inversion result are shown below the title with the form strike/dip/rake/depth/moment, where depth is in kilometres and seismic moment is in Nm. The top panel shows a lower hemisphere projection of the *P*-wave nodal planes, with the station distribution used in the best-fit inversion shown as capital letters. P and T axes are projected onto the focal sphere as a black filled circle and an open circle, respectively. Observed and modelled seismograms are 40 second time-series and are shown as black and red dashed lines, respectively. The seismogram station code is shown by the vertical text to the left of the corresponding seismogram. The time window of the seismograms used in the inversion is demarcated by vertical black ticks. The lower panel shows the equivalent for the *SH* waves. Seismograms that are labelled with SKS occur within the 80-85^o range from the epicentre, therefore may contain some signal from phases that have interacted with the core. Stations with an asterisk are weighted to 0 in the inversion, as they contain a large component of high frequency noise, but are included for comparison with the model predictions. The source-time function is labelled STF.

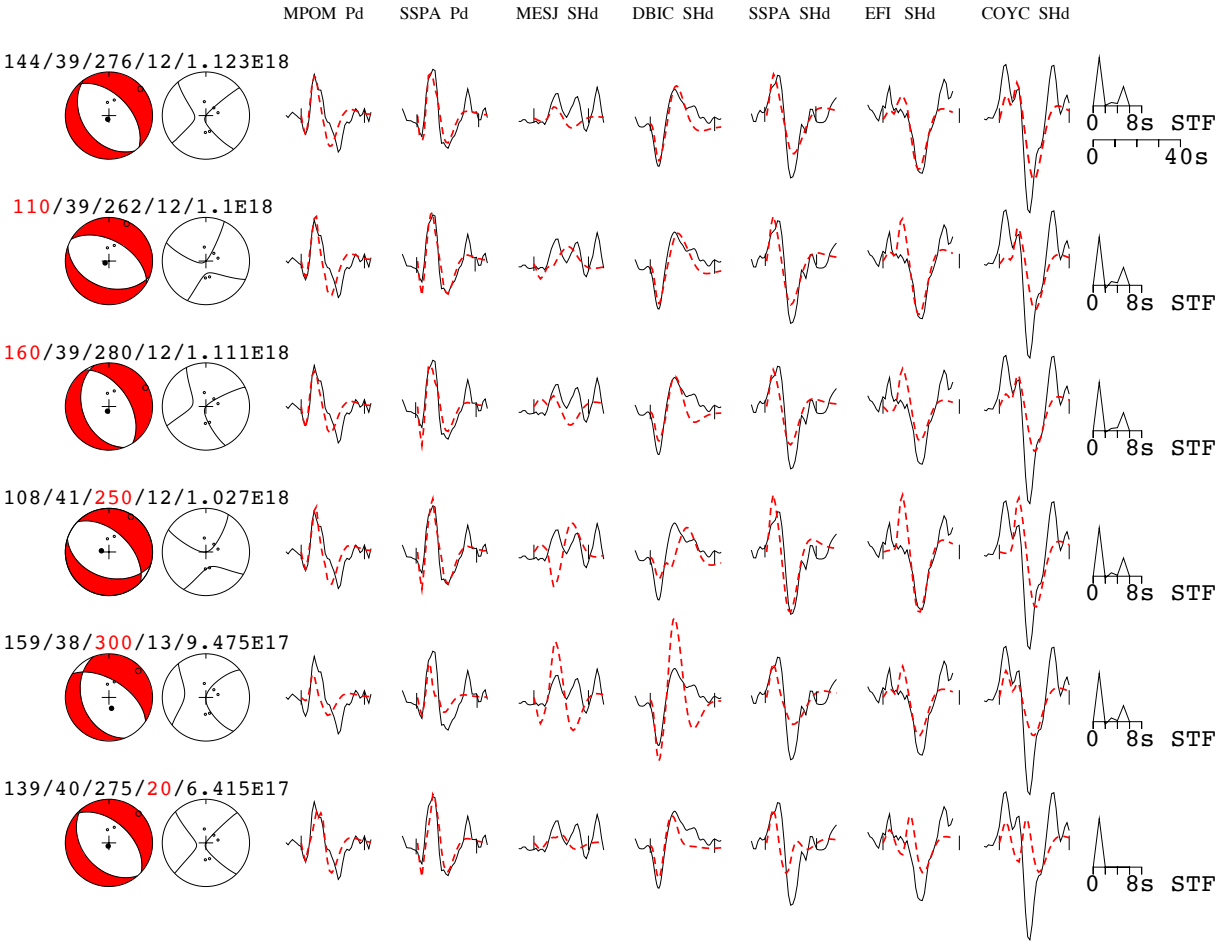

Figure 3.4 Sensitivity tests showing the fits between selected waveforms of the 2016 Parina earthquake given variations in the source parameters. Each row shows *P* and *SH* focal spheres, the fault parameters in strike/dip/rake/centroid depth/moment formation, the fit between modelled (red dashed) and observed (black solid) waveforms at a set of stations, and the source-time function for a particular model run. The station codes are given at the top of each column, where Pd are vertical-component waveforms and SHd are transverse waveforms. The best-fit model presented in Fig. 3.3 is shown on the top row. Each subsequent row shows different inversion results in which the parameter in red is held fixed, whilst all other parameters can vary.

3.2.3 Coseismic InSAR: Observations

I formed Sentinel-1 ascending- and descending-track interferograms covering the coseismic period of the Parina earthquake using the European Space Agency's SNAP software. The effect of topography on phase in the interferograms was removed using an SRTM 90 m elevation model [Farr et al., 2007], following which I phase filtered the interferograms [Goldstein et al., 1988], and unwrapped using the statistical-cost network-flow algorithm (SNAPHU) of Chen and Zebker [2001]. Additional information about the interferograms is provided in Table 3.1.

Parameter	Ascending	Descending
Date (Pre-event)	15th November 2016	26th November 2016
Date (Post-event)	9th December 2016	20th December 2016
Track	149	127
Swath	IW1	IW2
Polarisation	VV	VV
DEM	SRTM 90 m	SRTM 90 m
Heading	347.9^o	192.2^o
Perpendicular Baseline	-17 m	115 m
Incidence Angle	$30\text{-}37^o$	$36\text{-}42^o$
LOS vector [E,N,U]*	[-0.51,-0.13,0.84]	[0.63,-0.16,0.75]
Multi-look (az:rng)	1:4	1:4
Pixel Size (downsampled)	200×200 m	200×200 m
Topography-Phase correlation (r)	-0.46	-0.05

Table 3.1 Details of the coseismic interferograms used to model the source of the Parina earthquake. * LOS vector is shown for the centre of deformation in the interferograms, but the modelling uses the spatially variable LOS vector over the interferogram scene.

The wrapped interferograms (Fig. 3.5) show 5-6 concentric, elongate fringes (corresponding to a maximum of ∼15 cm of line-of-sight displacement) orientated ∼NW-SE in both the ascending and descending track, which is consistent with ground motion resulting from a fault with the same geometry as the body-waveform solution. In addition, the similar pattern of displacement in the ascending and descending tracks indicate the majority of the deformation was vertical, which is consistent with motion on a dip-slip fault [e.g. Copley et al., 2015]. The smooth fringe pattern, located to the SW of the surface ruptures, and the higher fringe density in the north east than the south west of the displacement patch, implies the majority of slip remained buried on a fault that dips south west, and has an up-dip projection coincident with the surface ruptures. The along-strike width of the fringes is ∼15 km, and faults that are ∼15 km long typically produce M_w 6.0-6.5 earthquakes [Wells and Coppersmith, 1994].

3.2.4 Coseismic InSAR: Modelling

I determined the source parameters of the fault responsible for the 2016 Parina earthquake by inverting the InSAR measurements of surface displacement for the best fitting constant-slip, rectangular, elastic

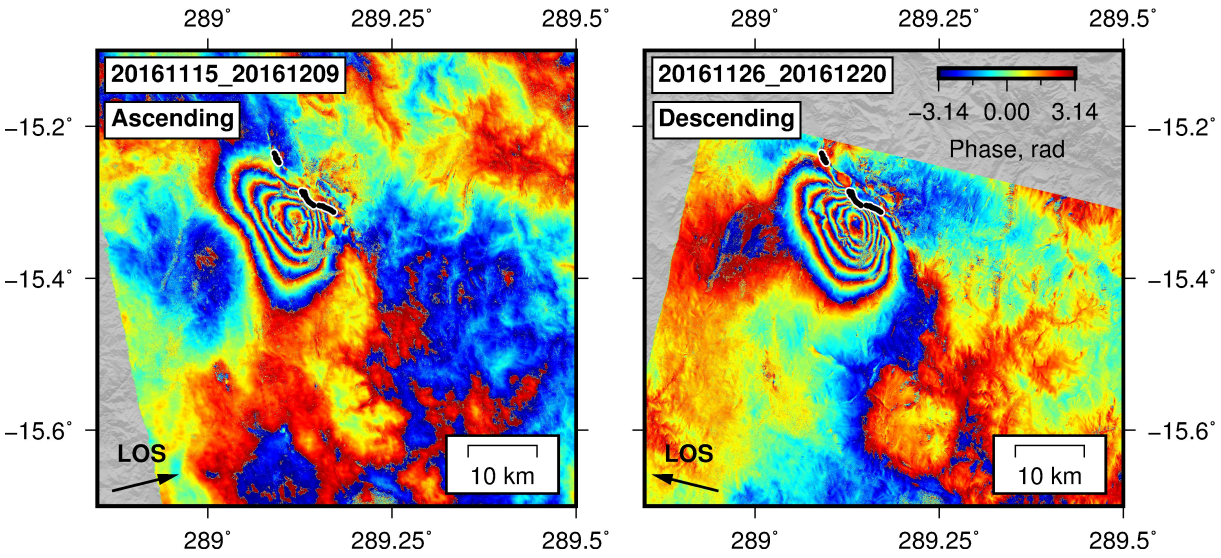

Figure 3.5 Coseismic interferograms covering the 1st December 2016 Parina earthquake. The dates of the pre- and post-event acquisitions are given in the form YYYYMMDD, and the horizontal projection of the line-of-sight vector is shown in the bottom left. The incidence angle of this vector relative to the Earth's surface is between 30-43^o. Black dots outline the locations of the coseismic surface ruptures.

dislocation [Okada, 1985] using a simulated annealing algorithm that minimizes the root-mean-square (RMS) misfit between model and observations [e.g. Copley et al., 2015]. I solved for the length, down-dip width, strike, dip, rake and location of the fault plane, as well as the amount of slip and a constant offset and linear ramp in line-of-sight (LOS) across each interferogram to account for long-wavelength atmospheric and orbital artefacts. The interferograms were down-sampled uniformly over the inversion window to 200 × 200 m pixels to reduce the number of data points in the inversion to ∼70,000. The starting model for the inversion was taken to be the SW-dipping nodal plane of the minimum-misfit body-waveform solution.

To assess the fit between the models and the observations, I estimated the noise levels in the interferograms using the magnitude of phase variations within non-deforming regions. Noise in the interferograms leads to apparent LOS variations between 1.0 and 1.1 cm in the ascending interferogram, and between 0.8 and 0.9 cm in the descending interferogram.

The inversion results suggest that the InSAR data are best-fit by ∼0.5 m of slip buried on a 13 km-long normal fault with a strike/dip/rake of 135/40/250 that mostly ruptured between 3 and 10 km depth (Fig. 3.6). The surface projection of the best-fit fault plane is coincident with the surface ruptures. RMS residuals between the best-fit model and the InSAR observations are 0.8 cm for the ascending track and 0.9 cm for the descending track, therefore the data are fit to within the noise levels, and a more complex model of distributed fault slip is not required or justified by the data.

To test the sensitivity of the InSAR measurements to changes in the fault geometry, I performed a grid search of inversions in which each fault parameter was independently fixed at a range of values, whilst all others could vary, and recorded how the misfit evolved (Fig. 3.7). I found that fault planes with strike = 120-145^o, dip = 35-55^o, rake = 250-270^o, top depth = 1.5-4.5 km and bottom depth = 6-14 km match the InSAR observations to within the noise levels. Together the range of acceptable solutions

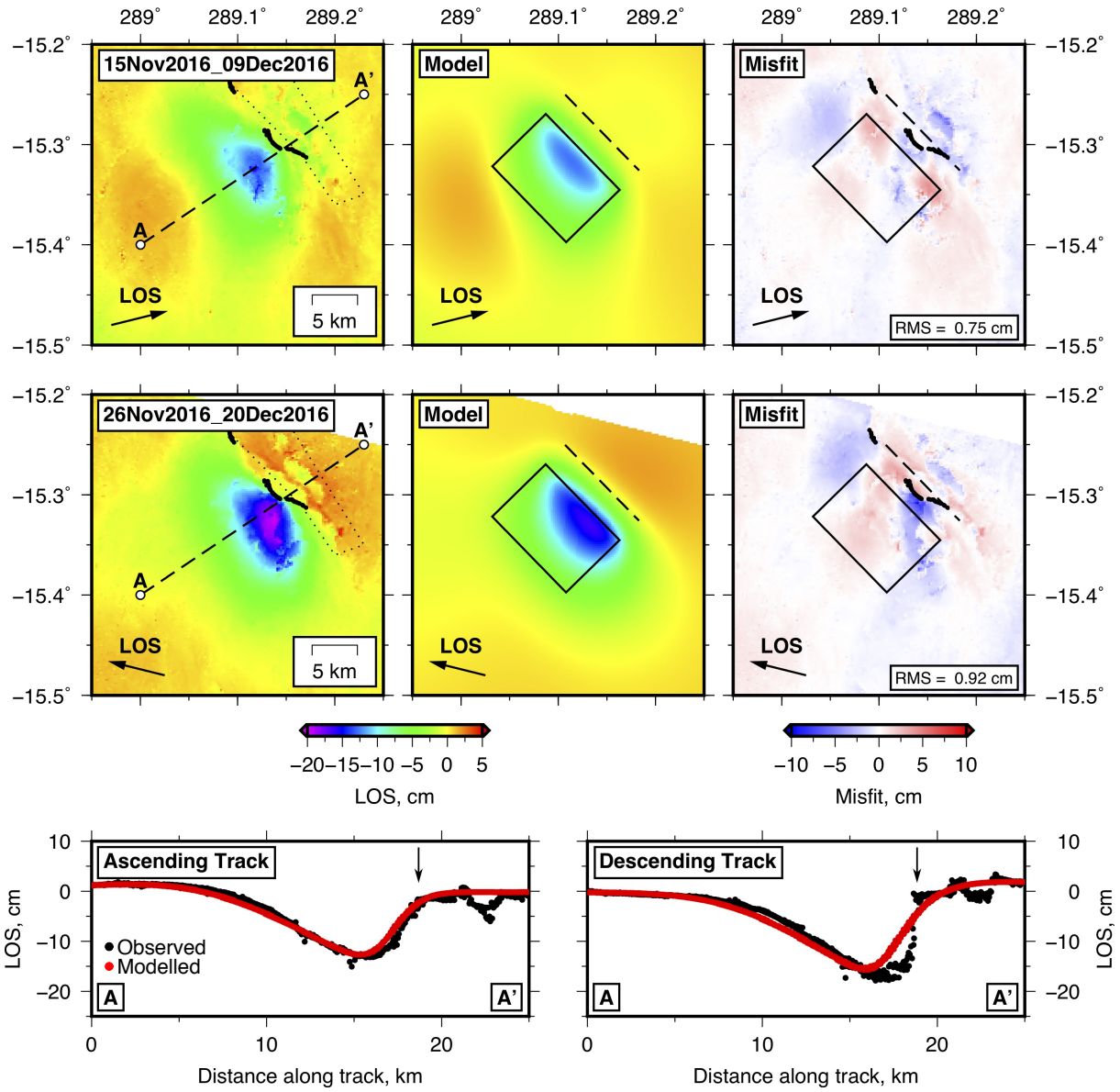

Figure 3.6 Results of inversions for the best-fitting elastic dislocation model to the InSAR observations. The left panels show the unwrapped and downsampled interferograms covering the coseismic period. I use the convention that positive LOS motion corresponds to motion towards the satellite. The black polygon outlines a region with short wavelength, spatially variable LOS displacements that result from landsliding and open-cast quarrying in the steep valley north east of Parina (Fig. 3.1b). The black dots are the mapped coseismic surface ruptures. The best-fitting model is shown in the middle panels, with the map view of the fault plane shown as a black rectangle, and its surface projection as a black dashed line. The misfit between the observations and models is shown in the panels on the right. Profiles between A-A' through the observations (black dots) and models (red dots) are shown below. Steep gradients of LOS displacement near the surface ruptures (shown by the vertical arrows) are clear in the descending-track profile, but not present in the smoother ascending track data. As the descending-track acquisition was collected 19 days after the earthquake, whilst the ascending track includes only 8 days of postseismic deformation, these differences between the surface displacements may reflect postseismic afterslip. I present models and a discussion of the postseismic deformation in Section 3.2.5.

allows the slip vector azimuth to be between 230^o and 280^o (Fig. 3.7). The teleseismic waveform modelling constrains the slip vector azimuth to be between 211^o and 245^o, therefore the range of slip vectors consistent with all of the InSAR, seismology and surface rupture constraints have an azimuth of 230-245^o (NE-SW; see Fig. 3.7).

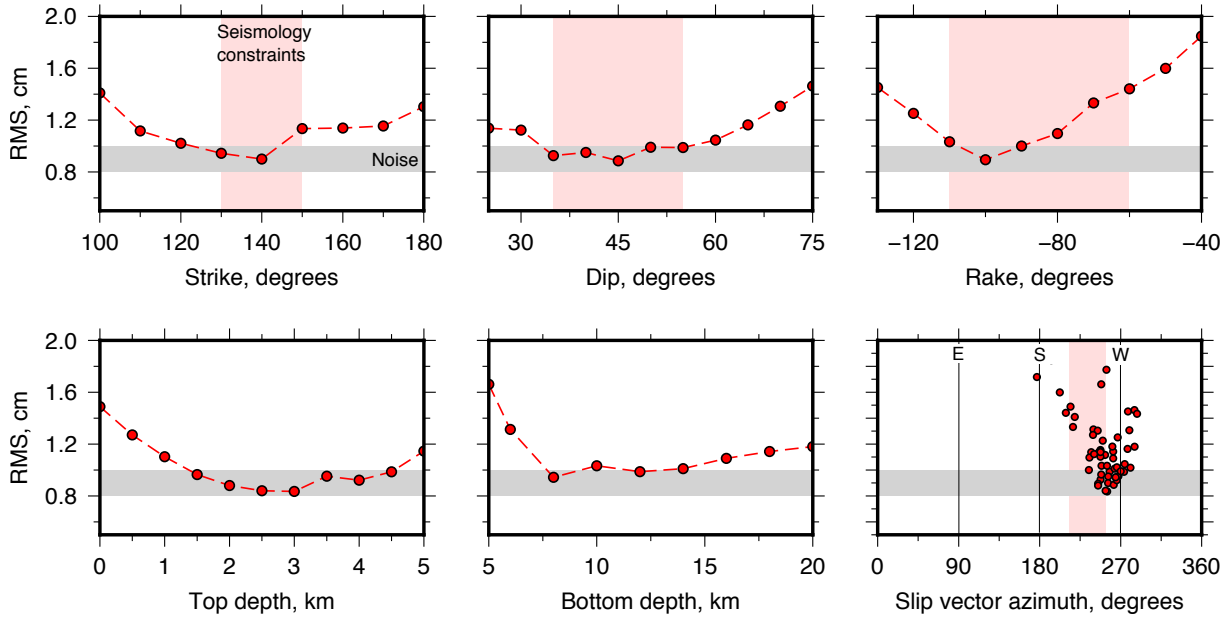

Figure 3.7 Sensitivity analysis of the InSAR slip inversions to the fault parameters. The light red bars mark the possible range of fault parameters determined from the seismological body-waveform modelling (Fig. 3.3, 3.4) and the orientation of the surface ruptures. The grey bar shows the noise levels in the interferograms. The slip vector azimuth is given as the motion of the hangingwall relative to the footwall in degrees clockwise from north.

3.2.5 Postseismic Deformation

Models of coseismic fault motion indicate that the majority of slip in the Parina earthquake remained buried below 3 km depth (Fig. 3.6, 3.7). However the 10-30 cm-high surface ruptures measured three days after the earthquake suggest that some coseismic slip may have reached the surface. Coseismic slip decreasing towards the surface on faults is commonly observed [e.g. Fialko et al., 2005] and has previously been recognised on normal faults [e.g. Copley et al., 2012; Bie et al., 2014]. Limited shallow coseismic slip is likely to reflect either inelastic deformation of the near-surface [Kaneko and Fialko, 2011], rate-strengthening frictional properties of the shallow fault zone [Marone and Scholz, 1988], or both. In the latter case, the fault may creep postseismically (afterslip), causing transient, short-wavelength surface deformation near the coseismic rupture.

I formed interferograms covering the first 8 months following the Parina earthquake (Fig. 3.8a) using the same method described in Section 3.2.3. In addition, I also generated a time series of postseismic deformation by extracting the relative LOS motions to either side of the surface ruptures from a series of interferograms that were formed with a common post-earthquake acquisition (collected within 19 days of the earthquake) as the reference image in each pair.

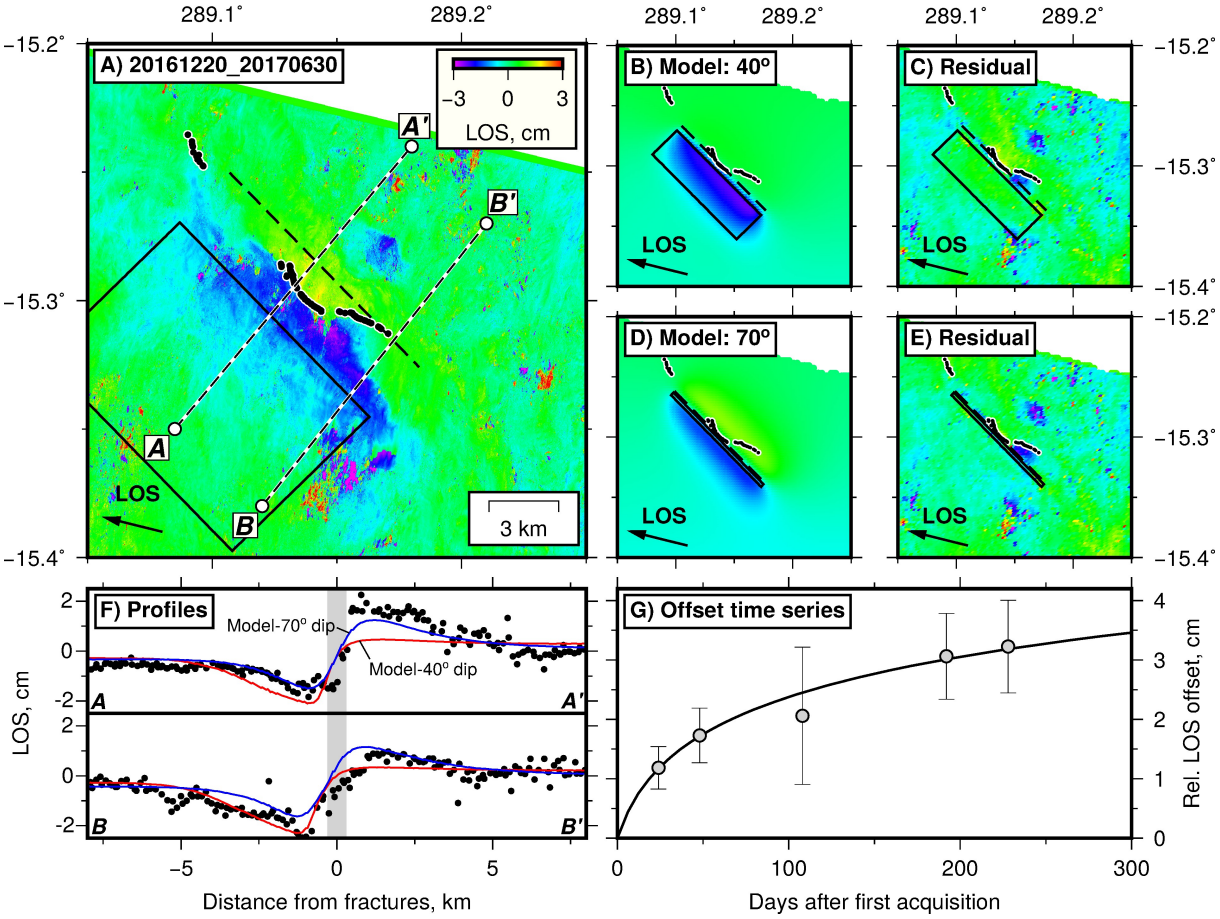

Figure 3.8 Postseismic deformation following the 2016 Parina earthquake. (a) Descending-track interferogram covering the first 6 months after the earthquake. The pre- and post-event acquisition dates are given in YYYYMMDD format in the top left, and the black dots represent the coseismic surface ruptures. The map view of the best-fit coseismic fault plane is shown as a black solid line, and its surface projection as a black dashed line. (b) The best-fit fault model to the postseismic surface displacement when the fault strike, dip and rake were fixed to the coseismic fault plane. (c) The residual for the model in (b). (d) Best-fit model when the strike and rake were fixed to their coseismic values, but the dip was fixed to 70^o. (e) The residual for the model in (d). (f) Profiles extracted through the modelled and the observed LOS motions for A-A' and B-B' in (a). The black dots are the observed LOS changes, the red lines are the model in (b), the blue lines are the model in (d) and the grey bar denotes the location of the surface ruptures. (g) Temporal evolution of the relative LOS motion between the immediate hangingwall and footwall of the Parina Fault. Error bars are the 1 standard deviation bounds. The black solid line is a best-fit curve of the form $a \ln(1 + t/t_r)$, showing that the postseismic deformation decays with the logarithm of elapsed time with $t_r = 12$ days.

The descending-track interferograms reveal a sharp offset in the LOS displacements across the central section of surface ruptures, with the size of the offset increasing with time after the earthquake (Fig. 3.8a,f). The LOS offset decays with distance perpendicular to the surface ruptures over a length scale of ∼3-5 km (Fig. 3.8f), indicating the majority of postseismic deformation is within the top 5 km of the crust. Postseismic signals are less clear in the ascending-track interferograms due to the larger component of atmospheric noise. The temporal evolution of the postseismic deformation follows a typical logarithmic transient decay [e.g. Smith and Wyss, 1968; Ingleby and Wright, 2017] with a relaxation time of 12 days (Fig. 3.8g), which is similar to estimates from a number of other studies [e.g. Savage et al., 2005; Fielding et al., 2009].

I interpreted the postseismic InSAR observations to reflect shallow afterslip on the up-dip extension of the coseismic fault plane, and not shallow poro-elastic deformation [e.g. Peltzer et al., 1998; Fielding et al., 2009], because the sharp step in LOS directly correlates with the location of the coseismic surface ruptures, and the polarity of the LOS motions are the same as those in the earthquake. I inverted the observed surface displacements 6 months after the Parina earthquake for the best fit, constant-slip fault (as in Section 3.2.4) with the rake fixed to that of the coseismic fault model. The postseismic InSAR measurements are consistent with ∼6-7 cm of afterslip on a fault with equivalent strike, dip and length to the coseismic fault plane, but with afterslip focused between 0 and 4 km depth (Fig. 3.8b,d). However, the constant-slip model cannot match both the smooth LOS displacement pattern across the margins of the surface ruptures, and the sharp change in LOS across the central section of the ruptures (Fig. 3.8a,f). This pattern indicates afterslip did not extend to the surface along the whole fault, but remained buried along the edges of the coseismic rupture. In addition, the symmetrical pattern of LOS motions across the surface ruptures implies the fault may become steeper (∼70^o) in the near-surface (Fig. 3.8a,f), which has commonly been inferred for normal faults [Jackson et al., 1982]. The minimum postseismic moment release due to afterslip needed to account for the surface displacements at Parina is 1.3×10^{17} Nm, which is equivalent to ∼5-10% of the coseismic moment release.

3.2.6 Parina Earthquake: Summary

I found that the Parina earthquake ruptured a 13 km-long, south west-dipping, shallow-crustal normal fault with a slip vector azimuth of 230-245^o. The majority of slip in the earthquake (∼0.5 m) was buried between 3 and 10 km depth, however a small component of slip did extend to the surface (0.1-0.3 m). Within 6 months of the earthquake around 15-35% of the shallow coseismic slip deficit was released through postseismic afterslip up-dip of the coseismic rupture (source models summarised in Table 3.2).

The seismological body-waveform model for the Parina earthquake derived in Section 3.2.2 yielded a coseismic moment release that is half the geodetic moment release determined from the InSAR fault model (Table 3.2). Sensitivity testing of the body-waveform model suggests that the small moment release is not a product of the trade-off between centroid depth and moment. The discrepancy is also unlikely to be caused by postseismic afterslip contributing additional moment to the geodetic model, as seismological source models using long-period body waves (45-100 s) and surface waves (50-300 s) from the gCMT and USGS W-phase inversions are consistent with the geodetic estimate of coseismic

moment release. This mismatch suggests that the body-waveform model is underestimating the true moment release in the earthquake.

Differences between the moment release estimated by seismological and geodetic methods do not occur systematically across the Andes [Holtkamp et al., 2011; Devlin et al., 2012], suggesting the low moment release in the body-waveform model is unlikely a product of inaccuracies in the regional-scale velocity structure [e.g. Penney et al., 2015]. This leaves the possibility that the attenuation of body waves around the Parina earthquake in the period band used by the body-waveform inversion, but not the regional moment tensor inversions such as gCMT or W-Phase (∼15-45 s), may be unusually high. The high attenuation could be a product of shallow intrusive magmatism [e.g. Myers et al., 1998].

Method	Strike	Dip	Rake	L, km	W, km	$\bar{u}$, m	M_0, Nm
gCMT	148	43	274	-	-	0.4‡	2.2×10^{18}
USGS	134	35	263	-	-	0.5‡	2.3×10^{18}
BWF	144	39	276	-	-	0.2‡	$0.8\text{-}1.4\times10^{18}$
InSAR	135	40	250	13	12	0.5	2.4×10^{18}
Ruptures	130-145	-	-	12	-	0.1-0.3	$0.4\text{-}1.3\times10^{18}$ †

Table 3.2 Comparison of the source parameters determined from the surface ruptures, seismology and InSAR observations of the Parina earthquake. gCMT is the global Centroid Moment Tensor best double-couple solution [Ekström et al., 2012], USGS is the W-phase best double-couple solution from the NEIC and BWF is the long-period body-waveform solution presented in Section 3.2.2. L and W are the along-strike length and down-dip width of the rupture patch, respectively. Moment is calculated using $M_0 = GA\bar{u}$, where G is the shear modulus (30 GPa), A is the fault area and $\bar{u}$ is the average fault slip. Values marked with † have been calculated assuming the fault rupture is square (i.e. $L \approx W$), and values marked with ‡ have been calculated assuming $L = W = 13$ km.

Only by combining geodetic, seismological and field observations have I been able to properly quantify the uncertainty in the earthquake slip vector, and show that the direction of extension at Parina is NE-SW. Seismicity surrounding Parina is typically confined to the top 10-15 km of the crust (Fig. 3.1a), suggesting the Parina earthquake ruptured most, if not all, of the seismogenic layer. As a result, the NE-SW extension is likely to be representative of the dominant strain within this region.

Shortening in the adjacent sub-Andean lowlands recorded in earthquake slip vectors and the orientation of fold axes and thrust fault scarps is parallel to the direction of extension at Parina (Fig. 3.1a), implying the mountains are locally deforming in plane strain. Smaller normal-faulting earthquakes with poorly-constrained source parameters show a similar pattern, but with significant variability, in which the direction of extension appears to be roughly orientated (within $\pm45^o$) with shortening in the adjacent sub-Andes [Cabrera and Sebrier, 1998; Devlin et al., 2012]. This is the pattern of fault slip expected if deformation within a mountain range is controlled by a contrast in gravitational potential energy between the mountains and its surrounding lowlands [e.g. Dalmayrac and Molnar, 1981].

In the next section I assess the extent to which potential energy contrasts control the deformation patterns in the Andes and the South American forelands, using well-constrained depths and mechanisms of recent moderate-to-large magnitude earthquakes and existing GPS measurements.

3.3 Kinematics and Dynamics of Deformation in the Andes

The forces controlling deformation in mountain ranges derive predominantly from: (1) relative motions of the bounding plates, (2) gravity acting on density contrasts within the lithosphere, and (3) shear tractions on the base of the overriding lithosphere from the underthrusting of rigid foreland material [Artyushkov, 1973; England and Houseman, 1989; Wdowinski et al., 1989]. These forces are in a quasi-static balance with each other, viscous resistance within the ductile lithosphere, and shear resistance on faults within the brittle crust. Different contributions of these forces to the overall balance will be reflected in the pattern of active faulting within the mountain range and its forelands [e.g. Molnar and Lyon-Caen, 1988].

In order to investigate the pattern of active faulting in the Andes and South America, I compiled a catalogue of earthquakes with $M_w > 5$ that have been modelled using body waveforms or P-wave first motions and 19 new solutions of my own (see Appendix B). In addition, I included well-constrained gCMT catalogue events with >80% double-couple moment tensors (as defined in Jackson et al. [2002]) from Dziewonski et al. [1981] and Ekström et al. [2012], with hypocentral depths taken from the catalogue of Engdahl et al. [1998] where available. I have included waveform-modelled earthquakes with M_w 5-5.5 in this compilation, as small earthquakes provide information on the depth extent of faulting in South America [e.g. Assumpção and Suarez, 1988; Assumpção, 1992; Devlin et al., 2012]. Below I describe the pattern of earthquakes, in conjunction with GPS and geomorphological information, and discuss the implications for the forces acting on the Andes and the South American foreland.

3.3.1 Faulting in the High Andes

Moderate-magnitude earthquakes in the crust of the high Andes are infrequent, but reveal a pattern of predominantly shallow (<10-15 km) normal and strike-slip faulting events [Doser, 1987; Cabrera and Sebrier, 1998; Holtkamp et al., 2011; Devlin et al., 2012; Jay et al., 2015, This study] (Fig. 3.1a). One exception to this pattern is seen adjacent to the Shira Uplift in south Peru, where oblique reverse faulting in the high Andes was observed in the 1969 Pariahuanca earthquakes [Philip and Megard, 1977; Suarez et al., 1983; Sébrier et al., 1988] (Fig. 3.1a; PH1969). Otherwise the majority of the reverse-faulting earthquakes are confined to regions <3000 m elevation [Suarez et al., 1983]. The dependence of faulting mechanism on elevation is typical of mountain ranges in which gravitational potential energy contrasts are an important factor in the forces controlling deformation [Dalmayrac and Molnar, 1981; Copley et al., 2009].

Nearly all of the moment release from recent normal-faulting seismicity in the high Andes has been focused in south Peru, whilst the Bolivian Altiplano and Puna plateau in northern Argentina have remained essentially aseismic over the same time period (Fig. 3.1a). Geomorphological evidence of recent normal faulting is also concentrated in south Peru, with a number studies identifying metre-high Holocene fault scarps bounding footwall uplifts with a few hundred metres of relief (e.g., Sangararra Fault [Suarez et al., 1983]; Tambomachay Fault [Mercier et al., 1992]; Langui-Layo Fault [Benavente et al., 2013]; Parina Fault [This study]; see also Chapter 4). GPS measurements in south Peru limit the cumulative NE-SW extension rate across the high Andes to $\ll$5 mm/yr [Kendrick et al., 2001;

Villegas-Lanza et al., 2016], which is equivalent to an extensional strain rate $< 2 \times 10^{-8}$ 1/yr over the 200 km-wide plateau. In contrast, there is no evidence of recent fault-controlled relief in the Bolivian Altiplano, and the shallow crust is inferred to be undeforming [Lamb and Hoke, 1997; Lamb, 2000; Weiss et al., 2016]. Schoenbohm and Strecker [2009] and Zhou et al. [2013] identified a number of putative normal faults within the Puna plateau in northern Argentina, however few of those mapped were associated with Holocene surface ruptures, and their estimated slip rates are $\lesssim$0.1 mm/yr over the last 0.5 Myrs. Therefore, both the recent seismicity and Holocene fault activity imply that the high Andes in south Peru is extending faster than the Bolivian Altiplano, and possibly faster than the Puna plateau.

Differences in strain rate within an isostatically-compensated mountain belt deforming in response to variations in gravitational potential energy are related to differences in elevation [England and Houseman, 1989; D'Agostino et al., 2014]. Crustal thickness estimates [Assumpção et al., 2013] and small (<50 mGal) free-air gravity anomalies within the Central Andes both suggest that the elevation contrasts on length-scales much larger than the elastic thickness of the Andean crust ($T_e \approx 10$ km; Rodríguez Tribaldos et al. [2017]) are predominantly isostatically supported. I isolated the long-wavelength, isostatically-compensated component of the topography by filtering the SRTM 90 m elevation model [Farr et al., 2007] using a Gaussian filter with a width of 100 km (i.e. $\gg T_e$). I found that the recent normal-faulting seismicity in south Peru occurs in a region with the highest modal elevation in the whole Andes at ∼4500 m, whilst the Altiplano and Puna have lower modal elevations of ∼3800 m and ∼4200 m, respectively (Fig. 3.9). Therefore the distribution of recent normal-faulting earthquakes may reflect higher extensional strain rates in the south Peruvian Andes compared to the surrounding mountains due to the region's high relative elevation [e.g. England and Molnar, 1997a].

The current elevation contrasts influencing the extension rates within the Andes can be used to calculate the material properties of the lithosphere and the time-scale over which elevation contrasts can be supported. Consider two unit columns of lithosphere within a mountain belt of thickness L_1 and L_2 separated by a height difference h. A simple 1-D horizontal force balance between body forces acting on these columns and viscous resistance, assuming shear stresses on horizontal planes are negligible, is given by [D'Agostino et al., 2014; England and Molnar, 2015]:

$$2L\frac{\partial \bar{\sigma}_{xx}}{\partial x} = \frac{\partial \Gamma}{\partial x}, \tag{3.1}$$

where $\bar{\sigma}_{xx}$ is the vertically-averaged horizontal deviatoric stress acting on the columns and Γ is the gravitational potential energy per unit area of the column. Assuming the lithosphere has a Newtonian rheology (i.e. $\bar{\sigma}_{xx} = 2\eta\dot{\varepsilon}_{xx}$), integrating Equation 3.1 and applying the condition that one of the columns is undeforming, yields:

$$\dot{\varepsilon}_{xx} = \frac{\Delta\Gamma}{4\eta L}, \tag{3.2}$$

where $\Delta\Gamma$ is the difference in gravitational potential energy between a column with zero strain rate and a deforming column. For Airy isostatic compensation $\Delta\Gamma$ can be approximated as γh, where γ is some constant scaling elevation contrasts between the deforming and undeforming area h to the gravitational potential energy contrast [D'Agostino et al., 2014]. From Equation 3.2, variations in elevation within a mountain range should be linearly proportional to variations in the deformation rates.

Assuming incompressibility of the lithosphere, and the conservation of area in cross section, horizontal extension of the lithosphere at strain rate $\dot{\varepsilon}_{xx}$ in response to horizontal contrasts in gravitational potential energy would lead to lithosphere thinning given by:

$$\frac{dL}{dt} = -\dot{\varepsilon}_{xx} L = -\frac{\gamma h}{4\eta} \tag{3.3}$$

The difference in the thickness between the columns $L_1 - L_2$ is related to the elevation contrast through an isostatic relationship $L_1 - L_2 = h\frac{\rho_m}{\Delta\rho}$, where $\Delta\rho$ is the density difference between mantle and crust. Substituting the isostatic relationship into Equation 3.3 gives the following first-order ordinary differential equation:

$$\frac{dh}{dt} + \frac{\gamma\Delta\rho}{4\eta\rho_m} h = 0 \tag{3.4}$$

Equation 3.4 has a particular solution of the form $h(t) = h_0 \exp(-t/t_r)$, where $t_r = \frac{4\eta\rho_m}{\gamma\Delta\rho}$ and h_0 is the initial elevation of the deforming column above the undeforming column. Therefore the elevation contrasts between deforming and undeforming regions within a mountain belt will decay exponentially at a rate dependent on the density contrasts between crust and mantle and the viscosity of the lithosphere.

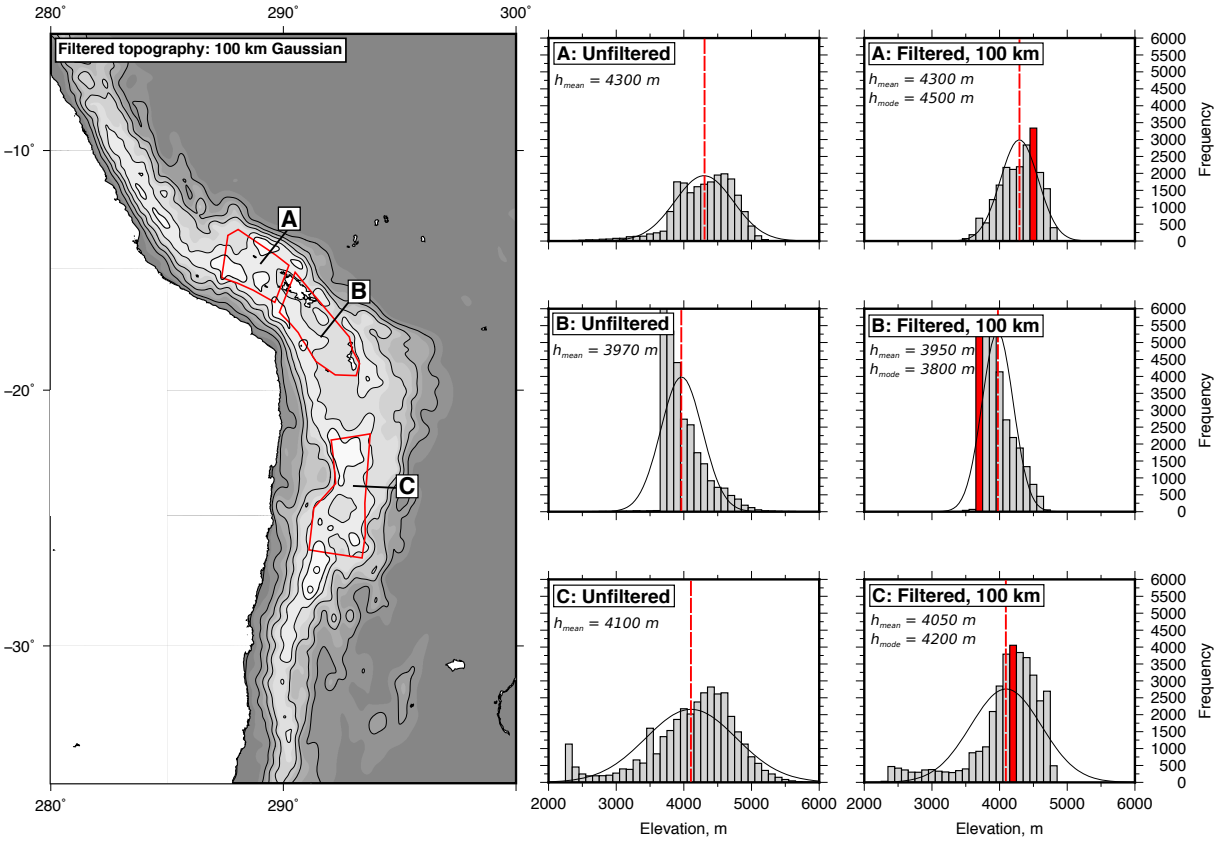

Figure 3.9 Along-strike variability in the smoothed topography in the high Andes. (left) SRTM 90 m topography smoothed with a Gaussian filter using a filter width of 100 km. (right) Histograms of elevations in three different regions along-strike. These regions have been selected because they have notably different deformation rates within the high mountains (see text). The red-dashed line marks the mean elevation on each histogram, and the red bar highlights the modal elevation. A best-fit Gaussian curve is shown in the background for each histogram, highlighting that the mean is not necessarily a representative metric of the "average" height.

Using the undeforming Bolivian Altiplano as a reference it is possible to estimate the average viscosity of the Andean lithosphere from the analysis presented above. Combining the current maximum extensional strain rate estimate in south Peru ($< 2 \times 10^{-8}$ 1/yr), the current elevation contrast between south Peru and the Bolivian Altiplano ($h \sim 700$ m), and taking γ to be 1.5×10^9 N/m per metre of elevation (see Section 3.4.1), Equation 3.2 can provide a lower bound on the vertically-averaged Newtonian viscosity of the Andean lithosphere of $\eta > 3 \times 10^{21}$ Pa s. Assuming the forces acting on the Andes have remained constant since the onset of extension, and given the lower bound on the lithosphere viscosity, elevation contrasts between south Peru and the surrounding high Andes will decay with a time constant t_r of at least ∼3 Myrs, and are unlikely to have existed much earlier than 10 Ma.

In addition to the normal faulting discussed above, strike-slip faulting also occurs in the high Andes south west of Cusco, particularly where there are significant along-strike changes in the geometry of the mountain belt and the amount of E-W shortening across the sub-Andes [Kley and Monaldi, 1998] (Fig. 3.1a). In these isolated regions the Andes does not behave in a two-dimensional manner, as there is a component of strain along-strike, and therefore balancing forces on cross-sections perpendicular to the range front is not appropriate. In this chapter, I focus on regions where extension in the high Andes is parallel to shortening in the adjacent lowlands, so the forces acting on the mountain belt can be treated in two dimensions [Dalmayrac and Molnar, 1981].

3.3.2 Faulting in the Eastern Cordillera

The Eastern Cordillera defines the area between the low-relief, high-elevation Andean plateau, and the sub-Andean lowlands (Fig. 3.1a). Seismicity in this region is sparse, but consists mainly of moderate magnitude reverse and strike-slip faulting, such as the 1998 M_w 6.6 Aiquile earthquake in Bolivia [Funning et al., 2005a] (Fig. 3.1a; AQ1998). The N-S trending strike-slip rupture of the Aiquile earthquake cut across pre-existing fold-thrust belt structures that were active at ∼10 Ma, which indicates the intermediate principal stress has switched from being horizontal at the time in which the fold-thrust belt was active, to vertical [Funning et al., 2005a]. This transition in stress state can be accounted for by recent uplift of the Eastern Cordillera, which caused the forces due to contrasts in gravitational potential energy between the Eastern Cordillera and forelands to increase, such that they now balance the compressional forces transmitted across the sub-Andes into the range interior.

North of the Aiquile earthquake epicentre are the Cochabamba and Punata basins (Fig. 3.1a). These asymmetrical half grabens are filled with post-Miocene sediments and are bounded by large (∼2 km basement relief), E-W striking normal faults [Renner and Velasco, 2000], which are oblique to the NW-SE trend of the range front in the adjacent sub-Andes. Kennan [1993] proposed the basins formed predominantly through range-parallel (NW-SE) extension. Faults with a similar geometry relative to the orogen front are seen in southern Tibet [e.g. Armijo et al., 1986] and the island of Crete in the overriding plate of the Hellenic subduction zone [e.g. Taymaz et al., 1990]. The arc-perpendicular normal faults in southern Tibet and Crete have been attributed to radial thrusting on the margins of the high regions causing along-strike extension in the overriding plate [e.g. Armijo et al., 1986; Copley et al., 2011b] — a feature that is also reflected in the earthquake slip vectors and GPS data from the Andes discussed in the next section (Fig. 3.10a). Therefore, a similar process may account for the

normal faults at Cochabamba and Punata. Between Cusco and Santa Cruz the direction of thrust transport in the sub-Andes rotates clockwise by $\sim 30^o$ (Fig. 3.10a). Given that the shortening rate in the back-arc is ∼5 mm/yr [Bevis et al., 2001], there must be ∼2.6 mm/yr of along-strike extension, the majority of which is probably taken up by the faults around Cochabamba.

3.3.3 Faulting in the sub-Andes and Peru-Chile Trench

Faulting on the western margin of the Andes is dominated by large-magnitude (M_w >7.5) megathrust earthquakes along the subduction interface between the Andean forearc and the subducting Nazca plate [e.g. Pritchard et al., 2007; Sladen et al., 2010; Lin et al., 2013]. Slip in these megathrust earthquakes is consistently parallel to independent estimates of the orientation of motion between the Nazca plate and the South American shield [Norabuena et al., 1999; DeMets et al., 2010] (Fig. 3.10a). Although there is evidence of recent reverse faulting within the Andean forearc [e.g. Hall et al., 2012; Benavente et al., 2017], motion on these faults is small compared to slip on the megathrust.

Unlike slip on the megathrust, the slip vectors of earthquakes on the eastern margin of the Andes vary significantly along-strike of the mountain belt, with the most conspicuous changes occurring between south Peru and northern Argentina. North of Cusco a thrust-faulting earthquake in 1998 (Fig. 3.10a; CZ1998) ruptured the shallow detachment beneath the sub-Andes with a NNE-directed slip vector orientated $\sim 70^o$ anti-clockwise to the Nazca-South America plate motion. Moving south along the range front, between southern Peru and northern Bolivia the earthquake slip vectors rotate clockwise from NNE to NE (Fig. 3.10a). Around the Santa Cruz bend the slip vectors rotate clockwise by a further ∼30-40^o to point roughly east [Chinn and Isacks, 1983; Assumpção and Araujo, 1993; Devlin et al., 2012] (Fig. 3.10a). Finally, within southern Bolivia and northern Argentina the slip vectors remain pointing east, orientated ∼20-30^o clockwise relative to Nazca-South America plate motion. The azimuth of the interseismic GPS velocity field in the eastern Andes relative to stable South America also rotates clockwise between south Peru and northern Argentina, mirroring the pattern in the earthquake slip vectors [Lamb, 2000; Weiss et al., 2016] (Fig. 3.10b).

Elastic strain accumulation within the Andes from oblique subduction of the Nazca plate beneath the Andean forearc has been proposed to account for the rotation in the interseismic GPS velocities in the eastern Andes [Bevis and Martel, 2001; Bevis et al., 2001]. Although the elastic block model of Bevis et al. [2001] fits the azimuth of GPS velocities south of the Santa Cruz bend, in southern Peru and northern Bolivia it consistently underpredicts the northward component of the GPS velocities and earthquake slip vectors (Fig. 3.10b and Fig. 3.11c,d). These spatially coherent misfits imply the elastic models are not capturing the orientation of the shortening direction in the sub-Andes. In addition, the assumption in Bevis et al. [2001] that shortening in the sub-Andes can be modelled as slip parallel to Nazca-South America plate motion on a detachment fault is not consistent with the observed earthquake slip vectors (Fig. 3.10a).

Alternatively, if the eastern Andes are deforming predominantly in response to horizontal contrasts in gravitational potential energy, then the direction of shortening will be parallel to topographic gradients [e.g. Lamb, 2000; Copley and McKenzie, 2007]. I found that earthquake slip vectors in the sub-Andes are consistently orientated parallel to gradients in the topography (Fig. 3.11b). The topographic

gradients also match the general pattern of clockwise rotating GPS azimuths between southern Peru and northern Argentina, the northward component of the GPS velocity field near Cusco, and the rotation of the GPS velocities around the Santa Cruz bend (Fig. 3.10b). In addition, the azimuth of shortening inferred from the GPS and earthquake slip vectors are statistically better-fit by the direction of topographic gradients than elastic models of strain accumulation on the subduction zone (Fig. 3.11). However, the fit to the GPS azimuths remains relatively poor in the south Peru and northern Bolivia, probably because the GPS data record the displacements due to slip on the sub-Andean detachment, plus the distant effects of transient elastic strain accumulation on the Peru-Chile megathrust [Bevis et al., 2001; Chlieh et al., 2011].

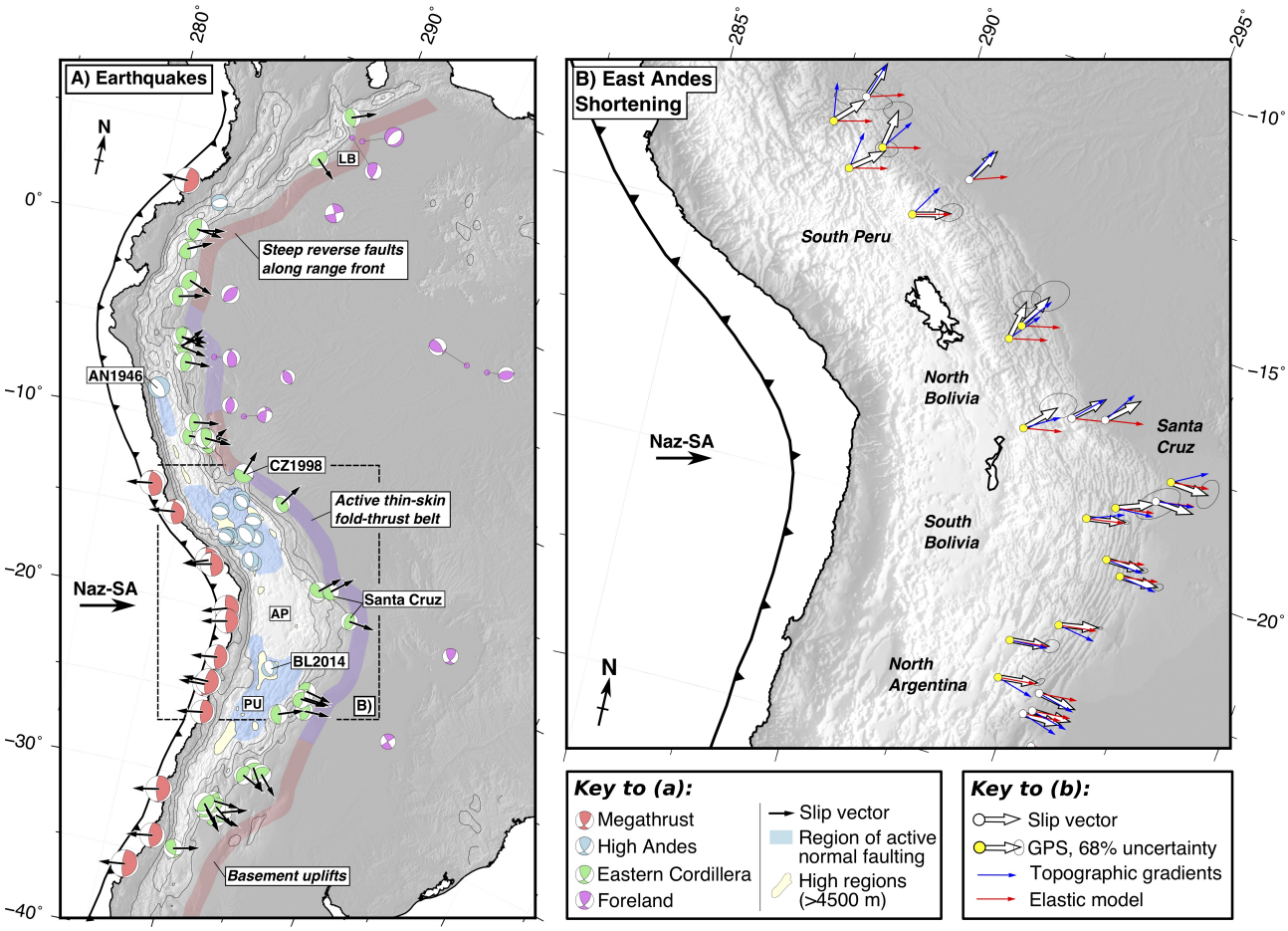

Figure 3.10 Earthquake and GPS data demonstrating the pattern of deformation on the margins of the Andes. (a) Slip vectors of moderate-magnitude earthquakes (see Table B.1). Thin black lines are the 1, 2, 3 and 4.5 km elevation contours from the Gaussian-filtered topography using a 300 km filter width. LB is the Llanos Basin, AP is the Altiplano and PU is the Puna plateau. Both (a) and (b) are in oblique Mercator projection about the Euler pole of the Nazca-South America convergence [DeMets et al., 2010], therefore slip vectors parallel to relative plate motion will be horizontal [McKenzie and Parker, 1967]. (b) Azimuth of shortening in the eastern Andes from selected earthquake slip vectors and interseismic GPS sites [Kendrick et al., 2001; Weiss et al., 2016], compared with gradients in the filtered topography and the elastic block model of Bevis et al. [2001]. GPS velocity azimuths in (b) are shown relative to stable South America with 1σ uncertainty ellipses. A comparison between the GPS and slip vector azimuths with topographic gradients and the elastic block model is shown in Fig. 3.11.

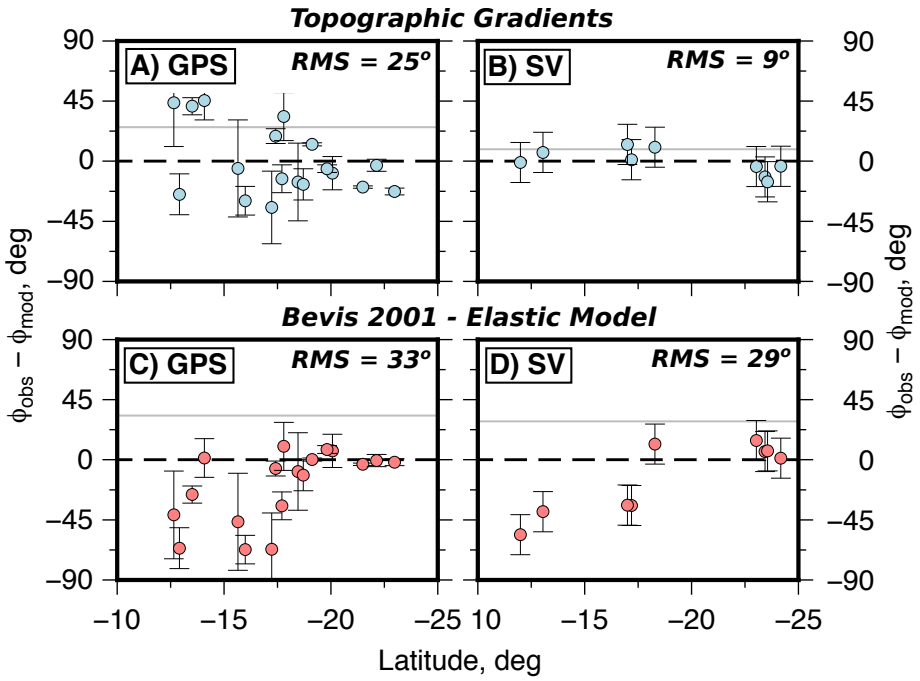

Figure 3.11 Comparison of earthquake slip vectors (SV) and GPS velocity azimuths as a function of latitude with topographic gradients (a,b) and the elastic model of Bevis et al. [2001] (c,d).

From the pattern of earthquake slip vectors and GPS, I conclude that the forces resulting from relative plate motion control the orientation of slip on the subduction interface on the western side of the Andes, whilst contrasts in gravitational potential energy between the mountains and forelands control the orientation of slip on faults on the Andes' eastern margin [Assumpção and Araujo, 1993; Lamb, 2000].

3.3.4 Faulting and Flexure in the South American Forelands

Reverse-faulting earthquakes in regions >300 km from the Andes range front (Fig. 3.10a) indicate that the South American foreland crust is breaking in response to compressional forces acting through the lithosphere [Assumpção, 1992]. However, within 300 km of the Andes range front, asymmetrical sedimentary basins [McGroder et al., 2015], long-wavelength, negative free-air gravity anomalies [Lyon-Caen et al., 1985], and shallow extensional faulting overlying compressional faulting at the base of the crust (Fig. 3.12, 3.13) imply that the forelands are bending in response to the load of the Andes [Lyon-Caen et al., 1985; Watts et al., 1995].

Evidence for extension in the Andes foreland is limited to a single M_w 6.4 normal-faulting earthquake beneath the Llanos Basin of Colombia (Fig. 3.10a). Long-period waveform modelling suggests this earthquake had a centroid depth of 18^{+5}_{-5} km (Fig. 3.12). The Moho beneath the Llanos Basin is at ∼40-45 km depth [Assumpção et al., 2013; Poveda et al., 2015], whilst the foreland basin sediment thickness is <8 km [McGroder et al., 2015], which indicates the normal-faulting earthquake reflects extension in the shallow crystalline basement of the bending South American foreland.

The transition from shallow extension to deeper compression beneath the Llanos Basin is captured by two M_w 5 reverse-faulting earthquakes close to the epicentral location of the normal-faulting event (Fig.

3.13a,c). These earthquakes were too small to study using the full long-period body-waveform modelling described above. Therefore, to estimate their centroid depths, I compared synthetic seismograms of the P, pP and sP phases to the observed vertical-component waveforms at teleseismic stations [e.g. Maggi et al., 2000b] (see Appendix B.3 for a more detailed discussion of the method). I found that the relative amplitude and arrival time of the depth phases in the seismograms for these two events can be matched if the earthquakes had centroid depths of 28^{+2}_{-2} km and 40^{+3}_{-2} km (Fig. B.12, B.16). Reverse faulting has also been recorded at 42 km depth beneath the Madre de Dios Basin in central Peru [Assumpção, 1992] (Fig. 3.13a), indicating that the bending portion of the South American lithosphere probably remains in compression from 26-30 km to at least the base of the crust (Fig. 3.13c).

Observations of shallow extensional earthquakes overlying deeper compressional earthquakes within the continental lithosphere are rare, and have only been documented previously in the forelands of the Himalaya [Molnar et al., 1977; Ni and Barazangi, 1984; Maggi et al., 2000b], and possibly in small (M_w <4.5) earthquakes recorded in the forelands of the Alborz mountains in northern Iran [Nemati et al., 2013]. The pattern of earthquakes in both the Tibetan and Andean forelands implies that flexural stresses are large enough to break faults in underthrusting continental lithosphere.

Treating the flexed South American forelands as a thin bending plate, the magnitude of the flexural stresses can be related to the curvature of the plate, and a factor that is governed by the assumed rheology of the plate [Turcotte and Schubert, 2002]:

$$\sigma_f = \frac{ET}{2(1-\nu^2)} \frac{d^2w}{dx^2}, \tag{3.5}$$

where σ_f is the maximum flexural stress, E is Young's modulus, ν is Poisson's ratio, T is either the effective elastic thickness of the plate (in a purely elastic model), or the thickness of the aseismic elastic core (in an elastic-plastic model with a constant yield stress), and $\frac{d^2w}{dx^2}$ is the curvature of the plate.

To estimate the curvature and effective elastic thickness T_e of the South American foreland beneath the Llanos Basin, I followed the method of McKenzie and Fairhead [1997] and modelled the free-air gravity anomalies produced by flexure of an elastic plate overlying an inviscid mantle half-space, with the plate overlain by low-density sediments. I found the gravity anomalies in the Llanos Basin could be fit by a plate model with a T_e of at least 20 km (Fig. 3.13b,d). However the misfit between the modelled and observed gravity field at large T_e values increases by only a fraction of the minimum misfit, suggesting the estimate represents only a lower bound (Fig. 3.13d). The results are consistent with those of Pérez-Gussinyé et al. [2007] and McKenzie et al. [2014], who found that T_e in the Andean forelands is 15-25 km, which is significantly smaller than the seismogenic thickness (40-45 km; Assumpção and Suarez [1988]). Stewart and Watts [1997] found a larger T_e of 50 km in the Llanos Basin, however their study relied on modelling individual Bouguer gravity profiles, and fixed the location of the plate break, which has typically been shown to overestimate T_e [e.g. Jackson et al., 2008; McKenzie et al., 2019].

The maximum curvature of the plate in the best-fit model is $\sim 4 \times 10^{-7}$ 1/m (Fig. 3.13b). Assuming the plate has a Young's modulus of 10^{11} Pa and Poisson's ratio of 0.25, Equation 3.5 would yield a maximum extensional flexural stress of ∼530 MPa. This stress will subject normal faults in the top half of the bending plate, which dip at $\sim 35^o$ relative to the plate surface (e.g. Llanos Basin earthquake; Fig. 3.12), to average shear stresses $\lesssim$130 MPa. For a simple elastic-plastic plate with a constant yield

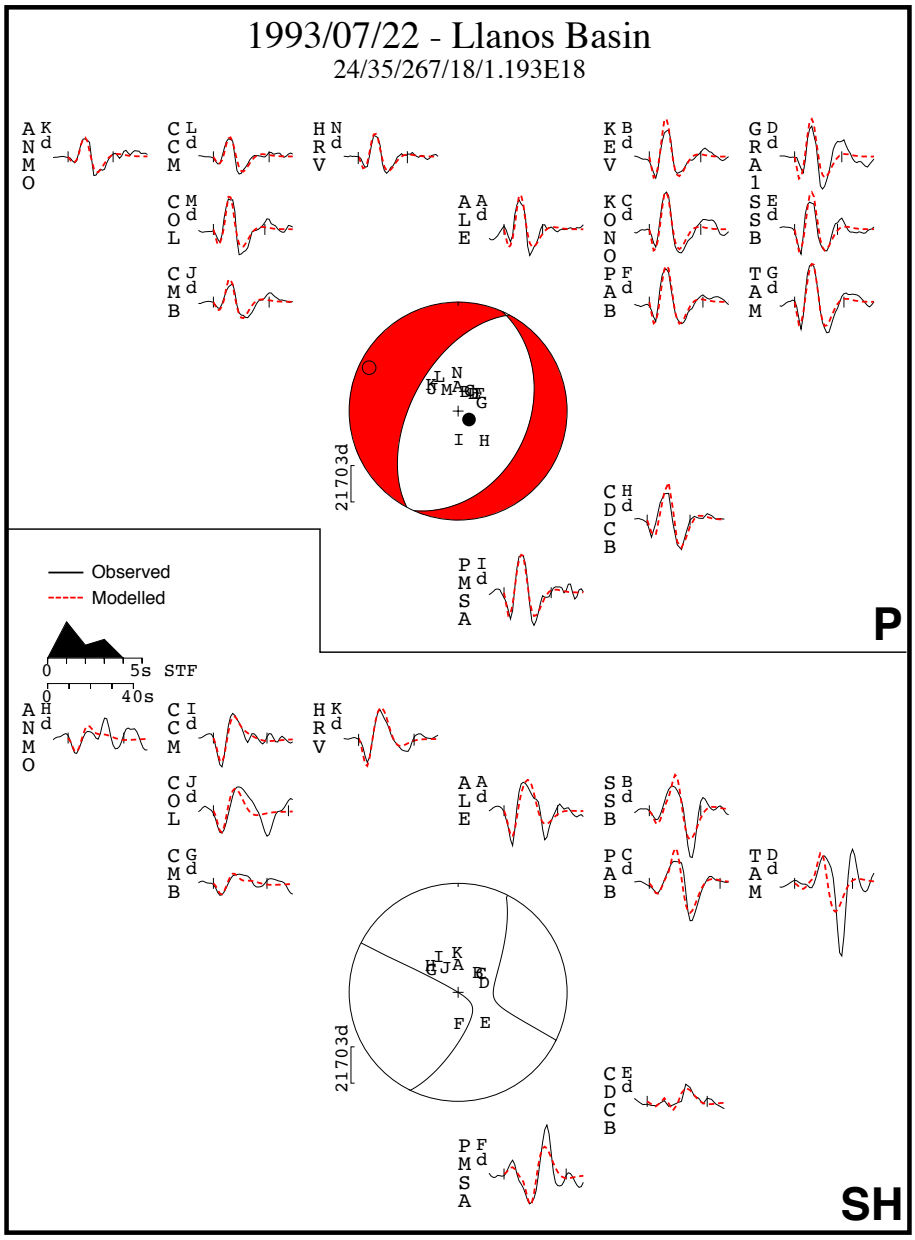

Figure 3.12 Minimum-misfit teleseismic body-waveform solution for the 22nd July 1993 Llanos Basin earthquake in Colombia. Figure layout is the same as for Fig. 3.3. The uncertainties in the fault parameters were estimated using the method described in Section 3.2.2. The parameter ranges are: strike = 0-50^o, dip = 30-40^o, rake = 242-293^o and depth = 13-23 km. The epicentral location of this event is shown in Fig. 3.13.

stress [Turcotte and Schubert, 2002], and an elastic core <17 km thick (based on the depth distribution of earthquakes; Fig. 3.13c), the maximum flexural stresses are reduced to $\lesssim$360 MPa, and the average shear stresses on faults to $\lesssim$90 MPa. Further earthquakes could reduce the estimate of the elastic core thickness, and therefore reduce the stress estimates. Nonetheless, this result would imply that faults in the foreland have an effective coefficient of friction $\mu' \lesssim 0.25$, which is far smaller than the $\mu' \sim 0.4$ suggested by Byerlee's rule derived from laboratory experiments of frictional sliding [Byerlee, 1978].

In contrast to the bending portion of the South American forelands, the normal faulting in the high Andes and reverse faulting throughout the foreland crust >300 km from the Andes range front appears to be primarily controlled by the forces per unit length exerted between the mountains and South America due to lateral contrasts in gravitational potential energy. In the next section I present calculations to estimate the forces acting through the South American forelands, and place an upper bound on the frictional strength of faults within the foreland crust.

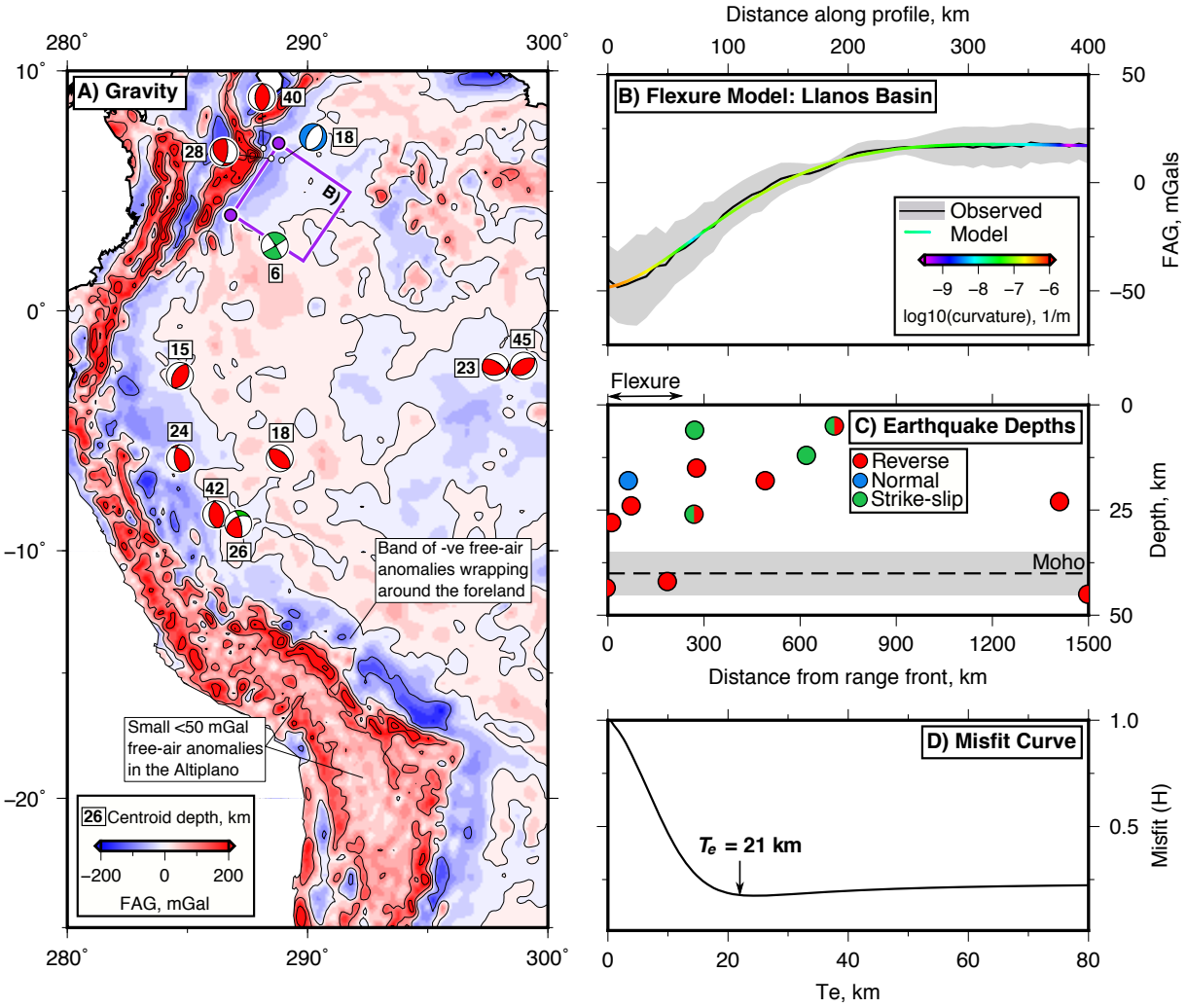

Figure 3.13 Free-air gravity (FAG), earthquakes and elastic plate models used to study the flexure of the South American forelands. (a) EIGEN-6c FAG map of South America [Shako et al., 2014] low-pass filtered to exclude signals with wavelength <50 km that are unrelated to flexure. The purple box is the region within which profiles through the gravity field have been stacked. (b) Stacked FAG anomalies from the Llanos Basin with 1 standard deviation (σ) bounds, and the best-fit model to the observed gravity profile. I assume that the sediments in the foreland basin are 500 kg/m^3 less dense than the mantle beneath the plate, and Young's modulus and Poisson's ratio of the plate are 10^{11} Pa and 0.25, respectively [Turcotte and Schubert, 2002]. The colour of the line shows the absolute curvature of the plate model. (c) Mechanisms of waveform-modelled foreland earthquakes as a function of distance from the Andes range front. The mean Moho depth and uncertainty ($\pm 1\sigma$) is taken from the catalogue of Assumpção et al. [2013]. (d) Weighted misfit between the flexure model and gravity observations for a range of elastic thicknesses, defined as $H = \frac{1}{N}\Sigma\left[\frac{g_m - g_o}{\sigma}\right]^2$, where g_m and g_o are the modelled and observed FAG, respectively, and N is the number of measurements along the profile.

3.4 Strength of the South American Forelands

3.4.1 Forces acting between the Andes and the South American Forelands

The forces per unit length due to potential energy contrasts between a mountain belt and its adjacent foreland can be calculated from lateral contrasts in the density structure between the two regions [e.g. Artyushkov, 1973; Dalmayrac and Molnar, 1981]. I build on the calculations of Dalmayrac and Molnar [1981] by using new estimates of the temperature structure, chemical composition and thickness of the crust and mantle lithosphere to refine the estimates of the forces per unit length acting between the Andes and South America, following a method similar to that of Copley and Woodcock [2016]. A summary of the parameters used in the calculations is provided in Table 3.3, and a description of the parameter selection is given below.

Variable	Value	Source
Forces:		
z_c^l	35-45 km	[Assumpção et al., 2013]
z_c^m	65-80 km	[Assumpção et al., 2013]
z_{lm}^l	120-140 km	[Priestley and McKenzie, 2013]
z_{lm}^m	180-220 km or 0 km	see Section 3.4.1
T_{moho}^l	600-700 ^oC	see Section 3.4.1
T_{moho}^m	700-1000 ^oC	[Weber et al., 2002]
T_p	1315 ^oC	[McKenzie et al., 2005]
α_c †	3×10^{-5} 1/K	[Turcotte and Schubert, 2002]
α_{lm} †	3-4.5$\times 10^{-5}$ 1/K	[Bouhifd et al., 1996]
ρ_a (0 ^oC)	3330 kg/m^3	[Turcotte and Schubert, 2002]
ρ_{lm} (0 ^oC)	$\rho_a - 50$ kg/m^3	[Lucassen et al., 2005]
ρ_c (0 ^oC)	2800 kg/m^3	[Lucassen et al., 1999]
Fault Strength:		
T_s	40-45 km	[Assumpção and Suarez, 1988]
z_{sed}	5-8 km	[McGroder et al., 2015]
z_{nf}	13-28 km	see Section 3.3.4
z_{core} ‡	1-20 km	see Section 3.3.4
θ	30-50^o	see Appendix B.1
E	540 kJ/mol	[Karato and Wu, 1993]
V	20 cm^3/mol	[Karato and Wu, 1993]
n	3	[Karato and Wu, 1993]
G	30 GPa	[Turcotte and Schubert, 2002]

Table 3.3 Parameters used to calculate for the force exerted between the Andes and South America, and the frictional strength of faults in the South American forelands. For an interpretation of the variables, see the text. Terms with superscripts ^{m} refer to the material beneath the mountains, whilst terms with superscript ^{l} refer to the material beneath the lowlands. (†) Linear coefficient of thermal expansion. (‡) The elastic core thickness is the extent of the region either side of the neutral fibre in the bending South American foreland over which the stress field changes from being extensional to compressional.

The density structure in the lithosphere is controlled by the thickness of the crust z_c and the lithospheric mantle z_{lm}, the composition of these layers ρ, and their temperature structure $T(z)$.

The crustal thickness in the Andes z_c^m and its forelands z_c^l has been determined using receiver functions to be 65-80 km and 35-45 km, respectively [Assumpção et al., 2013; Ryan et al., 2016]. The thickness of the lithospheric mantle is less well known. In the forelands, surface-wave tomography results infer the lithosphere z_{lm}^l is between 120 and 140 km thick [Priestley and McKenzie, 2013]. If the Andean lithosphere thickened by the same ratio as the crust during orogenesis it should be >200 km thick, which would be consistent with certain seismological results [e.g. Whitman et al., 1992; Priestley and McKenzie, 2013]. However the shallow-dipping Nazca slab may interfere with the lithospheric thickness estimates. It is possible that the Nazca slab could even limit the thickness of the lithosphere in places to <200 km [Ma and Clayton, 2014; Ward et al., 2016]. In addition, some seismological and geochemical studies have suggested that there may be no mantle lithosphere beneath parts of the Central Andes [e.g. Kay and Mahlburg Kay, 1993; Hoke and Lamb, 2007; Ward et al., 2016]. As a result, I took the Andean lithospheric mantle z_{lm}^m to be between 180 and 220 km thick, but also performed calculations in which there was no lithospheric mantle.

I assumed that the average density (at 0 ^oC) of the crust ρ_c in both the foreland and Andes was 2800 kg/m^3 [Turcotte and Schubert, 2002]. Changes in crustal density due to the effects of temperature were modelled using a thermal expansion coefficient α_c of 3×10^{-5} 1/K [Turcotte and Schubert, 2002]. The density of the lithospheric mantle ρ_{lm} was taken to be ∼50 kg/m^3 less than asthenosphere ρ_a at the same $P - T$ conditions, based on the mean density of mineral assemblages in xenoliths thought to sample the lithospheric mantle in the forelands and mountains [Lucassen et al., 2005; Carlier et al., 2005]. As the foreland lithospheric mantle is likely to be the source of the thickened Andean lithospheric mantle, both were assumed to have the same density at a particular temperature. The low-density lithospheric mantle is probably the result of ancient melt extraction, which left a residue depleted in the heavy incompatible elements [Jordan, 1978]. Similar geochemical inferences have also been made for a low-density lithospheric mantle beneath the mountains in Tibet and Iran [McKenzie and Priestley, 2016]. The thermal expansion of the mantle α_{lm} was modelled using the experimental results for olivine of Bouhifd et al. [1996].

The geotherm in the mountains and forelands was assumed to be in steady state, and consist of two linear sections between the surface and the Moho, and between the Moho and the base of the lithospheric mantle, where the mantle potential temperature T_p was fixed at 1315 ^oC. Earthquakes up to 45 km depth in the forelands [Assumpção and Suarez, 1988; Emmerson, 2007] suggest the whole crust (but not the mantle) is seismogenic, therefore the Moho temperature T_{moho}^l was taken to be between 600 and 700 ^oC [McKenzie et al., 2005]. Thick, radiogenic crust and extensive volcanism over the Cenozoic will have caused the crust in the Andes to be much hotter than the foreland, which is reflected in the high surface heat flow [Henry and Pollack, 1988], and crustal xenolith thermobarometry studies that indicate Moho temperatures T_{moho}^m could be as high as 700-1000 ^oC [Weber et al., 2002].

I calculated the horizontal force per unit length exerted between the Andes and South America by integrating the differences in vertical normal stress between the mountains and forelands $\Delta\sigma_{zz}$ from the surface to the depth of isostatic compensation ($F_{GPE} = \int \Delta\sigma_{zz}\, dz$) [Dalmayrac and Molnar, 1981]. By varying the temperature structure, composition and thickness of the crust and mantle lithosphere

within the range described above, I found that the horizontal force per unit length acting between the Andes and the South American foreland is 4-8$\times 10^{12}$ N per metre along-strike of the mountain range (Fig. 3.14a). This result is consistent with previous studies [Dalmayrac and Molnar, 1981; Froidevaux and Isacks, 1984; Molnar and Lyon-Caen, 1988; Meijer et al., 1997; Husson and Ricard, 2004; Oncken et al., 2012], but includes a larger range of uncertainty that is related to the range in possible lithospheric mantle thickness and the poorly-constrained temperature structure beneath the Andes that had previously not been considered [e.g. Molnar and Stock, 2009]. A similar estimate of 5×10^{12} N/m has been made for the horizontal forces acting between Tibet and India [Molnar and Stock, 2009; Copley et al., 2011a].

I also performed calculations in which the temperature structure beneath the mountains was cooled by the underthrusting South American foreland. The effect of underthrusting on the mantle temperature was simulated using a bi-cubic spline geotherm, which replicates the shape of the geotherms in Craig et al. [2012], to which I applied the following boundary conditions: (1) the temperature at the surface was 0 ^oC, (2) the temperature at the base of the Andean crust was 700-1000 ^oC, (3) a decrease in temperature between 50-150 ^oC occurs at the top of the lithospheric mantle as a result of the cold underthrusting South American shield, (4) the temperature at the base of the lithospheric mantle is equal to a mantle potential temperature of 1315 ^oC, and (5) the temperature gradient at the base of the lithospheric mantle is equal to the mantle adiabat of 0.3-0.6 ^oC/km [Turcotte and Schubert, 2002]. I found that cooling the lithospheric mantle reduces the average horizontal force acting between the Andes and South America by 1-2$\times 10^{12}$ N/m, but the range of the solutions remains the same.

3.4.2 Fault Friction in the South American Forelands

The forces per unit length due to contrasts in gravitational potential energy acting between the Andes and South America must be balanced by the forces acting through the South American foreland lithosphere. Reverse-faulting earthquakes throughout the non-bending regions of the South American forelands, outboard of the region of normal faulting in the high Andes, implies that these forces are large enough to exceed the static frictional strength of faults in the forelands (as is also seen in the Tibetan foreland in India [Copley et al., 2011a]).

I constructed one-dimensional yield stress profiles that reflect the stress state as a function of depth in the lithosphere east of the sub-Andean belt. I specifically consider two cases: the bending and non-bending part of the South American foreland. To calculate the force the lithosphere can support in these regions, I integrated the yield stresses over the lithosphere thickness $F_{fl} = \int \Delta\sigma_{xx}\, dz$ [e.g. Goetze and Evans, 1979; Brace and Kohlstedt, 1980]. I then compared the estimates of foreland strength F_{fl} with the estimates of the forces per unit length acting through the foreland lithosphere F_{GPE} to place an upper bound on the frictional strength of faults in the South American lithosphere.

Faults modulate the horizontal differential stresses $\Delta\sigma_{xx}$ that can be supported in the brittle portion of the lithosphere, which can be expressed as a function of the effective coefficient of friction μ' [Turcotte and Schubert, 2002]:

$$\Delta\sigma_{xx} = \frac{2\mu'\rho g z}{\pm \sin 2\theta - \mu'(1 + \cos 2\theta)}, \tag{3.6}$$

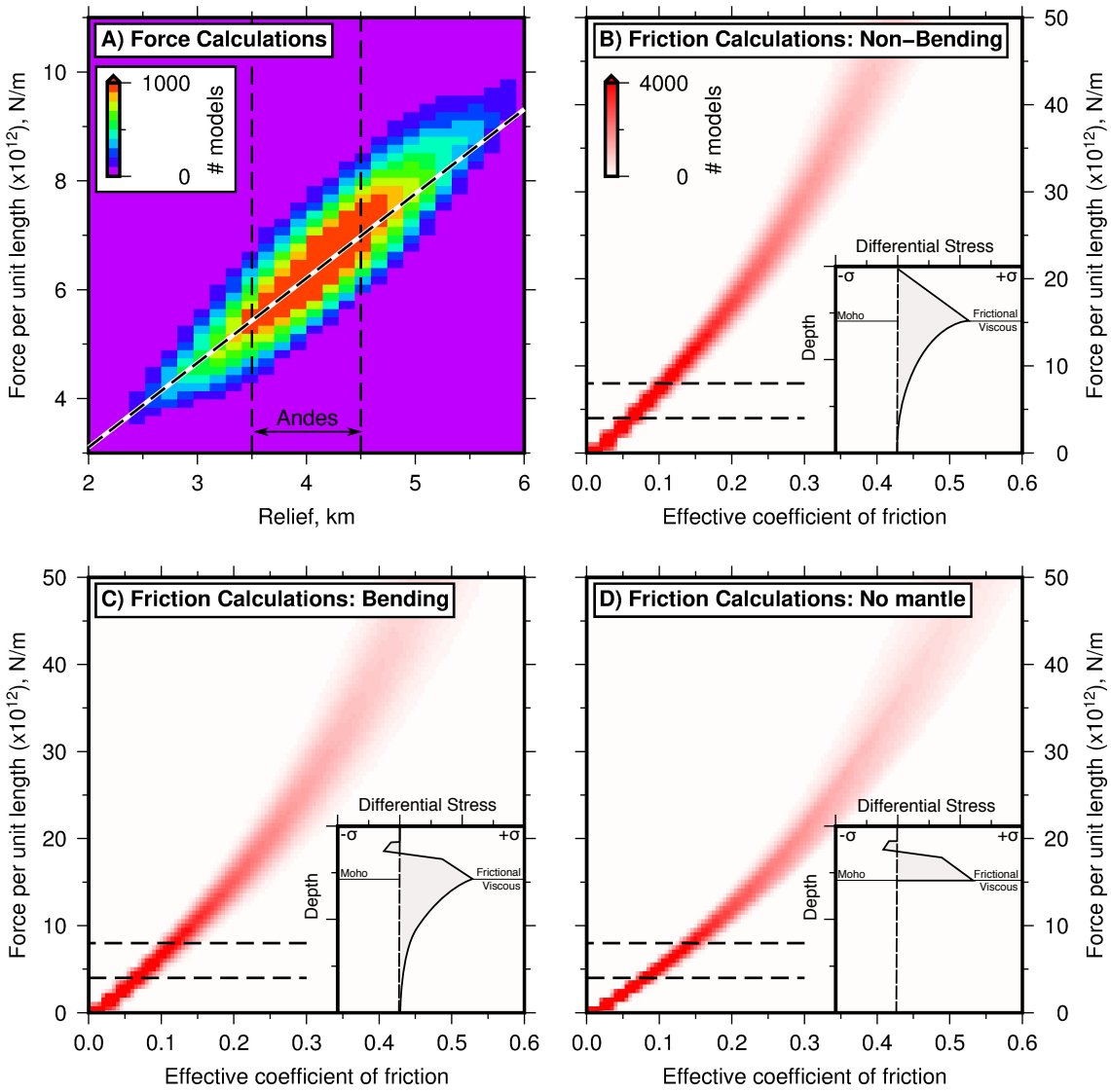

Figure 3.14 Calculations for the forces per unit length acting through the South American lithosphere. (a) Horizontal force acting between the Andes and South America as a function of relief between the mountains and forelands (described in Section 3.4.1). Vertical black dashed lines outline the range of appropriate solutions for the Andes. The dashed black-and-white line defines the relationship between relief and force assuming isostatic compensation at the base of the crust, with a crustal thickness of 70 km and 40 km in the mountains and lowlands. (b,c,d) Results of calculations for the maximum force that can be supported by the foreland lithosphere as a function of the effective coefficient of friction along faults (described in Section 3.4.2). The three different cases shown are: (b) the whole crust is in compression and there is no sediment layer (i.e. the foreland outside the bending region); (c) the top 5-8 km of crust is sediment that supports no force, the top 5-13 km of basement is in extension, and the bottom ~20 km is in compression (i.e. the foreland in the bending region); and (d) the end-member case when the lithosphere is bending, and the mantle supports no stress at all. Schematic yield stress profiles are shown inset. Horizontal black dashed lines are the bounds on the horizontal force acting through the South American lithosphere from (a). Where the envelope of models plots above these horizontal dashed lines, the foreland lithosphere would be too strong to break in earthquakes in response to the forces generated by contrasts in gravitational potential energy between the mountains and forelands.

where ρ is the average crustal density, g is the acceleration due to gravity, z is the depth and θ is the angle of the fault from the vertical. The $\pm \sin 2\theta$ term is negative if the faults are extensional and positive if they are compressional.

Within 300 km of the Andes range front the top ~5-8 km of the crust consists of sedimentary basins that contain no earthquakes [McGroder et al., 2015] (Fig. 3.13c). I assumed the sedimentary basins support negligible force. Outside of the sedimentary basins, earthquakes occur throughout the thickness of the crust [Assumpção and Suarez, 1988; Assumpção, 1992, This study] (Fig. 3.13c). In these regions I assumed that stresses in the basement crust are supported by frictional resistance on faults given by Equation 3.6.

Earthquakes are absent from the foreland mantle lithosphere beneath South America (Fig. 3.13c; see also Appendix B.4). A similar pattern of seismicity has been observed in other continental shield regions (e.g., India [Maggi et al., 2000a; Craig et al., 2012]; Africa [Craig et al., 2011]; Sibera [Sloan et al., 2011]), and has been attributed to the temperature of the continental lithospheric mantle generally exceeding ~600 ^oC [McKenzie et al., 2005; Jackson et al., 2008], so the mantle rocks deform predominantly by ductile creep mechanisms. I used a dry olivine dislocation creep law to estimate an upper bound on the ductile strength of the lithospheric mantle [Karato and Wu, 1993]:

$$\Delta\sigma_{xx} = G\dot{\varepsilon}_r^{\frac{1}{n}} A^{-\frac{1}{n}} \exp\left(\frac{E+pV}{nRT}\right), \tag{3.7}$$

where G is the shear modulus, $\dot{\varepsilon}_r$ is the reference strain rate which I calculated by imposing stress continuity at the brittle-ductile transition, A is a material constant, n is the power-law exponent, E is the active energy, p is the pressure, V is the activation volume, R is the gas constant and T is the temperature (parameters given in Table 3.3). It has been suggested that upper mantle rocks at temperatures less than 750 ^oC may deform by low temperature plasticity (Peierl's creep) [e.g. Mei et al., 2010; England and Molnar, 2015], which would support smaller differential stresses for a given strain rate than dislocation creep. If so, the forces supported by faults in the lithosphere would be slightly higher than the estimates presented in this chapter. However, I also performed calculations in which the lithospheric mantle supports no stress, providing an absolute upper bound on the possible forces acting on faults within the crust.

By performing a parameter sweep through the range of variables that control the shape of the yield stress envelope with depth (effective coefficient of friction μ', seismogenic thickness T_s, fault dips θ, neutral fibre depth z_{nf}, elastic core thickness z_{core} and sediment thickness z_{sed}; parameter range given in Table 3.3), I could define an envelope of the force that the lithosphere can support as a function of the effective coefficient of friction on crustal faults (Fig. 3.14b-d). In order to break in response to the 4-8$\times 10^{12}$ N/m force acting through the forelands, faults in the bending and non-bending regions of South America must have an effective coefficient of friction $\lesssim$0.15. If the lithospheric mantle supported no stress at all, which would resolve all the force acting through the foreland lithosphere onto faults in the crust, the maximum possible effective coefficient of friction on the faults would be 0.2 (Fig. 3.14d). If the faults in the South American crust were stronger, then they would not be breaking in earthquakes as a result of the forces per unit length generated by gravitational potential energy contrasts between the Andes and its bounding lowlands.

Faults within the 45 km-thick seismogenic crust that dip 45^o with an effective coefficient of friction $\lesssim$0.2 will support depth-averaged shear stresses of $\lesssim$85 MPa. A similar estimate for the average shear stresses causing faults to rupture of $\lesssim$90-130 MPa was derived from the analysis of foreland flexure and the earthquakes in the Llanos Basin in Section 3.3.4. Both of these results are consistent with studies that infer elevated pore-fluid pressures [Sibson, 2004] or foliated, phyllosilicate-rich fault gouges [Holdsworth, 2004; Collettini et al., 2009] may reduce the frictional strength of active fault zones relative to laboratory estimates that have implied μ = 0.6-0.85 [Copley et al., 2012; Copley, 2017].

3.5 Discussion

3.5.1 Late Miocene Change in the Dynamics of the Andes

The Parina earthquake and the surrounding seismicity demonstrates that the high Andes in south Peru are currently undergoing extension. A M_w 6.2-6.8 normal-faulting earthquake recorded in 1946 at Ancash in central Peru [Heim, 1949; Doser, 1987], and a M_w 5.4 earthquake in 2014 in the Bolivian Altiplano (Fig. 3.10a), suggest that a wider region of the high Central Andes is also currently extending.

Geological evidence of recent normal faulting in the high Andes is widespread, with examples of extensional structures in regions at elevations >3000 m from central and southern Peru [Dalmayrac and Molnar, 1981; Sébrier et al., 1985, 1988; Mercier et al., 1992; Veloza et al., 2012; Benavente et al., 2013; Kar et al., 2016, see Chapter 4 for more details], northern Chile [Tibaldi et al., 2009; Tibaldi and Bonali, 2018], southern and northern Bolivia [Mercier, 1981; Lavenu et al., 2000; Lamb, 2000] and northern Argentina [Cladouhos et al., 1994; Marrett et al., 1994; Lavenu et al., 2000; Schoenbohm and Strecker, 2009] (Fig. 3.10a, 3.15). The timing of motion on these normal faults can be bracketed by cross-cutting relationships with volcanic rocks that have erupted continually throughout the Andean orogeny. The earliest evidence of extension in the high Andes varies from ∼7-9 Ma in southern Bolivia and northern Argentina [Cladouhos et al., 1994; Montero Lopez et al., 2010], to ∼5-7 Ma in central and southern Peru [Mercier, 1981; Cabrera et al., 1991; Giovanni et al., 2010; Benavente et al., 2013; Kar et al., 2016], and follows an earlier period of widespread ∼E-W compression [Megard et al., 1984; Sébrier et al., 1985; Ellison et al., 1989; Mercier et al., 1992; Elger et al., 2005; Tibaldi et al., 2009]. Within the Bolivian Altiplano folded Pliocene strata in the Corque-Corococo basin imply the shallow crust experienced waning shortening between ∼10 Ma and 3 Ma [Hoke and Lamb, 2007; Lamb, 2011], and has recently been undeforming [Elger et al., 2005; Lamb, 2011] (Fig. 3.15). The transition from dominantly compression to extension within the high Andes of south Peru and Argentina since the late Miocene, and the slowing of shortening in the lower-elevation Bolivian Altiplano, is indicative of an orogen-wide change in the force balance.

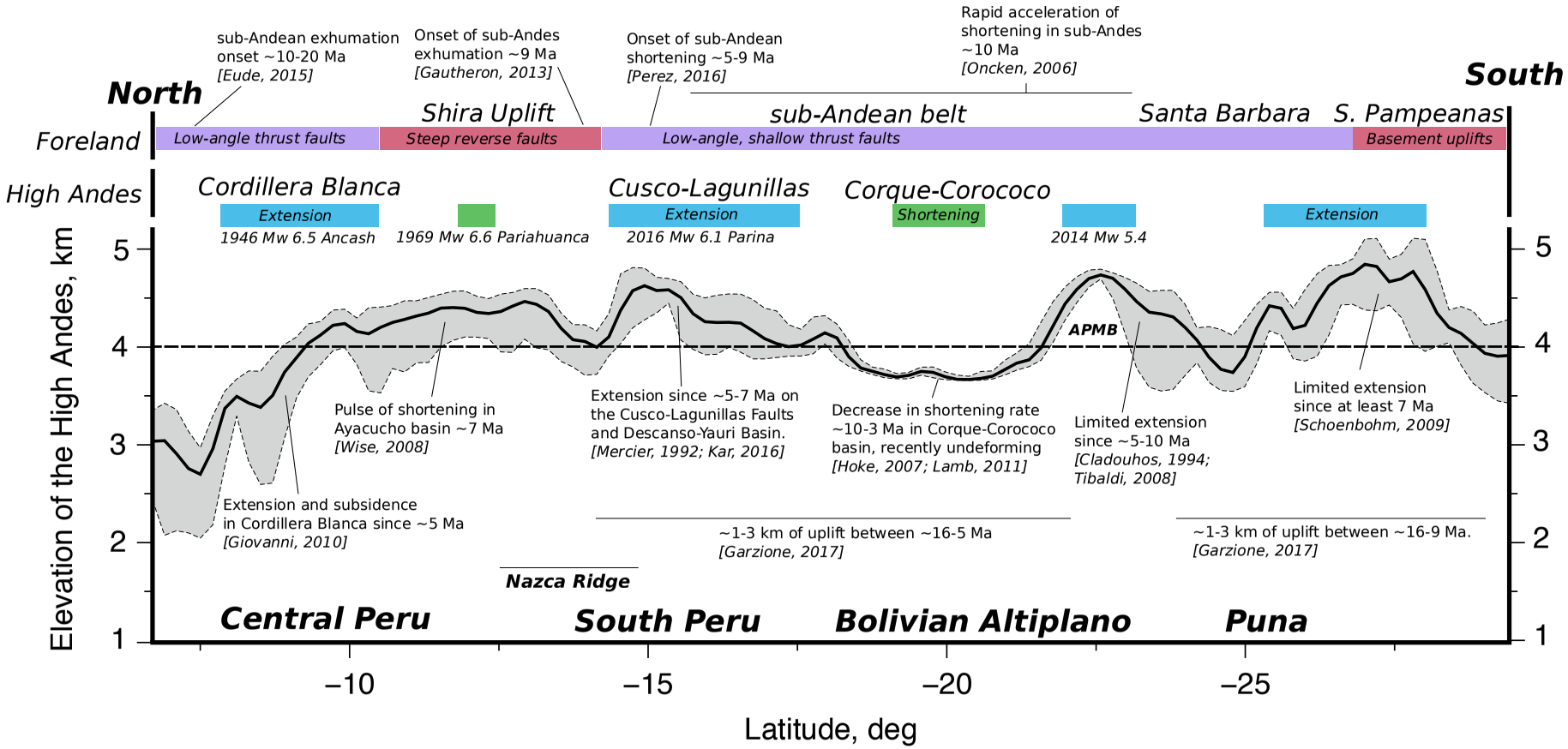

Figure 3.15 Summary of the topography and recent deformation history in the Andes between central Peru and northern Argentina. Topography is extracted in a ±30 km swath down the spine of the range from a 100 km Gaussian filtered version of the SRTM 90 m elevation model. The maximum, mean and minimum elevations from within the swath are shown. Evidence for the timing and pattern of deformation in the high Andes and the adjacent foreland is summarised above and below the elevation curve. APMB is the Altiplano-Puna magma body.

Over the same time interval (∼5-16 Ma) paleoelevation proxies, including clumped isotopes in carbonates and river incision histories, infer there has been 1-3 km of surface uplift in the high Andes of southern Peru and Bolivia [e.g. Garzione et al., 2006; Barke and Lamb, 2006; Garzione et al., 2008; Saylor and Horton, 2014; Kar et al., 2016; Garzione et al., 2017]. In addition, structural reconstructions and proxies for rock exhumation have recorded a distinct shift in the locus, rate and style of deformation on the eastern margin of the Andes. Prior to ∼10 Ma deformation in the eastern Andes consisted of slow, long-wavelength folding and bivergent reverse faulting of lower Paleozoic strata and metamorphic basement focused in the Eastern Cordillera [Kley, 1996; Oncken et al., 2006; Espurt et al., 2008; Perez et al., 2016a]. Since ∼10 Ma shortening rates in the eastern Andes have increased significantly [Oncken et al., 2006, 2012], and the locus of deformation has propagated rapidly eastwards into the sub-Andean lowlands [Gubbels et al., 1993; Echavarria et al., 2003; Gautheron et al., 2013; Perez et al., 2016a]. Within the sub-Andes Cenozoic and Mesozoic foreland basin fill is exposed in short-wavelength (∼5-10 km) anticlinal ridges bound by closely-spaced splay faults above shallow-dipping detachments [Kley, 1996].

Any attempt to explain the onset of normal faulting in the high Andes ∼5-9 Ma must also account for the observations described above (summarised in Fig. 3.15).

3.5.2 Possible causes of Normal Faulting in the High Andes

Removal of dense lower crust and mantle lithosphere (delamination) could increase the gravitational potential energy contrast between the mountains and forelands, leading to extension in the highest parts of the Andes [e.g. England and Houseman, 1989; Garzione et al., 2006]. Delamination has been proposed to account for the composition, timing and volume of ignimbrite and mafic volcanism [Kay and Mahlburg Kay, 1993], the Helium isotope ratios of hydrothermal fluids [Hoke and Lamb, 2007], and the possible rapid Miocene-recent uplift of the Central Andes [e.g. Garzione et al., 2006, 2008, 2017]. However the incoherent relationship between crustal thickening and uplift rates in the Bolivian Altiplano [Lamb, 2011, 2016], and inconsistent seismic models that independently infer thick, thin and variable thickness lithospheric mantle beneath the Andes [e.g. Whitman et al., 1992; Beck and Zandt, 2002; Phillips et al., 2012; Priestley and McKenzie, 2013; Ward et al., 2016], call into question whether delamination coeval with extension actually occurred.

Another mechanism that has been suggested to induce extension in the high Andes is dynamic uplift of central Peru due to the subduction of the buoyant Nazca Ridge [Mercier et al., 1992; McNulty and Farber, 2002; Margirier et al., 2017]. Normal-faulting earthquakes 400 km south of the Nazca Ridge (Fig. 3.15), in addition to evidence of extensional faulting within elevated regions across the Andes, irrespective of the nature of the underlying subducting plate (e.g. flat slab segments [Gutscher et al., 2000]), indicates that the pattern of extension is probably unrelated to subduction processes. Similarly, the distribution of normal-faulting earthquakes appears to be unrelated to the subduction zone earthquake cycle (but not necessarily their timing, see Section 4.3.3).

Changes in the horizontal forces supported by the lithosphere bounding the Andes could also cause the onset of extension in the high mountains. The switch in shortening style in the eastern Andes ∼10 Ma from steeply-dipping reverse faulting to shallow-dipping detachment faulting within the foreland

basin sediments could have reduced the shear stresses acting on the base of the overriding Andean lithosphere, leading to the onset of extension in the high mountains, a reduction in shortening rates in the Bolivia Altiplano, and enhanced shortening rates within the lowlands of the eastern Andes [e.g. Babeyko et al., 2006; Oncken et al., 2012]. I explore this possibility further below.

The spatial relationship between normal faulting and foreland deformation style is suggestive of a causal link. Late Miocene to recent normal faulting in the high Andes correlates along-strike with regions of wide thin-skinned fold-thrust belts [Kley et al., 1999], the locations of low-angle thrust-faulting earthquakes [Devlin et al., 2012], and thick Paleozoic and Mesozoic sediments in the adjacent foreland basin [McGroder et al., 2015]. In contrast, in regions where the foreland deformation comprises predominantly reverse faulting emerging at the front of steep topography (e.g., Shira Uplift of Peru [Kley et al., 1999]; Sierra Pampeanas of Argentina [Alvarado and Beck, 2006]; Oriente of Ecuador [Kley et al., 1999]) the faulting in the adjacent high Andes is dominantly compressional (Fig. 3.15). A particularly clear example of this is seen in the high Andes adjacent to the reverse-fault bounded Shira Uplift in central Peru, where faulting in the 1969 M_w 6.1 and 6.6 Pariahuanca earthquakes was compressional [Philip and Megard, 1977; Suarez et al., 1983; Sébrier et al., 1988] (see PH1969; Fig. 3.1a). However, both north and south of Shira, where the foreland has wide and active thin-skinned fold-thrust belts [Kley et al., 1999], the high Andes are extending [Heim, 1949; Doser, 1987; Devlin et al., 2012, This study] (Fig. 3.15).

It is possible that once the Andes reached the maximum elevation that could be supported by the steep reverse faults on the eastern margin of the range ∼5-9 Ma (Fig. 3.16a), the plateau widened as faulting propagated eastward into the thick foreland basin sediments that had accumulated concomitant with uplift [e.g. Molnar and Lyon-Caen, 1988]. Foreland deformation then became focused along weak detachment layers above the sediment-basement interface, and the rigid Brazilian Shield was underthrust further beneath the mountains [Kley et al., 1999; Lamb, 2006, 2011; Ma and Clayton, 2014] (Fig. 3.16b). As the local force balance in the eastern Andes is controlled by the horizontal shear stresses acting on the base of the overriding lithosphere [e.g. Lamb, 2006], reducing the frictional shear stresses along the nose of the foreland fold-thrust belt would be balanced by extensional viscous strain and normal-faulting within the overriding lithosphere [e.g. Craig and Copley, 2018] (see calculations in Section 4.3.2). In addition to the onset of extension within the high Andes, the ductile lower crust in front of the indenting foreland lithosphere would shorten and thicken [Barke and Lamb, 2006; Lamb, 2011], balancing the flux of material out over the South American foreland. At the surface this would be visible as the mountains rapidly thrusting eastwards over the forelands coeval with extension in the highest parts of the range — a feature that is reflected in the current pattern of crustal deformation (Fig. 3.16b).

Previous models of the dynamics in the Andes have typically treated the mountain belt in terms of vertically-averaged stress and strain (i.e. a thin-viscous sheet) [Lamb, 2000; Liu et al., 2002; Flesch and Kreemer, 2010]. Under the thin-sheet assumptions shear stresses on the base of the lithosphere are negligible, and weakening the eastern side of the Andes would simply enhance shortening strain rates in that region to maintain the horizontal force balance. My insight has been to include the influence of the underthrust South American foreland, which will partition the force balance with depth beneath the mountains (i.e. F_u and F_p in Fig. 3.16b), and accommodate extension of the upper crust in the Andes.

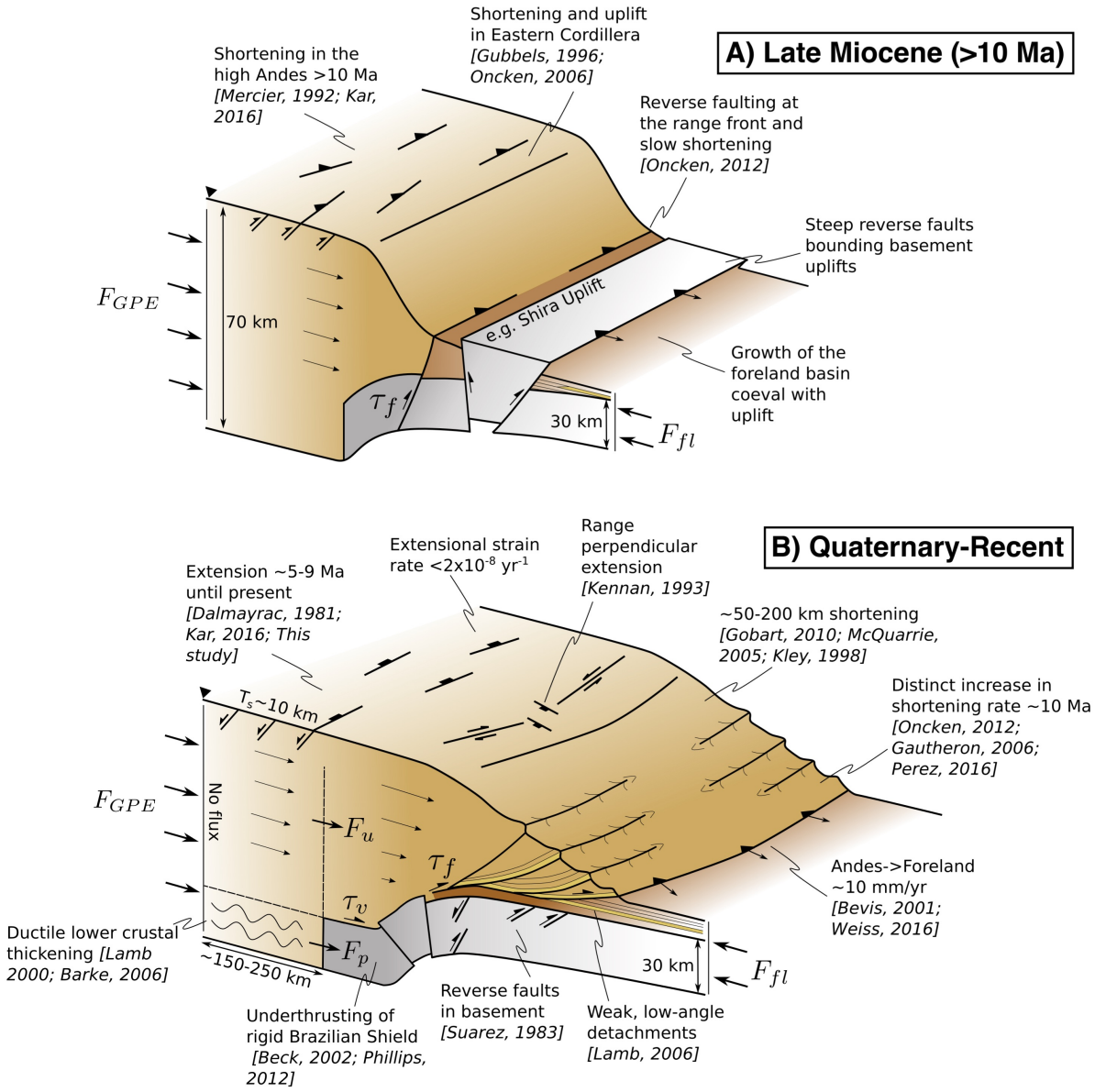

Figure 3.16 Sketch of the evolution of faulting in the Andes since the late Miocene. A reduction in the frictional shear stresses (τ_f) along the base of the eastern Andes ~5-9 Ma would have reduced the horizontal force acting through upper crust overriding the rigid foreland (F_u). A reduction in τ_f would be balanced ($F_{GPE} = F_u + F_p$) by an increase in the viscous resistance to shortening in the ductile lower crust (F_p), extensional viscous strain within the centre of the mountain belt, and an increase in the rate of propagation of the mountains over the rigid foreland.

3.5.3 Implications for the Evolution of Orogenic Belts

A generalisation of the model presented above, in which mountain belts weaken their forelands through syn-orogenic sedimentation, is likely to be broadly applicable to continental mountain building. For example, Lamb [2006] suggested that low-angle detachment faults and subduction megathrusts may be lubricated by the underthrusting of weak sediments from a comparison of the force balance above global subduction zones. More recently Reynolds et al. [2015] built on this idea, arguing that the thick sedimentary basins within the foreland of the Sulaiman Ranges in Pakistan have strongly influenced the evolution of the mountain belt by reducing the tractions between the foreland and the overriding mountain belt. Alternatively, Copley et al. [2009] argued that sedimentation in the Adriatic foreland of the Albanides may have had a different effect — thermally insulating and warming the underlying crust and therefore reducing the thickness of the strong, seismogenic layer, leading to the onset of extension in the mountains with similar kinematics to the faulting in the south Peruvian Andes.

The deformation style within the forelands of the Tien Shan also appears to be dependent on the thickness of the sedimentary basins bounding the basement uplifts [Kober et al., 2013]. Along range fronts adjacent to 10-15 km-thick sedimentary basins, anticlinal folding above buried thrust faults extends ∼30 km into the piedmont, suggesting shortening is beginning to step out from the basement-cutting faults onto low-angle detachments in the foreland stratigraphy [Avouac and Tapponnier, 1993]. However in regions where the basin sediments are thin (<5 km), faulting has remained focused along steep reverse faults that outcrop at the range front [Avouac and Tapponnier, 1993]. Quaternary-Holocene fault scarps [Thompson et al., 2002], and recent seismicity [Sloan et al., 2011], indicate shortening is still active throughout the interior of the Tien Shan, which probably reflects the fact that the steep, basement-cutting reverse faults can still transmit enough force into the mountain range to overcome the gravitational body forces acting to drive extension.

In contrast, within the southern forelands of Tibet, deformation has focused onto detachment horizons that cut through the foreland stratigraphy, and emerge ∼80-100 km south of the Himalaya [Lavé and Avouac, 2000]. Geomorphic evidence for uplift [Lavé and Avouac, 2000], and the pattern of shortening reflected in thrust-faulting earthquakes [Molnar and Lyon-Caen, 1989], is confined to the edges of the mountain belt, whilst E-W orientated, along-strike extension occurs simultaneously in the high plateau [Armijo et al., 1986]. Prior to the onset of along-strike extension at ∼18-10 Ma [Williams et al., 2001; Garzione et al., 2003] the southern margin of the mountain belt was extending across-strike on the South Tibetan Detachment, which exhumed a sequence of high-grade gneisses that form the core of the High Himalaya. These mid-crustal rocks are now cross-cut by active, N-S trending normal faults [e.g. Burchfiel et al., 1992]. Southern Tibet may therefore represent a more advanced stage of orogenic evolution than both the Tien Shan and the Altiplano. Shortening has localised into the foreland basin, there is predominantly strike-slip faulting within the centre of the plateau and the previous across-strike extensional regime has been replaced by along-strike extension due to the significant divergence of the thrust-transport direction along the southern margin of the range.

In summary, similar to Lamb [2006] and Copley et al. [2009] I suggest that the mechanical properties and nature of the stratigraphy within foreland basins may be important in modulating the forces

transmitted across mountain belt forelands, the stress field within mountain belts, and the elevation that mountain belts can attain.

3.6 Conclusions

The 2016 M_w 6.1 Parina earthquake was generated by slip on a shallow-crustal normal fault that accommodated NE-SW extension in the high Andes of south Peru. The orientation of the extension was parallel to the direction of shortening across the adjacent sub-Andean lowlands, which is parallel to gradients in the topography on the margin of the range. In addition, normal faulting earthquakes and geomorphological evidence for recent extension within the Andes is concentrated in regions with the highest elevations. Combined, these observations imply forces generated by lateral contrasts in gravitational potential energy are important in controlling deformation in the high Andes and its eastern lowlands. These horizontal forces are 4-8$\times10^{12}$ N per metre along-strike and are causing faults in the South American forelands with effective coefficients of friction $\mu' \lesssim 0.2$ to rupture in earthquakes.

Normal faulting in the Andes began in the late Miocene following a period of orogen-wide compression, which reflects a change in the force balance across the mountain range. Two observations suggest the onset of extension may be related to a reduction in the shear stresses transmitted across faults on the eastern margin of the Andes. Firstly, low-angle detachment faulting in the sub-Andes began coeval with the extension in the high Andes ∼5-9 Ma. Secondly, there is a spatial correlation between active extension in the high mountains and wide thin-skinned fold-thrust belts in the adjacent sub-Andes. I argued that the dynamics and evolution of the Andes is strongly influenced by the mechanical strength of the stratigraphy and faults in its forelands.

Chapter 4

Observations and Dynamical Implications of Active Normal Faulting in South Peru

Overview

Orogenic plateaus can exist in a delicate balance in which the buoyancy forces due to gravity acting on the high topography and thick crust of the plateau interior are balanced by the compressional forces acting across their forelands. Any shortening or extension within a plateau can indicate a perturbation to this force balance. In this chapter I present new observations of the kinematics, morphology and slip rates of active normal faults in south Peru from field studies, high-resolution DEMs, Quaternary dating and remote sensing, and investigate the implications of this faulting for the forces acting on the Andes. I find that the high mountains are extending ∼NNE-SSW to ∼NE-SW along a normal fault system that cuts obliquely across the Altiplano plateau, which in many places reactivates Miocene-age reverse faults. The orientation of extension is sub-parallel to the slip vectors of thrust earthquakes in the sub-Andean foreland. Dating of offset moraines and alluvial fan surfaces indicates horizontal extension rates across the fault system of between 1 and 3 mm/yr — equivalent to an extensional strain rate of 0.5-2$\times 10^{-8}$ 1/yr. I suggest the rate and pattern of extension implies there has been a change in the forces exerted between the foreland and the Andes mountains. A recent reduction in the average shear stresses on the sub-Andean foreland detachment of ∼0.02-3 MPa, which is equivalent to 0.1-30% of the total detachment shear strength, can account for the rate of extension. I infer that, within a mountain belt, the pattern of faulting is sensitive to small spatial and temporal variations in the strength of faults along their margins.

- *The fieldwork discussed in this chapter was completed in September-October 2018 with Alex Copley and Aisling O'Kane of Cambridge and Carlos Benavente, Briant Garcia, Lorena Rossell, Fabrizio Delgado and Enoch Aguirre of INGEMMET.*
- *High-resolution point clouds generated from drone-based photography were processed by Enoch Aguirre of INGEMMET. Subsequent post-processing of the DEMs from drone imagery, any Pleiades DEMs, and any interpretation of the DEMs is my own.*

4.1 Introduction

Mountain belts with low-relief, high-elevation interiors, such as the Bolivian Altiplano and central Tibet, are typically dominated by strike-slip faulting in their highest parts with little dip-slip faulting, suggesting that the crust is neither thickening nor thinning. In contrast, the lowlands bounding their edges undergo significant shortening and crustal thickening [e.g. Suarez et al., 1983; Molnar and Lyon-Caen, 1988]. This pattern of deformation implies that the horizontal forces due to gravity acting on the crustal thickness contrasts between these plateaus and their bounding lowlands must balance the compressional forces acting across their lowlands [Dalmayrac and Molnar, 1981; Molnar and Lyon-Caen, 1988]. A powerful corollary of this argument is that, in order to start deforming a plateau interior by dip-slip faulting, or to change the style of faulting, the forces acting on the mountain belt, the material properties of the lithosphere, or the geometry of the deforming region, must also change [e.g. England et al., 1988; England and Houseman, 1989].

In the Andes of south Peru there is geological and geomorphological evidence that the style of faulting has recently changed. Within the high plateau the active faulting is predominantly extensional along ∼NW-SE striking normal faults that cut obliquely across the plateau [Sébrier et al., 1985; Mercier et al., 1992; Benavente et al., 2013] (Fig. 4.1). The onset of this extension is thought to be at ∼5-9 Ma [Cabrera et al., 1991; Kar et al., 2016], by which time the mountain belt had reached its current elevation [Garzione et al., 2017]. Until ∼10-15 Ma, 1-4 km-thick accumulations of growth strata were forming in the footwalls of major reverse faults that trend sub-parallel to the active normal faults [Carlotto, 2013; Perez and Horton, 2014; Horton et al., 2015]. Therefore, the balance of forces in south Peru must have recently changed to account for the switch from reverse faulting to normal faulting in the high plateau [Sébrier et al., 1985; England and Houseman, 1989].

Some insights into why the force balance may have changed can be gained from studying the active faulting across the whole Andes. Firstly, all of the normal faulting occurs in areas higher than ∼3000-4000 m elevation [Dalmayrac and Molnar, 1981; Sébrier et al., 1985; Schoenbohm and Strecker, 2009]. Secondly, the extending regions in the high mountains correlate along-strike with areas of low-angle detachment faulting in the fold-thrust belt that wraps around the eastern edge of the Andes, known as the sub-Andes (see Chapter 3). Finally, the suggested timing for the onset of extension in the Andes correlates with a change in the location and rate of shortening in the sub-Andes at ∼5-9 Ma [e.g. Gubbels et al., 1993; Perez et al., 2016a]. These observations suggest that failure on weak detachment faults in the sub-Andes may have perturbed the force balance in the mountains, leading to extension in the highest part of the range (see Chapter 3).

In this chapter, I present new observations of the kinematics, morphology and slip rates of active normal faults in the high Andes of south Peru, between Cusco and Lake Titicaca (Fig. 4.1). I discuss the topography and drainage associated with the faulting, in addition to evidence of recent surface-rupturing earthquakes, geological indicators of the timing and rates of faulting, and the kinematics of the faults. These observations are then used to constrain a simple physical model relating changes in the strength of the sub-Andean foreland detachment to the faulting style and deformation rate within the plateau interior. I discuss the results in terms of the sensitivity of mountain belts to the rheology of faults in their forelands.

Although the late Miocene-Quaternary faulting appears to be accommodating extension in the high Andes of south Peru, GPS measurements made prior to the 2001 M_w 8.4 Arequipa earthquake captured shortening across the region (Fig. 4.1). This shortening is thought to be elastic [Bevis et al., 2001; Chlieh et al., 2011]. I discuss evidence that the transient accumulation and release of elastic strain in south Peru due to the megathrust earthquake cycle may modulate the slip history of the normal faults in the high Andes.

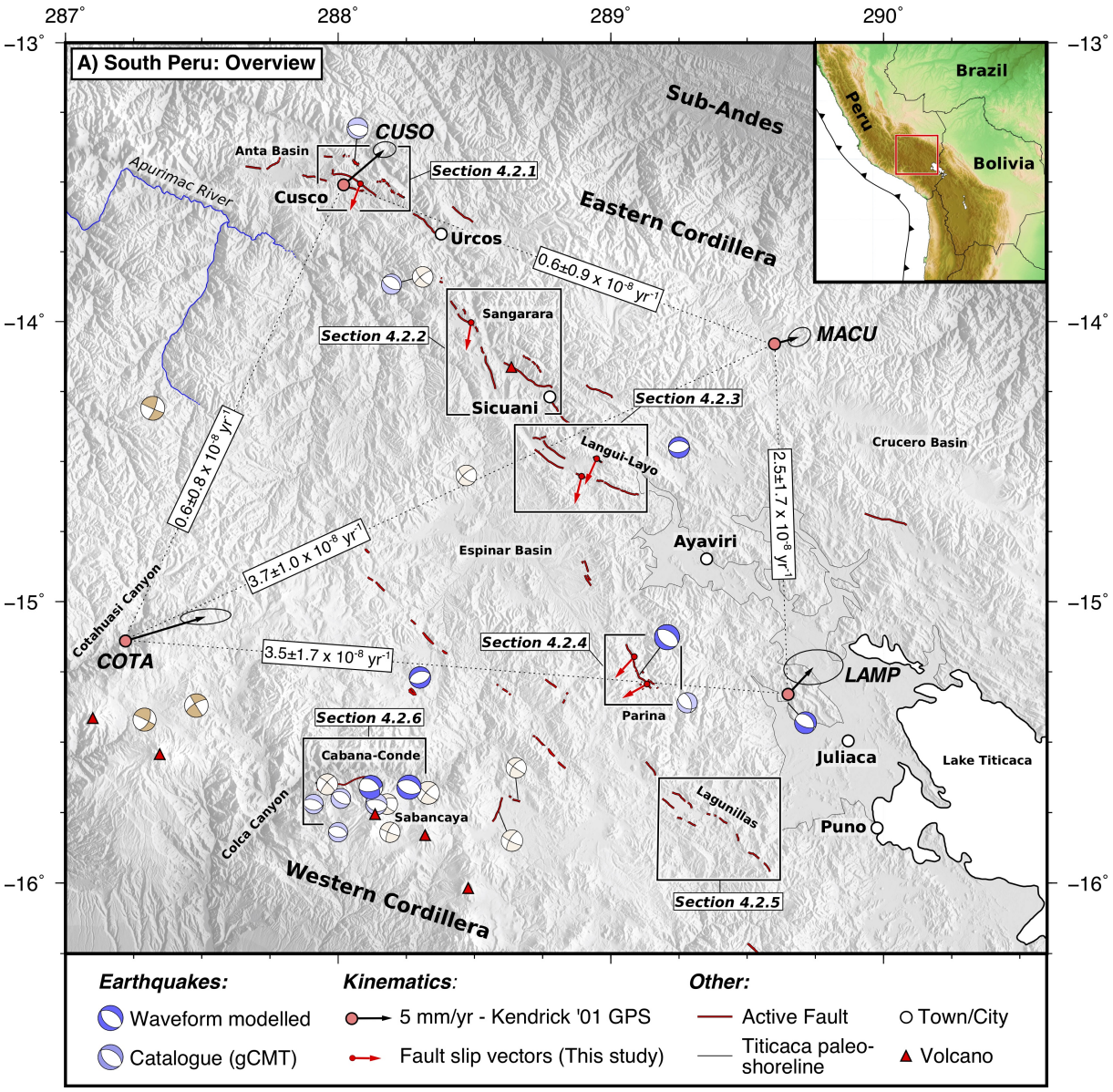

Figure 4.1 Mapped active faults in south Peru. Boxes refer to the regions discussed in Section 4.2. Waveform modelled earthquakes with centroid depths <50 km are taken from Suarez et al. [1983], Devlin et al. [2012] and the modelling in Chapter 3. Catalogue earthquakes with $M_w > 5$ are taken from the global CMT (www.globalcmt.org). GPS velocities are shown relative to stable South America from the collection of Kendrick et al. [2001] with 1σ (68%) uncertainty ellipses. The GPS measurements were made between 1993 and 2000, prior to the 2001 M_w 8.4 Arequipa earthquake that ruptured the megathrust offshore. Strain rates between the GPS stations are shown in the grey boxes with 1σ uncertainties, using the convention that positive strain rates are due to shortening.

4.2 Observations of Active Normal Faulting

The high Andes in southern Peru form the northern-most extent of the Altiplano — a ∼200 km-wide, low-relief plateau with average elevations of around 4000 m (Fig. 4.1). The earliest investigations of active faulting in the region by Suarez et al. [1983] and Sébrier et al. [1985] identified a system of normal faults cutting NW-SE across the plateau between Cusco and Langui-Layo (Fig. 4.1). Sébrier et al. [1985] inferred that the orientation of most recent slip on these normal faults was ∼N-S [see also Cabrera et al., 1991; Mercier et al., 1992], but could make no estimates of their slip rates. More recently, Benavente et al. [2013] presented an updated map of active faults throughout south Peru. Many of these faults are associated with metre-high fault scarps cutting recent glacial deposits. A key aim of this section is to estimate the extension rates and recent slip vectors on these faults.

An important recent development that aides estimating the slip rates on the faults in south Peru is the proliferation of moraine age estimates from cosmogenic radionuclide dating [e.g. Smith et al., 2005b; Rodbell et al., 2009; Jomelli et al., 2014; Ward et al., 2015; D'Arcy et al., 2019, and references therein]. Across most of south Peru, ice covered a large fraction of the mountain belt in the last major glacial, depositing lateral moraines and drift sheets. Boulders on the surfaces of these moraines typically return ages between ∼10 and 45 ka (Fig. C.1), which roughly correlates with the end of the global Last Glacial Maximum (LGM) [Clark et al., 2009]. Therefore, where scarps cut moraine surfaces that are the youngest in the area, it is likely the scarp formed sometime since the LGM.

In the following sections I discuss the active faults between Cusco and Lagunillas in turn, traversing from the north-western end of the fault system near Cusco to the south-eastern end at Lagunillas (see boxes in Fig. 4.1).

4.2.1 Cusco Basin

The Cusco Basin is an E-W trending intra-montane basin that contains Pliocene to Quaternary clastic sediments [Cabrera et al., 1991] (Fig. 4.1, 4.2). Subsidence is controlled by normal faults along the basin's northern edge, including the Qoricocha, Pachatusan, Tambomachay and Cusco Faults [Sébrier et al., 1985; Cabrera et al., 1991]. One or more of these faults is likely to have generated the earthquakes that heavily damaged Cusco in 1650 and 1950, in addition to a series of minor shocks [Ericksen et al., 1954; Silgado, 1978]. I discuss each of the faults in turn below.

Qoricocha Fault

The Qoricocha Fault outcrops within the mountains north of the Cusco Basin as a series of WNW-ESE trending, south-facing scarps, up to 6 m-high, that cut glacial drift on a low-relief plateau at 4000-4350 m elevation [Cabrera and Sebrier, 1998] (Fig. 4.2a, 4.3a). The scarps can be traced for 3 km along-strike in a right-stepping en-echelon pattern, and probably link to the Chinchero Fault 2 km west of Lake Qoricocha [Cabrera et al., 1991; Benavente et al., 2013] (Fig. 4.2a). Although the recent scarps are prominent, they are not associated with any large-amplitude topography (e.g. footwall escarpment), suggesting the Qoricocha Fault has accommodated little finite slip as a normal fault.

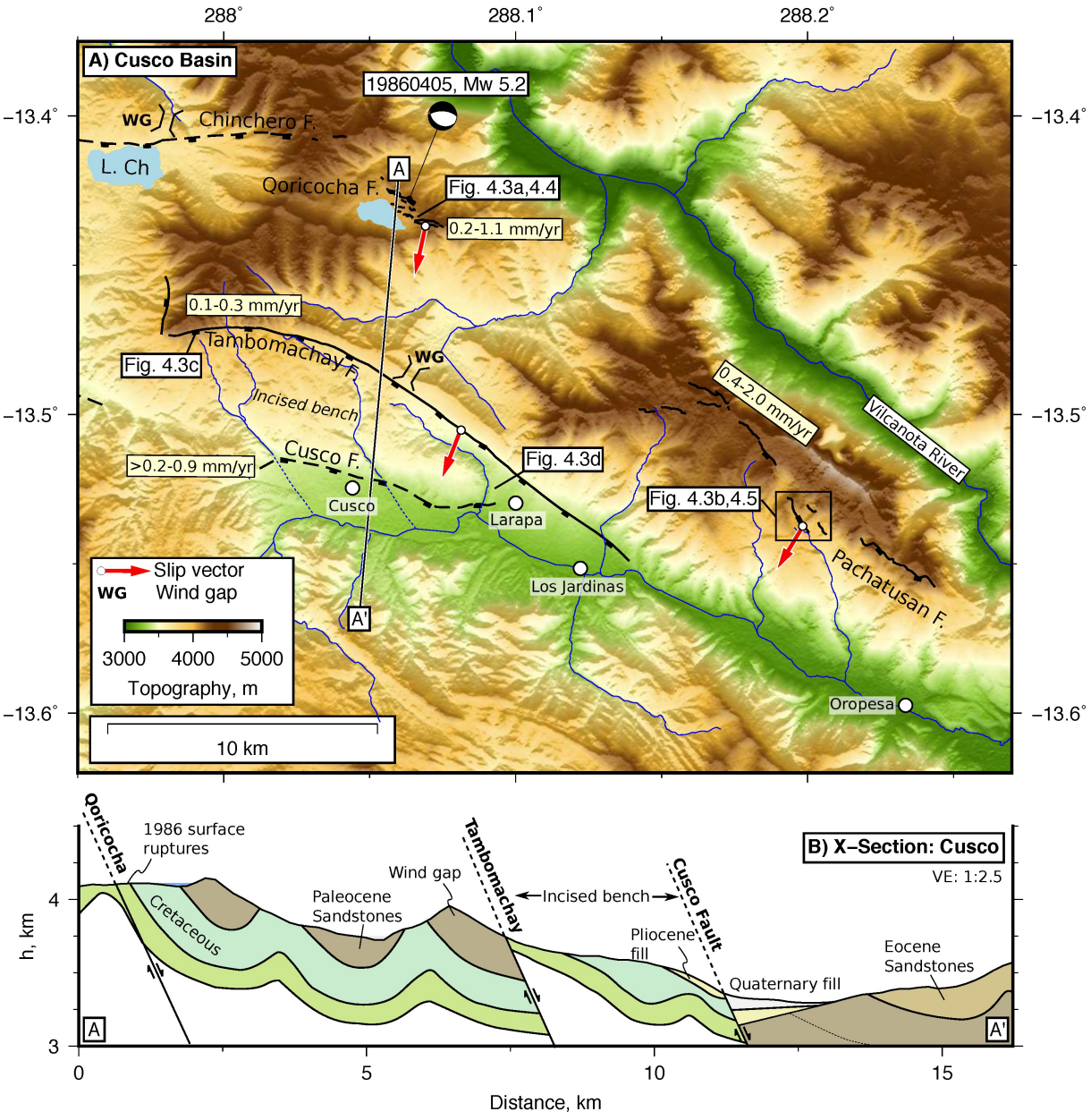

Figure 4.2 Morphology and active faults of the Cusco Basin. (a) SRTM 30 m DEM of the Cusco region with active faults and slip vectors marked. The fault map is updated from those of Cabrera et al. [1991] and Mercier et al. [1992]. Solid lines are observed faults, dashed lines are inferred faults and blue lines mark the rivers. Estimates of the fault extension rates are shown in light yellow boxes (see text for discussion). The mechanism for the 5th April 1986 earthquake is taken from the gCMT catalogue. (b) Cross section perpendicular to the active normal faults in the west of the Cusco Basin. The sub-surface geology is extrapolated from the INGEMMET 1:50,000 Cusco sheet 28-s-IV [Carlotto et al., 2010]. The exact throw across the Tambomachay Fault is not well known.

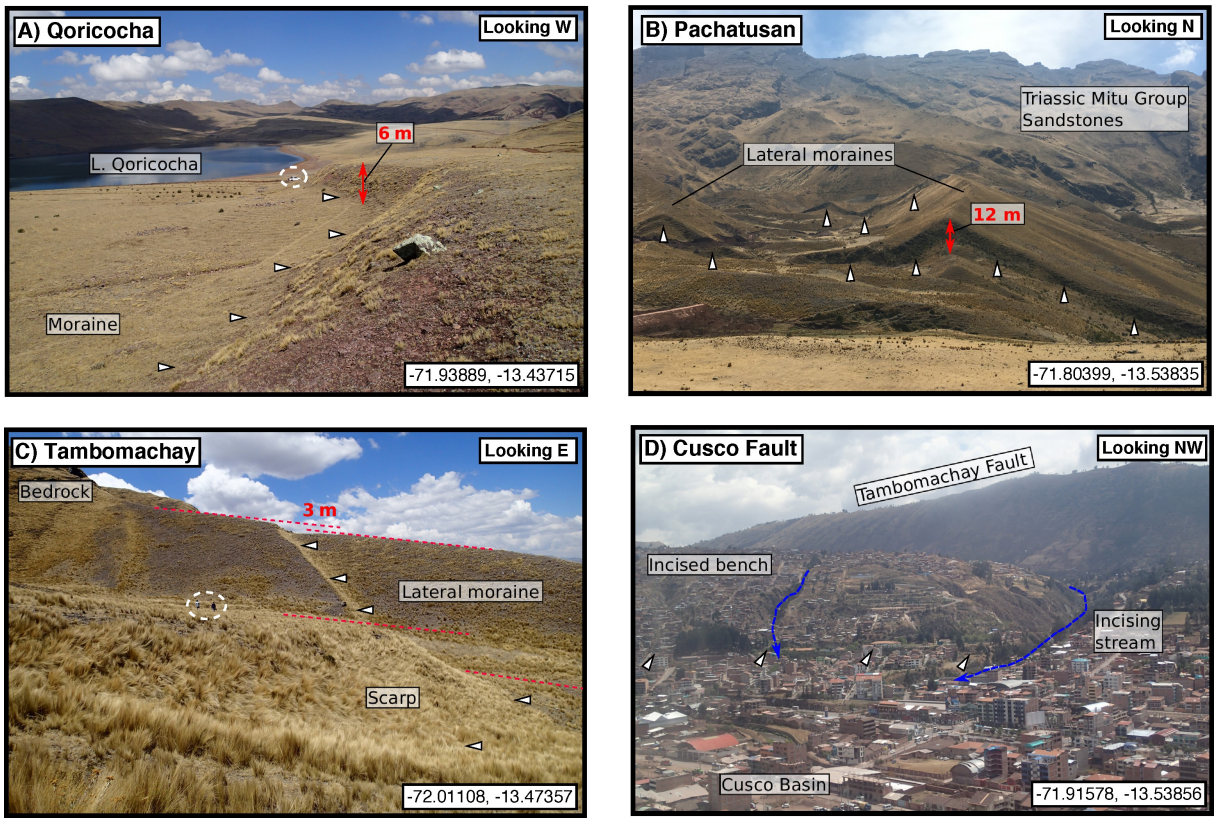

Figure 4.3 Field photographs of fault scarps around Cusco. White triangles indicate the fault scarps and red dashed lines mark the fault offsets. (a) South-facing scarp of the Qoricocha Fault, with Lake Qoricocha visible in the background. The vehicle highlighted in the background for scale (white dashed circle) is located next to the road cut shown in Fig. 4.4. (b) Sub-parallel normal fault scarps cutting lateral moraine crests on the Pachatusan Fault. Scarp offsets are measured from the DEM shown in Fig. 4.5. (c) South-facing normal-fault scarp of the Tambomachay Fault cutting a lateral moraine crest. People in the foreground for scale (white circle). (d) Uplifted and incised hangingwall of the Tambomachay Fault, with the ridge line of the Tambomachay Fault footwall visible in the background. The Cusco Fault runs along the sharp step in topography in the foreground, and is responsible for the incised drainage.

A road cut north east of Lake Qoricocha exposes an oblique slice through the fault near its highest-offset point (Fig. 4.4). The scarp footwall is formed of sub-angular cobbles and gravels in a red, sandy matrix that are characteristic of the glacial deposits surrounding Cusco. The hangingwall consists of a tapered wedge that thickens towards the fault, formed of poorly-sorted dark clays, fine sands and sub-angular cobbles. Underlying this fine-grained wedge of sediment is the same cobble-rich material that is exposed in the fault footwall. The hangingwall deposits are interpreted as a colluvial wedge of sediment formed by erosion of the uplifted and exposed scarp. A bulk radiocarbon sample from the base of the wedge yielded an age of 8.5-8.7 cal. kyr BP (see Table 4.1 and Fig. 4.4), which provides a minimum age for the fault offset. The typical uncertainty associated with bulk radiocarbon dating of sediment is on the order of ∼1 kyr, due to inheritance of older or younger material within the bioturbated samples [e.g. Grützner et al., 2016]. An upper bound on the age of scarp can be estimated from assuming the glacial deposits cut by the fault were formed during the LGM ∼10-45 ka.

As the length of the Qoricocha Fault is <10 km, it probably ruptures in earthquakes of M_w 6 with less than a few metres of slip [e.g. Wells and Coppersmith, 1994]. Therefore the 6 m scarp will have been formed in multiple surface-rupturing earthquakes, and the sediments at the base of the colluvial wedge will date from the first surface ruptures on the fault following the landscape being reset in the LGM. Given these age constraints the Holocene throw rate across the Qoricocha Fault is ∼0.1-0.7 mm/yr.

Sample	Material and Treatment	$\delta^{13}C$	Age (yr BC)	Calibrated Age (cal. yr BP)
QR-1	Organic sediment - acid wash	-25.1	6756-6566	8705-8515
SR-1	Organic sediment - acid wash	-24.5	5511-5364	7460-7313
SR-2	Organic sediment - acid wash	-25.4	5470-5304	7419-7253

Table 4.1 Results of bulk radiocarbon dating of samples collected in south Peru performed by Beta Analytic (FL, USA). $\delta^{13}C$ is given in % per mill. Calibration is performed using the Southern Hemisphere-specific calibration SHCAL13 [Hogg et al., 2013]. The influence of Northern Hemisphere-derived carbon on the calibration [see Marsh et al., 2018] is probably negligible relative to the uncertainties associated with the inheritance of younger or older carbon common to bulk sampling. Calibrated ages are given in years before 1950 as a range incorporating of the formal uncertainties 2 standard deviations about the mean, though realistic uncertainties are probably ∼1 kyr.

The slip vector azimuth on the Qoricocha Fault is constrained to be NNE-SSW from slickenline measurements [Mercier et al., 1992] and the focal mechanism of a M_w 5.2 earthquake that generated surface ruptures on the fault in 1986 [Cabrera and Sebrier, 1998]. Using the south-dipping nodal plane of the gCMT focal mechanism for the 1986 earthquake, which would be consistent with the sense of slip across the scarps, the fault has a slip vector plunging $\sim 29^o$. Therefore the horizontal extension rate and slip rate of the Qoricocha Fault is 0.2-1.1 mm/yr and 0.2-1.4 mm/yr, respectively.

Stratigraphy:

L1: Light grey topsoil containing extensive roots.

L2: Poorly sorted blackish-brown silty clay with a small fraction of sub-angular white cobbles and roots.

.

L3: Partially cemented reddish brown gravelly sand with sub-angular white cobbles.

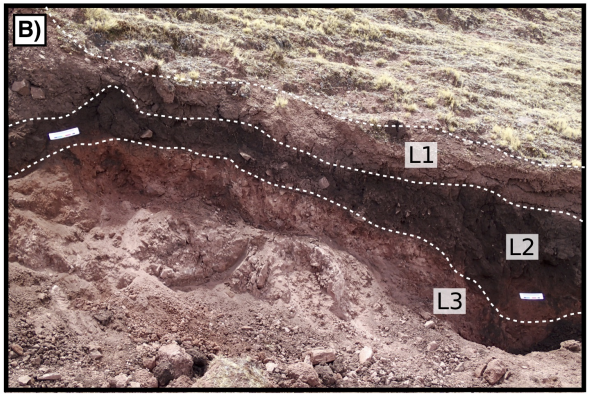

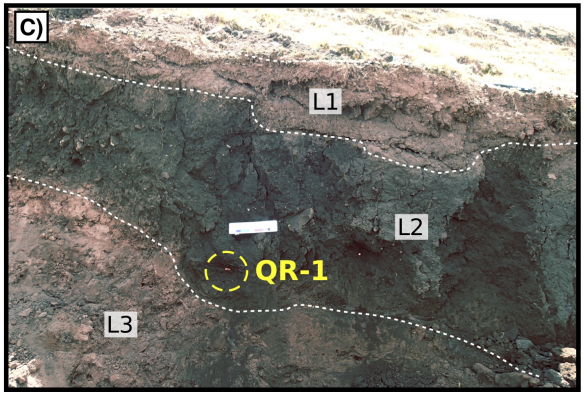

Figure 4.4 Road cut crossing the Qoricocha Fault scarp. (a) Panoramic photograph of the scarp. The road cut has a strike of 140^o, whilst the scarp itself has a strike of 120^o, resulting in an oblique section. (b) Transect through the scarp stratigraphy. At the base, Layer L3 is the cemented glacial drift in the scarp footwall. Overlying this is Layer L2, which is interpreted as talus deposits eroded and re-worked from the scarp surface. The layer thickens to the right as the exposure cuts into the thickest portion of the colluvial wedge. Where L2 crosses the scarp it contains a larger fraction of white, sub-angular cobbles, which is interpreted as a thin veneer of reworked material overlying the face of the scarp that may have been exposed to sub-aerial weathering. Layer L1 is the topsoil capping the glacial deposits and colluvial wedge material. Sample QR-1 was collected from the base of the thickest part of the colluvial wedge (L2) shown in (c). The scale card is 20 cm long and 5 cm high.

Pachatusan Fault

The Pachatusan Fault outcrops in the mountains north east of Cusco as a series of NW-SE trending, south-facing scarps with an along-strike length of ∼13 km [Sébrier et al., 1985; Benavente et al., 2013] (Fig. 4.2a). The fault bounds the contact between a ridge formed of the Triassic Mitu Group sandstones in its footwall, and a 4 km-wide, low-relief bench perched at 4000 m elevation in its hangingwall formed of Cretaceous sandstones and mudstones draped with lateral moraines (Fig. 4.3b).

Recent motion on the Pachatusan Fault has formed a complex series of sub-parallel normal-fault scarps that cut through the lateral moraines near the bedrock-moraine contact (Fig. 4.3b). A high-resolution digital elevation model (DEM) of the scarps is shown in Fig. 4.5. The DEM was formed using low-altitude drone photography and the structure-from-motion technique implemented in Agisoft Photoscan by Enoch Aguirre of INGEMMET [e.g. Westoby et al., 2012]. Ground-control points measured with differential GPS were used to guide the image matching and point cloud scaling. In order to reduce the number of data points for interpretation, I thinned and gridded the point cloud at 1×1 m resolution using splines in tension [Smith and Wessel, 1990]. The resulting DEM shown in Fig. 4.5a highlights two sub-parallel scarps — one running along the bedrock-moraine contact ('northern scarp') and one offset ∼500 m to the south ('southern scarp').

The best-preserved scarps vertically offset the lateral moraine crests by up to 15 m (measured by fitting lines of above and below the scarp using cross profiles and finding the vertical offset at the scarp foot; Fig. 4.5). Summing the vertical offsets across both the northern and southern scarp suggests the cumulative vertical offset is ∼20 m. Mackenzie and Elliott [2017] showed that, for shallowly-dipping surfaces ($< 10^o$) that are offset by a dip-slip fault with ∼30-60^o dip, the vertical offset of the surface is roughly equivalent to the fault throw to within 15%. Throughout this chapter I carefully select profiles to satisfy these constraints, therefore the cumulative vertical throw across the Pachatusan Fault is probably the range ∼17-20 m.

Horizontal offsets parallel to the fault strike are also evident across some of the moraine crests on the Pachatusan Fault, an example of which is highlighted in Fig. 4.5b. The northern-most moraine crest in Fig. 4.5b is not offset laterally within measurement precision, whilst the southern-most crest is horizontally offset by ∼20 m. A small antithetic fault in the hangingwall may accentuate these offsets. Nonetheless, in order for the northern crest to remain parallel either side of the fault scarp requires the horizontal projection of the fault slip vector to be roughly parallel to the moraine crest, which has an azimuth of ∼210^o (Fig. 4.5c). Therefore the Pachatusan Fault is accommodating ∼NNE-SSW extension.

The moraines at Pachatusan have not been directly dated. However, their fresh morphology implies they probably date to the end of the LGM ∼10-45 ka [Mercier et al., 1992]. Combining the cumulative fault throw and the estimated LGM moraine age yields a throw rate of ∼0.4-2.0 mm/yr. Given the fault slip vector azimuth, and assuming a dip of ∼45^o [e.g. Jackson and White, 1989], the horizontal extension rate across the fault would be 0.4-2.0 mm/yr and the fault slip rate would be 0.5-3 mm/yr. Notably, if the glacial deposits at Qoricocha are contemporaneous with the lateral moraines at Pachatusan, then the Pachatusan Fault may have a recent slip rate at least three-to-four times faster than the Qoricocha Fault.

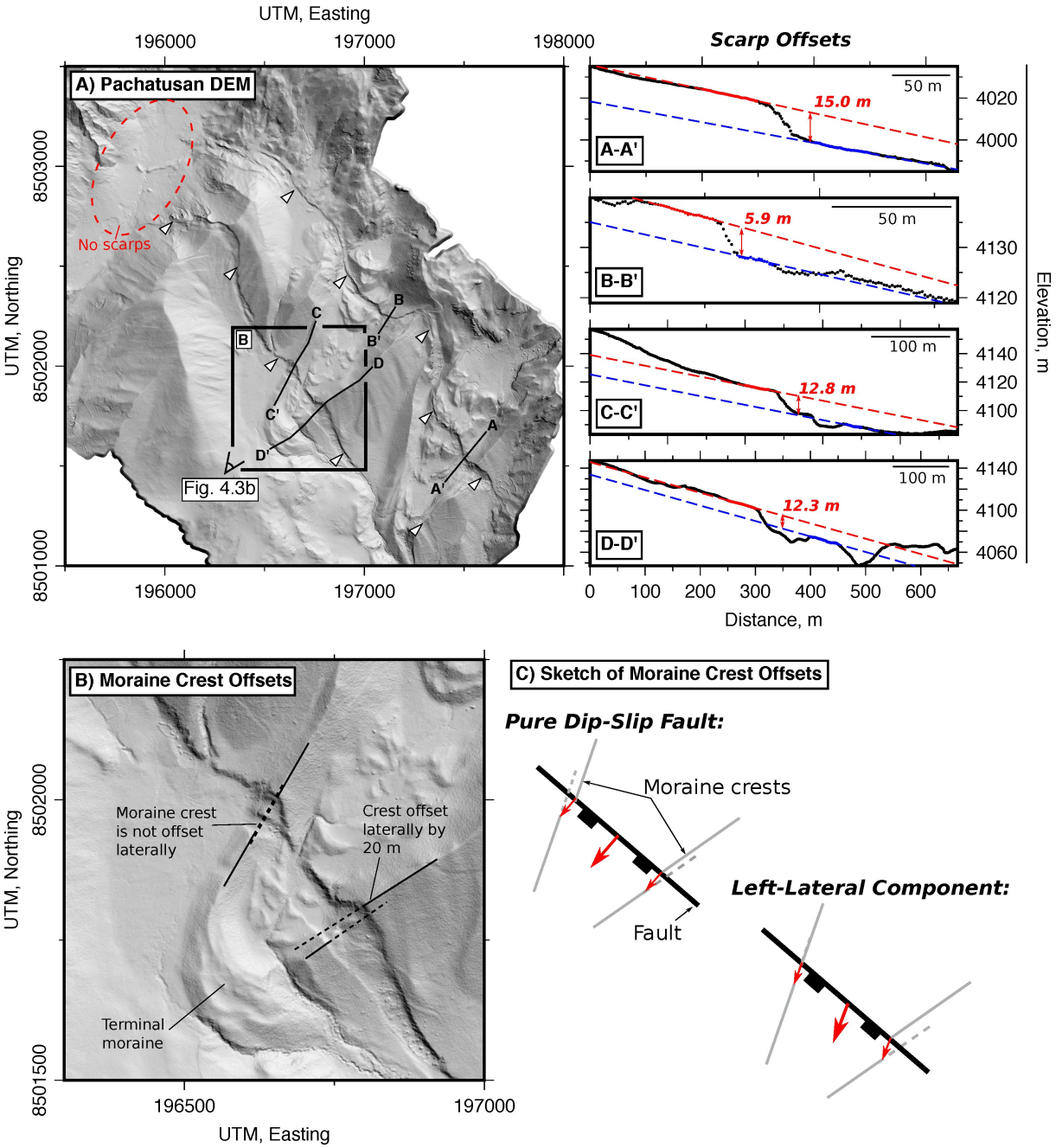

Figure 4.5 High-resolution DEM of the Pachatusan Fault. (a) Hillshade of the DEM (illuminated from the NE) of the two sets of sub-parallel scarps cutting lateral moraine deposits. Topographic profiles across the scarps are shown in the adjacent boxes. On the profiles, black dots are the measured elevations (relative elevations are accurate but absolute elevations are not), dashed lines are linear fits to the coloured points above (red) and below (blue) the scarp. The vertical scarp offset was measured as the difference between these two lines at the foot of the scarp. (b) Zoom in on the region in (a) with laterally-offset moraines. The moraine crests have been projected by black dashed lines. (c) Sketches of the moraine crest offsets expected for different fault slip vectors.

Tambomachay Fault

A ridge line with 200-350 m of relief formed of Paleocene-Eocene sandstones curves around the northern end of the Cusco Basin for 14 km, marking the uplifted footwall of the Tambomachay Fault [Sébrier et al., 1985; Cabrera et al., 1991] (Fig. 4.2a). Recent slip on the Tambomachay Fault has formed south-facing normal-fault scarps along the contact between the ridge line and a low-relief hangingwall surface [Cabrera et al., 1991] where Plio-Pleistocene basin fill and Cretaceous mudstones and sandstones outcrop (Fig. 4.2b). The fault still preserves a reverse-sense geological offset (Fig. 4.2b).

Near the fault's western tip, a scarp vertically offsets the crest of a lateral moraine by 3 m (Fig. 4.3c) [Mercier et al., 1992]. Bulk radiocarbon dating of sediment collected from the colluvial wedge in the scarp hangingwall returned dates between 0.9-8.5 cal. kyr BP, with the dates increasing towards the base of the wedge [Rossell, 2018]. These dates are consistent with a LGM age (10-45 ka) for the moraine surface underlying the wedge, which would indicate a throw rate of ∼0.1-0.3 mm/yr on the Tambomachay Fault.

Along the central section of the fault I identified exposures of polished bedrock with slickenlines mantled by unconsolidated sediments. The azimuth of the slickenlines were between 198^o and 205^o with a typical plunge $\sim 45^o$ [similar to Mercier et al., 1992], suggesting the most recent sense of motion on the fault is NNE-SSW extension. Given that the fault dips $\sim 45^o$ and the rake of the slickenlines are -90^o then the horizontal extension rate across the fault is the same as the throw rate (0.1-0.3 mm/yr), and the fault slip rate would be 0.1-0.4 mm/yr.

Unlike the Tambomachay Fault's footwall, the morphology of the fault's hangingwall changes significantly along-strike. At the fault's western tip, the hangingwall is formed of an incised, low-relief surface capped by Plio-Pleistocene alluvial deposits that are perched 100-300 m above the Cusco Basin [Mercier et al., 1992]. In contrast, at the fault's eastern tip near Larapa (Fig. 4.2a), the hangingwall consists of fans that grade gently into the Cusco Basin floor with no evidence of recent incision or uplift. I attribute these along-strike differences in the Tambomachay Fault hangingwall morphology to uplift in the footwall of the Cusco Fault (Fig. 4.2a).

Cusco Fault

The Cusco Fault is inferred to follow a ∼10 km-long, 150-300 m-high step in topography bounding the northern edge of the Cusco Basin (Fig. 4.2, 4.3d). The fault dips towards the south and controls the current locus of subsidence around Cusco, as well as the sharp transition in river incision across the northern edge of the Cusco Basin.

Recent slip on the Cusco Fault can account for the Plio-Pleistocene basin deposits that now outcrop on the incised bench north-west of Larapa [Cabrera et al., 1991; Mercier et al., 1992], which have been uplifted relative to the basin floor (Fig. 4.2b). Similar observations of uplifted and exposed hangingwall basin deposits in parallel normal-fault systems in Greece and Turkey are attributed to the basin-ward stepping of active faulting [Dart et al., 1995; Goldsworthy and Jackson, 2001], implying that the main locus of fault slip may have migrated from the Tambomachay Fault to the Cusco Fault. At least in

Greece the new, basin-ward fault in these systems becomes the most active and accommodates most of the local extension [Goldsworthy and Jackson, 2001].

No direct estimates of the slip rate on the Cusco Fault are known. However, if the base level of the Cusco Basin is relatively stable (headward erosion in the Vilcanota River valley has not reached that far upstream), then uplift in the footwall of the Cusco Fault must be outpacing subsidence in the hangingwall of the Tambomachay Fault in order to account for the pattern of recent stream incision. Given that the typical long-term footwall uplift to hangingwall subsidence ratio in normal fault systems is between 1:2 and 1:3 [e.g. King et al., 1988; Armijo et al., 1996; McNeill and Collier, 2004], then to account for uplift of the Tambomachay Fault hangingwall, the throw rate on the Cusco Fault must be significantly (i.e. $\gtrsim$2-3 times) larger than that on the Tambomachay Fault (i.e. $\gtrsim$0.2-0.9 mm/yr). Assuming a 45^o fault dip, and pure dip-slip motion, the horizontal extension rate would be $\gtrsim$0.2-0.9 mm/yr and the fault slip rate would be $\gtrsim$0.3-1.3 mm/yr.

Summary: Faulting near Cusco

In the western section of the Cusco Basin three sub-parallel normal faults (the Qoricocha, Tambomachay and Cusco Faults) accommodate cumulative ∼NNE-SSW extension at a rate of at least 0.5-2.3 mm/yr. East of Los Jardinas, roughly the same rate (0.4-2.0 mm/yr) and orientation extension is being accommodated by a single fault at Pachatusan.

The three sub-parallel faults in the western Cusco Basin are each separated by less than 5 km across-strike, but have been simultaneously active throughout the Holocene. Examples of a closely-spaced, sub-parallel set of normal faults with different slip rates accommodating regional extension are relatively rare, but this behaviour has been observed previously on the southern shore of the Gulf of Corinth in Greece. Copley et al. [2018] argued that, in order for systems of closely-spaced normal faults with different slip rates to accommodate the regional extension, as opposed to a single frictionally weak fault with a fast slip rate, requires that fault loading is controlled by persistently weak shear zones beneath each fault. The new examples from Cusco highlight that the observations of Copley et al. [2018] are not an outlier, and that weak sub-fault shear zones may therefore be a feature of many active faults.

4.2.2 Sangarara and Yanaoca Faults

South east of Cusco, between the towns of Sangarara and Yanaoca, lies a NNW-SSE trending, 40 km-long intra-montane valley containing a series of perched lake basins (Fig. 4.1, Fig. 4.6). The eastern side of the valley is bound by an escarpment that is incised by two gorges actively draining Lakes Pampamarca and Pomacanchi (Fig. 4.6a). The western side of the valley is formed of lower gradient slopes with gentle river incision and a sinuous bedrock-alluvium contact.

Suarez et al. [1983] identified a 3 km-long exposure of the Sangarara Fault at the northern end of the valley separating a south-west dipping fan surface from a sharp range front marked by ∼50 m-high, west-facing triangular facets (Fig. 4.6a). The morphology is consistent with recent normal-sense motion on the Sangarara Fault [Suarez et al., 1983; Sébrier et al., 1985].

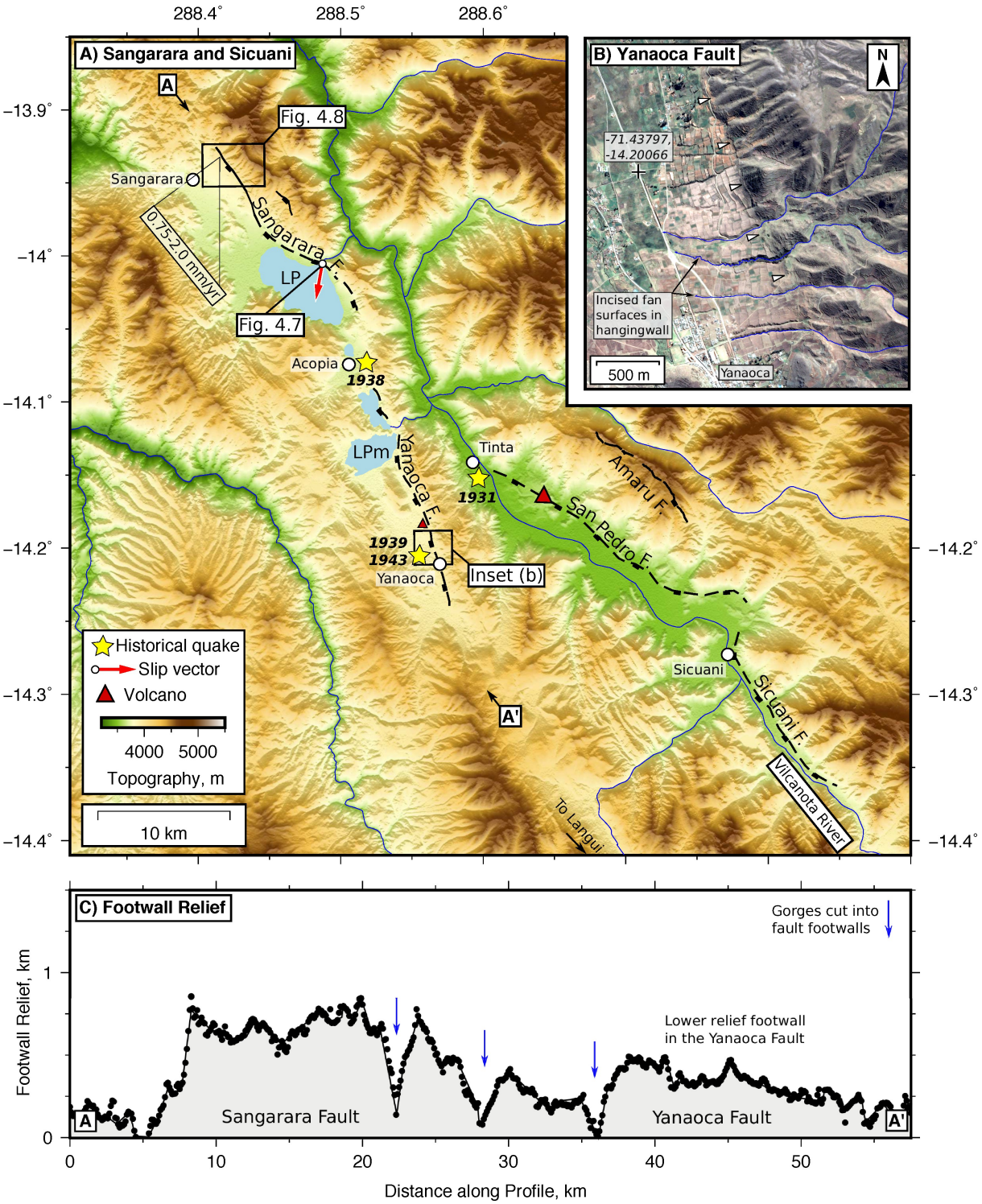

Figure 4.6 Overview of the active faulting between Sangarara and Sicuani. (a) SRTM 30 m DEM overlain with active faults. The legend is the same as in Fig. 4.2. The two lakes are: LP = Lake Pomacanchi and LPm = Lake Pampamarca. The Amaru Fault is associated with scarps discussed in Benavente et al. [2013]. (b) Digital Globe imagery from Google Earth of incision across the bedrock-alluvium contact along the Yanaoca Fault. Incision is also present in the hangingwall fan surfaces at Sangarara (see Fig. 4.8). (c) Footwall relief along the Sangarara-Yanaoca valley, highlighting the decrease in footwall relief between the Sangarara and Yanaoca Faults. Gorges that are being incised by rivers draining the perched lake basins are marked by blue arrows.

South east of Sangarara, at the head of the gorge draining Lake Pomacanchi, the Sangarara fault plane is exposed between andesitic footwall rocks and hangingwall basin conglomerates that include clasts of the footwall andesites (Fig. 4.7a). The hangingwall basin conglomerates have been exposed all along the edge of Lake Pomacanchi, suggesting the base level within the basin may have recently been lowered by headward erosion through the gorge draining the lake. The fault plane, which has orientation 168/36, preserves faint slickenlines in green precipitate with an azimuth of 190^o, implying the most recent sense of slip has been NNE-SSW extension with a component of left-lateral shear (Fig. 4.7b). Carlotto [2013] suggested that faults in the same area were accommodating shortening and left-lateral shear until ~5-7 Ma to account for the folded sediments in the Paruro Basin ~5 km north of Sangarara. Therefore the recent extension at Sangarara is likely to be younger than 5-7 Ma.

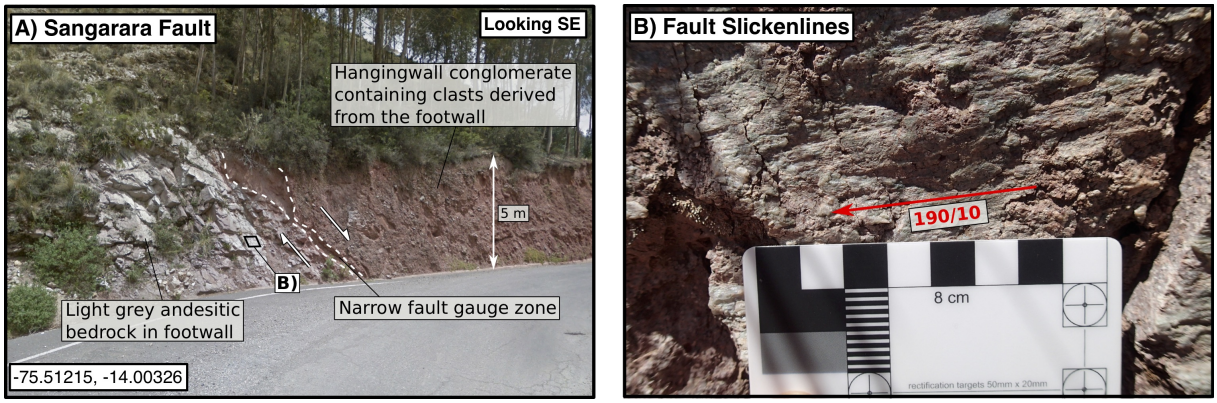

Figure 4.7 Field photographs of the Sangarara Fault at the head of the gorge draining Lake Pomacanchi. (a) The contact between andesitic footwall bedrock and the hangingwall conglomerates exposed in a road cut. (b) Slickenlines in green precipitate on the fault surface.

Near the north-western tip of the Sangarara Fault I identified an offset fan surface perched within the fault footwall (Fig. 4.8). Both the footwall and hangingwall sections of the fan are incised and abandoned. Therefore an estimate of the fan offset and its abandonment age can be used to determine the fault throw rate.

I estimated the timing of fan abandonment using bulk radiocarbon dating of a ~40 cm-thick, dark brown, organic-rich soil layer that overlays the fan gravels. Two samples from the base and middle of the soil layer returned consistent dates of 7.4-7.3 and 7.4-7.2 cal. kyr BP and place a minimum age on the fan (plus a likely ~1 kyr uncertainty from the bulk soil dating approach; Table 4.1, Fig. 4.8). Given the Holocene age of the soil, the most probable cause of fan abandonment was incision due to increased stream discharge at the end of the LGM ~10-20 ka [Mercer and Palacios, 1977; Seltzer, 1990; Smith et al., 2005b] or the Tauca climatic wet phase ~14-18 ka [e.g. Placzek et al., 2013]. Fan surfaces are also incised in the fault hangingwall near Yanaoca (Fig. 4.6b), which supports the proposition of climatically-controlled incision. Following fan abandonment, the 40 cm-thick soil layer probably took a few thousand years to develop [e.g. Goodman et al., 2001].

In order to determine the vertical offset of the fan surface I generated a DEM from Pleiades bistereo panchromatic imagery using the Leica Photogrammetry Suite in Erdas Imagine [e.g. Zhou et al., 2015;

Talebian et al., 2016]. The sensor and image geometry were defined using Rational Polynomial Functions, which were refined through a bundle adjustment using 30 automatically-selected and manually-edited tie points in both images [e.g. Fraser and Hanley, 2005]. The root-mean-square error between the tie points was typically <0.3 pixels. The resulting point cloud was averaged over 1×1 m pixels and gridded using splines in tension [Smith and Wessel, 1990] (Fig. 4.8a). An elevation profile across the fault indicates the fan is vertically offset by 30 m (Fig. 4.8; profile A-A'). Measurements from a barometric altimeter profile with horizontal location measured with hand-held GPS match those from the Pleiades DEM (see discussion in Appendix C.2). As the dip direction of the fan surface is perpendicular to the fault strike, and the dip of the fan surface is shallow ($< 10^o$), then the vertical offset measured from the profile will be a good proxy for the fault throw [Mackenzie and Elliott, 2017].

Given that the minimum age of the fan abandonment is 7.2 ka, and the fan is offset by ∼30 m, then the throw rate on the Sangarara Fault must be <4.4 mm/yr. Using the fault dip and slip vector azimuth measured at Lake Pomacanchi, and taking an average fault strike of 145^o in the location of the fan, the maximum extension rate across the fault would be 6 mm/yr and the total slip rate would be 10.5 mm/yr. Taking a more realistic fan abandonment age of ∼10-20 ka, which accounts for the time taken for the soils to develop on the fan surface following abandonment, the Sangarara Fault throw rate would be ∼1.5-3 mm/yr, and the horizontal extension rate and slip rate would be 2.0-4.5 mm/yr and 3.6-7.9 mm/yr, respectively.

A longer-term estimate of the throw rate can also be determined from the footwall relief across the Sangarara Fault. Using the typical long-term uplift to subsidence ratio on normal faults of 1:2 to 1:3 [e.g Armijo et al., 1996], the 750 m of footwall relief (Fig. 4.6c) implies a total normal-sense fault throw of ∼2250-3000 m. Given the estimated timing for the onset of extension being <5 Ma [Carlotto, 2013], the Pliocene-Quaternary throw rate must be >0.4-0.6 mm/yr, which is consistent with my estimate of the Holocene throw rate. Alternatively, if the 1.5-3 mm/yr Holocene throw rate was constant through time, it would take ∼1-2 Myrs to form the footwall relief at Sangarara, assuming the same uplift to subsidence ratio.

The relief across the Sangarara Fault dies off towards the south east near Acopia (Fig. 4.6), implying that the fault is ∼15 km long, which is roughly the same as the seismogenic thickness in the high Andes [e.g. Devlin et al., 2012, see Chapter 3]. Near the southern tip of the Sangarara Fault are a series of isolated lake basins (Fig. 4.6a) indicating dip-slip faulting continues further to the south towards Yanoaca. Between Lake Pampamarca and Yanaoca a 10 km-long, 2 km-wide basin is present and the relief between the basin floor and the surrounding mountains increases due to uplift in the footwall of the Yanaoca Fault (Fig. 4.6c). Exposures of the bedrock fault plane near Yanaoca town were heavily altered, potentially due to fluids associated with the nearby volcanism, therefore preserved no kinematic information.

It is likely that the Yanaoca Fault is active. The towns of Pampamarca, Pomacanchi, Yanaoca and Tinta have all experienced severe damage in a series of historical earthquakes on the 18th June 1931, 5th March 1938, 23rd June 1938 and the 23rd January 1943 that caused at least 100 fatalities [Ericksen et al., 1954; Silgado, 1978].

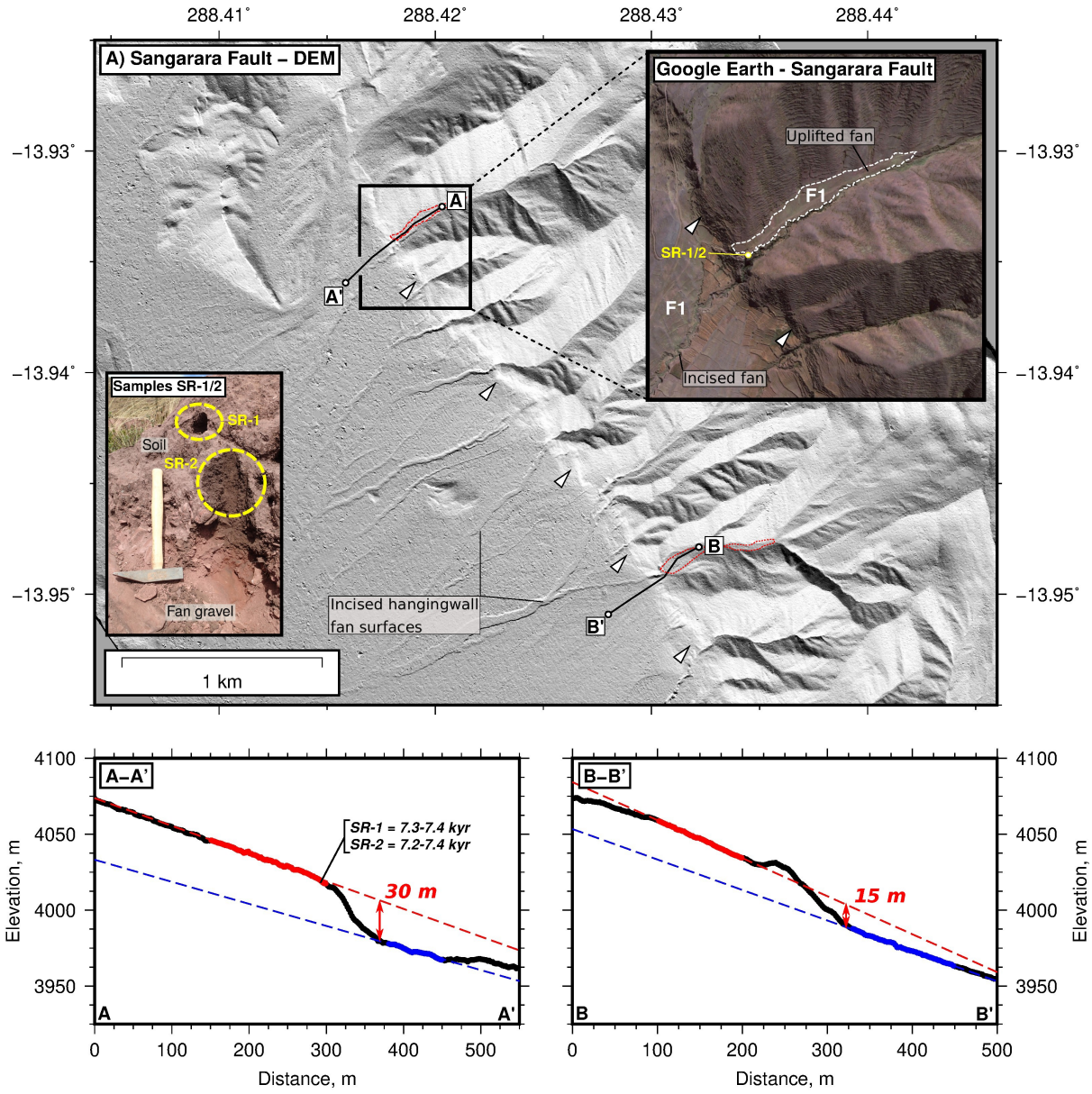

Figure 4.8 Pleiades satellite DEM, sample locations and profiles used to estimate the slip rate on the Sangarara Fault. (a) Hillshade of the Pleiades DEM gridded at 1 m resolution (see text for the method used to construct the DEM). Inset is a Digital Globe satellite image from Google Earth of the offset fan surface (F1; highlighted in white), with the location of the samples SR-1 and SR-2 also highlighted. Photographs of the soil samples collected from the top of the fan are also shown inset. Topographic profiles between points A-A' and B-B' are shown below. These profiles are non-linear as they track down-dip on the fan surfaces.

4.2.3 Langui-Layo Basin

Lake Langui-Layo is a NW-SE trending, intra-montane lake that sits in a 4 km-wide, 30-km long basin (Fig. 4.1, Fig. 4.9). To date the only documented evidence of active faulting in the region are $\sim$ 3 km-long, E-W trending scarps following the bedrock-alluvium contact north of Langui town [Sébrier et al., 1985] (Fig. 4.10a). These scarps mark a distinct change in the pattern of stream incision, suggesting they have been formed by a recently active fault. Nonetheless, the fault responsible for these scarps is unlikely to control the shape of the Langui-Layo Basin, as it trends oblique to the main strike of the lake and is only $\sim$3 km long.

North Langui, South Langui and East Layo Faults

Sébrier et al. [1985] suggested a NW-SE trending, south-west dipping normal fault outcropping along the northern-eastern side of the Langui-Layo Basin may be responsible for subsidence of the lake. I found evidence of this fault in the mountains north east of Layo town in the form of a 5 km-long, 20-30 m-high, south-facing bedrock fault plane (Fig. 4.9a, Fig. 4.10b,c; East Layo Fault). Moraine deposits in the hangingwall suggest the most recent sense of motion on this fault is normal, and the fault preserves slickenlines with an average azimuth of 204^o (Fig. 4.10b). However, as the fault is perched high above the basin edge, it is unlikely to be dominating the vertical motions in the Langui-Layo Basin.

Evidence for recently uplifted lacustrine deposits along the northern, southern and eastern shoreline of Lake Langui-Layo, possibly related to active faulting, also suggest that the East Layo fault is not the dominant fault in the region. There are at least three outcrops of laminated marl deposits situated well above the current lake level around Langui-Layo (Fig. 4.9a). The individual marl layers are between 3 and 6 m thick and contain a number of well-preserved bivalve and gastropod fauna, often in shelly lag horizons, typical of recent sub-aqueous sedimentation. South of Layo town two sub-horizontal layers of the marls are particularly well exposed 50 m and 60 m above the current lake level in the incised edge of a river bank (Locality M2 on Fig. 4.9a and Fig. 4.11). The lower part of the section consists of metre-scale cross-bedded sands and gravel lenses dipping towards the current lake shore, which were probably deposited by east-to-west flowing river systems entering the lake basin. The sands and gravels are overlain by a $\sim$1 m-thick conglomerate horizon, followed by the 3 m-thick lower marl deposit. Above the lower marl layer is another series of cross-bedded sands and gravels, which are capped by the upper marl layer near the top of the exposure. The stratigraphy, fossils and sedimentary structures in the exposure are typical of a near-shoreface, sub-aqueous depositional environment. There are two possible explanations for these sediments, and the other marl deposits at Localities M1 and M3 (Fig. 4.9a), now being at least 60 m above the lake level: (1) the lake was previously higher, or (2) there has been vertical motions caused by active faulting.

For the lake to be previously higher than today would require the outflow at the north-western edge of Lake Langui-Layo was at least 50 m higher than present (current lake level: 3960 m). However, I found no morphological evidence of an incised sill (e.g. landslide or moraine dams) near the lake outlet, which flows through a wide U-shaped valley with a local high point of 3994 m.

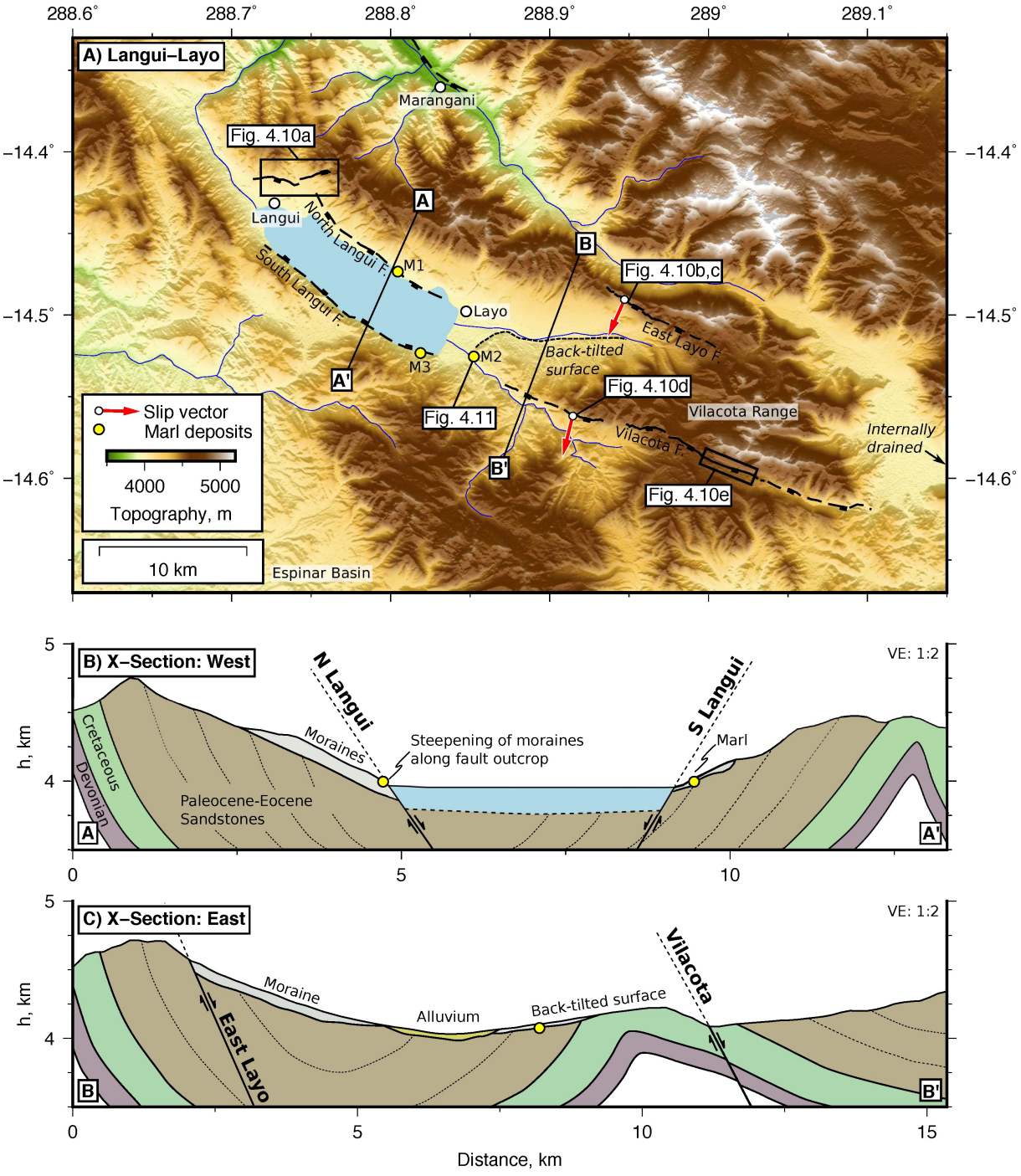

Figure 4.9 Overview of the active faulting around the Langui-Layo Basin. (a) SRTM 30 m DEM and active fault map. The locations of three exposures of marl layers around the edge of the lake are highlighted with yellow dots. Photographs and satellite imagery are shown in Fig. 4.10, a detailed view of the marl deposit at locality M2 is shown in Fig. 4.11. (b,c) Geological and topographic cross-sections through the centre and eastern part of the Langui-Layo Basin. The surface geology is taken from the INGEMMET 1:50,000 Sicuani Sheet 29-t-II [Carlotto and Roque, 2009].

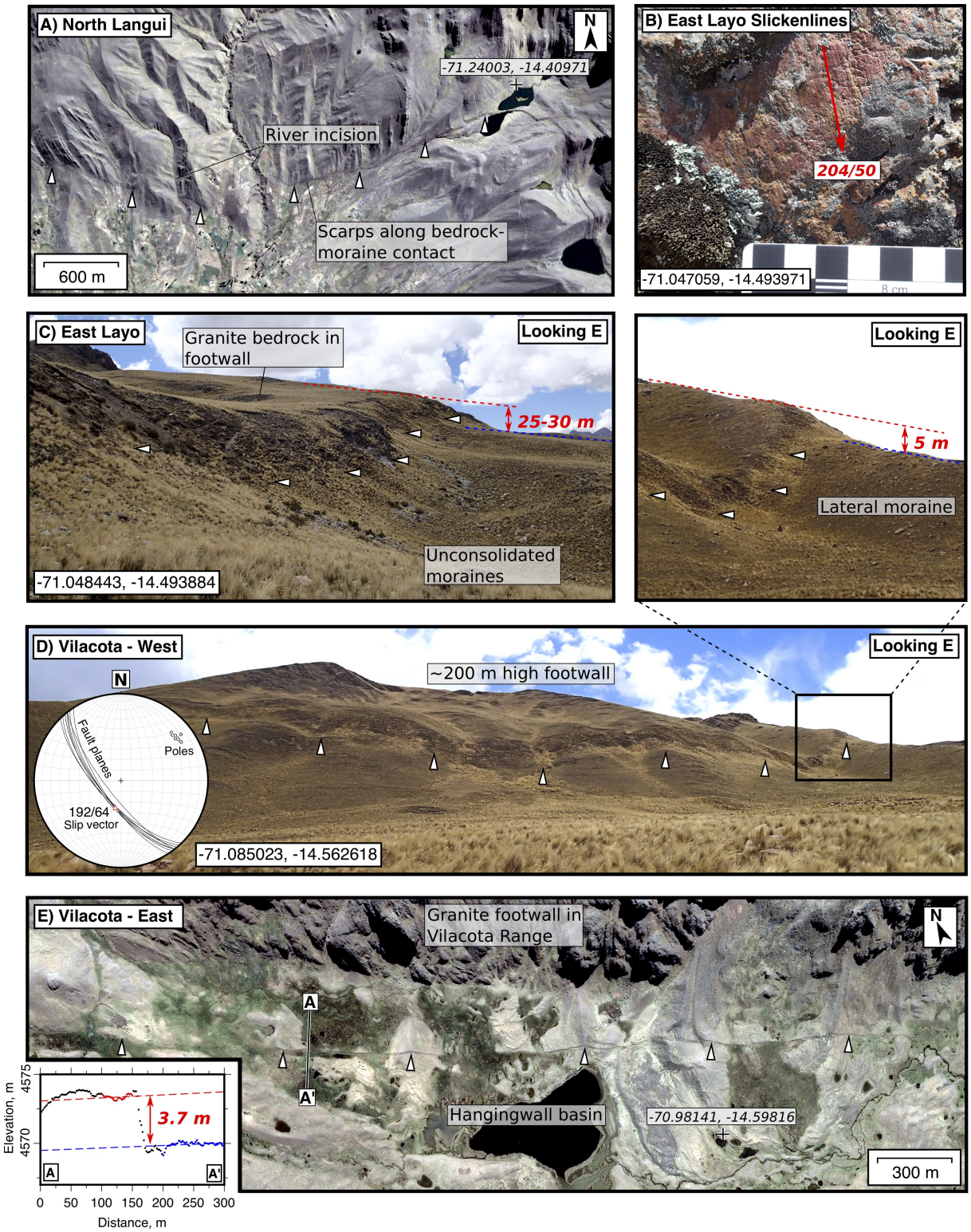

Figure 4.10 Photographs and satellite imagery of faults around Langui-Layo. (a) Digital Globe image from Google Earth of a scarp along the bedrock-alluvium contact north of Langui identified by Sébrier et al. [1985]. (b) Slickenlines on the surface of the East Layo Fault. (c) Photograph of the East Layo Fault showing the 25-30 m vertical offset measured from SRTM 30 m DEM. (d) Panoramic photograph of the Vilacota Fault cutting lateral moraine deposits near its western tip. Inset is a collection of fault plane orientation measurements from this section of the fault. The slip vector of the fault plane is marked by the small red triangle with orientation 192/64. (e) Digital Globe image from Google Earth of the scarps in the eastern portion of the Vilacota Fault cutting glacial deposits draped off the Vilacota Range to the north. Inset is an elevation profile taken across the scarp from a 1 m resolution Pleiades DEM.

Alternatively, there may have been vertical motions caused by faulting that either lowered the lake outlet or raised the lake shorelines relative to the past lake level. The linearity of the lake shorelines, and the steepening of the lateral moraine crests towards the lake shoreline, are suggestive of buried active normal faults along the lake edge, which could account for the relative uplift of marl deposits at localities M1 and M3 (Fig. 4.9; North and South Langui Faults).

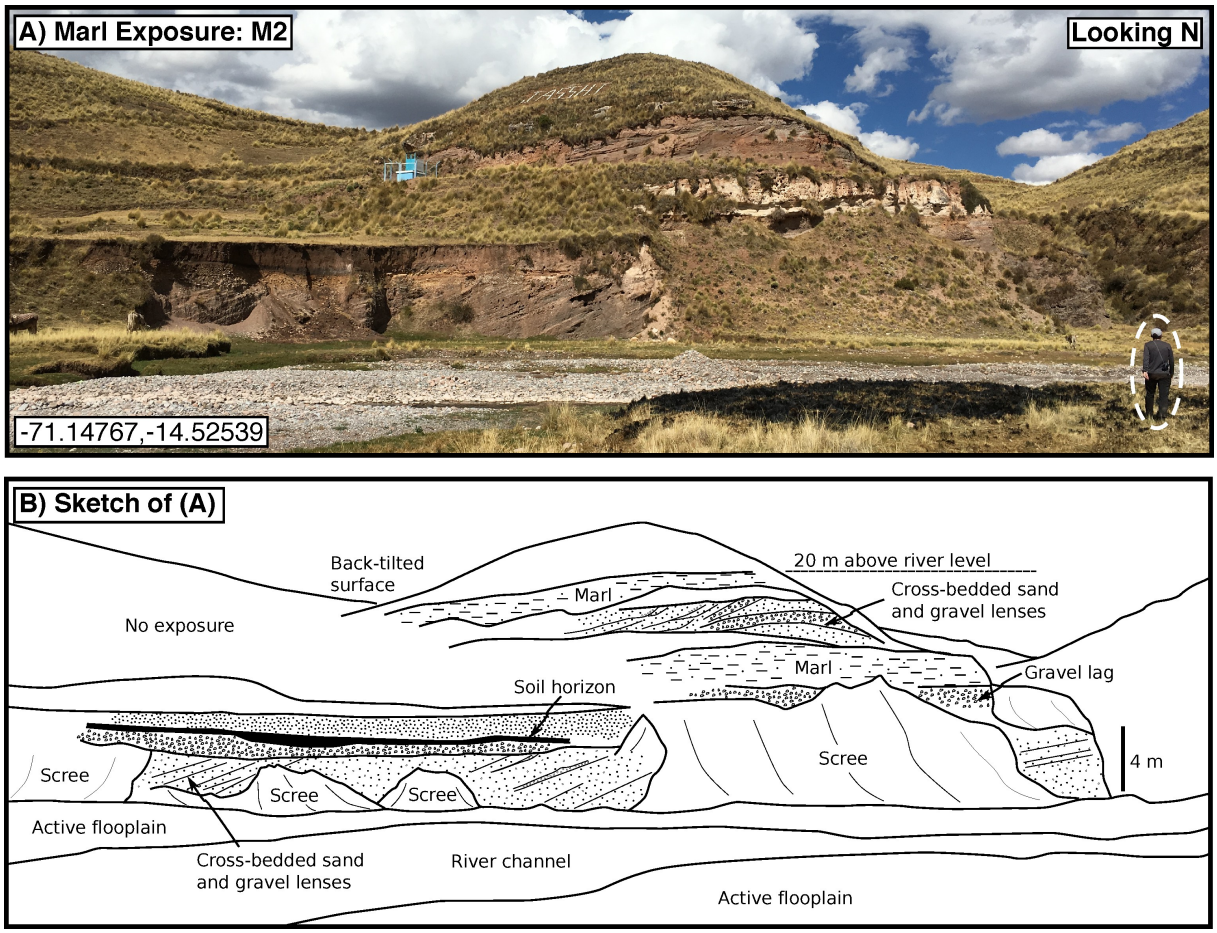

Figure 4.11 Exposed lacustrine marls near Lake Langui-Layo at Locality M2 on Fig. 4.9a. (a) An outcrop of two ∼3-6 m thick marl deposits overlying cross-bedded sands and gravels outcropping along the edge of a river bank south of Layo. The stratigraphy is interpreted to reflect lacustrine deposits now exposed 50-60 m above the current lake level. An interpreted sketch of (a) is shown in (b).

Vilacota Fault

The Vilacota Fault outcrops in the east of the Langui-Layo Basin (Fig. 4.9a) as ∼20 km of E-W trending, south-facing fault scarps cutting lateral moraines and glacial drift deposits (Fig. 4.10d,e). The sense of motion across the scarps is uplift to the north, which is consistent with uplifting the high mountains of the Vilacota Range, the marl deposits at locality M2 (Fig. 4.9c) and the back-tilted surface south-east of Layo (Fig. 4.9a,c).

I constructed a Pleiades DEM of the Vilacota Fault using the same method discussed in Section 4.2.2 to study the along-strike change in the height of recent fault scarps that outcrop on the southern side of the Vilacota Range. At the western tip of the fault scarps cutting the crests of lateral moraines are between 7 and 13 m high (Fig. 4.10d). Towards the fault's eastern tip the scarps are smaller, between 3 and 5 m-high, and can be traced on satellite imagery cutting through recent glacial and landslide deposits (Fig. 4.10e). No direct dating is available for the moraines at Vilacota, though an LGM age would yield a speculative fault throw rate of ∼0.1-1.3 mm/yr.

Exposures of the Vilacota Fault plane near its western tip contained no slickenlines. Therefore, I used the variations in the fault plane orientation to reconstruct the fault slip vector. Active normal faults that have been exposed by excavation are typically corrugated (e.g. Arkitsa Fault in Greece; Jackson and McKenzie [1999]), with the slickenlines sub-parallel to these corrugations. As a result, the corrugated planes will contain the fault slip vector. I found that all of the fault plane measurements contain a common vector of ∼192/64 (Fig. 4.10d, inset), which is equivalent to the slip vector on the Vilacota Fault. Using this kinematic information, the fault throw rate can be converted into a horizontal extension rate of ∼0.1-0.8 mm/yr and a slip rate of 0.1-1.6 mm/yr.

4.2.4 Parina Fault

The Parina Fault outcrops ∼70 km south of Ayaviri and represents a marked southward jump in the NW-SE trending fault system cutting across the mountain belt (Fig. 4.1, Fig. 4.12). The surface trace of the fault follows the contact between a 100-150 m-high, incised footwall escarpment formed of Oligo-Miocene volcaniclastic rocks and a 1-2 km-wide Quaternary hangingwall basin (Fig. 4.12). Along the southern section of the fault, Holocene fault scarps are found along this contact (Fig. 4.13). These morphological features at Parina are typical of the other normal faults between Cusco and Langui-Layo discussed earlier, but are more subdued. For example, the footwall relief at Parina is less than half that of the Tambomachay, Cusco and Sangarara Faults, suggesting the Parina Fault has accommodated less total slip. In addition, recent off-fault deformation preserved as scarps with the same kinematics as the Parina Fault (Fig. 4.13c,d) implies that strain may not have localised onto a single discrete structure.

The southern section of the Parina Fault ruptured in a M_w 6.1 normal-faulting earthquake in 2016 (see Chapter 3). Twelve kilometres of 10-30 cm-high surface ruptures were mapped south of Lake Saguanani that outcrop coincident with NW-SE trending, metre-high scarps cutting bedrock and the overlying moraine cover. DEMs from drone-based imagery over the sections of the fault that ruptured in 2016, one along the northern section near Lake Saguanani, and one along the southern section south of Parina (see discussion in Section 4.2.1 for details on the DEM construction method), are shown in Fig. 4.14. Near Lake Saguanani, the scarps vertically offset the crests of lateral moraines by up to 8 m and reverse the local slope direction, but preserve no evidence for lateral offsets (Fig. 4.14a). The right-stepping en-echelon nature of the scarp traces suggests there may be some left-lateral component to the fault slip vector. Near Saguanani the moraines have not been dated directly, though assuming an LGM age would yield a speculative throw rate between 0.1 and 0.5 mm/yr. South of Parina, profiles E-E' and F-F' indicate there is between 4 and 10 m of cumulative vertical offset across the scarps that ruptured in the 2016 earthquake (Fig. 4.14b). In some areas, there is evidence for multiple scarplets forming a

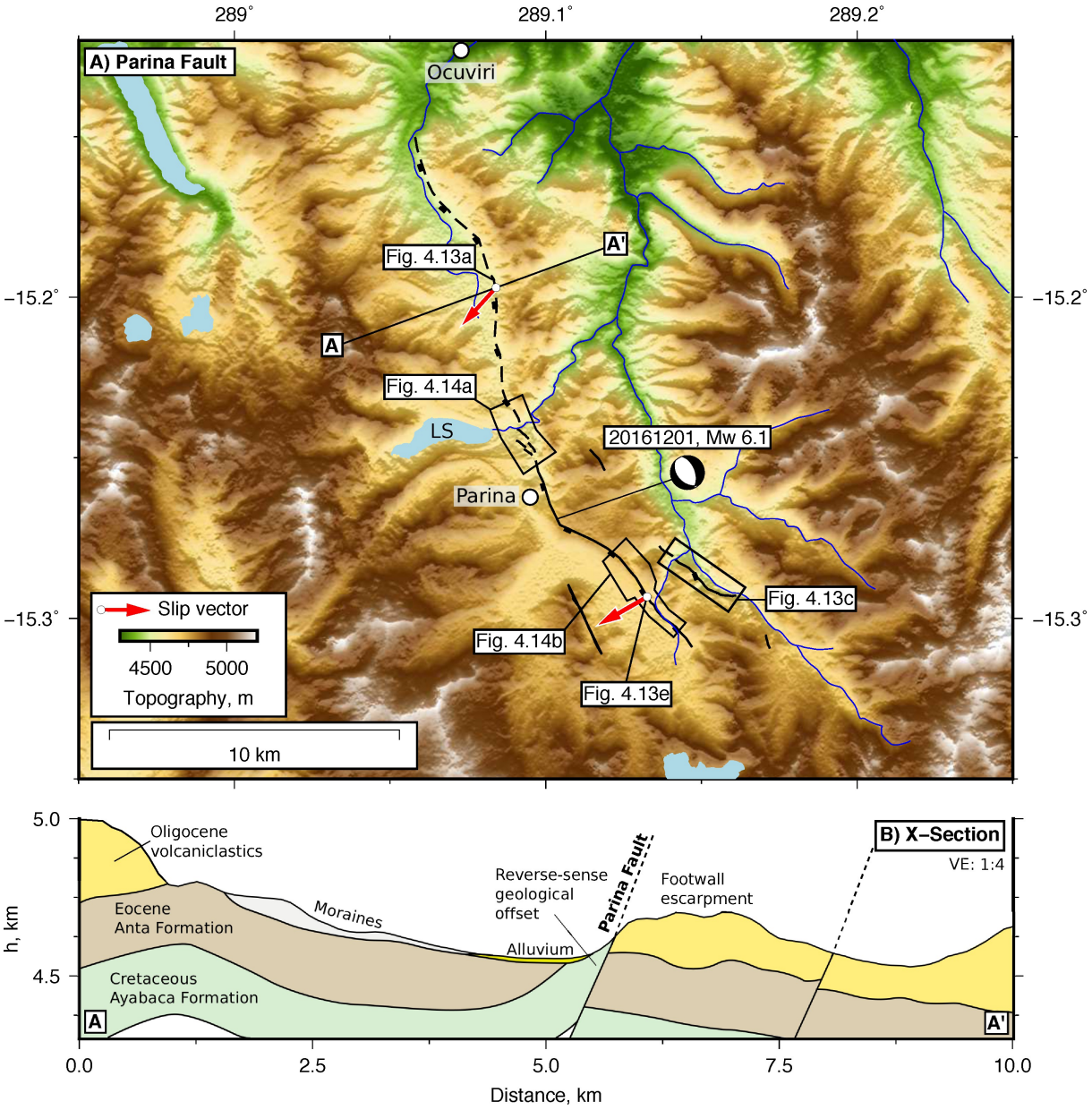

Figure 4.12 Overview of active faults at Parina. (a) SRTM 30 m DEM and mapped active faults. LS = Lake Saguanani. Field photographs of the fault scarps are shown in Fig. 4.13. Drone DEMs over the northern and southern section of the fault that ruptured in the 2016 Parina earthquake are shown in Fig. 4.14. (b) Geological and topographic cross section across the northern section of the Parina Fault, with the sub-surface geology extrapolated from the INGEMMET 1:50,000 Ocuviri Sheet 31-u-IV [Carlotto and Cardenas, 2009].

larger cumulative scarp, highlighting that the fault ruptures to the surface in a splay and not always on a single discrete trace.

The direction of slip on the Parina Fault is constrained by both field slip vector measurements (Fig. 4.13e) and modelling of the 2016 earthquake to be 235-245^o (see Chapter 3). In addition, along the northern section of the fault, between Ocuviri and Lake Saguanani, an exposure of bedrock fault plane perched 70 m above the hangingwall basin preserves the sense of recent fault slip with slickenlines that have azimuths between 222^o and 216^o (Fig. 4.13a). The same fault plane preserves a reverse-sense geological offset between Cretaceous rocks in the hangingwall and Oligo-Miocene rocks in the footwall (Fig. 4.13a). In addition, near the south-eastern tip of the Parina Fault, granites with radiometric ages spanning 18-22 Ma have faulted contacts with Miocene volcaniclastic rocks with a reverse-sense offset [Carlotto and Cardenas, 2008]. Combined, these observations suggest that the region around Parina was shortening in the mid-Miocene, and that the Parina Fault has been reactivated as a normal fault. Using the footwall relief (∼100-150 m) the total fault throw is likely to be on the order of 300-600 m, therefore with a throw rate of 0.1-0.5 mm/yr the Parina Fault may have become active sometime between 1 and 6 Ma.

4.2.5 Lagunillas

North and South Lagunillas Faults

Lake Lagunillas is a 17 km-long, 5 km-wide intra-montane lake (Fig. 4.1, 4.15). No active faults have previously been mapped in this area, though a number of the geomorphic features recognised from the active normal faults at Cusco, Sangarara and Langui-Layo are also apparent at Lagunillas. For example, the linearity of the lake's northern shoreline, the asymmetry of the topography either side of the lake, and the rivers draining the lake to the north that are incising deep gorges into bedrock all suggest the northern shore may be fault bounded (Fig. 4.15; North Lagunillas Fault).

Towards the south-eastern end of the lake both the northern and southern shorelines become lobate and the lake narrows (Fig. 4.15). In the same area, a ∼9 km-long scarp reverses the local slope direction sub-parallel to the southern shoreline of the lake (Fig. 4.16a). SRTM 30 m topography reveals the scarp is around 40 m high and faces to the south west (Fig. 4.16b), therefore uplift in the footwall of this fault may account for the narrowing shoreline at the southern end of Lake Lagunillas. As the fault reverses the local slope direction and is associated with no large-amplitude topography, the South Lagunillas Fault is likely to have accommodated little total slip.

Ululunasa and Willa-Willa Faults

Two kilometres east of Lake Lagunillas a set of south-facing, E-W trending scarps connect to a prominent ∼15 m-high bedrock fault plane damming Lake Ululunasa (Fig. 4.15, 4.16c). This bedrock fault plane occurs along the base of a 100-150 m-high footwall escarpment (Fig. 4.16c). Along the northern shore of Lake Ululunasa, a 10 m-wide wind gap is elevated ∼5 m above the current lake level, suggesting the lake basin has been downthrown in the hangingwall of a south-dipping normal fault (Ululunasa Fault;

Figure 4.13 Photographs and satellite imagery of fault scarps at Parina. (a) Exposed bedrock fault plane between Ocuviri and Lake Saguanani at the location of the cross section in Fig. 4.12b. The fault plane outcrops ∼70 m above the basin floor. People are highlighted for scale. (b) Digital Globe image from Google Earth of fault scarps cutting lateral moraines near Lake Saguanani that were coincident with surface ruptures from the 2016 Parina earthquake. Topographic profiles across these scarps are shown in Fig. 4.14a. (c) Digital Globe image from Google Earth of a fault scarp cutting the footwall of the Parina Fault. (d) Photograph of a sag pond along the scarp breaking the Parina Fault footwall shown in (c). (e) Photograph of the surface ruptures of the 2016 Parina earthquake and the offset features that can be used to reconstruct the fault slip vector (red arrow).

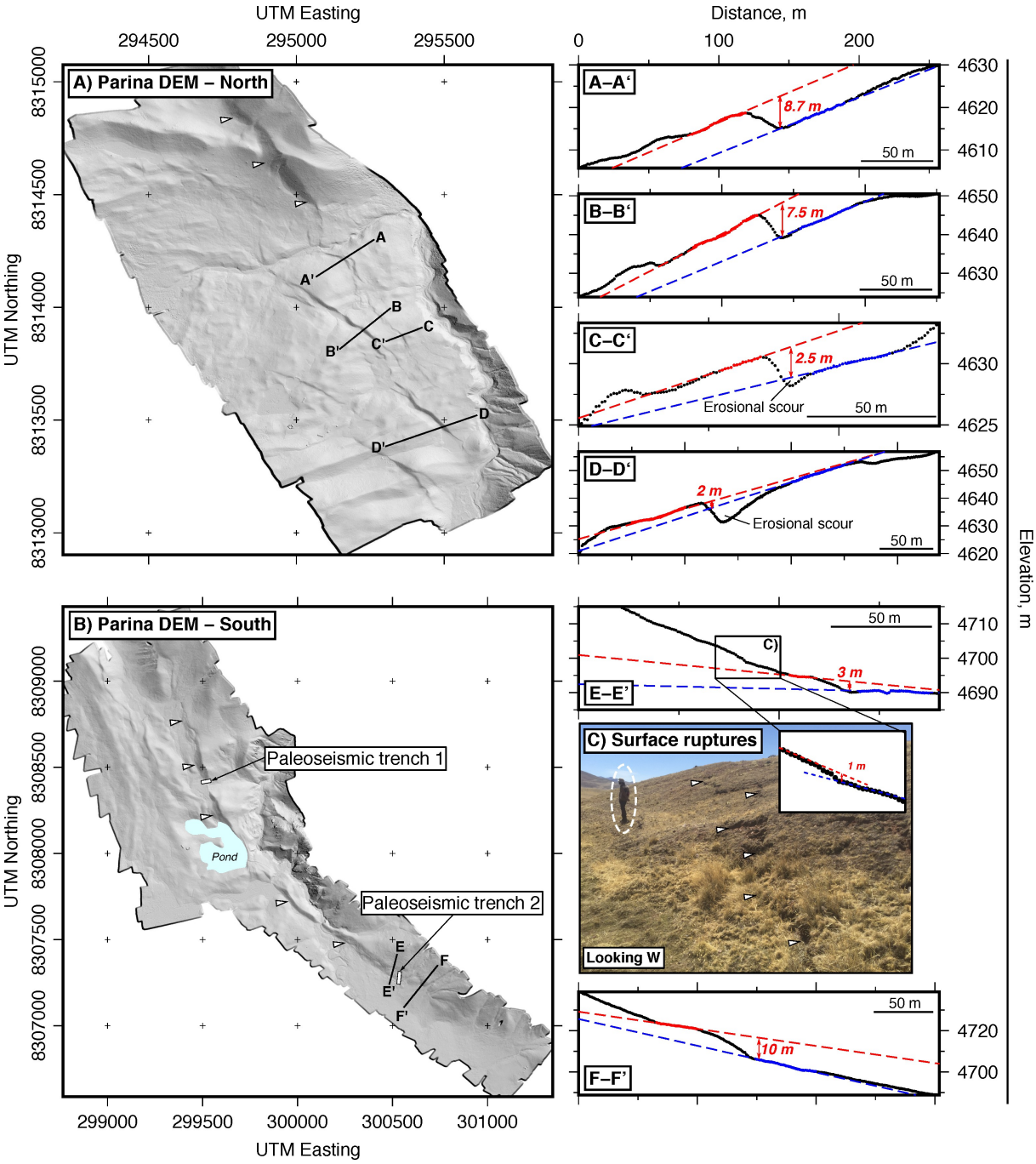

Figure 4.14 High-resolution DEMs covering sections of the Parina Fault that ruptured in the 2016 M_w 6.1 earthquake. (a) Hillshade of the DEM (illuminated from the NE) along the northern section of the fault, ∼1 km east of Lake Saguanani. A satellite image of the same region is shown in Fig. 4.13b. Topographic profiles across the surface scarps are shown adjacent. (b) Hillshade DEM of the southern section of the fault (illuminated from the NE), south of Parina village. (c) Photograph of the surface ruptures from the 2016 Parina earthquake perched up-slope of a ∼3 m-high topographic step. Robust surface offsets due to faulting are not clear along the southern section of the Parina Fault. *Paleoseismic trenches were opened in October 2018 in collaboration with Laurence Audin and Stephaine Baize and will not be discussed here.*

Fig 4.15). The bedrock fault plane did not preserve any kinematic information. Assuming the footwall ridge line has been uplifted following the onset of extension ∼5-9 Ma would yield a speculative fault throw rate on the order of ∼0.03-0.2 mm/yr.

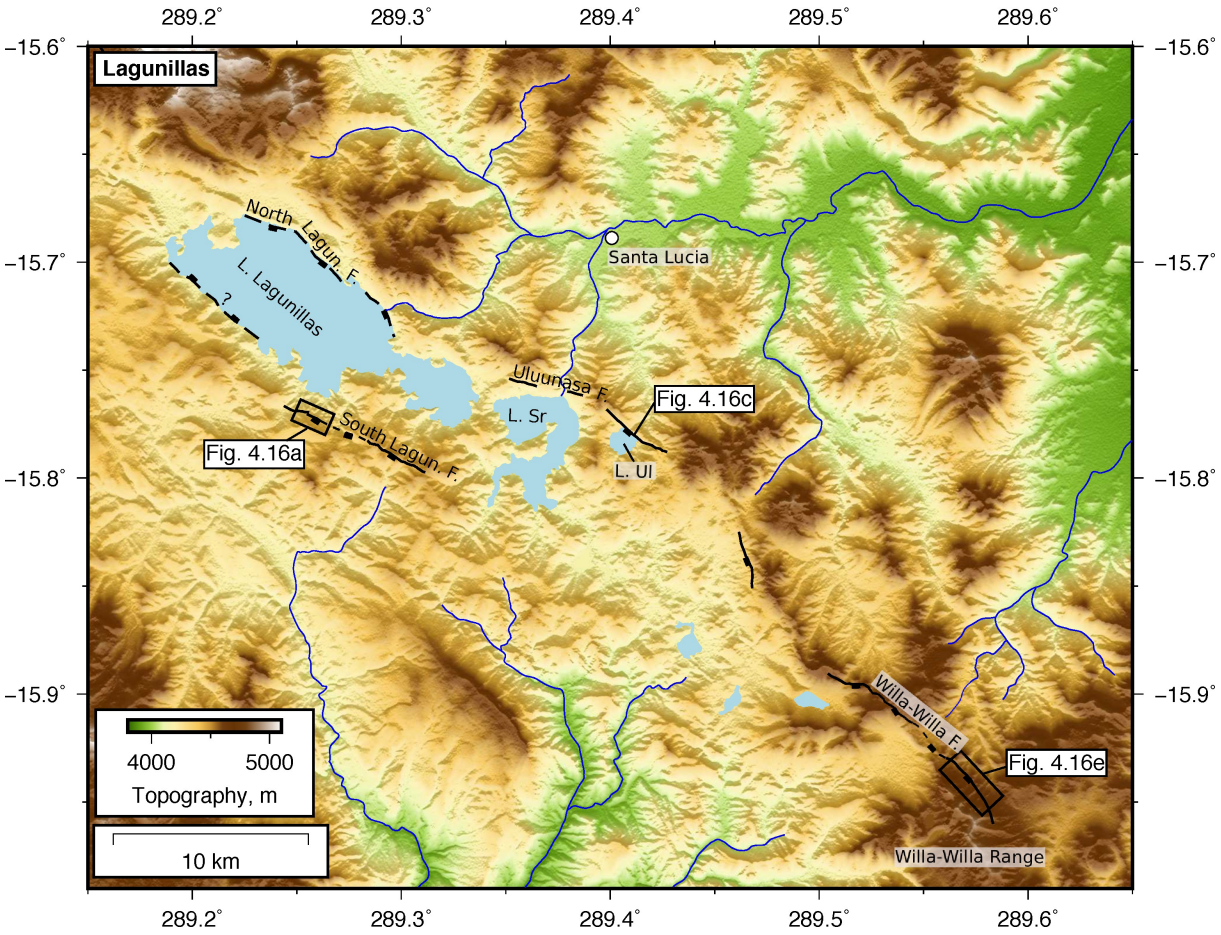

Figure 4.15 SRTM 30 m DEM and active faults near Lake Lagunillas and Santa Lucia. The lakes are: L. SR = Lake Sararacocha and L. Ul = Lake Ululunasa. Photographs and satellite imagery of the faults is shown in Fig. 4.16.

South east of Lake Ululunasa, the Willa-Willa Fault outcrops as ∼20 km of NW-SE trending scarps cutting across the ridge line of the Willa-Willa Range (Fig. 4.15). At the fault's south-eastern tip, normal-faulting scarps reverse the local slope direction, causing incision in the uplifting footwall and exposing ignimbrites within the stream walls (Fig. 4.16d,e). The lack of any large-amplitude topography associated with the Willa-Willa Fault indicates it has accommodated little total slip and may have only become active recently. At its north-western tip, the Willa-Willa Fault preserved a reverse-sense faulted contact between between Jurassic rocks of the Yura Group and a Neogene-age granitic intrusion [Meija and Frisancho, 2008], suggesting the recent extension has been accommodated on a previously-active reverse fault.

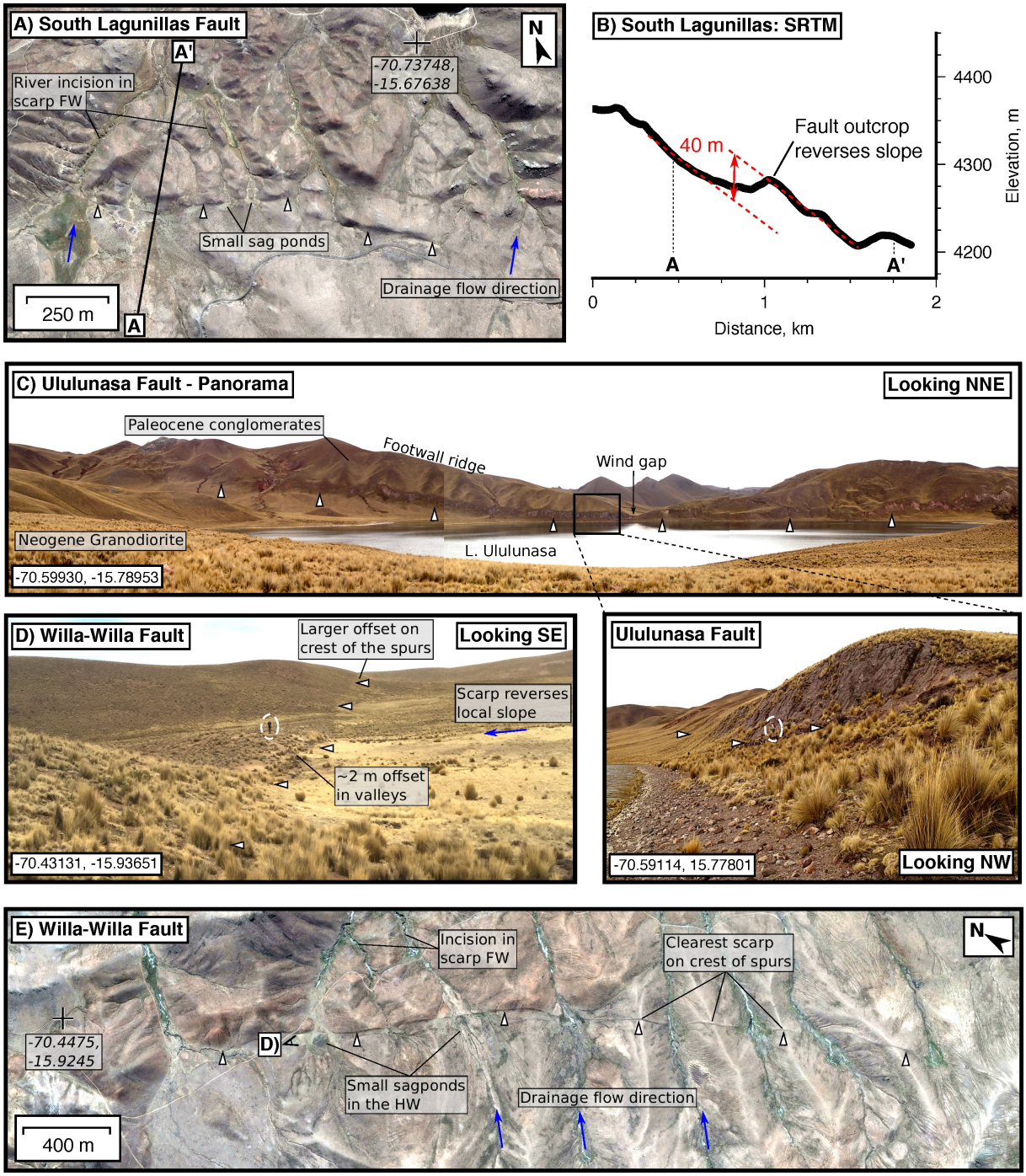

Figure 4.16 Satellite imagery and photographs of faults near Lake Lagunillas. (a) Digital Globe image from Google Earth of the South Lagunillas Fault (see Fig. 4.15). (b) Topographic profile extracted from the SRTM 30 m DEM across the scarp in (a), indicating that recent motion on the South Lagunillas Fault has a vertical offset of ~40 m. (c) Panoramic photograph of the Ululunasa Fault. The fault is damming a small lake by uplifting its outlet, forming a wind gap on the northern shore. A photograph of the exposed fault scarp is shown inset. (d) Photograph of the Willa-Willa Fault with people highlighted for scale by a white circle. At Willa-Willa there are two distinct offsets, with the crests of the parallel spurs being offset by more than the small scarps within the intervening valleys. (e) Digital Globe image from Google Earth of the Willa-Willa Fault.

4.2.6 Huambo-Cabana Conde Faults

On the southern edge of the high Andes, between the northern flank of Sabancaya Volcano and the Colca Canyon (Fig. 4.1), Sébrier et al. [1985] identified a 28 km-long set of E-W trending, south-dipping normal fault scarps that offset recent lava flows by 10-30 m. These scarps, collectively known as the Huambo-Cabana Conde Faults, preserve slickenlines with a N-S azimuth [Sébrier et al., 1985].

Between 2002 and 2013 three moderate magnitude earthquakes and a swarm of micro-seismicity occurred within the Huambo-Cabana Conde Fault Zone. Jay et al. [2015] used InSAR and regional seismic data to suggest the 2002-2013 earthquakes ruptured north-dipping normal faults that outcrop ∼5 km north of the faults mapped by Sébrier et al. [1985]. Both Sébrier et al. [1985] and Jay et al. [2015] attributed the kinematics of these faults to the regional pattern of N-S extension throughout south Peru. However, the observations presented above indicate that extension on the Cusco-Lagunillas Faults is not N-S, but NNE-SSW to NE-SW. Therefore, it is also possible that the Huambo-Cabana Conde faults are accommodating the horizontal motions due flank collapse of Sabancaya Volcano into the 3000 m-deep Colca Canyon, and their slip vectors do not necessarily reflect deformation in response to regional tectonic motions.

4.2.7 Summary of Faulting in the South Peruvian Andes

The faults described in this chapter form a ∼20 km-wide, right-stepping en-echelon band trending NW-SE obliquely across the high Andean plateau. Individual faults strike between E-W and NW-SE, have a predominantly south-westwards dip and are between 10 and 20 km long. The fault lengths are similar to the seismogenic thickness in the area [e.g. Devlin et al., 2012, see also Chapter 3]. The recent sense of slip on all of the faults is extensional with a varying component of left-lateral shear, and the faults consistently accommodate extension along slip vectors that are sub-parallel to the shortening direction in the adjacent sub-Andean forelands, irrespective of the fault strike (see Chapter 3). Near Cusco, this is manifest as NNE-SSW extension on mainly E-W striking faults, whilst near Parina the faulting is NE-SW extension on NNW-SSE striking faults. The extent to which recent extension is localised onto this one fault system, or whether it is more distributed across the high plateau, is difficult to assess from the geomorphology alone due to variations in preservation potential of the active faults (see Section 4.3.1).

The Pachatusan, Tambomachay and Parina Faults still preserve a reverse-sense geological offset. Similarly, the trend of the Cusco-Lagunillas Faults follows the predominantly NW-SE trend of Andean-age reverse faults in the south Peruvian Altiplano [Perez et al., 2016b], implying that the pre-existing structural fabric has been important in localising the recent extensional strain. Reactivation of north-eastward (i.e. foreland-ward) verging thrusts could account for the consistently south-westward dip of the active normal faults. Where the timing of last major shortening has been constrained, it is typically ∼6-15 Ma [e.g. Carlotto, 2013; Horton et al., 2015], placing the recent extension as post-Miocene in age. Extrapolating the throw rates on faults where there is good age control implies the current footwall relief on these faults formed in the last ∼1-5 Myrs. The post-Miocene extension along reactivated

reverse faults in south Peru mirrors the pattern and timing of deformation seen on the southern edge of the Puna plateau in Argentina [e.g. Schoenbohm and Strecker, 2009].

Robust age control was only available for the faults around Cusco and Sangarara. At both these localities the cumulative horizontal extension rate across the whole normal-fault system is in the range ∼1-3 mm/yr. Between Langui-Layo and Lagunillas there is no robust age control on the fault offsets. However, a number of the faults (e.g. Vilacota, Parina) offset lateral moraine deposits that probably date to the Last Glacial Maximum (∼10-45 ka), yielding extension rates $\lesssim$1 mm/yr. I was not able to make any estimates of the fault slip rates near Lagunillas.

In the following section, I discuss the morphology of the active normal faults, present simple calculations to explain the slip rates on the normal faults and discuss the relationship between the long-term extension and transient shortening across south Peru.

4.3 Discussion

4.3.1 Preservation and Morphology of Faulting in south Peru

A number of the normal faults discussed above were identified on the basis of metre-high fault scarps that outcrop in the mountains, perched above the local base level, and with no associated large-amplitude topography. A prime example is the spectacular scarps on the Qoricocha Fault (Fig. 4.3a). At first glance, the Qoricocha Fault may appear to be the dominant structure accommodating deformation in the area on the basis of the 6 m-high, fresh-looking scarp cutting an otherwise undisturbed surface. However, this fault has been uplifted relative to the Cusco Basin floor by faster vertical motions on the Tambomachay and Cusco Faults over the late Quaternary (<1 Ma). On these faster slipping faults, Holocene scarps are rarely preserved due to deposition in their hangingwalls and incision in their footwalls. Therefore, well-preserved fault scarps are not an accurate indicator of the long-term fault activity or the relative slip rates of faults in south Peru. The Qoricocha scarps are probably exceptionally preserved due to the recent deposition of glacial sediments and their subsequent abandonment in a low erosion rate environment.

A more accurate indicator of fault activity throughout the late Quaternary is the footwall relief and the pattern of stream incision across the fault outcrop. The Cusco Fault is uplifting both the Qoricocha and Tambomachay Faults in its footwall relative to the Cusco Basin floor, suggesting the Cusco Fault is the fastest slipping of the three (see Section 4.2.1). Sharp changes in river incision and ∼100-150 m of relief across the Cusco Fault outcrop make it easily identifiable in the field. However, the pattern of stream incision is only preserved because the Cusco Basin remains isolated from headward erosion along the Vilcanota River valley (Fig. 4.2a). In places where headward erosion has scoured the hangingwall basins of normal faults, such as the western portion of the Anta Basin west of Cusco (Fig. 4.17), the sharp transition in stream incision is no longer preserved, and the presence of normal faulting is more difficult to identify [e.g. D'Agostino et al., 2001]. At Sangarara and Yanoaca, the exposure of the incised hangingwall basin deposits around the edges of Lake Pampamarca and the incision in the hangingwall

sections of the fans indicates that headward erosion has begun scouring the hangingwall, but has not yet had time to erase evidence of the normal faulting (Fig. 4.6).

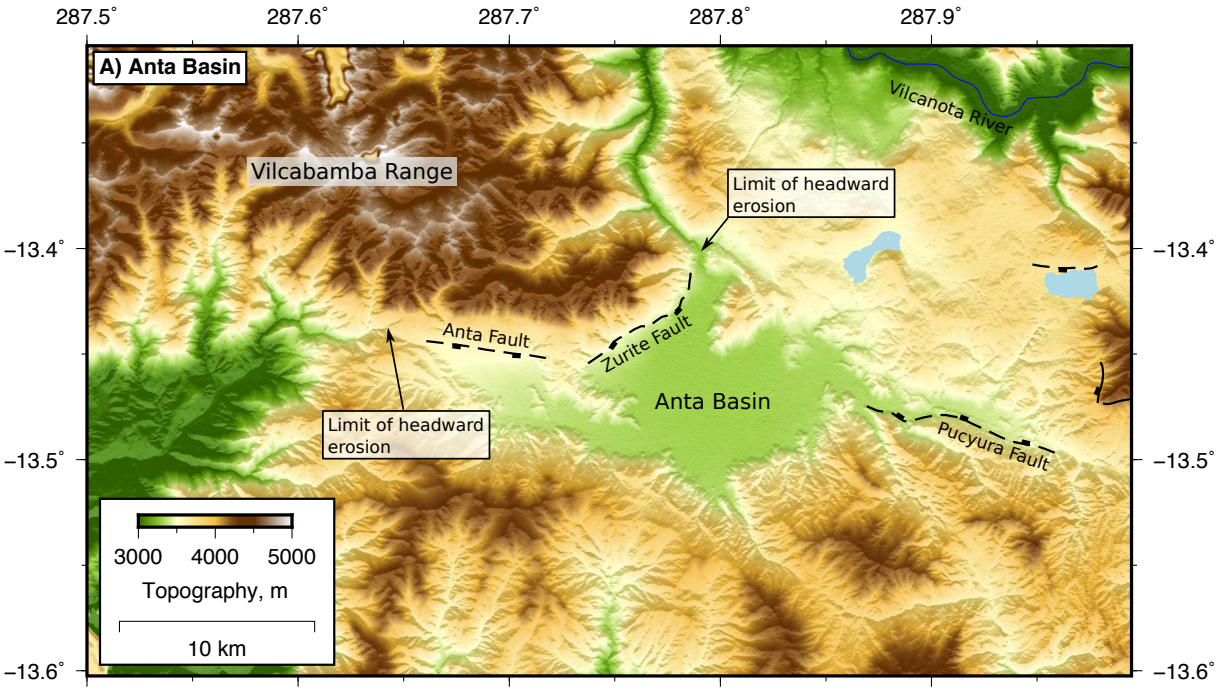

Figure 4.17 Morphology of the Anta Basin. A tributary of the Apurimac River (see Fig. 4.1) has incised the western portion of the basin. Limits of the active incision have been marked.

Another key indicator of fault activity is the height of normal fault's footwall escarpment, which is partly controlled by the footwall lithology, and therefore also subject to preservation bias [e.g. Goldsworthy and Jackson, 2000]. An excellent example of this preservation bias is seen at Sangarara (Fig. 4.6). Suarez et al. [1983] identified a ∼3 km-long section of the Sangarara Fault associated with 50 m-high triangular facets separating graded fan surfaces from the steep, incised footwall escarpment (see Fig. 4.8a). Along-strike of this well-preserved section, the fault morphology changes significantly. One kilometre north of Lake Pomacanchi, the Sangarara Fault has no triangular facets, but a rounded range front with little change in the pattern of stream incision across the bedrock-alluvium contact. The transition in the fault morphology correlates with a geological contact between Paleocene sandstones in the well-preserved section of the footwall, and a mixture of Cretaceous limestones, shales and evaporites forming the poorly-preserved section of the footwall [Carlotto et al., 2009].

From the discussion above, it is clear that the preservation of normal faulting in south Peru is highly variable. As a result, there may be parts of the study area not discussed so far where active normal faulting is taking place, most likely in the areas between the mapped faults, kinematically linking them together. One particular region is south of Cusco, where deep canyons cut by tributaries of the Apurimac River could have incised through the uplifting footwalls and subsiding hangingwalls of most faults, if present, leaving little detectable trace of active faulting (Fig. 4.1). Nonetheless, faults with similar slip rates (∼1 mm/yr) to those between Cusco and Lagunillas are expected to be associated with some morphological expression.

At the south-eastern end of the fault system near Lagunillas, many of the faults (e.g. Willa Willa, South Lagunillas Faults) reverse the local slope direction and are associated with no significant footwall escarpments. These morphological traits may reflect reduced slip rates on the south-eastern end of the fault system as the extension dies out, which would be consistent with the lack of recent extension in the Bolivian Altiplano [e.g. Lamb and Hoke, 1997; Lamb, 2000]. As the Bolivian Altiplano is on average 400-500 m lower elevation than the south Peruvian Altiplano, the along-strike decrease in the extension rates may be a product of the decreasing gravitational body forces acting on these different sections of the mountain range (Section 3.3.1).

4.3.2 Dynamical Implications

Active normal faults in south Peru that reactivate Miocene age reverse faults are evidence that the force balance in the mountain belt has recently changed. It is likely that, prior to the onset of extension, a balance between the forces acting on the boundary of the mountains and buoyancy forces did exist, leading to the formation of the high-elevation, low-relief plateau in south Peru [e.g. Molnar and Lyon-Caen, 1988]. However, sometime since the late Miocene the force balance has been perturbed, leading to the recent normal faulting and extension of the plateau interior [e.g. England and Houseman, 1989].

The orientation of slip on the normal faults suggests that the recent extension is a response to a decrease in the forces transmitted across the sub-Andes. In particular, the high Andes are extending parallel to the shortening direction in the sub-Andes, and parallel to gradients in the topography on the eastern side of the mountain belt (see Section 3.3.3). The pattern of deformation across south Peru is consistent with the Andean crust thrusting eastwards over the South American forelands due to a reduction in the shear stresses on the base of the sub-Andean fold-thrust belt, inducing extension in the high plateau (see Section 3.5.1). I used the measurements of the fault slip rates to estimate the decrease in the average shear stresses transmitted across faults in the sub-Andes.

I studied the dynamic implications of a reduction in the shear stresses transmitted across the sub-Andes using a two-dimensional, static force balance [modified from Lamb, 2006] (Fig. 4.18). The two-dimensional geometry is appropriate, as the extension across the normal faults is parallel to the direction of shortening in the sub-Andes, with little evidence for motion along-strike the mountain belt. Therefore it is only necessary to consider forces acting vertically and perpendicular to the strike of the mountain belt to account for the recent deformation [e.g. Dalmayrac and Molnar, 1981; Richardson and Coblentz, 1994]. The finite extensional strain accommodated by the normal faults is small ($\lesssim$1 %; Sébrier et al. [1985]), therefore changes in the crustal thickness and the geometry of the Andes has probably had little effect on the force balance since the extension began.

Three dominant forces act on the sub-Andes: (1) the weight of the sub-Andean crust overlying the detachment fault (Mg on Fig. 4.18), (2) the shear force supported by the sub-Andean detachment (F_s on Fig. 4.18), and (3) the horizontal force acting on the back of the sub-Andes (F_f on Fig. 4.18). All three must be in a quasi-static balance, therefore it is possible to write an expression for the shear force on the sub-Andean detachment [Lamb, 2006]:

$$F_s + Mg\sin\theta - F_f\cos\theta = 0, \tag{4.1}$$

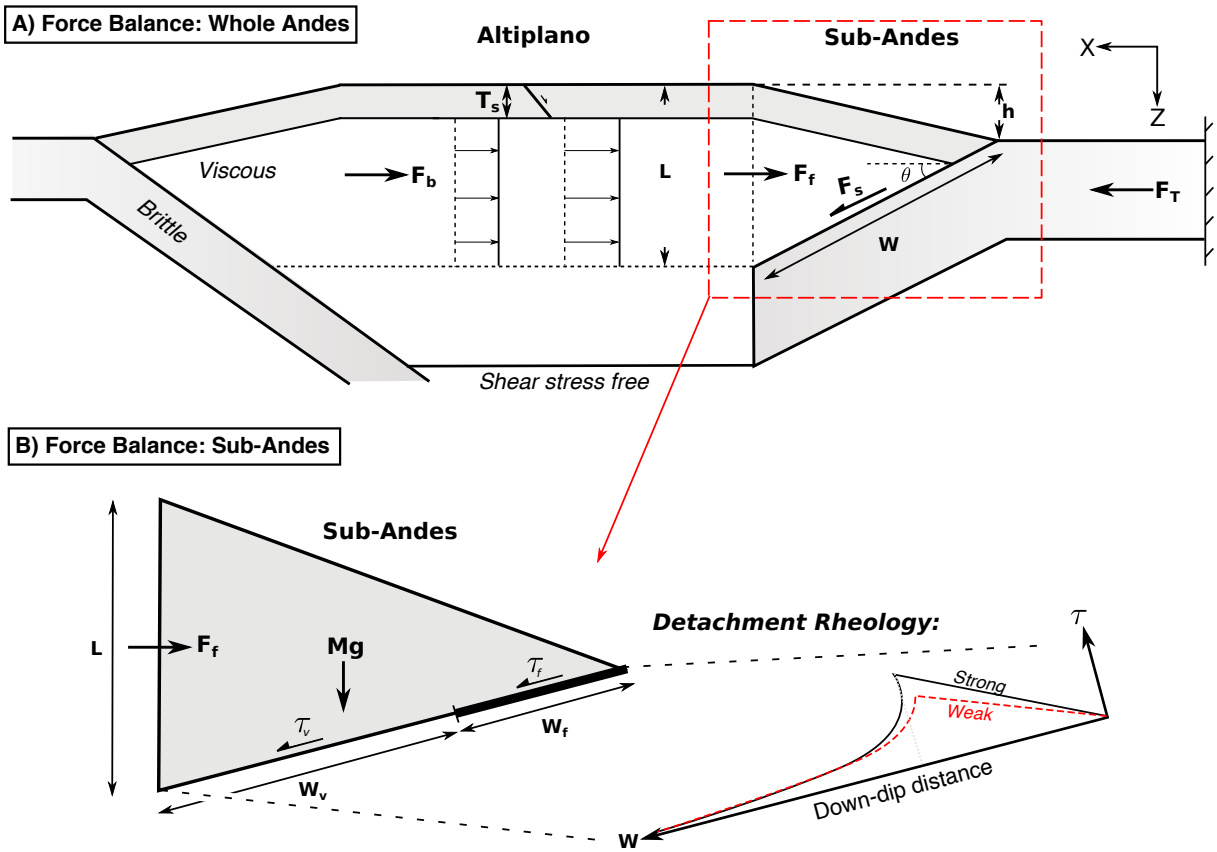

Figure 4.18 Schematic of the model used to study the force balance in the Andes. (a) A sketch of the force balance across the eastern Andes. F_b are the buoyancy forces caused by horizontal differences in the lithostatic stress, F_s is the shear force on the sub-Andean detachment and F_f is the horizontal force acting on the back of the sub-Andes. (b) Sketch of the force balance in the sub-Andes modified from Lamb [2006]. Frictional and viscous shear stresses on the detachment are denoted τ_f and τ_v, respectively, and Mg is the weight of the wedge. Inset is a schematic of the shear stress distribution as a function of down-dip width along the detachment for two cases: a frictionally weak and frictionally strong detachment. I explore the influence of changing the frictional shear strength of the detachment on the shear forces F_s in Fig. 4.19b.

where θ is the dip of the detachment. The force acting on the back of the sub-Andes F_f will be equivalent to the buoyancy forces resulting from horizontal differences in vertical normal stress $\Delta\sigma_{zz}$ between the mountains and the adjacent forelands [e.g. Dalmayrac and Molnar, 1981] and any differential stresses $\Delta\sigma$ from deformation within the mountains:

$$F_f = \int_0^L \Delta\sigma_{zz}\, dz + \int_0^L \Delta\sigma\, dz, \tag{4.2}$$

where L is the thickness of the crust above the down-dip edge of the detachment (Fig. 4.18). Together Equations 4.1 and 4.2 link the shear forces supported by faults on the edge of a mountain belt to the differential stresses within its interior.

Prior to the onset of extension, the differential stresses in the mountains were probably negligible, to satisfy the conditions required to form a wide and low-relief plateau [e.g. Molnar and Lyon-Caen, 1988]. Therefore, to account for the recent normal faulting, either the buoyancy forces have increased, Mg has decreased or F_s has decreased (see Equations 4.1 and 4.2). As the buoyancy forces are set by the thickness and density of the crust in the Andes and South American forelands, and crustal thinning caused by the recent extension in south Peru is $\ll$1%, the buoyancy forces have remained approximately constant. Similarly, Mg, which is controlled mainly by the area of the sub-Andean wedge, is unlikely to have decreased recently, as material is constantly being incorporated into the fold-thrust belt. Therefore the most likely explanation for the onset of recent extension is a reduction in the strength of the sub-Andean detachment F_s.

In order to maintain the force balance in Equation 4.1 following a decrease in the shear force δF_s on the detachment, the crust at the back of the sub-Andes would be subject to a force perturbation given by $\delta F_f / \cos\theta$. This force will be supported in the high Andes by frictional resistance along faults in the brittle crust and viscous resistance to deformation within the underlying ductile crust. Assuming that the brittle crust is thin and provides little resistance to deformation, the ductile crust must provide viscous resistance to deformation $\Delta\sigma$ given by (see Appendix C.3 for derivation):

$$\delta\tau = \Delta\sigma \cos\theta \left(\sin\theta + \frac{h}{W} \right), \tag{4.3}$$

where W is the down-dip width of the detachment, $\delta\tau = \delta F_s / W$ and h is the height of the mountains (Fig 4.18). The hot, ductile crust in the Andes will flow in response to the change in the differential stress. If the crust has some depth-averaged Newtonian viscosity η, the horizontal strain rate of the flow will be given by: $\dot{\varepsilon} = \Delta\sigma / 2\eta$. Therefore, given some knowledge of the strain rate of extension and the material properties of the crust in the Andes, Equation 4.3 can be used to calculate the decrease in the shear stresses on the sub-Andean detachment.

Calculating the extensional strain rate in south Peru from fault slip rates in the brittle crust requires some assumptions regarding the distribution of the deformation. The velocity field measured at the surface will be discontinuous (when neglecting the effect of elastic strain accumulation), as deformation is accommodated by slip on faults. It is generally assumed that the distribution and rate of fault slip reflects the more continuous pattern of deformation within the underlying ductile crust [Molnar, 1988], therefore by spatially-averaging the fault slip rates one can recover the horizontal components of the

strain rate field in the ductile layer [Haines and Holt, 1993; England and Molnar, 1997b]. In the case of south Peru, as the majority of the recent deformation has been plane strain in a vertical cross-section perpendicular to the mountain belt, and because normal faulting has been mapped between the Eastern and Western Cordillera (Fig. 4.1), a sensible length-scale over which the velocity gradients should be averaged would be the width of the plateau (∼150-200 km). Given the 1-3 mm/yr of cumulative extension across the normal faults, the late Quaternary extensional strain rate averaged over the high Andes would be 0.5-2×10^{-8} 1/yr. If the extensional strain in the ductile crust is concentrated into the ∼20-30 km around the Cusco-Lagunillas Faults, the local strain rate estimates would be ∼5 to 10 times higher, but the average deformation rates across the Andes would remain the same.

The average viscosity of the crust in the Andes has been estimated from the relationship between topography and deformation rates to be ∼ 10^{21}-10^{22} Pa s [Lamb, 2000; Husson and Ricard, 2004, Chapter 3], which is typical for vertically-averaged crustal viscosities in mountain belts [e.g. Flesch et al., 2001]. Combining the extensional strain rate and the viscosity estimates, the differential stresses $\Delta\sigma$ causing the ductile crust to extend in the Andes are between 0.5 and 9 MPa (Fig. 4.19a), which is equivalent to a horizontal force of 0.006-0.3 TN per metre along-strike using a detachment dip of 7^o and width of 200 km. Using Equation 4.3 and taking $\theta \sim$ 5-10^o, $h \sim$ 4 km and $W \sim$ 100-200 km then $\delta\tau$ would be in the range 0.02-3 MPa (Fig. 4.19a). The average shear stresses on the detachment determined from similar force balance methods yields $\tau \sim$ 10-25 MPa [Lamb, 2006; Oncken et al., 2012]. Therefore the fractional change in τ needed to account for the current extension rate across south Peru is ∼0.1-30%.

The key result of these calculations is that a small change in the forces transmitted across faults on the edge of a mountain belt can have a significant affect on the rate and mechanism of faulting within the high plateau, because of the delicate balance of forces in this setting. This conclusion is independent of the rheological law used for the detachment.

If the shallow (<10 km), seismogenic portion of the sub-Andean detachment has a frictional rheology described by $\tau = \mu'\sigma_n$, where σ_n is normal stress and μ' is the effective friction, the necessary weakening could be caused by decreasing the intrinsic frictional strength or increasing the pore-fluid pressures on the fault (Fig. 4.18b, inset). It is also possible that increasing the thermal gradient along the detachment could have reduced the down-dip width of frictional coupling, reducing the forces transmitted between the foreland and the Andes (Fig. 4.18b, inset). Calculations for the shear forces on the shallow portion of the sub-Andean detachment using Equation 8 of Wang and He [1999] demonstrate that changing either the effective friction μ', or the down-dip width of frictional coupling W_f, even by a small amount, can easily account for the perturbation to the force balance inferred from the faulting observations (see arrows on Fig. 4.19b). Alternatively, part of the detachment may have a viscous rheology of the form $\tau = A\dot{\varepsilon}^{1/n}$, where $A \propto \exp(1/T)$ is a material property dependent on temperature T and n is the stress exponent [e.g. Ranalli, 1995]. Small increases in the temperatures along the detachment, or the incorporation of new material with a lower creep strength, could also account for the change in the force balance. However, from my observations alone, I cannot determine what mechanism caused the strength of the detachment to decrease.

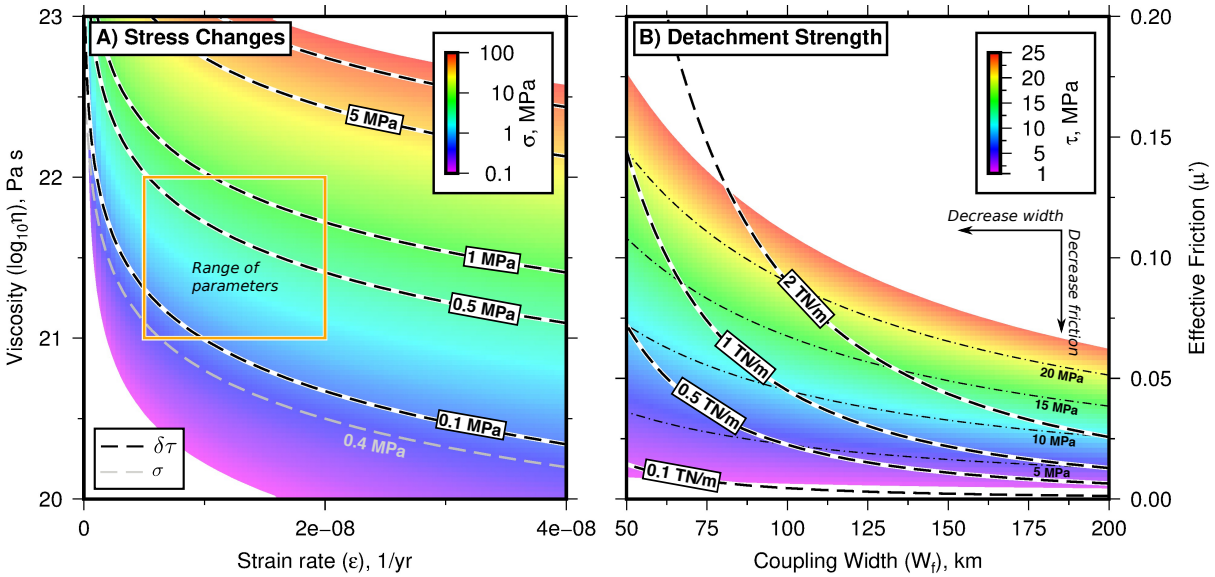

Figure 4.19 Calculations for the stress changes needed to account for the rate of normal faulting in the Andes. (a) The extensional differential stresses $\Delta\sigma$ in the Andes (coloured background) and the average shear stress change on the sub-Andean detachment $\delta\tau$ (dashed contours) as a function of the extensional strain rate in the high Andes and the viscosity of the Andean crust. The shear stress change is calculated from Equation 4.3 assuming $W = 200$ km, $h = 4$ km and $\theta = 7^o$. The orange box represents the appropriate range of crustal viscosity and extensional strain rate for south Peru (see text). (b) Shear stresses (coloured background) and the shear force (dashed contours) supported by the frictional portion of the sub-Andean detachment (thick black line in Fig. 4.18b) as a function of the frictionally-coupled width W_f and the effective coefficient of friction μ' on the fault (using Equation 8 of Wang and He [1999]). Calculations in (b) have been performed with the same W_f, h and θ as in (a).

4.3.3 Transient Strain and Stress

In addition to changes in the force balance in the Andes over the last ∼1-5 Myrs, there is also evidence that the force balance changes periodically over ∼100-300 years due to the accumulation and release of elastic strain in earthquakes along the margins of the mountain belt. In this section, I discuss observations from GPS, active faulting and earthquakes collected before and after the 2001 M_w 8.4 Arequipa earthquake that suggest permanent deformation within the high Andes occurs dominantly following megathrust earthquakes, and that slip on the normal faults is temporarily suppressed by the elastic compression during the interseismic period.

Interseismic GPS measurements collected between 1993 and 2000, prior to the 2001 M_w 8.4 Arequipa megathrust earthquake, captured shortening across the Cusco-Lagunillas Fault system with a strain rate of $\sim 3 \pm 1 \times 10^{-8}$ 1/yr between COTA and MACU (Fig. 4.20a) — that is 9 ± 3 mm/yr over a length-scale 280 km. Bevis et al. [2001] demonstrated that these velocity gradients can be matched by a model of elastic strain accumulation on the Peru-Chile megathrust and the sub-Andean detachment, suggesting the deformation will be relaxed following megathrust earthquakes on either margin of the Andes. The lack of active reverse faults within the area studied in this chapter, and the occurrence of three M_w 5-5.2 normal-faulting earthquakes between 1980 and 2001, are consistent with the suggestion the majority of the shortening strain is elastic (Fig. 4.20d).

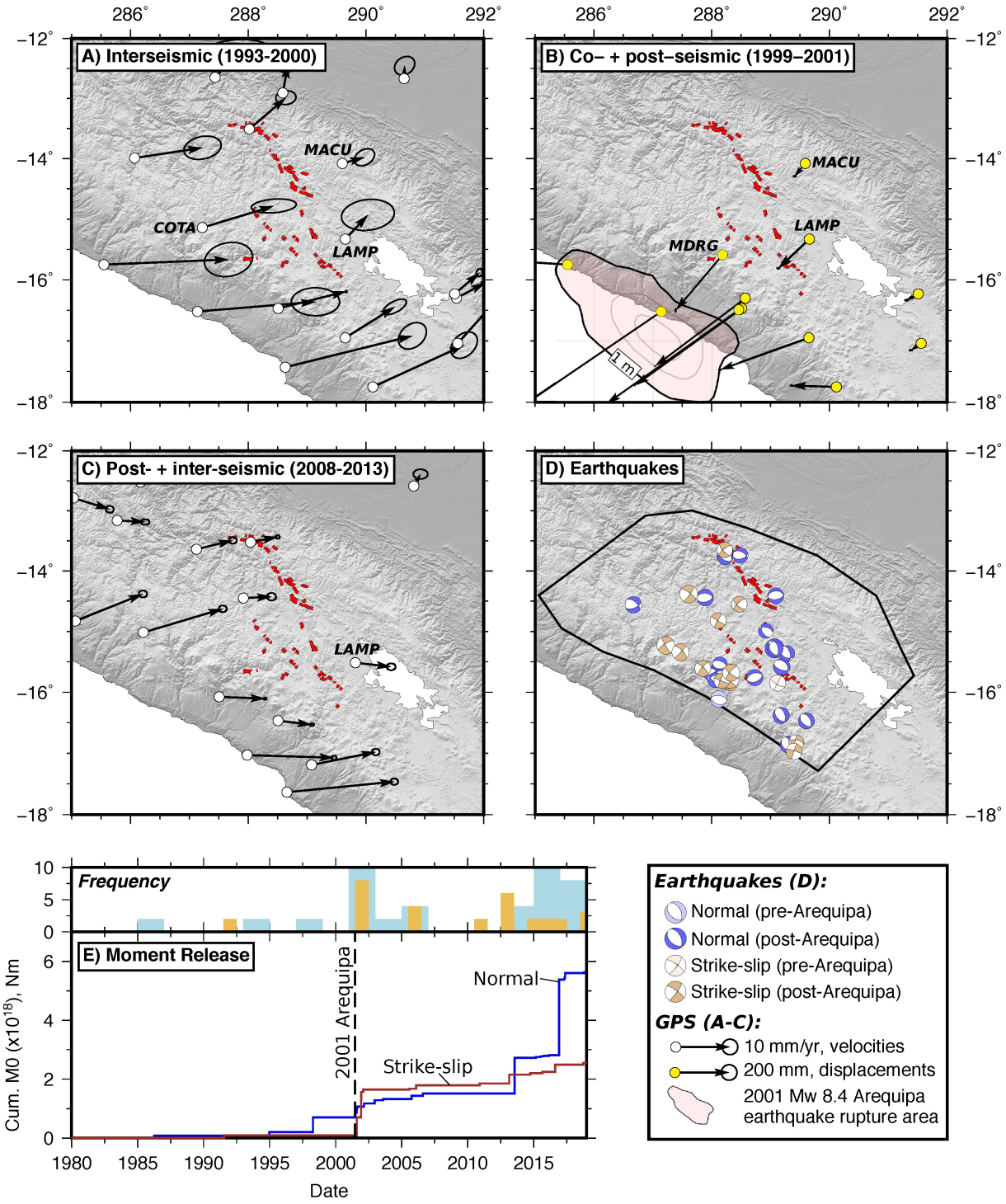

Figure 4.20 GPS, earthquake and active faulting evidence for transient strain in south Peru. (a) Interseismic GPS measurements of the velocity field between 1993-2000 from Kendrick et al. [2001]. All GPS measurements are given relative to stable South America. Red lines are the mapped normal faults. (b) Co- and early post-seismic displacements from Pritchard et al. [2007] capturing the deformation in the 2001 M_w 8.4 Arequipa earthquake. The 1 m (black), 3 m and 5 m (grey) coseismic slip contours for the Arequipa earthquake are taken from Chlieh et al. [2011]. The GPS measurements span June 1999 to October 2001. (c) Late post- and inter-seismic velocities measured by Villegas-Lanza et al. [2016] between 2008 and 2013. (d) Shallow (<50 km) earthquakes with $M_w > 4.5$ beneath the high Andes taken from the global CMT catalogue. (e) Cumulative moment release from earthquakes in the high Andes as a function of time, with all mechanisms shown in (d).

Coseismic and early postseismic slip on the megathrust in the 2001 Arequipa earthquake led to significant NE-SW extension across south Peru, reversing the interseismic motions at many of the re-occupied GPS stations (see LAMP in Fig. 4.20a,b). GPS measurements between MDRG and MACU, which span the Cusco-Lagunillas Faults, captured 216 mm of margin-normal extension between 1999 and 2001 (Fig. 4.20b). Over the same time period, the frequency and moment release from earthquakes in the high Andes increased (Fig. 4.20d), suggesting some fraction of this strain may be permanent.

Later in the postseismic period, between 2008 and 2013, the GPS velocities at all stations returned to pointing landward, with shortening concentrated between the coastal stations but no shortening strain within the high Andes (Fig. 4.20c). Differences in the azimuth of the GPS velocity vector at station LAMP measured before and after the Arequipa earthquake indicate that postseismic deformation was still ongoing in 2008-2013 (Fig. 4.20a,c). The largest normal-faulting earthquakes within the time-frame 1980-2019 occurred after this period, in 2013 and 2016, presumably whilst the strain rates in the plateau were small or neutral (Fig. 4.20d).

Normal-faulting earthquakes occurred in the high Andes both before, and after, the 2001 Arequipa earthquake, suggesting the shallow crust in the mountains remained in a state of deviatoric tension despite the transient compression due to elastic strain accumulation captured by the pre-2001 GPS measurements. However, the moment release from normal-faulting earthquakes increased significantly in the 18 years following the Arequipa earthquake. Therefore, although the transient compression was *not* large enough to switch the mountains from a state of extension to compression, it *may* have been large enough to temporarily suppress slip on the normal faults between Cusco and Lagunillas. During and following the megathrust earthquake the overriding plate was extended, relaxing the transient compression and unclamping the normal faults, causing them to rupture in earthquakes. As the effects of afterslip and visco-elastic relaxation wane and the subduction interface re-locks, it is expected that the high Andes will return to a state of transient compression probably in the next decade, leading to a decrease in the moment release rate from normal-faulting earthquakes. A sketch of the evolution of strain within the high Andes is shown in Fig. 4.21. Similar behaviour has been documented previously in the Nankai, Cascadia and Makran subduction zones [e.g. Wang, 2000; Penney et al., 2017].

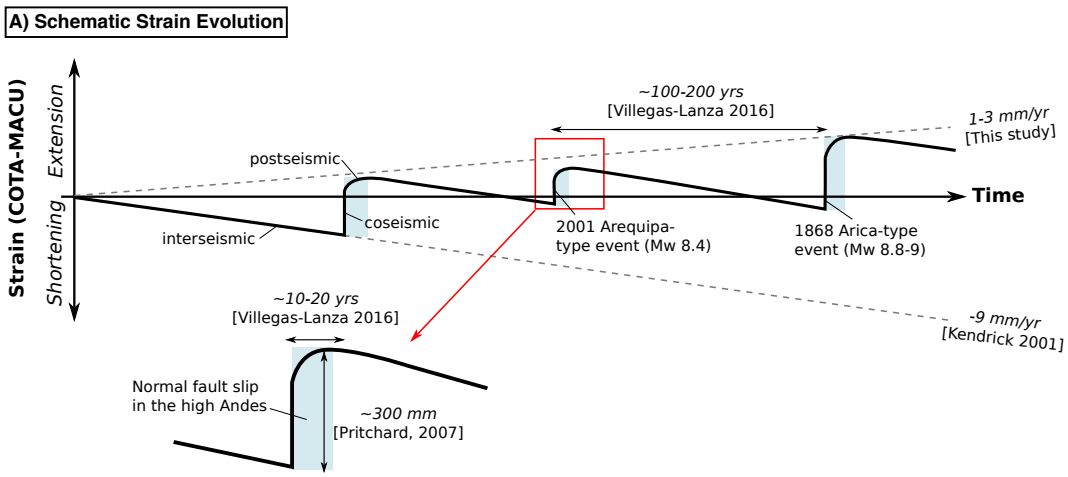

Figure 4.21 Sketch of the temporal evolution of strain between two GPS stations on the NE and SW margins of the high Andes in south Peru (MACU and COTA in Fig. 4.20a).

4.4 Conclusions

The high Andes of south Peru are extending by ∼1-3 mm/yr on a system of 10-20 km-long, right-stepping normal faults that trend NW-SE across the Altiplano plateau between Cusco and Lagunillas. The azimuth of the extension rotates clockwise from NNE-SSW near Cusco to NE-SW near Parina, which mirrors the rotation of thrust earthquake slip vectors in the sub-Andean foreland. Extension on these normal faults began probably in the last ∼1-5 Myrs and has reactivated a number of Miocene-age reverse faults. At the south-eastern end of the fault system, towards the Bolivian border, most of the faults reverse the local slope direction and are not associated with any large-amplitude topography, indicating they either have slow slip rates or only became recently active (<1 Ma). Extension in the last 5 Myr has followed an episode of shortening that ended in the late Miocene, suggesting that the forces acting on the Andes have changed. The extension rates on the Cusco-Lagunillas normal faults indicate that the average shear stresses transmitted across the sub-Andean detachment are likely to have decreased by ∼0.02-3 MPa, that is 0.1-30% of their absolute value. This result highlights the delicate balance of forces that controls the dynamics on the margins of mountain ranges and the faulting within their interiors.

Chapter 5

Concluding Remarks

This thesis has explored the stresses acting on faults, the rheological properties of faults and the implications of fault rheology on the dynamics of continental mountain building.

In Chapter 2, I presented calculations that indicate the limited postseismic slip following the 2003 Bam earthquake was caused by frictional locking on the fault zone adjacent to the coseismic rupture. As a result, it may be possible to use the postseismic to coseismic moment release ratio on a fault as a metric for the fraction of frictional locking. Particularly in regions with slow deformation rates, this type of analysis opens up new possibilities for assessing the frictional properties of a wider range of active faults. Following the launch of Sentinel-1A/B in 2014, there is now a long enough back-catalogue of SAR data to record postseismic transients with high spatial and temporal accuracy. The next stage in this research is to systematically compare the co- and post-seismic slip between earthquakes, including those with small postseismic transients that have previously been overlooked. Combining these observations with geophysical and geological evidence for the fluid conditions, loading rates and materials in fault zones may offer a more comprehensive way of deciphering what controls aseismic creep or seismogenic slip on natural faults.

The advent of quasi-dynamic and fully-dynamic models of fault slip also offers an exciting new opportunity to test the rheological properties of fault zones. In Chapter 2, I used stress-driven afterslip models to show that, following the Bam earthquake, kilometre-sized patches of the fault shouldering the coseismic rupture moved with $\lesssim$20 cm of afterslip, which partly overlapped with areas that moved with $\lesssim$1 m of coseismic slip. Robust evidence for the overlap of aseismic creep and seismogenic slip is rare, so the observations presented in Chapter 2 form an important contribution to the literature surrounding the slip behaviour on natural faults. In addition, I presented novel stress-driven afterslip calculations for the 'far-field' stresses acting on the fault system needed to explain the long-term growth of the ridge, in addition to the short-term postseismic InSAR measurements. I found that an E-W orientated 2-10 MPa deviatoric stress is likely to be compressing the fault system, driving thrust-orientated creep on the Bam-Baravat Fault. These small deviatoric stresses imply the creeping fault has an apparent effective friction $<$0.1, and is therefore weak compared to traditional views of fault strength.

Chapter 3 focused on the dynamical implications for the 2016 M_w 6.1 Parina normal-faulting earthquake in south Peru. The orientation and style of the faulting in the high Andes near Parina and the adjacent

forelands indicates that the horizontal forces resulting from spatial variations in gravitational potential energy are important in controlling the deformation. Using calculations for the magnitude of these forces, and calculations of the stresses generated by flexure, I showed that faults in the South American foreland must have an effective coefficient of friction $\mu' \lesssim 0.2$ and support average shear stresses $\lesssim$85-130 MPa. These results expand the range of natural examples where low effective friction along seismogenic faults have been recognised. However, the causes of such low effective friction on natural examples of both creeping (Chapter 2) and seismogenic (Chapter 3) faults remain enigmatic.

In order for the high Andes to be extending, the force balance acting on the mountain belt must have changed. In Chapter 3, I proposed that a reduction in the shear stresses acting along the margin of the eastern Andes due to failure of weak detachment horizons in the foreland basin is likely to have perturbed the local force balance. As a result, shortening stepped rapidly into the sub-Andean fold-thrust belt and extension began in the high Andes. As the thermal structure and sediment thickness in a foreland basin will evolve as a result of uplift of the mountain range along its margin, the deformation within a mountain belt is inherently coupled to the deformation along its margin. An intriguing future direction for dynamical models of continental mountain building should be to investigate the effects of foreland sediments on the temporal evolution of deformation in mountain ranges.

In Chapter 4, I studied the rate, kinematics and evolution of normal faulting in the high Andes of south Peru to place constraints on the changes to the forces acting on the mountain belt. I determined that a system of active normal faults trends NW-SE across the Altiplano plateau between Cusco and Lake Titicaca that have accommodated NNE-SSW to NE-SW extension at rates of $\sim$1-3 mm/yr over the last 1-5 Myrs. The rate and kinematics of the normal faults in south Peru indicated there has been a $\sim$0.02-3 MPa reduction in the average shear stresses transmitted across the sub-Andean detachment around $\sim$5 Ma. It is not clear what caused this change, but it could feasibly have been small perturbations to the intrinsic frictional properties, fluid pressures or temperature structure of the sub-Andean detachment. Nonetheless, these results highlight that the faulting within a mountain belt interior is highly sensitive to the rheological properties of faults along its margins.

Despite the geomorphological evidence for Quaternary extension across south Peru, the pattern of transient strain measured by GPS in the region prior to a M_w 8.4 megathrust earthquake in 2001 was shortening perpendicular to the normal faults. In Chapter 4, I inferred that the transient compressional stresses associated with elastic strain accumulation along the megathrust are significantly smaller than the deviatoric stresses acting to break the normal faults between Cusco and Lagunillas. However, there is evidence that transient compression may act to temporarily suppress normal-faulting seismicity, and following the megathrust earthquake, normal faults in the overriding plate may be more likely to rupture.

References

Allmann, B. P. and Shearer, P. M. (2009). Global variations of stress drop for moderate to large earthquakes. *Journal of Geophysical Research: Solid Earth*, 114(1):B01310.

Allmendinger, R. W., Smalley, R., Bevis, M., Caprio, H., and Brooks, B. (2005). Bending the Bolivian orocline in real time. *Geology*, 33(11):905–908.

Alvarado, P. and Beck, S. (2006). Source characterization of the San Juan (Argentina) crustal earthquakes of 15 January 1944 (Mw 7.0) and 11 June 1952 (Mw 6.8). *Earth and Planetary Science Letters*, 243(3-4):615–632.

Alvarado, P., Beck, S., Zandt, G., Araujo, M., Triep, E., Isacks, B. L., Araujo, M., Puebla, N. P., and Sistena, J. A. (2005). Crustal deformation in the south-central Andes backarc terranes as viewed from regional broad-band seismic waveform modelling. *Geophysical Journal International*, 163(2):580–598.

Ambraseys, N. N. and Melville, C. P. (2005). *A History of Persian Earthquakes*, volume 10. Cambridge University Press.

Armijo, R., Meyer, B., King, G. C., Rigo, A., and Papanastassiou, D. (1996). Quaternary evolution of the Corinth Rift and its implications for the Late Cenozoic evolution of the Aegean. *Geophysical Journal International*, 126(1):11–53.

Armijo, R., Tapponnier, P., Mercier, J. L., and Han, T.-L. (1986). Quaternary extension in southern Tibet: Field observations and tectonic implications. *Journal of Geophysical Research: Solid Earth*, 91(B14):13803–13872.

Artyushkov, E. V. (1973). Stresses in the lithosphere caused by crustal thickness inhomogeneities. *Journal of Geophysical Research*, 78(32):7675–7708.

Assumpção, M. (1992). The Regional Intraplate Stress Field in South America. *Journal of Geophysical Research: Solid Earth*, 87(11):11889–11903.

Assumpção, M. and Araujo, M. (1993). Effect of the Altiplano-Puna plateau, South America, on the regional intraplate stresses. *Tectonophysics*, 221(3-4):475–496.

Assumpção, M., Feng, M., Tassara, A., and Julià, J. (2013). Models of crustal thickness for South America from seismic refraction, receiver functions and surface wave tomography. *Tectonophysics*, 609:82–96.

Assumpção, M. and Suarez, G. (1988). Source mechanisms of moderate-size earthquakes and stress orientation in mid-plate South America. *Geophysical Journal International*, 92(2):253–267.

Atzori, S., Hunstad, I., Chini, M., Salvi, S., Tolomei, C., Bignami, C., Stramondo, S., Trasatti, E., Antonioli, A., and Boschi, E. (2009). Finite fault inversion of DInSAR coseismic displacement of the 2009 L'Aquila earthquake (central Italy). *Geophysical Research Letters*, 36(15):L15305.

Avouac, J.-P., Ayoub, F., Leprince, S., Konca, O., and Helmberger, D. V. (2006). The 2005, Mw 7.6 Kashmir earthquake: Sub-pixel correlation of ASTER images and seismic waveforms analysis. *Earth and Planetary Science Letters*, 249(3-4):514–528.

Avouac, J.-P., Meng, L., Wei, S., Wang, T., and Ampuero, J.-P. (2015). Lower edge of locked Main Himalayan Thrust unzipped by the 2015 Gorkha earthquake. *Nature Geoscience*, 8(9):708–711.

Avouac, J.-P. and Tapponnier, P. (1993). Kinematic model of active deformation in central Asia. *Geophysical Research Letters*, 20(10):895.

Baba, T., Hirata, K., Hori, T., and Sakaguchi, H. (2006). Offshore geodetic data conducive to the estimation of the afterslip distribution following the 2003 Tokachi-oki earthquake. *Earth and Planetary Science Letters*, 241(1-2):281–292.

Babeyko, A. Y., Sobolev, S. V., Vietor, T., Oncken, O., and Trumbull, R. B. (2006). Numerical Study of Weakening Processes in the Central Andean Back-Arc. In Oncken, O., editor, *The Andes - Active Subduction Orogeny*, pages 495–512. Springer Berlin Heidelberg.

Barbot, S. and Fialko, Y. (2010a). A unified continuum representation of post-seismic relaxation mechanisms: semi-analytic models of afterslip, poroelastic rebound and viscoelastic flow. *Geophysical Journal International*, 182(3):1124–1140.

Barbot, S. and Fialko, Y. (2010b). Fourier-domain Green's function for an elastic semi-infinite solid under gravity, with applications to earthquake and volcano deformation. *Geophysical Journal International*, 182(2):568–582.

Barbot, S., Fialko, Y., and Bock, Y. (2009). Postseismic deformation due to the Mw 6.0 2004 Parkfield earthquake: Stress-driven creep on a fault with spatially variable rate-and-state friction parameters. *Journal of Geophysical Research: Solid Earth*, 114(B7):B07405.

Barke, R. and Lamb, S. (2006). Late Cenozoic uplift of the Eastern Cordillera, Bolivian Andes. *Earth and Planetary Science Letters*, 249(3-4):350–367.

Barnhart, W. D., Murray, J. R., Briggs, R. W., Gomez, F., Miles, C. P. J., Svarc, J., Riquelme, S., and Stressler, B. J. (2016). Coseismic slip and early afterslip of the 2015 Illapel, Chile, earthquake: Implications for frictional heterogeneity and coastal uplift. *Journal of Geophysical Research: Solid Earth*, 121(8):6172–6191.

Barnhart, W. D., Murray, J. R., Yun, S., Svarc, J. L., Samsonov, S. V., Fielding, E. J., Brooks, B. A., and Milillo, P. (2015). Geodetic Constraints on the 2014 M 6.0 South Napa Earthquake. *Seismological Research Letters*, 86(2A):335–343.

Beck, S. L. and Zandt, G. (2002). The nature of orogenic crust in the central Andes. *Journal of Geophysical Research: Solid Earth*, 107(B10):ESE–7.

Béjar-Pizarro, M., Carrizo, D., Socquet, A., Armijo, R., Barrientos, S., Bondoux, F., Bonvalot, S., Campos, J., Comte, D., de Chabalier, J. B., Charade, O., Delorme, A., Gabalda, G., Galetzka, J., Genrich, J., Nercessian, A., Olcay, M., Ortega, F., Ortega, I., Remy, D., Ruegg, J. C., Simons, M., Valderas, C., and Vigny, C. (2010). Asperities and barriers on the seismogenic zone in North Chile: state-of-the-art after the 2007 Mw 7.7 Tocopilla earthquake inferred by GPS and InSAR data. *Geophysical Journal International*, 183(1):390–406.

Benavente, C., Delgado, F., Taipe, E., Audin, L., and Pari, W. (2013). Neotectonica y Peligro Sismico en el Region Cusco. Technical report, Instituto Geologico Minera y Metalurgico.

Benavente, C., Zerathe, S., Audin, L., Hall, S. R., Robert, X., Delgado, F., Carcaillet, J., and Team, A. (2017). Active transpressional tectonics in the Andean forearc of southern Peru quantified by 10-Be surface exposure dating of an active fault scarp. *Tectonics*, 36(9):1662–1678.

Bendick, R., Bilham, R., Khan, M. A., and Khan, S. F. (2007). Slip on an active wedge thrust from geodetic observations of the 8 October 2005 Kashmir earthquake. *Geology*, 35(3):267.

Berardino, P., Fornaro, G., Lanari, R., and Sansosti, E. (2002). A new algorithm for surface deformation monitoring based on small baseline differential SAR interferograms. *IEEE Transactions on Geoscience and Remote Sensing*, 40(11):2375–2383.

Berberian, M. (1976). Quaternary Faults in Iran. Technical report, Geological Survery of Iran.

Berberian, M. (2005). The 2003 Bam Urban Earthquake: A Predictable Seismotectonic Pattern Along the Western Margin of the Rigid Lut Block, Southeast Iran. *Earthquake Spectra*, 21(S1):35–99.

Berberian, M. (2014). *Earthquakes and Coseismic Surface Faulting on the Iranian Plateau*. Elsevier Science.

Berberian, M., Jackson, J. A., Fielding, E., Parsons, B. E., Priestley, K., Qorashi, M., Talebian, M., Walker, R., Wright, T. J., and Baker, C. (2001). The 1998 March 14 Fandoqa earthquake (Mw 6.6) in Kerman province, southeast Iran: re-rupture of the 1981 Sirch earthquake fault, triggering of slip on adjacent thrusts and the active tectonics of the Gowk fault zone. *Geophysical Journal International*, 146(2):371–398.

Berberian, M., Jackson, J. A., Qorashi, M., Talebian, M., Khatib, M., and Priestley, K. (2000). The 1994 Sefidabeh earthquakes in eastern Iran: blind thrusting and bedding-plane slip on a growing anticline, and active tectonics of the Sistan suture zone. *Geophysical Journal International*, 142(2):283–299.

Bevis, M., Kendrick, E., Smalley, R., Brooks, B., Allmendinger, R., and Isacks, B. (2001). On the strength of interplate coupling and the rate of back arc convergence in the central Andes: An analysis of the interseismic velocity field. *Geochemistry, Geophysics, Geosystems*, 2(11).

Bevis, M. and Martel, S. J. (2001). Oblique plate convergence and interseismic strain accumulation. *Geochemistry Geophysics Geosystems*, 2(8).

Bie, L., Ryder, I., Nippress, S. E. J., and Burgmann, R. (2014). Coseismic and post-seismic activity associated with the 2008 Mw 6.3 Damxung earthquake, Tibet, constrained by InSAR. *Geophysical Journal International*, 196(2):788–803.

Biggs, J., Wright, T., Lu, Z., and Parsons, B. (2007). Multi-interferogram method for measuring interseismic deformation: Denali Fault, Alaska. *Geophysical Journal International*, 170(3):1165–1179.

Bilham, R. (2019). Himalayan earthquakes: a review of historical seismicity and early 21st century slip potential. *Geological Society of London, Special Publications*, 483:SP483.16.

Binet, R. and Bollinger, L. (2005). Horizontal coseismic deformation of the 2003 Bam (Iran) earthquake measured from SPOT-5 THR satellite imagery. *Geophysical Research Letters*, 32(2):L02307.

Bird, P. (1978). Finite element modeling of lithosphere deformation: The Zagros collision orogeny. *Tectonophysics*, 50(2-3):307–336.

Blanpied, M. L., Lockner, D. A., and Byerlee, J. D. (1995). Frictional slip of granite at hydrothermal conditions. *Journal of Geophysical Research: Solid Earth*, 100(B7):13045–13064.

Bodin, P. and Horton, S. (2004). Source Parameters and Tectonic Implications of Aftershocks of the Mw 7.6 Bhuj Earthquake of 26 January 2001. *Bulletin of the Seismological Society of America*, 94(3):818–827.

Bouhifd, M., Andrault, D., Fiquet, G., and Richet, P. (1996). Thermal expansion of forsterite up to the melting point. *Geophysical Research Letters*, 23(10):1143–1146.

Brace, W. F. and Kohlstedt, D. L. (1980). Limits on lithospheric stress imposed by laboratory experiments. *Journal of Geophysical Research: Solid Earth*, 85(B11):6248–6252.

Briggs, R. W., Sieh, K., Meltzner, A. J., Natawidjaja, D., Galetzka, J., Suwargadi, B., Hsu, Y.-J., Simons, M., Hananto, N., Suprihanto, I., Prayudi, D., Avouac, J.-P., Prawirodirdjo, L., and Bock, Y. (2006). Deformation and slip along the Sunda megathrust in the great 2005 Nias-Simeulue earthquake. *Science*, 311(5769):1897–901.

Brune, J. N. (1968). Seismic moment, seismicity, and rate of slip along major fault zones. *Journal of Geophysical Research*, 73(2):777–784.

Burchfiel, B. C., Zhiliang, C., Hodges, K. V., Yuping, L., Royden, L. H., Changrong, D., and Jiene, X. (1992). The South Tibetan Detachment System, Himalayan Orogen: Extension Contemporaneous With and Parallel to Shortening in a Collisional Mountain Belt. In *The South Tibetan Detachment System, Himalayan Orogen: Extension Contemporaneous With and Parallel to Shortening in a Collisional Mountain Belt*, pages 1–41. Geological Society of America.

Bürgmann, R. and Dresen, G. (2008). Rheology of the Lower Crust and Upper Mantle: Evidence from Rock Mechanics, Geodesy, and Field Observations. *Annual Review of Earth and Planetary Sciences*, 36:531–567.

Burov, E. B. and Watts, a. B. (2006). The long-term strength of continental lithosphere: "jelly sandwich" or "crème brûlée"? *GSA Today*, 16(1):4–10.

Byerlee, J. (1978). Friction of rocks. *Pure and Applied Geophysics*, 116(4-5):615–626.

Cabrera, J. and Sebrier, M. (1998). Surface Rupture Associated with a 5.3 mb Earthquake: The 5 April 1986 Cuzco Earthquake and Kinematics of the Chincheros-Qoricocha Faults of the High Andes, Peru. *Bulletin of the Seismological Society of America*, 88(1):242–255.

Cabrera, J., Sébrier, M., and Mercier, J. L. (1991). Plio-Quaternary geodynamic evolution of a segment of the Peruvian Andean Cordillera located above the change in the subduction geometry: the Cuzco region. *Tectonophysics*, 190(2-4):331–362.

Çakir, Z., de Chabalier, J.-B., Armijo, R., Meyer, B., Barka, A., and Peltzer, G. (2003). Coseismic and early post-seismic slip associated with the 1999 Izmit earthquake (Turkey), from SAR interferometry and tectonic field observations. *Geophysical Journal International*, 155(1):93–110.

Candela, T., Renard, F., Bouchon, M., Brouste, A., Marsan, D., Schmittbuhl, J., and Voisin, C. (2009). Characterization of Fault Roughness at Various Scales: Implications of Three-Dimensional High Resolution Topography Measurements. *Pure and Applied Geophysics*, 166(10-11):1817–1851.

Carlier, G., Lorand, J. P., Liégeois, J. P., Fornari, M., Soler, P., Carlotto, V., and Cárdenas, J. (2005). Potassic-ultrapotassic mafic rocks delineate two lithospheric mantle blocks beneath the southern Peruvian Altiplano. *Geology*, 33(7):601–604.

Carlotto, V. (2013). Paleogeographic and tectonic controls on the evolution of Cenozoic basins in the Altiplano and Western Cordillera of southern Peru. *Tectonophysics*, 589:195–219.

Carlotto, V. and Cardenas, J. (2008). Mapa Geologico del Cuadrangulo de Ocuviri Escala 1:50,000 Hoja 31-u Cuadrante III.

Carlotto, V. and Cardenas, J. (2009). Mapa Geologico del Cuadrangulo de Ocuviri Escala 1:50,000 Hoja 31-u Cuadrante IV.

Carlotto, V., Mejia, R. R., and Mena, M. O. (2009). Mapa Geologico del Cuadrangulo del Cusco Escala 1:50,000 Hoja 28-s Cuadrante II.

Carlotto, V., Mejia, R. R., and Mena, M. O. (2010). Mapa Geologico del Cuadrangulo del Cusco Escala 1:50,000 Hoja 28-vs Cuadrante IV.

Carlotto, V. and Roque, J. C. (2009). Mapa Geologico del Cuadrangulo de Sicuani Escala 1:50,000 Hoja 29-t Cuadrante II.

Cetin, E., Meghraoui, M., Cakir, Z., Akoglu, A. M., Mimouni, O., and Chebbah, M. (2012). Seven years of postseismic deformation following the 2003 Mw = 6.8 Zemmouri earthquake (Algeria) from InSAR time series. *Geophysical Research Letters*, 39(10):L10307.

Chang, S.-H., Avouac, J.-P., Barbot, S., and Lee, J.-C. (2013). Spatially variable fault friction derived from dynamic modeling of aseismic afterslip due to the 2004 Parkfield earthquake. *Journal of Geophysical Research: Solid Earth*, 118(7):3431–3447.

Chapman, C. H. (1978). A new method for computing synthetic seismograms. *Geophysical Journal International*, 54(3):481–518.

Cheloni, D., D'Agostino, N., D'Anastasio, E., Avallone, A., Mantenuto, S., Giuliani, R., Mattone, M., Calcaterra, S., Gambino, P., Dominici, D., Radicioni, F., and Fastellini, G. (2010). Coseismic and initial post-seismic slip of the 2009 Mw 6.3 L'Aquila earthquake, Italy, from GPS measurements. *Geophysical Journal International*, 181(3):1539–1546.

Chen, C. W. and Zebker, H. A. (2001). Two-dimensional phase unwrapping with use of statistical models for cost functions in nonlinear optimization. *Journal of the Optical Society of America A*, 18(2):338.

Cheng, L.-W., Lee, J.-C., Hu, J.-C., and Chen, H.-Y. (2009). Coseismic and postseismic slip distribution of the 2003 Mw=6.5 Chengkung earthquake in eastern Taiwan: Elastic modeling from inversion of GPS data. *Tectonophysics*, 466(3):335–343.

Ching, K.-E., Rau, R.-J., and Zeng, Y. (2007). Coseismic source model of the 2003 Mw 6.8 Chengkung earthquake, Taiwan, determined from GPS measurements. *Journal of Geophysical Research: Solid Earth*, 112(B6):B06422.

Chinn, D. S. and Isacks, B. L. (1983). Accurate source depths and focal mechanisms of shallow earthquakes in western South America and in the New Hebrides Island Arc. *Tectonics*, 2(6):529–563.

Chlieh, M., Avouac, J.-P., Hjorleifsdottir, V., Song, T.-R. A., Ji, C., Sieh, K., Sladen, A., Hebert, H., Prawirodirdjo, L., Bock, Y., and Galetzka, J. (2007). Coseismic Slip and Afterslip of the Great Mw 9.15 Sumatra-Andaman Earthquake of 2004. *Bulletin of the Seismological Society of America*, 97(1A):S152–S173.

Chlieh, M., de Chabalier, J. B., Ruegg, J. C., Armijo, R., Dmowska, R., Campos, J., and Feigl, K. L. (2004). Crustal deformation and fault slip during the seismic cycle in the North Chile subduction zone, from GPS and InSAR observations. *Geophysical Journal International*, 158(2):695–711.

Chlieh, M., Perfettini, H., Tavera, H., Avouac, J.-P., Remy, D., Nocquet, J.-M., Rolandone, F., Bondoux, F., Gabalda, G., and Bonvalot, S. (2011). Interseismic coupling and seismic potential along the Central Andes subduction zone. *Journal of Geophysical Research: Solid Earth*, 116(B12):B12405.

Cladouhos, T. T., Allmendinger, R. W., Coira, B., and Farrar, E. (1994). Late cenozoic deformation in the Central Andes: fault kinematics from the northern Puna, northwestern Argentina and southwestern Bolivia. *Journal of South American Earth Sciences*, 7(2):209–228.

Clapperton, C. (1983). The glaciation of the Andes. *Quaternary Science Reviews*, 2(2-3):83–155.

Clark, P. U., Dyke, A. S., Shakun, J. D., Carlson, A. E., Clark, J., Wohlfarth, B., Mitrovica, J. X., Hostetler, S. W., and McCabe, A. M. (2009). The Last Glacial Maximum. *Science*, 325(5941):710–714.

Cochran, E. S., Li, Y.-G., Shearer, P. M., Barbot, S., Fialko, Y., and Vidale, J. E. (2009). Seismic and geodetic evidence for extensive, long-lived fault damage zones. *Geology*, 37(4):315–318.

Collettini, C., Niemeijer, A., Viti, C., and Marone, C. (2009). Fault zone fabric and fault weakness. *Nature*, 462(7275):907–910.

Copley, A. (2008). Kinematics and dynamics of the southeastern margin of the Tibetan Plateau. *Geophysical Journal International*, 174(3):1081–1100.

Copley, A. (2014). Postseismic afterslip 30 years after the 1978 Tabas-e-Golshan (Iran) earthquake: observations and implications for the geological evolution of thrust belts. *Geophysical Journal International*, 197(2):665–679.

Copley, A. (2017). The strength of earthquake-generating faults. *Journal of the Geological Society*, 174.

Copley, A., Avouac, J.-P., Hollingsworth, J., and Leprince, S. (2011a). The 2001 Mw 7.6 Bhuj earthquake, low fault friction, and the crustal support of plate driving forces in India. *Journal of Geophysical Research: Solid Earth*, 116(B8):B08405.

Copley, A., Avouac, J.-P., and Wernicke, B. P. (2011b). Evidence for mechanical coupling and strong Indian lower crust beneath southern Tibet. *Nature*, 472(7341):79–81.

Copley, A., Boait, F., Hollingsworth, J., Jackson, J., and McKenzie, D. (2009). Subparallel thrust and normal faulting in Albania and the roles of gravitational potential energy and rheology contrasts in mountain belts. *Journal of Geophysical Research: Solid Earth*, 114(B5):B05407.

Copley, A., Grützner, C., Howell, A., Jackson, J., Penney, C., and Wimpenny, S. (2018). Unexpected earthquake hazard revealed by Holocene rupture on the Kenchreai Fault (central Greece): Implications for weak sub-fault shear zones. *Earth and Planetary Science Letters*, 486:141–154.

Copley, A., Hollingsworth, J., and Bergman, E. (2012). Constraints on fault and lithosphere rheology from the coseismic slip and postseismic afterslip of the 2006 M w 7.0 Mozambique earthquake. *Journal of Geophysical Research: Solid Earth*, 117(B3):B03404.

Copley, A. and Jolivet, R. (2016). Fault rheology in an aseismic fold-thrust belt (Shahdad, eastern Iran). *Journal of Geophysical Research: Solid Earth*, 121(1):412–431.

Copley, A., Karasozen, E., Oveisi, B., Elliott, J. R., Samsonov, S., and Nissen, E. (2015). Seismogenic faulting of the sedimentary sequence and laterally variable material properties in the Zagros Mountains (Iran) revealed by the August 2014 Murmuri (E. Dehloran) earthquake sequence. *Geophysical Journal International*, 203(2):1436–1459.

Copley, A. and McKenzie, D. (2007). Models of crustal flow in the India-Asia collision zone. *Geophysical Journal International*, 169(2):683–698.

Copley, A. and Reynolds, K. (2014). Imaging topographic growth by long-lived postseismic afterslip at Sefidabeh, east Iran. *Tectonics*, 33:1–16.

Copley, A. and Woodcock, N. (2016). Estimates of fault strength from the Variscan foreland of the northern UK. *Earth and Planetary Science Letters*, 451:108–113.

Craig, T. J. and Copley, A. (2018). Forearc collapse, plate flexure, and seismicity within the downgoing plate along the Sunda Arc west of Sumatra. *Earth and Planetary Science Letters*, 484:81–91.

Craig, T. J., Copley, A., and Jackson, J. A. (2012). Thermal and tectonic consequences of India underthrusting Tibet. *Earth and Planetary Science Letters*, 353-354:231–239.

Craig, T. J., Copley, A., and Middleton, T. A. (2014). Constraining fault friction in oceanic lithosphere using the dip angles of newly-formed faults at outer rises. *Earth and Planetary Science Letters*, 392:94–99.

Craig, T. J., Jackson, J. A., Priestley, K., and McKenzie, D. (2011). Earthquake distribution patterns in Africa: their relationship to variations in lithospheric and geological structure, and their rheological implications. *Geophysical Journal International*, 185(1):403–434.

D'Agostino, N., Cheloni, D., Fornaro, G., Giuliani, R., and Reale, D. (2012). Space-time distribution of afterslip following the 2009 L'Aquila earthquake. *Journal of Geophysical Research: Solid Earth*, 117(B2):B02402.

D'Agostino, N., England, P., Hunstad, I., and Selvaggi, G. (2014). Gravitational potential energy and active deformation in the Apennines. *Earth and Planetary Science Letters*, 397:121–132.

D'Agostino, N., Jackson, J. A., Dramis, F., and Funiciello, R. (2001). Interactions between mantle upwelling, drainage evolution and active normal faulting: An example from the Central Appennines (Italy). *Geophysical Journal International*, 147(2):475–497.

Dalmayrac, B. and Molnar, P. (1981). Parallel thrust and normal faulting in Peru and constraints on the state of stress. *Earth and Planetary Science Letters*, 55(3):473–481.

D'Arcy, M., Schildgen, T. F., Strecker, M. R., Wittmann, H., Duesing, W., Mey, J., Tofelde, S., Weissmann, P., and Alonso, R. N. (2019). Timing of past glaciation at the Sierra de Aconquija, northwestern Argentina, and throughout the Central Andes. *Quaternary Science Reviews*, 204:37–57.

Dart, C., Cohen, H. A., Akyuz, H. S., and Barka, A. (1995). Basinward migration of rift-border faults: implications for facies distributions and preservation potential. *Geology*, 23(1):69–72.

Daxberger, H. and Riller, U. (2015). Kinematics of Neogene to Recent upper-crustal deformation in the southern Central Andes (23-28S) inferred from fault-slip analysis: Evidence for gravitational spreading of the Puna Plateau. *Tectonophysics*, 642(1):16–28.

de Michele, M., Raucoules, D., Aochi, H., Baghdadi, N., and Carnec, C. (2008). Measuring coseismic deformation on the northern segment of the Bam-Baravat escarpment associated with the 2003 Bam (Iran) earthquake, by correlation of very-high-resolution satellite imagery. *Geophysical Journal International*, 173(2):459–464.

Delouis, B., Vallée, M., Meghraoui, M., Calais, E., Maouche, S., Lammali, K., Mahsas, A., Briole, P., Benhamouda, F., and Yelles, K. (2004). Slip distribution of the 2003 Boumerdes-Zemmouri earthquake, Algeria, from teleseismic, GPS, and coastal uplift data. *Geophysical Research Letters*, 31(18):L18607.

DeMets, C., Gordon, R. G., Argus, D. F., Watkins, M. M., Webb, F. H., Jago, J. B., Piana, E., and Schlich, R. (2010). Geologically current plate motions. *Geophysical Journal International*, 181(1):1–80.

Devlin, S., Isacks, B. L., Pritchard, M. E., Barnhart, W. D., and Lohman, R. B. (2012). Depths and focal mechanisms of crustal earthquakes in the central Andes determined from teleseismic waveform analysis and InSAR. *Tectonics*, 31(2):1–33.

Dieterich, J. H. (1978). Time-dependent friction and the mechanics of stick-slip. *Pure and Applied Geophysics*, 116(4-5):790–806.

Donnellan, A. and Lyzenga, G. A. (1998). GPS observations of fault afterslip and upper crustal deformation following the Northridge earthquake. *Journal of Geophysical Research: Solid Earth*, 103(B9):21285–21297.

Dorbath, C. (1996). Velocity structure of the Andes of central Peru from locally recorded earthquakes. *Geophysical Research Letters*, 23(2):205–208.

Doser, D. I. (1987). The Ancash, Peru, earthquake of 1946 November 10: evidence for low-angle normal faulting in the high Andes of northern Peru. *Geophysical Journal International*, 91(1):57–71.

Dreger, D. S., Huang, M., Rodgers, A., Taira, T., and Wooddell, K. (2015). Kinematic Finite-Source Model for the 24 August 2014 South Napa, California, Earthquake from Joint Inversion of Seismic, GPS, and InSAR Data. *Seismological Research Letters*, 86(2A):327–334.

Dziewonski, A. M., Chou, T.-A., and Woodhouse, J. H. (1981). Determination of earthquake source parameters from waveform data for studies of global and regional seismicity. *Journal of Geophysical Research: Solid Earth*, 86(B4):2825–2852.

Echavarria, L., Hernández, R., Allmendinger, R., and Reynolds, J. (2003). Subandean thrust and fold belt of northwestern Argentina: Geometry and timing of the Andean evolution. *AAPG Bulletin*, 87(6):965–985.

Ekström, G., Nettles, M., and Dziewoński, A. (2012). The global CMT project 2004–2010: Centroid-moment tensors for 13,017 earthquakes. *Physics of the Earth and Planetary Interiors*, 200:1–9.

Elger, K., Oncken, O., and Glodny, J. (2005). Plateau-style accumulation of deformation: Southern Altiplano. *Tectonics*, 24(4):1–19.

Elliott, J. R., Parsons, B., Jackson, J. A., Shan, X., Sloan, R. A., and Walker, R. T. (2011). Depth segmentation of the seismogenic continental crust: The 2008 and 2009 Qaidam earthquakes. *Geophysical Research Letters*, 38(6):L06305.

Elliott, J. R., Walters, R. J., England, P. C., Jackson, J. A., Li, Z., and Parsons, B. (2010). Extension on the Tibetan plateau: Recent normal faulting measured by InSAR and body wave seismology. *Geophysical Journal International*, 183(2):503–535.

Ellison, R., Klinck, B., and Hawkins, M. (1989). Deformation events in the Andean orogenic cycle in the Altiplano and Western Cordillera, southern Peru. *Journal of South American Earth Sciences*, 2(3):263–276.

Emmerson, B. (2007). *The relationship between intraplate earthquakes and temperature*. PhD thesis, University of Cambridge.

Engdahl, E. R., Jackson, J. A., Myers, S. C., Bergman, E. A., and Priestley, K. (2006). Relocation and assessment of seismicity in the Iran region. *Geophysical Journal International*, 167(2):761–778.

Engdahl, E. R., van der Hilst, R., and Buland, R. (1998). Global Teleseismic Earthquake Relocation with Improved Travel Times and Procedures for Depth Determination. *Bulletin of the Seismological Society of America*, 88(3):722–743.

England, P. (2018). On Shear Stresses, Temperatures, and the Maximum Magnitudes of Earthquakes at Convergent Plate Boundaries. *Journal of Geophysical Research: Solid Earth*, 123(8):7165–7202.

England, P. and Houseman, G. (1989). Extension during continental convergence, with application to the Tibetan Plateau. *Journal of Geophysical Research*, 94(B12):17561.

England, P. and McKenzie, D. (1982). A thin viscous sheet model for continental deformation. *Geophysical Journal International*, 70(2):295–321.

England, P. and Molnar, P. (1997a). Active Deformation of Asia: From Kinematics to Dynamics. *Science*, 278(5338):647–650.

England, P. and Molnar, P. (1997b). The field of crustal velocity in Asia calculated from Quaternary rates of slip on faults. *Geophysical Journal International*, 130(3):551–582.

England, P. and Molnar, P. (2015). Rheology of the lithosphere beneath the central and western Tien Shan. *Journal of Geophysical Research: Solid Earth*, 120(5):3803–3823.

England, P. C., Houseman, G. A., Osmaston, M. F., and Ghosh, S. (1988). The Mechanics of the Tibetan Plateau [and Discussion]. *Philosophical Transactions of the Royal Society A: Mathematical, Physical and Engineering Sciences*, 326(1589):301–320.

Ericksen, G. E., Fernandez Concha, J., and Silgado, E. (1954). The Cusco, Peru, Earthquake of May 21 1950. *Bulletin of the Seismological Society of America*, 44(2A):97–112.

Espurt, N., Brusset, S., Baby, P., Hermoza, W., Bolaños, R., Uyen, D., and Déramond, J. (2008). Paleozoic structural controls on shortening transfer in the Subandean foreland thrust sytem, Ene and southern Ucayali basins, Peru. *Tectonics*, 27(3):1–21.

Farr, T. G., Rosen, P. A., Caro, E., Crippen, R., Duren, R., Hensley, S., Kobrick, M., Paller, M., Rodriguez, E., Roth, L., Seal, D., Shaffer, S., Shimada, J., Umland, J., Werner, M., Oskin, M., Burbank, D., and Alsdorf, D. (2007). The Shuttle Radar Topography Mission. *Reviews of Geophysics*, 45(2):RG2004.

Fattahi, H., Amelung, F., Chaussard, E., and Wdowinski, S. (2015). Coseismic and postseismic deformation due to the 2007 M 5.5 Ghazaband fault earthquake, Balochistan, Pakistan. *Geophysical Research Letters*, 42(9):3305–3312.

Fattahi, M., Walker, R., Hollingsworth, J., Bahroudi, A., Nazari, H., Talebian, M., Armitage, S., and Stokes, S. (2006). Holocene slip-rate on the Sabzevar thrust fault, NE Iran, determined using optically stimulated luminescence (OSL). *Earth and Planetary Science Letters*, 245(3):673–684.

Feigl, K. L., Sarti, F., Vadon, H., McClusky, S., Ergintav, S., Durand, P., Bürgmann, R., Rigo, A., Massonnet, D., and Reilinger, R. (2002). Estimating Slip Distribution for the Izmit Mainshock from Coseismic GPS, ERS-1, RADARSAT, and SPOT Measurements. *Bulletin of the Seismological Society of America*, 92(1):138–160.

Feng, G., Hetland, E. A., Ding, X., Li, Z., and Zhang, L. (2010). Coseismic fault slip of the 2008 Mw 7.9 Wenchuan earthquake estimated from InSAR and GPS measurements. *Geophysical Research Letters*, 37(1):L01302.

Fialko, Y., Sandwell, D., Agnew, D., Simons, M., Shearer, P., and Minster, B. (2002). Deformation on nearby faults induced by the 1999 Hector Mine earthquake. *Science*, 297(5588):1858–62.

Fialko, Y., Sandwell, D., Simons, M., and Rosen, P. (2005). Three-dimensional deformation caused by the Bam, Iran, earthquake and the origin of shallow slip deficit. *Nature*, 435(7040):295–299.

Fielding, E. J., Lundgren, P. R., Bürgmann, R., and Funning, G. J. (2009). Shallow fault-zone dilatancy recovery after the 2003 Bam earthquake in Iran. *Nature*, 458(7234):64–68.

Fielding, E. J., Sladen, A., Li, Z., Avouac, J.-P., Burgmann, R., and Ryder, I. (2013). Kinematic fault slip evolution source models of the 2008 M7.9 Wenchuan earthquake in China from SAR interferometry, GPS and teleseismic analysis and implications for Longmen Shan tectonics. *Geophysical Journal International*, 194(2):1138–1166.

Flesch, L. M., Haines, A. J., and Holt, W. E. (2001). Dynamics of the India-Eurasia collision zone. *Journal of Geophysical Research: Solid Earth*, 106(B8):16435–16460.

Flesch, L. M. and Kreemer, C. (2010). Gravitational potential energy and regional stress and strain rate fields for continental plateaus: Examples from the central Andes and Colorado Plateau. *Tectonophysics*, 482(1-4):182–192.

Floyd, M. A., Walters, R. J., Elliott, J. R., Funning, G. J., Svarc, J. L., Murray, J. R., Hooper, A. J., Larsen, Y., Marinkovic, P., Bürgmann, R., Johanson, I. A., and Wright, T. J. (2016). Spatial variations in fault friction related to lithology from rupture and afterslip of the 2014 South Napa, California, earthquake. *Geophysical Research Letters*, 43(13):6808–6816.

Fraser, C. S. and Hanley, H. B. (2005). Bias-compensated RPCs for Sensor Orientation of High-resolution Satellite Imagery. *Photogrammetric Engineering & Remote Sensing*, 71(8):909–915.

Freed, A. M. (2007). Afterslip (and only afterslip) following the 2004 Parkfield, California, earthquake. *Geophysical Research Letters*, 34(6):L06312.

Freed, A. M. and Bürgmann, R. (2004). Evidence of power-law flow in the Mojave desert mantle. *Nature*, 430(6999):548–551.

Froidevaux, C. and Isacks, B. L. (1984). The mechanical state of the lithosphere in the Altiplano-Puna segment of the Andes. *Earth and Planetary Science Letters*, 71(2):305–314.

Fu, B., Ninomiya, Y., Lei, X., Toda, S., and Awata, Y. (2004). Mapping active fault associated with the 2003 Mw 6.6 Bam (SE Iran) earthquake with ASTER 3D images. *Remote Sensing of Environment*, 92(2):153–157.

Fukushima, Y., Toda, S., Miura, S., Ishimura, D., Fukuda, J., Demachi, T., and Tachibana, K. (2018). Extremely early recurrence of intraplate fault rupture following the Tohoku-Oki earthquake. *Nature Geoscience*, 11(10):777–781.

Funning, G. J., Barke, R. M. D., Lamb, S. H., Minaya, E., Parsons, B., and Wright, T. J. (2005a). The 1998 Aiquile, Bolivia earthquake: A seismically active fault revealed with InSAR. *Earth and Planetary Science Letters*, 232(1-2):39–49.

Funning, G. J., Parsons, B., Wright, T. J., Jackson, J. A., and Fielding, E. J. (2005b). Surface displacements and source parameters of the 2003 Bam (Iran) earthquake from Envisat advanced synthetic aperture radar imagery. *Journal of Geophysical Research: Solid Earth*, 110(B9):B09406.

Furuya, M. and Satyabala, S. P. (2008). Slow earthquake in Afghanistan detected by InSAR. *Geophysical Research Letters*, 35(6):L06309.

Gao, X. and Wang, K. (2014). Strength of stick-slip and creeping subduction megathrusts from heat flow observations. *Science*, 345(6200):1038–1041.

Garzione, C. N., DeCelles, P. G., Hodkinson, D. G., Ojha, T. P., and Upreti, B. N. (2003). East-west extension and miocene environmental change in the southern Tibetan plateau: Thakkhola graben, central Nepal. *Bulletin of the Geological Society of America*, 115(1):3–20.

Garzione, C. N., Hoke, G. D., Libarkin, J. C., Withers, S., MacFadden, B., Eiler, J., Ghosh, P., and Mulch, A. (2008). Rise of the Andes. *Science*, 320(5881):1304–1307.

Garzione, C. N., McQuarrie, N., Perez, N. D., Ehlers, T. A., Beck, S. L., Kar, N., Eichelberger, N., Chapman, A. D., Ward, K. M., Ducea, M. N., Lease, R. O., Poulsen, C. J., Wagner, L. S., Saylor, J. E., Zandt, G., and Horton, B. K. (2017). Tectonic Evolution of the Central Andean Plateau and Implications for the Growth of Plateaus. *Annual Review of Earth and Planetary Sciences*, 45:529–559.

Garzione, C. N., Molnar, P., Libarkin, J. C., and MacFadden, B. J. (2006). Rapid late Miocene rise of the Bolivian Altiplano: Evidence for removal of mantle lithosphere. *Earth and Planetary Science Letters*, 241(3-4):543–556.

Gautheron, C., Espurt, N., Barbarand, J., Roddaz, M., Baby, P., Brusset, S., Tassan-Got, L., and Douville, E. (2013). Direct dating of thick- and thin-skin thrusts in the Peruvian Subandean zone through apatite (U-Th)/He and fission track thermochronometry. *Basin Research*, 25(4):419–435.

Giovanni, M. K., Horton, B. K., Garzione, C. N., McNulty, B., and Grove, M. (2010). Extensional basin evolution in the Cordillera Blanca, Peru: Stratigraphic and isotopic records of detachment faulting and orogenic collapse in the Andean hinterland. *Tectonics*, 29(6):1–21.

Goetze, C. and Evans, B. (1979). Stress and temperature in the bending lithosphere as constrained by experimental rock mechanics. *Geophysical Journal of the Royal Astronomical Society*, 59(3):463–478.

Goldstein, R. M. and Werner, C. L. (1998). Radar interferogram filtering for geophysical applications. *Geophysical Research Letters*, 25(21):4035–4038.

Goldstein, R. M., Zebker, H. A., and Werner, C. L. (1988). Satellite radar interferometry: Two-dimensional phase unwrapping. *Radio Science*, 23(4):713–720.

Goldsworthy, M. and Jackson, J. A. (2000). Active normal fault evolution in Greece revealed by geomorphology and drainage patterns. *Journal of the Geological Society*, 157(5):967–981.

Goldsworthy, M. and Jackson, J. A. (2001). Migration of activity within normal fault systems: Examples from the Quaternary of mainland Greece. *Journal of Structural Geology*, 23(2-3):489–506.

Gonzalez-Ortega, A., Fialko, Y., Sandwell, D., Alejandro Nava-Pichardo, F., Fletcher, J., Gonzalez-Garcia, J., Lipovsky, B., Floyd, M., and Funning, G. (2014). El Mayor-Cucapah (Mw 7.2) earthquake: Early near-field postseismic deformation from InSAR and GPS observations. *Journal of Geophysical Research: Solid Earth*, 119(2):1482–1497.

Goodman, A. Y., Rodbell, D. T., Seltzer, G. O., and Mark, B. G. (2001). Subdivision of glacial deposits in southeastern Peru based on pedogenic development and radiometric ages. *Quaternary Research*, 56(1):31–50.

Grützner, C., Schneiderwind, S., Papanikolaou, I., Deligiannakis, G., Pallikarakis, A., and Reicherter, K. (2016). New constraints on extensional tectonics and seismic hazard in northern Attica, Greece: The case of the Milesi Fault. *Geophysical Journal International*, 204(1):180–199.

Guangcai, F., Zhiwei, L., Xinjian, S., Bing, X., and Yanan, D. (2015). Source parameters of the 2014 Mw 6.1 South Napa earthquake estimated from the Sentinel 1A, COSMO-SkyMed and GPS data. *Tectonophysics*, 655:139–146.

Gubbels, T. L., Isacks, B. L., and Farrar, E. (1993). High-level surfaces, plateau uplift, and foreland development, Bolivian central Andes. *Geology*, 21(8):695.

Gutscher, M.-A., Spakman, W., Bjiwaard, H., and Enghdahl, E. R. (2000). Geodynamics of flat subduction: Seismicity and tomographic constraints from the Andean margin. *Tectonics*, 19(5):814–833.

Haines, A. J. and Holt, W. E. (1993). A procedure for obtaining the complete horizontal motions within zones of distributed deformation from the inversion of strain rate data. *Journal of Geophysical Research: Solid Earth*, 98(B7):12057–12082.

Hall, S. R., Farber, D. L., Audin, L., and Finkel, R. C. (2012). Recently active contractile deformation in the forearc of southern Peru. *Earth and Planetary Science Letters*, 337-338:85–92.

Hammer, P., Berthet, T., Hetényi, G., Cattin, R., Drukpa, D., Chophel, J., Lechmann, S., Moigne, N. L., Champollion, C., and Doerflinger, E. (2013). Flexure of the India plate underneath the Bhutan Himalaya. *Geophysical Research Letters*, 40(16):4225–4230.

Hao, M., Cui, D., Wang, Q., Gan, W., Qin, S., and Wang, W. (2013). Spatial distribution of afterslip from the 2008 wenchuan earthquake, China. *Geophysical Journal International*, 194(3).

Hashimoto, M., Enomoto, M., and Fukushima, Y. (2010). Coseismic Deformation from the 2008 Wenchuan, China, Earthquake Derived from ALOS/PALSAR Images. *Tectonophysics*, 491(1):59–71.

Hayes, G. P., Wald, D. J., and Johnson, R. L. (2012). Slab1.0: A three-dimensional model of global subduction zone geometries. *Journal of Geophysical Research: Solid Earth*, 117(1):B01302.

Heim, A. (1949). Observaciones Geologicas en La Region del Terremoto de Ancash de Noviembre de 1946. Technical report, Socieda Geologica del Peru.

Heki, K., Miyazaki, S., and Tsuji, H. (1997). Silent fault slip following an interplate thrust earthquake at the Japan Trench. *Nature*, 386(6625):595–598.

Henry, S. and Pollack, H. (1988). Terrestrial Heat Flow Above the Andean Subduction Zone in Bolivia and Peru. *Journal of Geophysical Research*, 93(B12):153–162.

Hessami, K., Tabassi, H., Okumura, K., Abbassi, M. R., and Azuma, T. (2005). Surface Deformation and the Fault Responsible for the 2003 Bam, Iran, Earthquake. *Earthquake Spectra*, 21(S1):113–123.

Heyburn, R. and Bowers, D. (2008). Earthquake depth estimation using the F trace and associated probability. *Bulletin of the Seismological Society of America*, 98(1):18–35.

Hoechner, A., Sobolev, S. V., Einarsson, I., and Wang, R. (2011). Investigation on afterslip and steady state and transient rheology based on postseismic deformation and geoid change caused by the Sumatra 2004 earthquake. *Geochemistry, Geophysics, Geosystems*, 12(7).

Hogg, A. G., Hua, Q., Blackwell, P. G., Niu, M., Buck, C. E., Guilderson, T. P., Heaton, T. J., Palmer, J. G., Reimer, P. J., Reimer, R. W., Turney, C. S. M., and Zimmerman, S. R. H. (2013). SHCal13 Southern Hemisphere Calibration, 0–50,000 Years cal BP. *Radiocarbon*, 55(04):1889–1903.

Hoke, L. and Lamb, S. (2007). Cenozoic behind-arc volcanism in the Bolivian Andes, South America: implications for mantle melt generation and lithospheric structure. *Journal of the Geological Society*, 164(4).

Holdsworth, R. (2004). Weak Faults - Rotten Cores. *Science*, 303(5655):181–182.

Holtkamp, S. G., Pritchard, M. E., and Lohman, R. B. (2011). Earthquake swarms in South America. *Geophysical Journal International*, 187(1):128–146.

Hooper, A., Segall, P., and Zebker, H. (2007). Persistent scatterer interferometric synthetic aperture radar for crustal deformation analysis, with application to Volcán Alcedo, Galápagos. *Journal of Geophysical Research: Solid Earth*, 112(B7):B07407.

Hooper, A., Zebker, H., Segall, P., and Kampes, B. (2004). A new method for measuring deformation on volcanoes and other natural terrains using InSAR persistent scatterers. *Geophysical Research Letters*, 31(23):L23611.

Horton, B. K., Perez, N. D., Fitch, J. D., and Saylor, J. E. (2015). Punctuated shortening and subsidence in the Altiplano Plateau of southern Peru: Implications for early Andean mountain building. *Lithosphere*, 7(2):117–137.

Howell, A., Palamartchouk, K., Papanikolaou, X., Paradissis, D., Raptakis, C., Copley, A., England, P., and Jackson, J. (2016). The 2008 Methoni earthquake sequence: the relationship between the earthquake cycle on the subduction interface and coastal uplift in SW Greece. *Geophysical Journal International*, 208(3):1592–1610.

Hsu, Y.-J., Bechor, N., Segall, P., Yu, S.-B., Kuo, L.-C., and Ma, K.-F. (2002). Rapid afterslip following the 1999 Chi-Chi, Taiwan Earthquake. *Geophysical Research Letters*, 29(16):1–4.

Hsu, Y.-J., Simons, M., Avouac, J.-P., Galetzka, J., Sieh, K., Chlieh, M., Natawidjaja, D., Prawirodirdjo, L., and Bock, Y. (2006). Frictional afterslip following the 2005 Nias-Simeulue earthquake, Sumatra. *Science*, 312(5782):1921–1926.

Hsu, Y.-J., Yu, S. B., and Chen, H. Y. (2009). Coseismic and postseismic deformation associated with the 2003 Chengkung, Taiwan, earthquake. *Geophysical Journal International*, 176(2):420–430.

Hudnut, K. W., Bock, Y., Cline, M., Fang, P., Feng, Y., Freymueller, J., Ge, X., Gross, W. K., Jackson, D., Kim, M., King, N. E., Langbein, J., Larsen, S. C., Lisowski, M., Shen, Z.-K., Svarc, J., and Zhang, J. (1994). Co-seismic displacements of the 1992 landers earthquake sequence. *Bulletin of the Seismological Society of America*, 84(3):625–645.

Husson, L. and Ricard, Y. (2004). Stress balance above subduction: Application to the Andes. *Earth and Planetary Science Letters*, 222(3-4):1037–1050.

Iinuma, T., Hino, R., Kido, M., Inazu, D., Osada, Y., Ito, Y., Ohzono, M., Tsushima, H., Suzuki, S., Fujimoto, H., and Miura, S. (2012). Coseismic slip distribution of the 2011 off the Pacific Coast of Tohoku Earthquake (M9.0) refined by means of seafloor geodetic data. *Journal of Geophysical Research: Solid Earth*, 117(B7):B07409.

Ikari, M. J., Marone, C., and Saffer, D. M. (2011). On the relation between fault strength and frictional stability. *Geology*, 39(1):83–86.

Ingleby, T. and Wright, T. J. (2017). Omori-like decay of postseismic velocities following continental earthquakes. *Geophysical Research Letters*, 44(7):3119–3130.

Jackson, J. A. (2002). Strength of the continental lithosphere: Time to abandon the jelly sandwich? *GSA Today*, 12(9):4.

Jackson, J. A. and Blenkinsop, T. (1997). The Bilila-Mtakataka fault in Malaŵi: An active, 100-km long, normal fault segment in thick seismogenic crust. *Tectonics*, 16(1):137–150.

Jackson, J. A., Bouchon, M., Fielding, E., Funning, G., Ghorashi, M., Hatzfeld, D., Nazari, H., Parsons, B., Priestley, K., Talebian, M., Tatar, M., Walker, R., and Wright, T. (2006). Seismotectonic, rupture process, and earthquake-hazard aspects of the 2003 December 26 Bam, Iran, earthquake. *Geophysical Journal International*, 166(3):1270–1292.

Jackson, J. A., Gagnepain, J., Houseman, G., King, G. C. P., Papadimitriou, P., Soufleris, C., and Viriuex, J. (1982). Seismicity, normal faulting, and the geomorphological development of the Gulf of Corinth (Greece): the Corinth earthquakes of February and March 1981. *Earth and Planetary Science Letters*, 57(2):377–397.

Jackson, J. A. and McKenzie, D. (1984). Active tectonics of the Alpine–Himalayan Belt between western Turkey and Pakistan. *Geophysical Journal International*, 77(1):185–264.

Jackson, J. A. and McKenzie, D. (1999). A hectare of fresh striations on the Arkitsa Fault, central Greece. *Journal of Structural Geology*, 21(1):1–6.

Jackson, J. A., McKenzie, D., Priestley, K., and Emmerson, B. (2008). New views on the structure and rheology of the lithosphere. *Journal of the Geological Society*, 165(2):453–465.

Jackson, J. A., Priestley, K., Allen, M., and Berberian, M. (2002). Active tectonics of the South Caspian Basin. *Geophysical Journal International*, 148(2):214–245.

Jackson, J. A. and White, N. J. (1989). Normal faulting in the upper continental crust: observations from regions of active extension. *Journal of Structural Geology*, 11(1-2):15–36.

Jacobs, A., Sandwell, D., Fialko, Y., and Sichoix, L. (2002). The 1999 (Mw 7.1) Hector Mine, California, Earthquake: Near-Field Postseismic Deformation from ERS Interferometry. *Bulletin of the Seismological Society of America*, 92(4):1433–1442.

Jay, J. A., Delgado, F. J., Torres, J. L., Pritchard, M. E., Macedo, O., and Aguilar, V. (2015). Deformation and seismicity near Sabancaya volcano, southern Peru, from 2002 to 2015. *Geophysical Research Letters*, 42(8):2780–2788.

Ji, C., Choi, K. K., King, N., Larson, K. M., and Hudnut, K. W. (2004). Co-seismic slip history and early afterslip of the 2004 Parkfield earthquake. *American Geophysical Union, Fall Meeting 2004, abstract #S53D-04*.

Johanson, I. A., Fielding, E. J., Rolandone, F., and Bürgmann, R. (2006). Coseismic and Postseismic Slip of the 2004 Parkfield Earthquake from Space-Geodetic Data. *Bulletin of the Seismological Society of America*, 96(4B):S269–S282.

Johnson, K. M., Bürgmann, R., and Larson, K. (2006). Frictional Properties on the San Andreas Fault near Parkfield, California, Inferred from Models of Afterslip following the 2004 Earthquake. *Bulletin of the Seismological Society of America*, 96(4B):S321–S338.

Johnson, K. M., Hsu, Y.-J., Segall, P., and Yu, S.-B. (2001). Fault geometry and slip distribution of the 1999 Chi-Chi, Taiwan Earthquake imaged from inversion of GPS data. *Geophysical Research Letters*, 28(11):2285–2288.

Jolivet, R., Lasserre, C., Doin, M.-P., Guillaso, S., Peltzer, G., Dailu, R., Sun, J., Shen, Z.-K., and Xu, X. (2012). Shallow creep on the Haiyuan Fault (Gansu, China) revealed by SAR Interferometry. *Journal of Geophysical Research: Solid Earth*, 117(B6):B06401.

Jolivet, R., Lasserre, C., Doin, M.-P., Peltzer, G., Avouac, J.-P., Sun, J., and Dailu, R. (2013). Spatio-temporal evolution of aseismic slip along the Haiyuan fault, China: Implications for fault frictional properties. *Earth and Planetary Science Letters*, 377-378:23–33.

Jomelli, V., Favier, V., Vuille, M., Braucher, R., Martin, L., Blard, P. H., Colose, C., Brunstein, D., He, F., Khodri, M., Bourlès, D. L., Leanni, L., Rinterknecht, V., Grancher, D., Francou, B., Ceballos, J. L., Fonseca, H., Liu, Z., and Otto-Bliesner, B. L. (2014). A major advance of tropical Andean glaciers during the Antarctic cold reversal. *Nature*, 513(7517):224–228.

Jones, R., Kokkalas, S., and McCaffrey, K. (2009). Quantitative analysis and visualization of nonplanar fault surfaces using terrestrial laser scanning (LIDAR)–The Arkitsa fault, central Greece, as a case study. *Geosphere*, 5(6):465–482.

Jónsson, S. (2008). Importance of post-seismic viscous relaxation in southern Iceland. *Nature Geoscience*, 1(2):136–139.

Jónsson, S., Segall, P., Pedersen, R., and Björnsson, G. (2003). Post-earthquake ground movements correlated to pore-pressure transients. *Nature*, 424(6945):179–183.

Jordan, T. E., Isacks, B. l., Allmendinger, R. E., Brewer, J. A., Ramos, V. A., and Ando, C. J. (1983). Andean tectonics related to geometry of subducted Nazca plate. *Geological Society of America Bulletin*, 94(3):341.

Jordan, T. H. (1978). Composition and development of the continental tectosphere. *Nature*, 274(5671):544–548.

Jouanne, F., Awan, A., Madji, A., Pêcher, A., Latif, M., Kausar, A., Mugnier, J. L., Khan, I., and Khan, N. A. (2011). Postseismic deformation in Pakistan after the 8 October 2005 earthquake: Evidence of afterslip along a flat north of the Balakot-Bagh thrust. *Journal of Geophysical Research: Solid Earth*, 116(7):1–22.

Kadinsky-Cade, K., Reilinger, R., and Isacks, B. (1985). Surface deformation associated with the November 23, 1977, Caucete, Argentina, earthquake sequence. *Journal of Geophysical Research: Solid Earth*, 90(14):12691–12700.

Kampes, B. and Usai, S. (1999). Doris: The Delft object-oriented radar interferometric package. *2nd International symposium of operationalization of remote sensing, Enschede, the Netherlands*, 16:20.

Kaneko, Y. and Fialko, Y. (2011). Shallow slip deficit due to large strike-slip earthquakes in dynamic rupture simulations with elasto-plastic off-fault response. *Geophysical Journal International*, 186(3):1389–1403.

Kar, N., Garzione, C. N., Jaramillo, C., Shanahan, T., Carlotto, V., Pullen, A., Moreno, F., Anderson, V., Moreno, E., and Eiler, J. (2016). Rapid regional surface uplift of the northern Altiplano plateau revealed by multiproxy paleoclimate reconstruction. *Earth and Planetary Science Letters*, 447:33–47.

Karato, S.-i. and Wu, P. (1993). Rheology of the Upper Mantle: A Synthesis. *Science*, 260(5109).

Karimiparidari, S., Zaré, M., Memarian, H., and Kijko, A. (2013). Iranian earthquakes, a uniform catalog with moment magnitudes. *Journal of Seismology*, 17(3):897–911.

Kaverina, A., Dreger, D., and Price, E. (2002). The Combined Inversion of Seismic and Geodetic Data for the Source Process of the 16 October 1999 Mw 7.1 Hector Mine, California, Earthquake. *Bulletin of the Seismological Society of America*, 92(4):1266–1280.

Kay, R. and Mahlburg Kay, S. (1993). Delamination and delamination magmatism. *Tectonophysics*, 219(1-3):177–189.

Kendrick, E., Bevis, M., and Brooks, B. (2001). An integrated crustal velocity field for the central Andes. *Geochemistry, Geophysics, Geosystems*, 2.

Kennan, L. (1993). Cenezoic Evolution of the Cochabamba Area, Bolivia. In *Second ISAG*, pages 21–23, Oxford.

Kennett, B. L. N., Engdahl, E. R., and Buland, R. (1995). Constraints on seismic velocities in the Earth from traveltimes. *Geophysical Journal International*, 122(1):108–124.

King, G. C. P., Stein, R. S., and Rundle, J. B. (1988). The Growth of Geological Structures by Repeated Earthquakes 1. Conceptual Framework. *Journal of Geophysical Research: Solid Earth*, 93(B11):13307–13318.

Kley, J. (1996). Transition from basement-involved to thin-skinned thrusting in the Cordillera Oriental of southern Bolivia. *Tectonics*, 15(4):763–775.

Kley, J. and Monaldi, C. R. (1998). Tectonic shortening and crustal thickness in the Central Andes: How good is the correlation? *Geology*, 26(8):723–726.

Kley, J., Monaldi, C. R., and Salfity, J. A. (1999). Along-strike segmentation of the Andean foreland: Causes and consequences. *Tectonophysics*, 301(1-2):75–94.

Kober, M., Seib, N., Kley, J., and Voigt, T. (2013). Thick-skinned thrusting in the northern Tien Shan foreland, Kazakhstan: structural inheritance and polyphase deformation. *Geological Society, London, Special Publications*, 377(1):19–42.

Konca, A. O., Avouac, J.-P., Sladen, A., Meltzner, A. J., Sieh, K., Fang, P., Li, Z., Galetzka, J., Genrich, J., Chlieh, M., Natawidjaja, D. H., Bock, Y., Fielding, E. J., Ji, C., and Helmberger, D. V. (2008). Partial rupture of a locked patch of the Sumatra megathrust during the 2007 earthquake sequence. *Nature*, 456(7222):631–5.

Kreemer, C., Blewitt, G., and Maerten, F. (2006). Co- and postseismic deformation of the 28 March 2005 Nias Mw 8.7 earthquake from continuous GPS data. *Geophysical Research Letters*, 33(7):28–31.

Lamb, S. (2006). Shear stresses on megathrusts: Implications for mountain building behind subduction zones. *Journal of Geophysical Research: Solid Earth*, 111(B7):B07401.

Lamb, S. (2011). Did shortening in thick crust cause rapid Late Cenozoic uplift in the northern Bolivian Andes? *Journal of the Geological Society*, 168(5):1079–1092.

Lamb, S. (2016). Cenozoic uplift of the Central Andes in northern Chile and Bolivia—reconciling paleoaltimetry with the geological evolution. *Canadian Journal of Earth Sciences*, 53(11):1227–1245.

Lamb, S. and Hoke, L. (1997). Origin of the high plateau in the Central Andes, Bolivia, South America. *Journal of Geophysical Research: Solid Earth*, 16(4):623–649.

Lamb, S. H. (2000). Active deformation in the Bolivian Andes, South America. *Journal of Geophysical Research: Solid Earth*, 105(B11):25627–25653.

Langbein, J., Murray, J. R., and Snyder, H. A. (2006). Coseismic and Initial Postseismic Deformation from the 2004 Parkfield, California, Earthquake, Observed by Global Positioning System, Electronic Distance Meter, Creepmeters, and Borehole Strainmeters. *Bulletin of the Seismological Society of America*, 96(4B):S304–S320.

Lavé, J. and Avouac, J.-P. (2000). Active folding of fluvial terraces across the Siwaliks Hills, Himalayas of central Nepal. *Journal of Geophysical Research: Solid Earth*, 105(B3):5735–5770.

Lavenu, A., Thiele, R., Machette, M., Dart, R., Lee-Ann, B., and Haller, K. (2000). Maps and Database of Quaternary Faults in Bolivia and Chile. Technical report, United States Geological Survey.

Lay, T., Kanamori, H., Ammon, C. J., Nettles, M., Ward, S. N., Aster, R. C., Beck, S. L., Bilek, S. L., Brudzinski, M. R., Butler, R., DeShon, H. R., Ekström, G., Satake, K., and Sipkin, S. (2005). The Great Sumatra-Andaman Earthquake of 26 December 2004. *Science*, 308(5725).

Lin, Y. N. N., Sladen, A., Ortega-Culaciati, F., Simons, M., Avouac, J. P., Fielding, E. J., Brooks, B. A., Bevis, M., Genrich, J., Rietbrock, A., Vigny, C., Smalley, R., and Socquet, A. (2013). Coseismic and postseismic slip associated with the 2010 Maule Earthquake, Chile: Characterizing the Arauco Peninsula barrier effect. *Journal of Geophysical Research: Solid Earth*, 118(6):3142–3159.

Lisiecki, L. E. and Raymo, M. E. (2005). A Pliocene-Pleistocene stack of 57 globally distributed benthic δ18O records. *Paleoceanography*, 20(1):1–17.

Liu, M., Yang, Y., Stein, S., and Klosko, E. (2002). Crustal Shortening and Extension in the Central Andes: Insights from a Viscoelastic Model. *Plate Boundary Zones*, pages 325–339.

Lucassen, F., Franz, G., Viramonte, J., Romer, R. L., Dulski, P., and Lang, A. (2005). The late Cretaceous lithospheric mantle beneath the Central Andes: Evidence from phase equilibria and composition of mantle xenoliths. *Lithos*, 82(3-4):379–406.

Lucassen, F., Lewerenz, S., Franz, G., Viramonte, J., and Mezger, K. (1999). Metamorphism, isotopic ages and composition of lower crustal granulite xenoliths from the Cretaceous Salta Rift, Argentina. *Contributions to Mineralogy and Petrology*, 134(4):325–341.

Lyon-Caen, H., Molnar, P., and Suárez, G. (1985). Gravity anomalies and flexure of the Brazilian Shield beneath the Bolivian Andes. *Earth and Planetary Science Letters*, 75(1):81–92.

Ma, Y. and Clayton, R. W. (2014). The crust and uppermost mantle structure of Southern Peru from ambient noise and earthquake surface wave analysis. *Earth and Planetary Science Letters*, 395:61–70.

Mackenzie, D. and Elliott, A. (2017). Untangling tectonic slip from the potentially misleading effects of landform geometry. *Geosphere*, 13(4):1310–1328.

Maggi, A., Jackson, J. A., McKenzie, D., and Priestley, K. (2000a). Earthquake focal depths, effective elastic thickness, and the strength of the continental lithosphere. *Geology*, 28(6):495.

Maggi, A., Jackson, J. A., Priestley, K., and Baker, C. (2000b). A re-assessment of focal depth distributions in southern Iran, the Tien Shan and northern India: do earthquakes really occur in the continental mantle? *Geophysical Journal International*, 143(3):629–661.

Mahsas, A., Lammali, K., Yelles, K., Calais, E., Freed, A. M., and Briole, P. (2008). Shallow afterslip following the 2003 May 21, Mw = 6.9 Boumerdes earthquake, Algeria. *Geophysical Journal International*, 172(1):155–166.

Margirier, A., Audin, L., Robert, X., Pêcher, A., and Schwartz, S. (2017). Stress field evolution above the Peruvian flat-slab (Cordillera Blanca, northern Peru). *Journal of South American Earth Sciences*, 77:58–69.

Marone, C. (2003). Laboratory-derived friction laws and their application to seismic faulting. *Annual Reviews in Earth and Planetary Sciences*, 26:643–696.

Marone, C. and Scholz, C. H. (1988). The depth of seismic faulting and the upper transition from stable to unstable slip regimes. *Geophysical Research Letters*, 15(6):621–624.

Marone, C. J., Scholtz, C. H., and Bilham, R. (1991). On the mechanics of earthquake afterslip. *Journal of Geophysical Research: Solid Earth*, 96(B5):8441.

Marrett, R. A., Allmendinger, R. W., Alonso, R. N., and Drake, R. E. (1994). Late Cenozoic tectonic evolution of the Puna Plateau and adjacent foreland, northwestern Argentine Andes. *Journal of South American Earth Sciences*, 7(2):179–207.

Marsh, E. J., Bruno, M. C., Fritz, S. C., Baker, P., Capriles, J. M., and Hastorf, C. A. (2018). IntCal, SHCal, or a Mixed Curve? Choosing a 14C Calibration Curve for Archaeological and Paleoenvironmental Records from Tropical South America. *Radiocarbon*, 60(03):925–940.

McCaffrey, R. and Abers, G. (1988). Syn3: a program for inversion of teleseismic body waveforms on microcomputers.

McCaffrey, R., Abers, G., and Zwick, P. (1991). Inversion of teleseismic body waves. In *IASPEI Software Library*, chapter 3. IASPEI Software Library, 3 edition.

McGroder, M. F., Lease, R. O., and Pearson, D. M. (2015). Along-strike variation in structural styles and hydrocarbon occurrences, Subandean fold-and-thrust belt and inner foreland, Colombia to Argentina. In DeCelles, P. G., Ducea, M. N., Carrapa, B., and Kapp, P. A., editors, *Geodynamics of a Cordilleran Orogenic System: The Central Andes of Argentina and Northern Chile*. Geological Society of America.

McKenzie, D. and Fairhead, D. (1997). Estimates of the effective elastic thickness of the continental lithosphere from Bouguer and free air gravity anomalies. *Journal of Geophysical Research: Solid Earth*, 102(B12):27523–27552.

McKenzie, D., Jackson, J., and Priestley, K. (2005). Thermal structure of oceanic and continental lithosphere. *Earth and Planetary Science Letters*, 233(3):337–349.

McKenzie, D., McKenzie, J., and Fairhead, D. (2019). The mechanical structure of Tibet. *Geophysical Journal International*, 217(2):950–969.

McKenzie, D. and Priestley, K. (2016). Speculations on the formation of cratons and cratonic basins. *Earth and Planetary Science Letters*, 435:94–104.

McKenzie, D., Yi, W., and Rummel, R. (2014). Estimates of Te from GOCE Data. *Earth and Planetary Science Letters*, 399:116–127.

McKenzie, D. P. and Parker, R. L. (1967). The North Pacific: an Example of Tectonics on a Sphere. *Nature*, 216(5122):1276–1280.

McNeill, L. and Collier, R. (2004). Uplift and slip rates of the eastern Eliki fault segment, Gulf of Corinth, Greece, inferred from Holocene and Pleistocene terraces. *Journal of the Geological Society*, 161(1):81–92.

McNulty, B. and Farber, D. (2002). Active detachment faulting above the Peruvian flat slab. *Geology*, 30(6):567–570.

Megard, F., Noble, D., McKee, E., and Bellon, H. (1984). Multiple pulses of Neogene compressive deformation in the Ayacucho intermontane basin, Andes of central Peru. *Geological Society of America Bulletin*, 95(9):1108.

Meghraoui, M., Maouche, S., Chemaa, B., Cakir, Z., Aoudia, A., Harbi, A., Alasset, P., Ayadi, A., Bouhadad, Y., and Benhamouda, F. (2004). Coastal uplift and thrust faulting associated with the Mw = 6.8 Zemmouri (Algeria) earthquake of 21 May, 2003. *Geophysical Research Letters*, 31(19):L19605.

Mei, S., Suzuki, A. M., Kohlstedt, D. L., Dixon, N. A., and Durham, W. B. (2010). Experimental constraints on the strength of the lithospheric mantle. *Journal of Geophysical Research: Solid Earth*, 115(B8):B08204.

Meija, R. and Frisancho, E. (2008). Mapa Cuadrangulo de Lagunillas Escala 1:50,000 Hoja 32-u Cuadrante II.

Meijer, P., Govers, R., and Wortel, M. (1997). Forces controlling the present-day state of stress in the Andes. *Earth and Planetary Science Letters*, 148(1-2):157–170.

Melbourne, T. I., Webb, F. H., Stock, J. M., and Reigber, C. (2002). Rapid postseismic transients in subduction zones from continuous GPS. *Journal of Geophysical Research: Solid Earth*, 107(B10):ET10.

Mencin, D., Bendick, R., Upreti, B. N., Adhikari, D. P., Gajurel, A., Bhattarai, R. R., Shrestha, H. R., Bhattarai, T. N., Manandhar, N., Galetzka, J., Knappe, E., Pratt-Sitaula, B., Aoudia, A., and Bilham, R. (2016). Himalayan strain reservoir inferred from limited afterslip following the Gorkha earthquake. *Nature Geoscience*, 9(7):533–537.

Mercer, J. H. and Palacios, M. O. (1977). Radiocarbon dating of the last glaciation in Peru. *Geology*, 5(10):600.

Mercier, J. L. (1981). Extensional-Compressional Tectonics Associated with the Aegean Arc: Comparison with the Andean Cordillera of South Peru - North Bolivia. *Philosophical Transactions of the Royal Society of London A: Mathematical, Physical and Engineering Sciences*, 300(1454).

Mercier, J. L., Sebrier, M., Lavenu, A., Cabrera, J., Bellier, O., Dumont, J.-F., and Machrare, J. (1992). Changes in the tectonic regime above a subduction zone of Andean Type: The Andes of Peru and Bolivia during the Pliocene-Pleistocene. *Journal of Geophysical Research*, 97(B8):11945.

Middleton, T. A. and Copley, A. (2014). Constraining fault friction by re-examining earthquake nodal plane dips. *Geophysical Journal International*, 196(2):671–680.

Miura, S., Iinuma, T., Yui, S., Uchida, N., Sato, T., Tachibana, K., and Hasegawa, A. (2006). Co- and post-seismic slip associated with the 2005 Miyagi-oki earthquake (M7.2) as inferred from GPS data. *Earth, Planets and Space*, 58(12):1567–1572.

Miyazaki, S., Larson, K. M., Choi, K., Hikima, K., Koketsu, K., Bodin, P., Haase, J., Emore, G., and Yamagiwa, A. (2004a). Modeling the rupture process of the 2003 September 25 Tokachi-Oki (Hokkaido) earthquake using 1-Hz GPS data. *Geophysical Research Letters*, 31(21):2–5.

Miyazaki, S., Segall, P., Fukuda, J., and Kato, T. (2004b). Space time distribution of afterslip following the 2003 Tokachi-oki earthquake: Implications for variations in fault zone frictional properties. *Geophysical Research Letters*, 31(6):L06623.

Molnar, P. (1988). Continental tectonics in the aftermath of plate tectonics. *Nature*, 335(6186):131–137.

Molnar, P., Chen, W.-P., Fitch, T. J., Tapponnier, P., Warsi, W. E. K., and Wu, F. (1977). Structure and Tectonics of the Himalaya: A brief summary of relevant geophysical observations. In *Collogue Internationaux du CNRS, No. 268, Himalaya: Sciences de la Terre*, pages 269–294, Paris. du Centre National de la Recherche Scientifique.

Molnar, P. and Lyon-Caen, H. (1988). Some simple physical aspects of the support, structure, and evolution of mountain belts. In *Geological Society of America Special Papers*, volume 218, pages 179–208. Geological Society of America.

Molnar, P. and Lyon-Caen, H. (1989). Fault plane solutions of earthquakes and active tectonics of the Tibetan Plateau and its margins. *Geophysical Journal International*, 99(1):123–154.

Molnar, P. and Stock, J. M. (2009). Slowing of India's convergence with Eurasia since 20 Ma and its implications for Tibetan mantle dynamics. *Tectonics*, 28(3):TC3001.

Montero Lopez, M. C., Hongn, F. D., Strecker, M. R., Marrett, R., Seggiaro, R., and Sudo, M. (2010). Late Miocene-early Pliocene onset of N-S extension along the southern margin of the Central Andean Puna Plateau: Evidence from magmatic, geochronological and structural observations. *Tectonophysics*, 494(1-2):48–63.

Motagh, M., Klotz, J., Tavakoli, F., Djamour, Y., Arabi, S., Wetzel, H.-U., and Zschau, J. (2006). Combination of Precise Leveling and InSAR Data to Constrain Source Parameters of the Mw = 6.5, 26 December 2003 Bam Earthquake. *Pure and Applied Geophysics*, 163(1):1–18.

Motagh, M., Walter, T. R., Sharifi, M. A., Fielding, E., Schenk, A., Anderssohn, J., and Zschau, J. (2008). Land subsidence in Iran caused by widespread water reservoir overexploitation. *Geophysical Research Letters*, 35(16):L16403.

Mouthereau, F., Watts, A. B., and Burov, E. (2013). Structure of orogenic belts controlled by lithosphere age. *Nature Geoscience*, 6(9):785–789.

Myers, S. C., Beck, S., Zandt, G., and Wallace, T. (1998). Lithospheric-scale structure across the Bolivian Andes from tomographic images of velocity and attenuation for P and S waves. *Journal of Geophysical Research: Solid Earth*, 103(B9):21233–21252.

Nakamura, T., Suzuki, S., Sadeghi, H., Mahmoud Fatemi Aghda, S., Matsushima, T., Ito, Y., Keivan Hosseini, S., Jafar Gandomi, A., and Maleki, M. (2005). Source fault structure of the 2003 Bam earthquake, southeastern Iran, inferred from the aftershock distribution and its relation to the heavily damaged area: Existence of the Arg-e-Bam fault proposed. *Geophysical Research Letters*, 32(9):L09308.

Nemati, M., Hollingsworth, J., Zhan, Z., Bolourchi, M. J., and Talebian, M. (2013). Microseismicity and seismotectonics of the South Caspian Lowlands, NE Iran. *Geophysical Journal International*, 193(3):1053–1070.

Ni, J. and Barazangi, M. (1984). Seismotectonics of the Himalayan Collision Zone: Geometry of the underthrusting Indian Plate beneath the Himalaya. *Journal of Geophysical Research: Solid Earth*, 89(B2):1147–1163.

Nishimura, T., Tobita, M., Yarai, H., Amagai, T., Fujiwara, M., Une, H., and Koarai, M. (2008). Episodic growth of fault-related fold in northern Japan observed by SAR interferometry. *Geophysical Research Letters*, 35(13):L13301.

Nissen, E., Yamini-Fard, F., Tatar, M., Gholamzadeh, A., Bergman, E., Elliott, J., Jackson, J., and Parsons, B. (2010). The vertical separation of mainshock rupture and microseismicity at Qeshm island in the Zagros fold-and-thrust belt, Iran. *Earth and Planetary Science Letters*, 296(3):181–194.

Noda, H. and Lapusta, N. (2013). Stable creeping fault segments can become destructive as a result of dynamic weakening. *Nature*, 493(7433):518–21.

Norabuena, E. O., Dixon, T. H., Stein, S., and Harrison, C. G. A. (1999). Decelerating Nazca-South America and Nazca-Pacific Plate motions. *Geophysical Research Letters*, 26(22):3405–3408.

Okada, Y. (1985). Surface deformation due to shear and tensile faults in a half-space. *Bulletin of the Seismological Society of America*, 75(4):1135–1154.

Oncken, O., Boutelier, D., Dresen, G., and Schemmann, K. (2012). Strain accumulation controls failure of a plate boundary zone: Linking deformation of the Central Andes and lithosphere mechanics. *Geochemistry, Geophysics, Geosystems*, 13(12).

Oncken, O., Hindle, D., Kley, J., Elger, K., Victor, P., and Schemmann, K. (2006). Deformation of the Central Andean Upper Plate System — Facts, Fiction, and Constraints for Plateau Models. In *The Andes*, pages 3–27. Springer Berlin Heidelberg.

Ordóñez-Carmona, O., Restrepo Álvarez, J. J., and Pimentel, M. M. (2006). Geochronological and isotopical review of pre-Devonian crustal basement of the Colombian Andes. *Journal of South American Earth Sciences*, 21(4):372–382.

Ozawa, S., Kaidzu, M., Murakami, M., Imakiire, T., and Hatanaka, Y. (2004). Coseismic and postseismic crustal deformation after the Mw 8 Tokachi-oki earthquake in Japan. *Earth, Planets and Space*, 56(7):675–680.

Ozawa, S., Nishimura, T., Suito, H., Kobayashi, T., Tobita, M., and Imakiire, T. (2011). Coseismic and postseismic slip of the 2011 magnitude-9 Tohoku-Oki earthquake. *Nature*, 475(7356):373–376.

Parsons, B., Wright, T., Rowe, P., Andrews, J., Jackson, J., Walker, R., Khatib, M., Talebian, M., Bergman, E., and Engdahl, E. R. (2006). The 1994 Sefidabeh (eastern Iran) earthquakes revisited: new evidence from satellite radar interferometry and carbonate dating about the growth of an active fold above a blind thrust fault. *Geophysical Journal International*, 164(1):202–217.

Pathier, E., Fielding, E. J., Wright, T. J., Walker, R., Parsons, B. E., and Hensley, S. (2006). Displacement field and slip distribution of the 2005 Kashmir earthquake from SAR imagery. *Geophysical Research Letters*, 33(20):L20310.

Peltzer, G., Rosen, P., Rogez, F., and Hudnut, K. (1998). Poroelastic rebound along the Landers 1992 earthquake surface rupture. *Journal of Geophysical Research: Solid Earth*, 103(B12):30131–30145.

Peng, Z. and Zhao, P. (2009). Migration of early aftershocks following the 2004 Parkfield earthquake. *Nature Geoscience*, 2(12):877–881.

Penney, C., Copley, A., and Oveisi, B. (2015). Subduction tractions and vertical axis rotations in the Zagros–Makran transition zone, SE Iran: the 2013 May 11 Mw 6.1 Minab earthquake. *Geophysical Journal International*, 202(2):1122–1136.

Penney, C., Tavakoli, F., Saadat, A., Nankali, H. R., Sedighi, M., Khorrami, F., Sobouti, F., Rafi, Z., Copley, A., Jackson, J., and Priestley, K. (2017). Megathrust and accretionary wedge properties and behaviour in the Makran subduction zone. *Geophysical Journal International*, 209(3):1800–1830.

Perez, N., Horton, B., McQuarrie, N., Stubner, K., and Ehlers, T. (2016a). Andean shortening, inversion and exhumation associated with thin- and thick-skinned deformation in southern Peru. *Geological Magazine*, 153(5-6):1013–1041.

Perez, N. D. and Horton, B. K. (2014). Oligocene-miocene deformational and depositional history of the andean hinterland basin in the northern altiplano Plateau, Southern Peru. *Tectonics*, 33(9):1819–1847.

Perez, N. D., Horton, B. K., and Carlotto, V. (2016b). Structural inheritance and selective reactivation in the central Andes: Cenozoic deformation guided by pre-Andean structures in southern Peru. *Tectonophysics*, 671:264–280.

Pérez-Gussinyé, M., Lowry, A. R., and Watts, A. B. (2007). Effective elastic thickness of South America and its implications for intracontinental deformation. *Geochemistry, Geophysics, Geosystems*, 8(5).

Perfettini, H. (2004). Postseismic relaxation driven by brittle creep: A possible mechanism to reconcile geodetic measurements and the decay rate of aftershocks, application to the Chi-Chi earthquake, Taiwan. *Journal of Geophysical Research: Solid Earth*, 109(B2):B02304.

Perfettini, H. and Avouac, J.-P. (2007). Modeling afterslip and aftershocks following the 1992 Landers earthquake. *Journal of Geophysical Research: Solid Earth*.

Perfettini, H., Avouac, J.-P., Tavera, H., Kositsky, A., Nocquet, J.-M., Bondoux, F., Chlieh, M., Sladen, A., Audin, L., Farber, D. L., and Soler, P. (2010). Seismic and aseismic slip on the Central Peru megathrust. *Nature*, 465(7294):78–81.

Peyret, M., Chéry, J., Djamour, Y., Avallone, A., Sarti, F., Briole, P., and Sarpoulaki, M. (2007). The source motion of 2003 Bam (Iran) earthquake constrained by satellite and ground-based geodetic data. *Geophysical Journal International*, 169(3):849–865.

Philip, H. and Megard, F. (1977). Structural analysis of the superficial deformation of the 1969 Pariahuanca earthquakes (Central Peru). *Tectonophysics*, 38(3-4):259–278.

Phillips, K., Clayton, R. W., Davis, P., Tavera, H., Guy, R., Skinner, S., Stubailo, I., Audin, L., and Aguilar, V. (2012). Structure of the subduction system in southern Peru from seismic array data. *Journal of Geophysical Research: Solid Earth*, 117(11):B11306.

Placzek, C. J., Quade, J., and Patchett, P. J. (2013). A 130ka reconstruction of rainfall on the Bolivian Altiplano. *Earth and Planetary Science Letters*, 363:97–108.

Poiata, N., Miyake, H., Koketsu, K., and Hikima, K. (2012). Strong-Motion and Teleseismic Waveform Inversions for the Source Process of the 2003 Bam, Iran, Earthquake. *Bulletin of the Seismological Society of America*, 102(4):1477–1496.

Poveda, E., Monsalve, G., and Vargas, C. A. (2015). Receiver functions and crustal structure of the northwestern Andean region, Colombia. *Journal of Geophysical Research: Solid Earth*, 120(4):2408–2425.

Priestley, K. and McKenzie, D. (2013). The relationship between shear wave velocity, temperature, attenuation and viscosity in the shallow part of the mantle. *Earth and Planetary Science Letters*, 381:78–91.

Pritchard, M. E., Norabuena, E. O., Ji, C., Boroschek, R., Comte, D., Simons, M., Dixon, T. H., and Rosen, P. A. (2007). Geodetic, teleseismic, and strong motion constraints on slip from recent southern Peru subduction zone earthquakes. *Journal of Geophysical Research*, 112(B3):B03307.

Pritchard, M. E., Simons, M., Rosen, P. A., Hensley, S., and Webb, F. H. (2002). Co-seismic slip from the 1995 July 30 Mw = 8.1 Antofagasta, Chile, earthquake as constrained by InSAR and GPS observations. *Geophysical Journal International*, 150(2):362–376.

Ranalli, G. (1995). *Rheology of the Earth*. Chapman & Hall.

Reilinger, R., McClusky, S., Vernant, P., Lawrence, S., Ergintav, S., Cakmak, R., Ozener, H., Kadirov, F., Guliev, I., Stepanyan, R., Nadariya, M., Hahubia, G., Mahmoud, S., Sakr, K., ArRajehi, A., Paradissis, D., Al-Aydrus, A., Prilepin, M., Guseva, T., Evren, E., Dmitrotsa, A., Filikov, S. V., Gomez, F., Al-Ghazzi, R., and Karam, G. (2006). GPS constraints on continental deformation in the Africa-Arabia-Eurasia continental collision zone and implications for the dynamics of plate interactions. *Journal of Geophysical Research: Solid Earth*, 111(B5):B05411.

Reilinger, R. E. (2000). Coseismic and Postseismic Fault Slip for the 17 August 1999, M = 7.5, Izmit, Turkey Earthquake. *Science*, 289(5484):1519–1524.

Renner, S. and Velasco, C. (2000). Geologia E Hidrogeologia Del Valle Central De Cochabamba. Technical report, German-Bolivian Agreement on Groundwater (CABAS).

Reynolds, K., Copley, a., and Hussain, E. (2015). Evolution and dynamics of a fold-thrust belt: the Sulaiman Range of Pakistan. *Geophysical Journal International*, 201(2):683–710.

Richardson, R. M. and Coblentz, D. D. (1994). Stress modeling in the Andes: Constraints on the South American intraplate stress magnitudes. *Journal of Geophysical Research: Solid Earth*, 99(B11):22015–22025.

Riller, U., Clark, M. D., Daxberger, H., Doman, D., Lenauer, I., Plath, S., and Santimano, T. (2017). Fault-slip inversions : Their importance in terms of strain, heterogeneity, and kinematics of brittle deformation. *Journal of Structural Geology*, 101:B2–B6.

Rodbell, D. T., Smith, J. A., and Mark, B. G. (2009). Glaciation in the Andes during the Lateglacial and Holocene. *Quaternary Science Reviews*, 28(21-22):2165–2212.

Rodríguez Tribaldos, V., White, N. J., Roberts, G. G., and Hoggard, M. J. (2017). Spatial and temporal uplift history of South America from calibrated drainage analysis. *Geochemistry, Geophysics, Geosystems*, 18(6):2321–2353.

Rollins, C., Barbot, S., and Avouac, J.-P. (2015). Postseismic Deformation Following the 2010 M = 7.2 El Mayor-Cucapah Earthquake: Observations, Kinematic Inversions, and Dynamic Models. *Pure and Applied Geophysics*, 172(5):1305–1358.

Rosen, P. A., Hensley, S., Peltzer, G., and Simons, M. (2004). Updated repeat orbit interferometry package released. *Eos, Transactions American Geophysical Union*, 85(5):47–47.

Rossell, L. (2018). *Estudio Morfotectonico y Paleosismico de las Fallas Tambomachay y Qoricocha, Implicancia en el Peligro Seismico de la Region Cusco*. Masters thesis, Universidad Nacional de San Antonio Abab del Cusco.

Rousset, B., Barbot, S., Avouac, J.-P., and Hsu, Y.-J. (2012). Postseismic deformation following the 1999 Chi-Chi earthquake, Taiwan: Implication for lower-crust rheology. *Journal of Geophysical Research: Solid Earth*, 117(B12):B12405.

Ruegg, J. C., Campos, J., Armijo, R., Barrientos, S., Briole, P., Thiele, R., Arancibia, M., Cañuta, J., Duquesnoy, T., Chang, M., Lazo, D., Lyon-Caen, H., Ortlieb, L., Rossignol, J. C., and Serrurier, L. (1996). The Mw =8.1 Antofagasta (North Chile) Earthquake of July 30, 1995: First results from teleseismic and geodetic data. *Geophysical Research Letters*, 23(9):917–920.

Ruegg, J. C., Olcay, M., and Lazo, D. (2001). Co-, Post- and Pre(?)-seismic Displacements Associated with the Mw 8.4 Southern Peru Earthquake of 23 June 2001 from Continuous GPS Measurements. *Seismological Research Letters*, 72(6):673–678.

Ruina, A. (1983). Slip instability and state variable friction laws. *Journal of Geophysical Research: Solid Earth*, 88(B12):10359–10370.

Ryan, J., Beck, S., Zandt, G., Wagner, L., Minaya, E., and Tavera, H. (2016). Central Andean crustal structure from receiver function analysis. *Tectonophysics*, 682:120–133.

Ryder, I., Bürgmann, R., and Sun, J. (2010). Tandem afterslip on connected fault planes following the 2008 Nima-Gaize (Tibet) earthquake. *Journal of Geophysical Research: Solid Earth*, 115(3):1–16.

Ryder, I., Parsons, B., Wright, T. J., and Funning, G. J. (2007). Post-seismic motion following the 1997 Manyi (Tibet) earthquake: InSAR observations and modelling. *Geophysical Journal International*, 169(3):1009–1027.

Sagy, A. and Brodsky, E. E. (2009). Geometric and rheological asperities in an exposed fault zone. *Journal of Geophysical Research*, 114(B2):B02301.

Sagy, A., Brodsky, E. E., and Axen, G. J. (2007). Evolution of fault-surface roughness with slip. *Geology*, 35(3):283–286.

Savage, J. C. and Svarc, J. L. (1997). Postseismic deformation associated with the 1992 Mw 7.3 Landers earthquake, southern California. *Journal of Geophysical Research: Solid Earth*, 102(B4):7565–7577.

Savage, J. C., Svarc, J. L., and Yu, S.-B. (2005). Postseismic relaxation and transient creep. *Journal of Geophysical Research*, 110(B11):B11402.

Saylor, J. E. and Horton, B. K. (2014). Nonuniform surface uplift of the Andean plateau revealed by deuterium isotopes in Miocene volcanic glass from southern Peru. *Earth and Planetary Science Letters*, 387:120–131.

Schoenbohm, L. M. and Strecker, M. R. (2009). Normal faulting along the southern margin of the Puna Plateau, northwest Argentina. *Tectonics*, 28(5):TC5008.

Scholz, C. H. (1998). Earthquakes and friction laws. *Nature*, 391(6662):37–42.

Scholz, C. H. (2002). *The Mechanics of Earthquakes and Faulting*. Cambridge University Press.

Scholz, C. H., Wyss, M., and Smith, S. W. (1969). Seismic and aseismic slip on the San Andreas Fault. *Journal of Geophysical Research*, 74(8):2049–2069.

Schurr, B., Asch, G., Rietbrock, A., Kind, R., Pardo, M., Heit, B., and Monfret, T. (1999). Seismicity and average velocities beneath the Argentine Puna Plateau. *Geophysical Research Letters*, 26(19):3025–3028.

Scott, C., Lohman, R., Pritchard, M., Alvarado, P., and Sánchez, G. (2014). Andean earthquakes triggered by the 2010 Maule, Chile (Mw8.8) earthquake: Comparisons of geodetic, seismic and geologic constraints. *Journal of South American Earth Sciences*, 50:27–39.

Sébrier, M., Mercier, J. L., Macharé, J., Bonnot, D., Cabrera, J., and Blanc, J. L. (1988). The state of stress in an overriding plate situated above a flat slab: The Andes of central Peru. *Tectonics*, 7(4):895–928.

Sébrier, M., Mercier, J. L., Mégard, F., Laubacher, G., and Carey-Gailhardis, E. (1985). Quaternary normal and reverse faulting and the state of stress in the central Andes of south Peru. *Tectonics*, 4(7):739–780.

Seltzer, G. O. (1990). Recent glacial history and paleoclimate of the Peruvian-Bolivian Andes. *Quaternary Science Reviews*, 9(2-3):137–152.

Shako, R., Forste, C., Abrikosov, O., Bruinsma, S., Marty, J.-C., Lemoine, J.-M., Flechtner, F., Neumayer, H., and Dahle, C. (2014). EIGEN-6C: A High-Resolution Global Gravity Combination Model Including GOCE Data. *Observation of the System Earth from Space - CHAMP, GRACE, GOCE and future missions*, pages 155–161.

Shao, Z., Wang, R., Wu, Y., and Zhang, L. (2011). Rapid afterslip and short-term viscoelastic relaxation following the 2008 M W7.9 Wenchuan earthquake. *Earthquake Science*, 24(2):163–175.

Shen, Z.-K., Jackson, D. D., Feng, Y., Cline, M., Kim, M., Fang, P., and Bock, Y. (1994). Postseismic deformation following the Landers earthquake, California, 28 June 1992. *Bulletin of the Seismological Society of America*, 84(3):780–791.

Shen, Z.-K., Sun, J., Zhang, P., Wan, Y., Wang, M., Bürgmann, R., Zeng, Y., Gan, W., Liao, H., and Wang, Q. (2009). Slip maxima at fault junctions and rupturing of barriers during the 2008 Wenchuan earthquake. *Nature Geoscience*, 2(10):718–724.

Sibson, R. H. (2004). Controls on maximum fluid overpressure defining conditions for mesozonal mineralisation. *Journal of Structural Geology*, 26(6-7):1127–1136.

Silgado, E. (1978). Historia de los Sismos Mas Notables Ocurridos en el Peru (1513-1974). Technical report, Instituto de Geologia y Mineria, Lima.

Simons, M., Fialko, Y., and Rivera, L. (2002). Coseismic Deformation from the 1999 Mw 7.1 Hector Mine, California, Earthquake as Inferred from InSAR and GPS Observations. *Bulletin of the Seismological Society of America*, 92(4):1390–1402.

Sladen, A., Tavera, H., Simons, M., Avouac, J. P., Konca, A. O., Perfettini, H., Audin, L., Fielding, E. J., Ortega, F., and Cavagnoud, R. (2010). Source model of the 2007 Mw 8.0 Pisco, Peru earthquake: Implications for seismogenic behavior of subduction megathrusts. *Journal of Geophysical Research*, 115(B2):B02405.

Sloan, R. A. and Jackson, J. A. (2012). Upper-mantle earthquakes beneath the Arafura Sea and south Aru Trough: Implications for continental rheology. *Journal of Geophysical Research: Solid Earth*, 117(5):B05402.

Sloan, R. A., Jackson, J. A., McKenzie, D., and Priestley, K. (2011). Earthquake depth distributions in central Asia, and their relations with lithosphere thickness, shortening and extension. *Geophysical Journal International*, 185(1):1–29.

Smalley, R. and Isacks, B. L. (1987). Seismotectonics of thin- and thick-skinned deformation in the Andean Foreland from local network data: Evidence for a seismogenic lower crust. *Journal of Geophysical Research*, 95(B8):12487.

Smith, J. A., Finkel, R. C., Farber, D. L., Rodbell, D. T., and Seltzer, G. O. (2005a). Moraine preservation and boulder erosion in the tropical Andes: Interpreting old surface exposure ages in glaciated valleys. *Journal of Quaternary Science*, 20(7-8):735–758.

Smith, J. A., Seltzer, G. O., Rodbell, D. T., and Klein, A. G. (2005b). Regional synthesis of last glacial maximum snowlines in the tropical Andes, South America. *Quaternary International*, 138-139:145–167.

Smith, S. W. and Wyss, M. (1968). Displacement on the San Andreas fault subsequent to the 1966 Parkfield earthquake. *Bulletin of the Seismological Society of America*, 58(6):1955–1973.

Smith, W. H. F. and Wessel, P. (1990). Gridding with continuous curvature splines in tension. *Geophysics*, 55(3):193–305.

Stein, S. and Okal, E. A. (2005). Seismology: Speed and size of the Sumatra earthquake. *Nature*, 434(7033):581–582.

Stevens, V. L. and Avouac, J. P. (2015). Interseismic coupling on the main Himalayan thrust. *Geophysical Research Letters*, 42(14):5828–5837.

Stewart, J. and Watts, A. B. (1997). Gravity anomalies and spatial variations of flexural rigidity at mountain ranges. *Journal of Geophysical Research: Solid Earth*, 102(B3):5327–5352.

Stramondo, S., Moro, M., Tolomei, C., Cinti, F., and Doumaz, F. (2005). InSAR surface displacement field and fault modelling for the 2003 Bam earthquake (southeastern Iran). *Journal of Geodynamics*, 40(2-3):347–353.

Suarez, G., Molnar, P., and Burchfiel, B. C. (1983). Seismicity, fault plane solutions, depth of faulting, and active tectonics of the Andes of Peru, Ecuador, and southern Colombia. *Journal of Geophysical Research*, 88(B12):10403–10428.

Sun, J., Shen, Z., Xu, X., and Bürgmann, R. (2008). Synthetic normal faulting of the 9 January 2008 Nima (Tibet) earthquake from conventional and along-track SAR interferometry. *Geophysical Research Letters*, 35(22):1–6.

Takada, Y., Kobayashi, T., Furuya, M., and Murakami, M. (2009). Coseismic displacement due to the 2008 Iwate-Miyagi Nairiku earthquake detected by ALOS/PALSAR: preliminary results. *Earth, Planets and Space*, 61(4):9–12.

Talebian, M. (2004). The 2003 Bam (Iran) earthquake: Rupture of a blind strike-slip fault. *Geophysical Research Letters*, 31(11):L11611.

Talebian, M., Copley, A. C., Fattahi, M., Ghorashi, M., Jackson, J. A., Nazari, H., Sloan, R. A., and Walker, R. T. (2016). Active faulting within a megacity: The geometry and slip rate of the Pardisan thrust in central Tehran, Iran. *Geophysical Journal International*, 207(3):1688–1699.

Tanioka, Y., Ruff, L., and Satake, K. (1996). The Sanriku-Oki, Japan, Earthquake of December 28, 1994 (Mw 7.7): Rupture of a different asperity from a previous earthquake. *Geophysical Research Letters*, 23(12):1465–1468.

Tatar, M., Hatzfeld, D., Moradi, A. S., and Paul, A. (2005). The 2003 December 26 Bam earthquake (Iran), Mw 6.6, aftershock sequence. *Geophysical Journal International*, 163(1):90–105.

Tavera, H. and Buforn, E. (2001). Source mechanism of earthquakes in Peru. *Journal of Seismology*, 5(4):519–539.

Taymaz, T., Jackson, J. A., and Westaway, R. (1990). Earthquake mechanisms in the Hellenic Trench near Crete. *Geophysical Journal International*, 102(3):695–731.

Thomas, M. Y., Avouac, J.-P., Champenois, J., Lee, J.-C., and Kuo, L.-C. (2014a). Spatiotemporal evolution of seismic and aseismic slip on the Longitudinal Valley Fault, Taiwan. *Journal of Geophysical Research: Solid Earth*, 119(6):5114–5139.

Thomas, M. Y., Avouac, J. P., Gratier, J. P., and Lee, J. C. (2014b). Lithological control on the deformation mechanism and the mode of fault slip on the Longitudinal Valley Fault, Taiwan. *Tectonophysics*, 632:48–63.

Thompson, S. C., Weldon, R. J., Rubin, C. M., Abdrakhmatov, K., Molnar, P., and Berger, G. W. (2002). Late Quaternary slip rates across the central Tien Shan, Kyrgyzstan, central Asia. *Journal of Geophysical Research: Solid Earth*, 107(B9):7–32.

Tibaldi, A. and Bonali, L. I. (2018). Contemporary recent extension and compression in the central Andes. *Journal of Structural Geology*, 107:73–92.

Tibaldi, A., Corazzato, C., and Rovida, A. (2009). Miocene-Quaternary structural evolution of the Uyuni-Atacama region, Andes of Chile and Bolivia. *Tectonophysics*, 471(1-2):114–135.

Tong, X., Sandwell, D. T., and Fialko, Y. (2010). Coseismic slip model of the 2008 Wenchuan earthquake derived from joint inversion of interferometric synthetic aperture radar, GPS, and field data. *Journal of Geophysical Research*, 115(B4):B04314.

Turcotte, D. L. and Schubert, G. (2002). *Geodynamics*. Cambridge University Press.

Vega, A. and Buforn, E. (1991). Focal mechanisms of intraplate earthquakes in South America. *Pure and Applied Geophysics*, 136(4).

Veloza, G., Styron, R., and Taylor, M. (2012). Open-source archive of active faults for northwest South America. *GSA Today*, 22(10):4–10.

Vernant, P., Nilforoushan, F., Hatzfeld, D., Abbassi, M. R., Vigny, C., Masson, F., Nankali, H., Martinod, J., Ashtiani, A., Bayer, R., Tavakoli, F., and Chéry, J. (2004). Present-day crustal deformation and plate kinematics in the Middle East constrained by GPS measurements in Iran and northern Oman. *Geophysical Journal International*, 157(1):381–398.

Vigny, C., Simons, W. J. F., Abu, S., Bamphenyu, R., Satirapod, C., Choosakul, N., Subarya, C., Socquet, A., Omar, K., Abidin, H. Z., and Ambrosius, B. A. C. (2005). Insight into the 2004 Sumatra–Andaman earthquake from GPS measurements in southeast Asia. *Nature*, 436(7048):201–206.

Villegas-Lanza, J. C., Chlieh, M., Cavalié, O., Tavera, H., Baby, P., Chire-Chira, J., and Nocquet, J. M. (2016). Active tectonics of Peru: Heterogeneous interseismic coupling along the Nazca megathrust, rigid motion of the Peruvian Sliver, and Subandean shortening accommodation. *Journal of Geophysical Research: Solid Earth*, 121(10):7371–7394.

Wald, D. J., Heaton, T. H., and Hudnut, K. W. (1996). The slip history of the 1994 Northridge, California, earthquake determined from strong-motion, teleseismic, GPS, and leveling data. *Bulletin of the Seismological Society of America*, 86(1B):S49–S70.

Walker, R. and Jackson, J. (2004). Active tectonics and late Cenozoic strain distribution in central and eastern Iran. *Tectonics*, 23(5):TC5010.

Walker, R., Jackson, J., and Baker, C. (2003). Surface expression of thrust faulting in eastern Iran: source parameters and surface deformation of the 1978 Tabas and 1968 Ferdows earthquake sequences. *Geophysical Journal International*, 152(3):749–765.

Walker, R. T., Bergman, E. A., Elliott, J. R., Fielding, E. J., Ghods, A.-R., Ghoraishi, M., Jackson, J., Nazari, H., Nemati, M., Oveisi, B., Talebian, M., and Walters, R. J. (2013). The 2010-2011 South Rigan (Baluchestan) earthquake sequence and its implications for distributed deformation and earthquake hazard in southeast Iran. *Geophysical Journal International*, 193(1):349–374.

Walker, R. T., Bergman, E. A., Szeliga, W., and Fielding, E. J. (2011). Insights into the 1968-1997 Dasht-e-Bayaz and Zirkuh earthquake sequences, eastern Iran, from calibrated relocations, InSAR and high-resolution satellite imagery. *Geophysical Journal International*, 187(3):1577–1603.

Walker, R. T., Talebian, M., Saiffori, S., Sloan, R. A., Rasheedi, A., MacBean, N., and Ghassemi, A. (2010). Active faulting, earthquakes, and restraining bend development near Kerman city in southeastern Iran. *Journal of Structural Geology*, 32(8):1046–1060.

Walpersdorf, A., Manighetti, I., Mousavi, Z., Tavakoli, F., Vergnolle, M., Jadidi, A., Hatzfeld, D., Aghamohammadi, A., Bigot, A., Djamour, Y., Nankali, H., and Sedighi, M. (2014). Present-day kinematics and fault slip rates in eastern Iran, derived from 11 years of GPS data. *Journal of Geophysical Research: Solid Earth*, 119(2):1359–1383.

Walters, R. J., Elliott, J. R., D'Agostino, N., England, P. C., Hunstad, I., Jackson, J. A., Parsons, B., Phillips, R. J., and Roberts, G. (2009). The 2009 L'Aquila earthquake (central Italy): A source mechanism and implications for seismic hazard. *Geophysical Research Letters*, 36(17):L17312.

Wang, K. (2000). Stress-strain 'paradox', plate coupling, and forearc seismicity at the Cascadia and Nankai subduction zones. *Tectonophysics*, 319(4):321–338.

Wang, K. and Fialko, Y. (2015). Slip model of the 2015 Mw 7.8 Gorkha (Nepal) earthquake from inversions of ALOS-2 and GPS data. *Geophysical Research Letters*, 42(18):7452–7458.

Wang, K. and He, J. (1999). Mechanics of low-stress forearcs: Nankai and Cascadia. *Journal of Geophysical Research: Solid Earth*, 104(B7):15191–15205.

Ward, D. J., Cesta, J. M., Galewsky, J., and Sagredo, E. (2015). Late pleistocene glaciations of the arid subtropical Andes and new results from the Chajnantor Plateau, northern Chile. *Quaternary Science Reviews*, 128:98–116.

Ward, K. M., Zandt, G., Beck, S. L., Wagner, L. S., and Tavera, H. (2016). Lithospheric structure beneath the northern Central Andean Plateau from the joint inversion of ambient noise and earthquake-generated surface waves. *Journal of Geophysical Research: Solid Earth*, 121(11):8217–8238.

Watts, A., Lamb, S., Fairhead, J., and Dewey, J. (1995). Lithospheric flexure and bending of the Central Andes. *Earth and Planetary Science Letters*, 134(1-2):9–21.

Wdowinski, S., Oconnell, R. J., and England, P. (1989). A continuum model of continental deformation above subduction zones - Application to the Andes and the Aegean. *Journal of Geophysical Research-Solid Earth and Planets*, 94(B8):10331–10346.

Weber, M. B. I., Tarney, J., Kempton, P. D., and Kent, R. W. (2002). Crustal make-up of the northern Andes: evidence based on deep crustal xenolith suites, Mercaderes, SW Colombia. *Tectonophysics*, 345:49–82.

Wei, S., Barbot, S., Graves, R., Lienkaemper, J. J., Wang, T., Hudnut, K., Fu, Y., and Helmberger, D. (2015). The 2014 Mw 6.1 South Napa Earthquake: A Unilateral Rupture with Shallow Asperity and Rapid Afterslip. *Seismological Research Letters*, 86(2A):344–354.

Wei, S., Fielding, E., Leprince, S., Sladen, A., Avouac, J.-P., Helmberger, D., Hauksson, E., Chu, R., Simons, M., Hudnut, K., Herring, T., and Briggs, R. (2011). Superficial simplicity of the 2010 El Mayor–Cucapah earthquake of Baja California in Mexico. *Nature Geoscience*, 4(9):615–618.

Weiss, J. R., Brooks, B. A., Foster, J. H., Bevis, M., Echalar, A., Caccamise, D., Heck, J., Kendrick, E., Ahlgren, K., Raleigh, D., Smalley, R., and Vergani, G. (2016). Isolating active orogenic wedge deformation in the southern Subandes of Bolivia. *Journal of Geophysical Research: Solid Earth*, 121(8):6192–6218.

Wells, D. L. and Coppersmith, K. J. (1994). New empirical relationships among magnitude, rupture length, rupture width, rupture area, and surface displacement. *Bulletin of the Seismological Society of America*, 84(4):974–1002.

Westoby, M., Brasington, J., Glasser, N., Hambrey, M., and Reynolds, J. (2012). 'Structure-from-Motion' photogrammetry: A low-cost, effective tool for geoscience applications. *Geomorphology*, 179:300–314.

Whitman, D., Isacks, B. L., Chatelain, J.-L., Chiu, J.-M., and Perez, A. (1992). Attenuation of high-frequency seismic waves beneath the central Andean Plateau. *Journal of Geophysical Research*, 97(B13):19929–19947.

Williams, H., Turner, S., Kelley, S., and Harris, N. (2001). Age and composition of dikes in Southern Tibet: New constraints on the timing of east-west extension and its relationship to postcollisional volcanism. *Geology*, 29(4):339–342.

Wu, Y. M., Chen, Y. G., Shin, T. C., Kuochen, H., Hou, C. S., Hu, J. C., Chang, C. H., Wu, C. F., and Teng, T. L. (2006). Coseismic versus interseismic ground deformations, fault rupture inversion and segmentation revealed by 2003 Mw 6.8 Chengkung earthquake in eastern Taiwan. *Geophysical Research Letters*, 33(2):L02312.

Yagi, Y., Kikuchi, M., and Nishimura, T. (2003). Co-seismic slip, post-seismic slip, and largest aftershock associated with the 1994 Sanriku-haruka-oki, Japan, earthquake. *Geophysical Research Letters*, 30(22):3–6.

Yamasaki, T. and Houseman, G. A. (2012). The crustal viscosity gradient measured from post-seismic deformation: A case study of the 1997 Manyi (Tibet) earthquake. *Earth and Planetary Science Letters*, 351-352:105–114.

Yan, Y., Trouvé, E., Pinel, V., Mauris, G., Pathier, E., and Galichet, S. (2012). Fusion of D-InSAR and sub-pixel image correlation measurements for coseismic displacement field estimation: Application to the Kashmir earthquake (2005). *International Journal of Image and Data Fusion*, 3(1):71–92.

Yelles, K., Lammali, K., Mahsas, A., Calais, E., and Briole, P. (2004). Coseismic deformation of the May 21st, 2003, Mw = 6.8 Boumerdes earthquake, Algeria, from GPS measurements. *Geophysical Research Letters*, 31(13):L13610.

Yu, S.-B., Hsu, Y., Kuo, L., Chen, H., and Liu, C. (2003). GPS measurement of postseismic deformation following the 1999 Chi-Chi, Taiwan, earthquake. *Journal of Geophysical Research*, 108(B11):2520.

Zhang, Y., Zhang, G., Hetland, E. A., Shan, X., Wen, S., and Zuo, R. (2016). Coseismic Fault Slip of the September 16, 2015 Mw 8.3 Illapel, Chile Earthquake Estimated from InSAR Data. *Pure and Applied Geophysics*, 173(4):1029–1038.

Zhou, R., Schoenbohm, L. M., and Cosca, M. (2013). Recent, slow normal and strike-slip faulting in the Pasto Ventura region of the southern Puna Plateau, NW Argentina. *Tectonics*, 32(1):19–33.

Zhou, Y., Parsons, B., Elliott, J. R., Barisin, I., and Walker, R. T. (2015). Assessing the ability of Pleiades stereo imagery to determine height changes in earthquakes: A case study for the El Mayor-Cucapah epicentral area. *Journal of Geophysical Research: Solid Earth*, 120(12):8793–8808.

Zhou, Y., Walker, R. T., Hollingsworth, J., Talebian, M., Song, X., and Parsons, B. (2016). Coseismic and postseismic displacements from the 1978 Mw 7.3 Tabas-e-Golshan earthquake in eastern Iran. *Earth and Planetary Science Letters*, 452:185–196.

Zwick, P., McCaffrey, R., and Abers, G. (1994). MT5 Program.

Appendix A

A.1 Co- and Post-seismic Moment Scaling

Earthquake	**Coseismic Reference(s)**	M_c (Nm)	**Postseismic Reference(s)**	M_p (Nm)	**Ratio** (M_p/M_c)
Bam	[Funning et al., 2005b]	9.8×10^{18}	[Fielding et al., 2009]	1.0×10^{17}	0.01
	[Fialko et al., 2005]	7.0×10^{18}	[This study]	$< 5.0 \times 10^{17}$	
	[Motagh et al., 2006]	6.8×10^{18}			
L'Aquila	[D'Agostino et al., 2012]	2.9×10^{18}	[D'Agostino et al., 2012]	6.5×10^{17}	0.21
	[Cheloni et al., 2010]	3.9×10^{18}			
	[Walters et al., 2009]	2.8×10^{18}			
	[Atzori et al., 2009]	2.7×10^{18}			
Chi Chi	[Hsu et al., 2002]	1.5×10^{20}	[Hsu et al., 2002]	2.1×10^{19}	0.14
	[Johnson et al., 2001]	2.8×10^{20}	[Yu et al., 2003]	4.7×10^{19}	
Parkfield	[Barbot et al., 2009]	2.0×10^{18}	[Barbot et al., 2009]	3.7×10^{18}	1.72
	[Ji et al., 2004]	9.0×10^{17}			
	[Johanson et al., 2006]	2.2×10^{18}	[Johanson et al., 2006]	1.6×10^{18}	
	[Langbein et al., 2006]	1.2×10^{18}	[Freed, 2007]	3.2×10^{18}	
Nias	[Hsu et al., 2006]	1.0×10^{22}	[Hsu et al., 2006]	2.5×10^{21}	0.25
	[Briggs et al., 2006]	9.8×10^{21}	[Kreemer et al., 2006]	2.0×10^{21}	
Nima-Gaiza	[Ryder et al., 2010]	5.9×10^{18}	[Ryder et al., 2010]	1.2×10^{18}	0.26
	[Sun et al., 2008]	2.0×10^{18}			
	[Elliott et al., 2010]	5.6×10^{18}			
Damxung	[Bie et al., 2014]	3.7×10^{18}	[Bie et al., 2014]	3.8×10^{17}	0.11
	[Elliott et al., 2010]	3.1×10^{18}			
Miyagi	[Miura et al., 2006]	6.4×10^{19}	[Miura et al., 2006]	3.9×10^{19}	0.88
	[Takada et al., 2009]	2.5×10^{19}			
Northridge	[Donnellan and Lyzenga, 1998]	1.3×10^{19}	[Donnellan and Lyzenga, 1998]	2.9×10^{18}	0.22
	[Wald et al., 1996]	1.3×10^{19}			
Napa Valley	[Floyd et al., 2016]	1.7×10^{18}	[Floyd et al., 2016]	5.0×10^{17}	0.31
	[Dreger et al., 2015]	1.3×10^{18}			
	[Barnhart et al., 2015]	1.4×10^{18}			
	[Guangcai et al., 2015]	2.0×10^{18}			
Wenchuan	[Hao et al., 2013]	7.3×10^{20}	[Hao et al., 2013]	1.7×10^{20}	0.13
	[Shen et al., 2009]	8.0×10^{20}	[Shao et al., 2011]	1.8×10^{19}	
	[Tong et al., 2010]	6.8×10^{20}			
	[Hashimoto et al., 2010]	5.4×10^{20}			
	[Feng et al., 2010]	8.0×10^{20}			
	[Fielding et al., 2013]	9.5×10^{20}			
Kashmir	[Pathier et al., 2006]	3.4×10^{20}	[Pathier et al., 2006]	7.5×10^{19}	0.51
	[Avouac et al., 2006]	2.8×10^{20}	[Jouanne et al., 2011]	2.3×10^{20}	
	[Bendick et al., 2007]	2.9×10^{20}			
	[Yan et al., 2012]	3.0×10^{20}			
Chengkung	[Hsu et al., 2009]	2.0×10^{19}	[Hsu et al., 2009]	2.7×10^{18}	0.34
	[Thomas et al., 2014a]	1.9×10^{19}	[Thomas et al., 2014a]	1.5×10^{19}	
	[Wu et al., 2006]	1.8×10^{19}	[Cheng et al., 2009]	1.8×10^{18}	
	[Ching et al., 2007]	1.9×10^{19}			
	[Cheng et al., 2009]	2.0×10^{19}			
Boumerdes	[Yelles et al., 2004]	1.7×10^{19}	[Mahsas et al., 2008]	3.2×10^{18}	0.15
	[Delouis et al., 2004]	2.9×10^{19}	[Cetin et al., 2012]	4.1×10^{18}	
	[Meghraoui et al., 2004]	2.8×10^{19}			
Izmit	[Reilinger, 2000]	1.7×10^{20}	[Reilinger, 2000]	2.9×10^{19}	0.16
	[Çakir et al., 2003]	1.9×10^{20}			
	[Feigl et al., 2002]	1.8×10^{20}			
El-Mayor Cucapah	[Gonzalez-Ortega et al., 2014]	7.9×10^{19}	[Rollins et al., 2015]	7.0×10^{19}	0.08
	[Wei et al., 2011]	9.9×10^{19}			
Methoni	[Howell et al., 2016]	2.9×10^{19}	[Howell et al., 2016]	4.0×10^{19}	1.38
Sefidabeh	[Parsons et al., 2006]	7.5×10^{18}	[Copley and Reynolds, 2014]	5.0×10^{17}	0.07
Landers	[Savage and Svarc, 1997]	9.0×10^{19}	[Savage and Svarc, 1997]	1.4×10^{19}	0.16
	[Hudnut et al., 1994]	1.0×10^{20}	[Shen et al., 1994]	1.7×10^{19}	
Hector Mine	[Simons et al., 2002]	7.0×10^{19}	[Jacobs et al., 2002]	1.0×10^{18}	0.015

	[Kaverina et al., 2002]	6.8×10^{19}			
Gorkha	[Avouac et al., 2015]	7.2×10^{20}	[Mencin et al., 2016]	7.2×10^{19}	0.11
	[Wang and Fialko, 2015]	6.1×10^{20}			
Sanriku-Oki	[Yagi et al., 2003]	4.4×10^{20}	[Yagi et al., 2003]	1.8×10^{20}	0.48
	[Tanioka et al., 1996]	3.1×10^{20}			
Tokachi-Oki	[Miyazaki et al., 2004a]	2.2×10^{21}	[Miyazaki et al., 2004b]	4.0×10^{20}	0.24
			[Baba et al., 2006]	9.7×10^{20}	
			[Ozawa et al., 2004]	5.6×10^{20}	
Antofagasta	[Pritchard et al., 2002]	2.4×10^{21}	[Chlieh et al., 2004]	1.6×10^{20}	0.11
	[Ruegg et al., 1996]	1.5×10^{20}			
Pisco	[Perfettini et al., 2010]	1.3×10^{21}	[Perfettini et al., 2010]	1.7×10^{20}	0.14
	[Motagh et al., 2008]	1.2×10^{21}			
	[Sladen et al., 2010]	1.2×10^{21}			
Tohoku-Oki	[Ozawa et al., 2011]	3.4×10^{22}	[Ozawa et al., 2011]	3.4×10^{21}	0.09
	[Iinuma et al., 2012]	4.0×10^{22}			
Illapel	[Barnhart et al., 2016]	1.0×10^{22}	[Barnhart et al., 2016]	2.0×10^{20}	0.03
	[Zhang et al., 2016]	3.3×10^{21}			
Tocopilla	[Béjar-Pizarro et al., 2010]	3.2×10^{20}	[Béjar-Pizarro et al., 2010]	2.0×10^{19}	0.06
Sumatra-Andaman	[Lay et al., 2005]	8.8×10^{22}	[Chlieh et al., 2007]	2.4×10^{22}	0.03
	[Vigny et al., 2005]	3.0×10^{22}	[Hoechner et al., 2011]	1.2×10^{22}	
	[Chlieh et al., 2007]	6.9×10^{22}			
	[Stein and Okal, 2005]	1.0×10^{23}			
Maule	[Lin et al., 2013]	2.3×10^{21}	[Lin et al., 2013]	4.4×10^{20}	0.19
Arequipa	[Ruegg et al., 2001]	4.4×10^{21}	[Melbourne et al., 2002]	1.7×10^{21}	0.39

Table A.1 Compilation of geodetic slip inversions used in determining the empirical scaling between coseismic and postseismic geodetic moment release presented in Chapter 2. For events where there are multiple estimates, the ratio M_p/M_c given in the final column is calculated from the arithmetic means of all the estimates.

Appendix B

B.1 Earthquake Catalogue for the Andes

Year	Lon. (°)	Lat. (°)	z (km)	Method	Strike	Dip	Rake	M_w	γ (%)	Ref.
WFM										
19440115	-68.50	-31.55	11	BWF	45	35	110	7.0	-	[Alvarado and Beck, 2006]
19461110	-77.86	-8.47	16	BWF	135	30	-90	6.8	-	[Doser, 1987]
19631103	-77.91	-3.49	13	BWF	173	37	95	6.3	-	[Chinn and Isacks, 1983]
19631214	-61.01	-2.3	45	BWF	243	52	96	5.1	-	[Assumpção and Suarez, 1988]
19640213	-18.06	-56.69	5	BWF	130	60	37	5.0	-	[Assumpção and Suarez, 1988]
19670809	-73.80	-8.50	42	BWF	346	45	82	5.1	-	[Assumpção, 1992]
19680619	-77.26	-5.56	20	BWF	0	35	70	6.8	-	[Suarez et al., 1983]
19680620	-77.26	-5.52	16	BWF	143	40	47	5.8	-	[Suarez et al., 1983]
19680827	-72.89	-8.90	26	BWF	240	48	157	4.9	-	[Assumpção and Suarez, 1988]
19681201	-74.83	-10.64	18	BWF	171	40	90	5.8	-	[Chinn and Isacks, 1983]
19690718	-63.34	-18.29	15	BWF	182	37	95	5.5	-	[Assumpção and Araujo, 1993]
19690724	-75.08	-11.86	6	BWF	205	30	142	6.1	-	[Suarez et al., 1983]
19691001	-75.19	-11.84	5	BWF	160	25	113	6.6	-	[Suarez et al., 1983]
19700214	-75.54	-9.91	28	BWF	350	36	90	6.0	-	[Suarez et al., 1983]
19711015	-73.40	-14.18	8	BWF	310	80	10	5.6	-	[Suarez et al., 1983]
19720320	-76.78	-6.81	38	BWF	357	35	90	6.4	-	[Suarez et al., 1983]
19720926	-68.17	-30.94	20	BWF	360	40	81	6.0	-	[Chinn and Isacks, 1983]
19740927	-71.37	2.73	6	BWF	59	87	-175	6.0	-	[Suarez et al., 1983]
19760515	-74.42	-11.62	18	BWF	62	65	12	6.7	-	[Suarez et al., 1983]
19771123	-67.75	-31.73	17	BWF	10	45	80	7.3	-	[Kadinsky-Cade et al., 1985]
19771128	-67.39	-31.47	15	BWF	338	60	84	6.1	-	[Chinn and Isacks, 1983]
19771206	-67.90	-31.24	-	BWF	180	39	62	5.9	-	[Chinn and Isacks, 1983]
19800306	-71.16	-6.17	18	BWF	134	41	92	4.8	-	[Assumpção and Suarez, 1988]
19820808	-58.10	-24.80	12	BWF	126	88	-1	4.9	-	[Assumpção and Suarez, 1988]
19821111	-74.69	-10.61	14	DP	1	34	116	6.3	-	[Assumpção, 1992]
19830805	-62.17	-3.59	23	BWF	305	60	120	5.5	-	[Assumpção and Suarez, 1988]
19860405	-71.81	-13.41	6	DP	121	32	-64	5.2	89	[Devlin et al., 2012]
19870913	-70.03	-34.35	13	BWF	111	43	46	5.9	-	[Assumpção, 1992]
19890316	-65.01	-17.00	20	BWFd	171	9	127	5.3	85	[Devlin et al., 2012]
19890624	-66.25	-28.34	22	BWFd	53	42	89	5.6	-	[Emmerson, 2007]
19900530	-77.20	-6.02	23	BWF	166	25	109	6.4	-	[Tavera and Buforn, 2001]
19910404	-77.13	-6.05	21	BWF	196	24	96	6.2	-	[Tavera and Buforn, 2001]
19930722	-71.18	6.49	18	BWF	24	35	-93	6.1	-	This study
19930802	-74.17	-11.73	24	BWFd	293	61	4	5.4	81	[Devlin et al., 2012]
19940531	-72.04	7.39	6	BWF	138	38	78	6.1	-	This study
19950119	-72.94	5.04	21	BWF	214	57	97	6.5	-	This study
19950612	-75.86	-8.33	31	DP	359	29	85	5.4	94	[Emmerson, 2007]
19951003	-77.53	-2.55	19	BWF	216	40	103	6.8	-	This study
19951206	-75.91	-8.32	33	BWF	350	31	82	5.4	-	[Devlin et al., 2012]
19960310	-69.44	-13.05	31	BWF	300	40	74	5.7	-	[Devlin et al., 2012]
19960406	-75.13	-10.24	25	DP	299	26	72	5.2	86	[Emmerson, 2007]
19980110	-72.03	-11.99	7	BWF	82	14	67	6.3	-	[Emmerson, 2007]
19980219	-74.31	-10.94	6	DP	131	41	82	5.9	85	[Emmerson, 2007]
19980306	-74.50	-10.90	7	DP	142	17	106	5.3	89	[Emmerson, 2007]
19980310	-74.45	-10.93	6	DP	146	36	105	5.3	76	[Emmerson, 2007]
19980412*	-71.88	-15.66	10	BWFd	313	44	-47	5.8	43	[Devlin et al., 2012]
19980522	-65.54	-17.86	11	BWF	358	84	179	6.7	-	[Devlin et al., 2012]
19980526	-65.33	-17.84	13	BWF	206	86	180	5.2	-	[Devlin et al., 2012]
19980529	-65.25	-17.71	5	BWFd	84	81	2	5.4	90	[Devlin et al., 2012]
19981004	-76.24	-8.44	5	DP	188	28	113	5.5	98	[Emmerson, 2007]
19981025*	-69.39	-17.97	9	BWFd	155	60	115	5.3	45	[Devlin et al., 2012]
19991004	-75.61	-10.70	12	BWF	176	33	90	5.8	-	[Devlin et al., 2012]
19991225	-75.30	-6.17	24	BWF	176	54	113	5.6	-	[Devlin et al., 2012]
20010221	-74.45	-11.34	15	BWF	157	14	83	5.5	-	[Emmerson, 2007]
20010629	-70.35	-15.37	6	DP	110	58	-107	5.4	82	This study

20010704	-65.73	-17.19	14	BWF	89	34	51	6.1	-	[Devlin et al., 2012]
20010724	-69.25	-19.52	8	BWF	23	71	187	6.4	-	[Devlin et al., 2012]
20010809	-72.68	-14.31	12	BWF	113	87	13	5.9	-	[Devlin et al., 2012]
20010812	-70.03	-16.76	6	DP	130	45	-108	5.1	87	This study
20011012	-69.81	-33.29	5	BWF	301	73	-15	5.1	-	[Alvarado et al., 2005]
20011204*	-72.52	-15.37	17	BWFd	239	73	-178	5.8	53	[Devlin et al., 2012]
20011208	-72.71	-15.42	13	BWF	296	88	-31	5.7	-	[Devlin et al., 2012]
20011214	-68.02	-31.79	6	BWF	20	64	91	5.3	-	[Alvarado et al., 2005]
20020224	-70.13	-16.38	10	BWFd	342	51	-72	5.3	91	[Devlin et al., 2012]
20020528	-66.74	-28.95	14	BWF	188	29	78	6.0	-	[Emmerson, 2007]
20020811	-74.70	-10.79	6	DP	127	42	100	5.1	88	[Emmerson, 2007]
20021213	-71.70	-15.27	7	BWFd	71	46	-92	5.3	95	[Devlin et al., 2012]
20040322	-64.44	-23.03	14	BWFd	112	27	17	5.7	94	[Devlin et al., 2012]
20040907	-65.58	-28.57	18	BWF	227	29	94	6.2	-	[Emmerson, 2007]
20050503	-74.67	-14.88	32	BWF	282	55	-2	5.9	-	[Devlin et al., 2012]
20060809	-70.75	-14.45	8	DP	82	51	-93	5.2	87	This study
20061120*	-70.23	-17.67	37	BWFd	239	24	72	5.4	70	[Devlin et al., 2012]
20091106	-64.46	-23.44	20	DP	224	30	131	5.4	92	This study
20100227	-65.76	-24.85	9	BWFd	162	25	97	6.2	99	This study
20111006	-64.22	-24.18	15	BWF	176	56	91	5.9	-	This study
20130717	-71.74	-15.66	6	BWF	108	46	-90	6.0	-	[Devlin et al., 2012]
20140217†	-71.58	6.64	28	DP	8	67	117	5.3	70	This study
20151129	-64.65	-23.56	13	DP	222	29	129	5.8	98	This study
20161031	-74.63	3.37	40	DP	213	51	131	5.6	85	This study
20161201	-71.00	-15.28	10	BWF	144	39	-84	6.2	-	This study
20170206	-74.67	3.40	44	DP	215	42	116	5.5	85	This study
20170418	-75.31	-2.73	15	BWFd	28	42	88	5.9	88	This study
20170516†	-73.33	-14.56	9	DP	58	57	-137	5.4	68	This study
20180719	-74.61	3.42	49	DP	45	60	90	4.9	93	This study
20190214	-74.16	-11.97	21	DP	159	50	93	5.6	91	This study
nWFM										
19721205	-66.20	-17.30	43(?)	FM	97	52	152	5.0	-	[Vega and Buforn, 1991]
19760222	-65.30	-18.30	41(?)	FM	117	61	151	5.2	-	[Vega and Buforn, 1991]
19790106	-75.72	-8.92	32	EHB-gCMT	351	26	65	5.7	96	[Ekström et al., 2012]
19810418	-74.37	-13.12	41	EHB-gCMT	197	18	123	5.5	83	[Ekström et al., 2012]
19810723	-64.90	-17.00	38(?)	FM	103	66	163	5.3	-	[Vega and Buforn, 1991]
19821119	-74.65	-10.62	10	EHB-gCMT	0	34	116	6.6	98	[Ekström et al., 2012]
19831004	-70.56	-26.01	39	gCMT	9	20	110	7.7	97	[Ekström et al., 2012]
19840605	-76.69	-7.87	24	EHB-gCMT	200	20	114	5.6	91	[Ekström et al., 2012]
19841210	-75.22	-14.80	48	EHB-gCMT	254	9	-139	5.6	82	[Ekström et al., 2012]
19850303	-71.71	-33.92	41	gCMT	11	26	110	8.0	97	[Ekström et al., 2012]
19850319	-63.70	-18.60	42(?)	FM	136	39	104	5.5	-	[Vega and Buforn, 1991]
19850322	-63.60	-18.60	39(?)	FM	347	46	117	5.5	-	[Vega and Buforn, 1991]
19860509	-65.60	-17.10	13(?)	FM	106	64	157	5.6	-	[Vega and Buforn, 1991]
19860619	-65.60	-17.00	15(?)	FM	110	44	121	5.4	-	[Vega and Buforn, 1991]
19861220	-75.43	-7.69	41	EHB-gCMT	57	9	-31	5.2	99	[Ekström et al., 2012]
19870305	-70.93	-24.38	42	gCMT	12	23	106	7.6	94	[Ekström et al., 2012]
19870306	-77.67	0.04	13	EHB-gCMT	198	20	118	6.4	98	[Ekström et al., 2012]
19870306	-77.79	0.08	17	EHB-gCMT	195	27	98	7.1	98	[Ekström et al., 2012]
19870813	-70.91	-17.90	38	EHB-gCMT	327	18	76	6.5	94	[Ekström et al., 2012]
19870922	-78.03	-1.01	5	EHB-gCMT	218	42	147	6.3	98	[Ekström et al., 2012]
19871002	-77.96	-8.17	30	EHB-gCMT	296	43	-157	5.6	92	[Ekström et al., 2012]
19871115	-75.68	-9.40	16	EHB-gCMT	210	12	120	5.4	81	[Ekström et al., 2012]
19910405	-75.49	-14.21	50	EHB-gCMT	13	21	-22	6.3	99	[Ekström et al., 2012]
19930802	-74.05	-11.55	15	EHB-gCMT	293	61	4	5.4	80	[Ekström et al., 2012]
19931007	-75.77	-14.13	46	EHB-gCMT	55	33	-1	5.3	83	[Ekström et al., 2012]
19941226	-71.86	-15.72	44	EHB-gCMT	111	35	-79	5.3	87	[Ekström et al., 2012]
19950730	-70.74	-24.17	29	gCMT	354	22	87	8.0	94	[Ekström et al., 2012]
19961112	-75.37	-15.04	37	gCMT	312	33	55	7.7	98	[Ekström et al., 2012]
19961114	-75.69	-14.75	27	EHB-gCMT	304	22	43	5.7	92	[Ekström et al., 2012]
19971212	-78.81	2.32	20	gCMT	30	16	118	8.1	94	[Ekström et al., 2012]
20010623	-72.71	-17.28	30	gCMT	310	18	63	8.4	90	[Ekström et al., 2012]
20010707	-72.45	-17.45	25	gCMT	306	14	52	7.6	94	[Ekström et al., 2012]
20020203	-72.04	-15.65	1	EHB-gCMT	220	78	168	5.2	96	[Ekström et al., 2012]
20030808	-71.73	-13.85	46	EHB-gCMT	206	33	-83	5.0	88	[Ekström et al., 2012]
20040915	-75.46	-14.96	29	EHB-gCMT	322	29	71	5.0	90	[Ekström et al., 2012]
20041220	-75.21	-15.27	31	EHB-gCMT	324	19	62	5.5	86	[Ekström et al., 2012]
20051001	-70.64	-16.73	5	InSAR	340	64	-92	5.6	-	[Holtkamp et al., 2011]
20060221	-75.51	-10.28	14	EHB-gCMT	131	24	44	6.1	94	[Ekström et al., 2012]
20070707	-75.12	-15.19	30	EHB-gCMT	335	37	78	5.0	85	[Ekström et al., 2012]
20070815	-77.04	-13.73	34	gCMT	321	28	63	8.0	93	[Ekström et al., 2012]
20070817	-76.11	-14.20	20	EHB-gCMT	335	23	78	5.6	89	[Ekström et al., 2012]
20070818	-76.30	-13.81	30	EHB-gCMT	323	19	81	6.0	88	[Ekström et al., 2012]
20071114	-70.62	-22.64	38	gCMT	358	20	98	7.8	98	[Ekström et al., 2012]
20090526	-75.98	-14.42	15	PDE-gCMT	319	16	55	5.4	92	[Ekström et al., 2012]
20090615	-76.13	-13.56	42	PDE-gCMT	330	31	67	5.4	81	[Ekström et al., 2012]
20091017	-63.35	-18.58	34	PDE-gCMT	170	42	66	5.0	86	[Ekström et al., 2012]
20100227	-73.15	-35.98	23	gCMT	19	18	116	8.8	92	[Ekström et al., 2012]
20101017	-72.22	-11.72	10	PDE-gCMT	91	25	75	4.8	90	[Ekström et al., 2012]
20111028	-75.84	-14.51	10	PDE-gCMT	334	23	69	5.6	97	[Ekström et al., 2012]
20120702	-75.60	-14.42	40	PDE-gCMT	325	26	65	5.8	87	[Ekström et al., 2012]
20121003	-76.05	-14.29	24	PDE-gCMT	333	23	78	5.1	92	[Ekström et al., 2012]

20130222	-71.31	-15.70	10	PDE-gCMT	218	62	-174	5.0	86	[Ekström et al., 2012]
20130222	-71.43	-15.75	8	PDE-gCMT	210	71	-170	5.3	85	[Ekström et al., 2012]
20130725	-72.00	-15.82	19	PDE-gCMT	290	44	-81	4.8	94	[Ekström et al., 2012]
20131015	-63.27	-18.50	38	PDE-gCMT	198	41	120	5.2	93	[Ekström et al., 2012]
20140401	-70.81	-19.70	22	gCMT	355	15	106	8.2	98	[Ekström et al., 2012]
20140403	-70.60	-20.43	29	gCMT	358	14	103	7.8	97	[Ekström et al., 2012]
20140928	-71.69	-13.84	10	PDE-gCMT	138	72	-13	5.1	82	[Ekström et al., 2012]
20141031	-76.36	-7.61	18	PDE-gCMT	38	48	41	5.2	90	[Ekström et al., 2012]
20150228	-71.99	-15.70	12	PDE-gCMT	293	34	-97	5.0	81	[Ekström et al., 2012]
20150709	-75.83	-9.11	27	PDE-gCMT	2	34	111	5.2	97	[Ekström et al., 2012]
20150828	-71.81	-15.82	9	PDE-gCMT	203	73	-175	5.0	95	[Ekström et al., 2012]
20150916	-72.09	-31.13	17	gCMT	7	19	109	8.3	95	[Ekström et al., 2012]
20151001	-72.09	-15.72	30	PDE-gCMT	92	37	-104	4.8	92	[Ekström et al., 2012]
20160220	-71.82	-15.72	10	PDE-gCMT	230	40	-158	5.1	81	[Ekström et al., 2012]
20160723	-67.18	-22.42	20	gCMT	346	48	-62	5.1	94	[Ekström et al., 2012]
20161202	-70.72	-15.36	28	gCMT	115	43	-129	5.0	90	[Ekström et al., 2012]
20161225	-74.43	-43.41	33	gCMT	4	19	96	7.6	98	[Ekström et al., 2012]

Table B.1 Earthquake catalogue used to study the seismicity in the Andes. Earthquakes in the section **WFM** have been studied using some form of waveform modelling, whilst those in the section **nWFM** are taken from global catalogues, first motions studies and InSAR modelling. For the methods, BWF refers to earthquakes modelled using the inversion of long-period body-waveforms described in Section 3.2.2, in which the mechanism, moment, source-time function and the depth of the earthquake are solved for; $BWFd$ uses the same method, but fixes the mechanism to the best double-couple gCMT solution whilst inverting for depth, moment and source-time function only; DP events are modelled using synthetic seismograms that are fit to the vertical-component broadband waveforms to determine the earthquake hypocentre depth (see Section B.3); $EHB\text{-}gCMT$ are events with depths from the EHB catalogue [Engdahl et al., 1998] and mechanisms from the gCMT catalogue; $PDE\text{-}gCMT$ are events with depths from the NEIC catalogue (https://earthquake.usgs.gov/data/pde.php) and mechanisms from the gCMT catalogue; FM are events modelled using P-wave first motions and $InSAR$ are events modelled using radar geodesy. γ is the percentage double-couple of the gCMT solution, defined as $\gamma = (1 - \frac{3\lambda_2}{\lambda_1+\lambda_3}) \times 100$, where λ_1,λ_2 and λ_3 are, respectively, the absolute value of the minimum, intermediate and maximum eigenvalues of the moment tensor [Jackson et al., 2002]. Events marked (*) have percentage double-couple less than 80%, however their long-period waveforms are fit by the gCMT solution in the modelling of Devlin et al. [2012]. Events marked † have been modelled using stacked vertical-component waveforms from small-aperture arrays (see Section B.4).

B.2 Teleseismic Body-Waveform Models

In this appendix I present the results of long-period teleseismic body-waveform modelling of earthquakes in South America using the MT5 program to determine the strike, dip, rake, depth, seismic moment and source-time function. The methodology is described in Section 3.2.2. I found that the uncertainty in the source parameters, particularly the strike, dip and rake, for earthquakes in South America are generally larger than is standard for this technique, mainly due to the poor station coverage at teleseismic distances around South America. Ocean island stations that are within teleseismic distances tend to have low signal-to-noise ratios, as a result of ocean-related noise (e.g. ocean swell). Therefore, in a number of the inversions the mechanism was fixed to the best double-couple solution from the gCMT catalogue, and I solved for the depth, moment and source-time function only. Empirical uncertainties are provided as a range over which the synthetic seismograms do not violate the first motions and match the relative amplitudes and shapes of the observed waveforms. The uncertainties are estimated in the same way as described in the Section 3.2.2. For the uncertainty analysis, I varied the parameters with 5 degree increments in strike/dip/rake and 1 km increments in centroid depth.

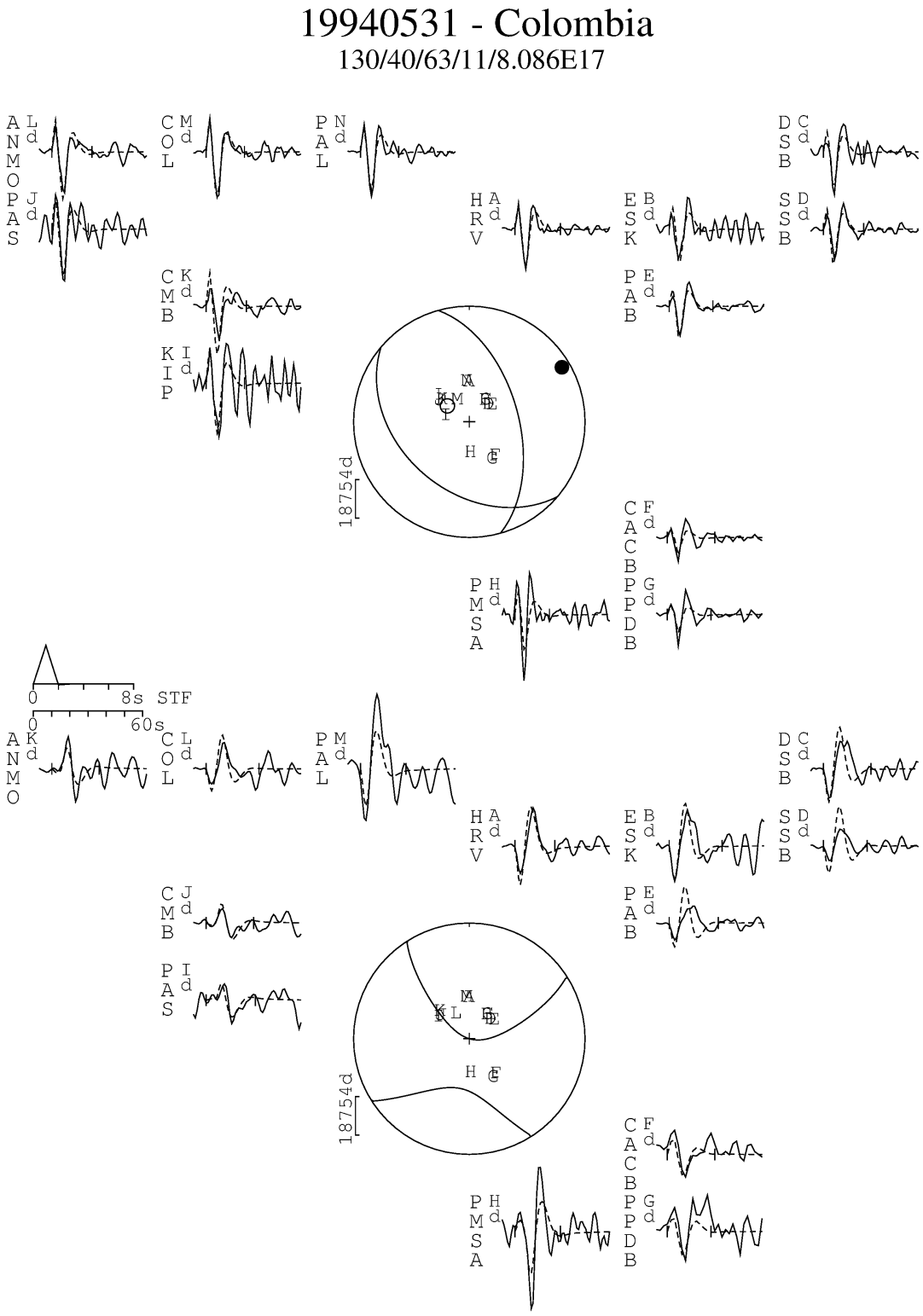

Figure B.1 Minimum-misfit teleseismic body-waveform model for the 31st June 1994 reverse-faulting earthquake in the forelands of the Colombian/Venezualan border region. The layout of the figure is the same as for Fig. 3.3 in the main text. The strike/dip/rake/depth/moment is shown beneath the title for the minimum-misfit solution. Observed (solid) and synthetic (dashed) seismograms are shown around the focal mechanism, with the station name and reference letter to the left of each seismogram. Uncertainties in the fault parameters are: strike = $^{+30}_{-25}$ (limited station coverage in the *SH* focal sphere leads to significant trade-off with changes in rake), dip = $\pm 5^o$, rake = $\pm 15^o$ and centroid depth = ± 6 km.

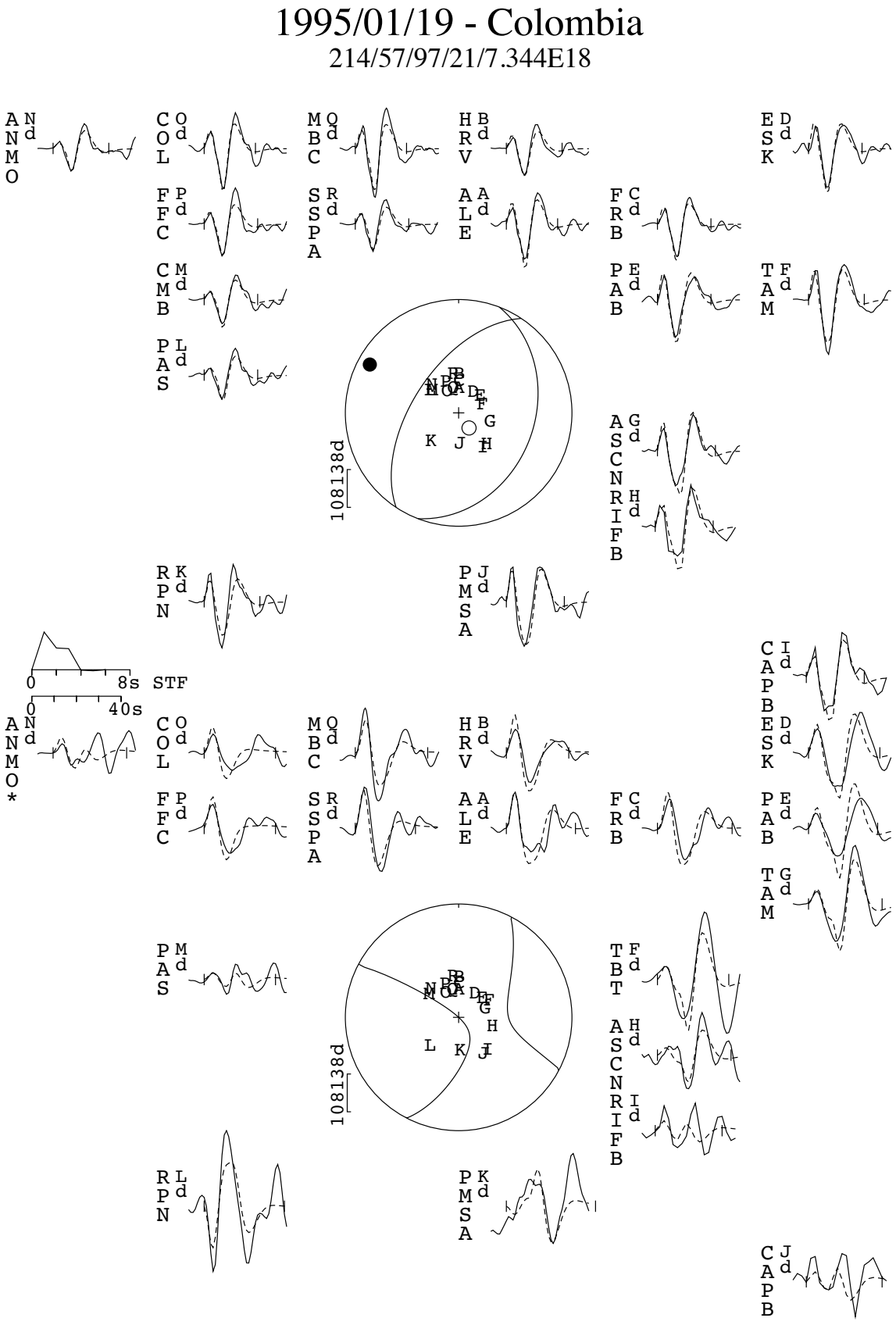

Figure B.2 Minimum-misfit teleseismic body-waveform model for the 19th January 1995 reverse-faulting earthquake along the eastern Andes range front in Colombia. Uncertainties the fault parameters are: strike $= {}^{+15}_{-35}$, dip $= {}^{+3}_{-5}$, rake $= \pm 20^{o}$ and centroid depth $= {}^{+4}_{-6}$ km.

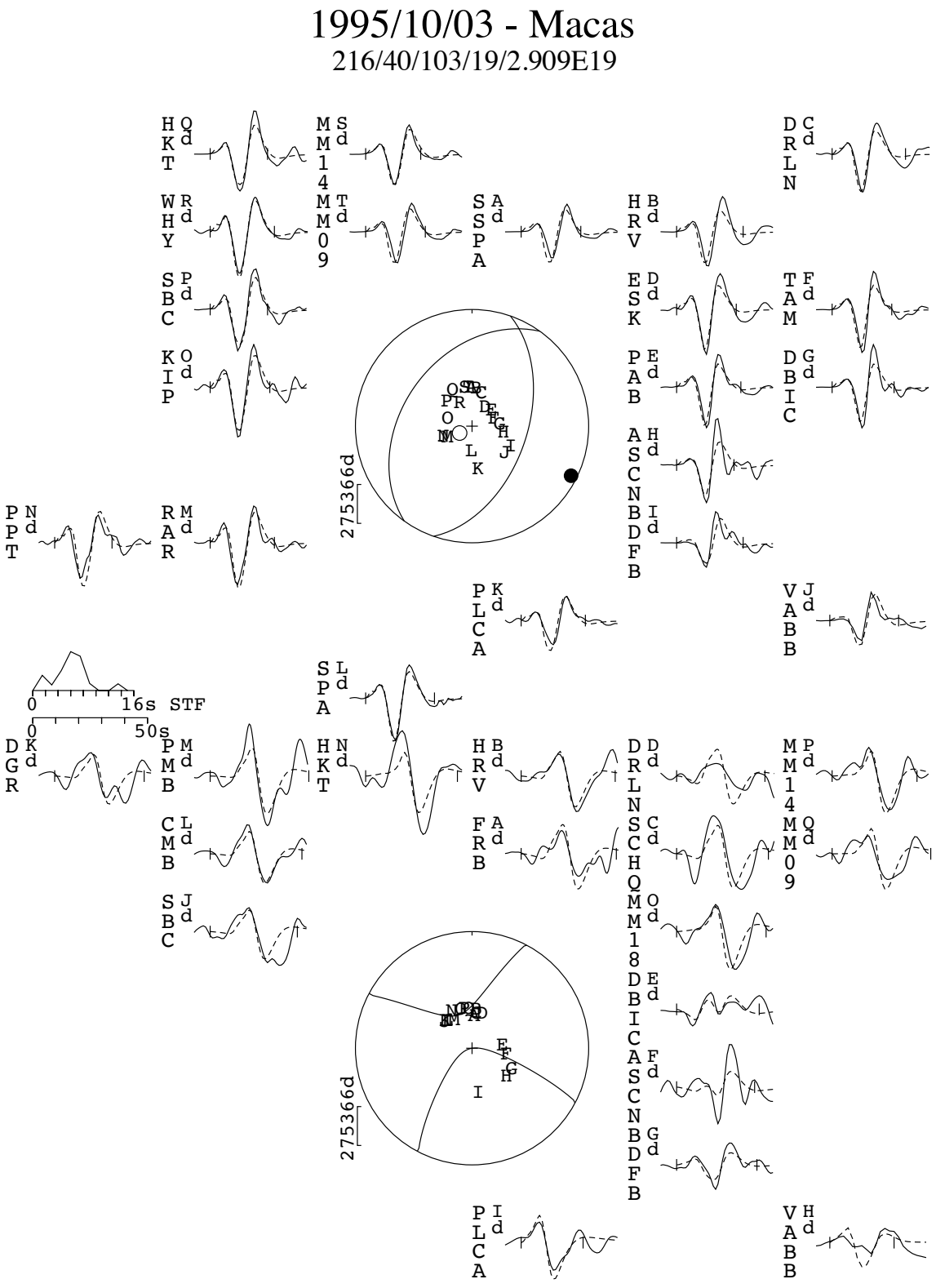

Figure B.3 Minimum-misfit teleseismic body-waveform model for the 3rd October Macas reverse-faulting earthquake along the range front of the eastern Andes in Ecuador. Uncertainties the fault parameters are: strike = $\pm 25^o$, dip = $\pm 10^o$, rake = $\pm 25^o$ and centroid depth = ± 5 km .

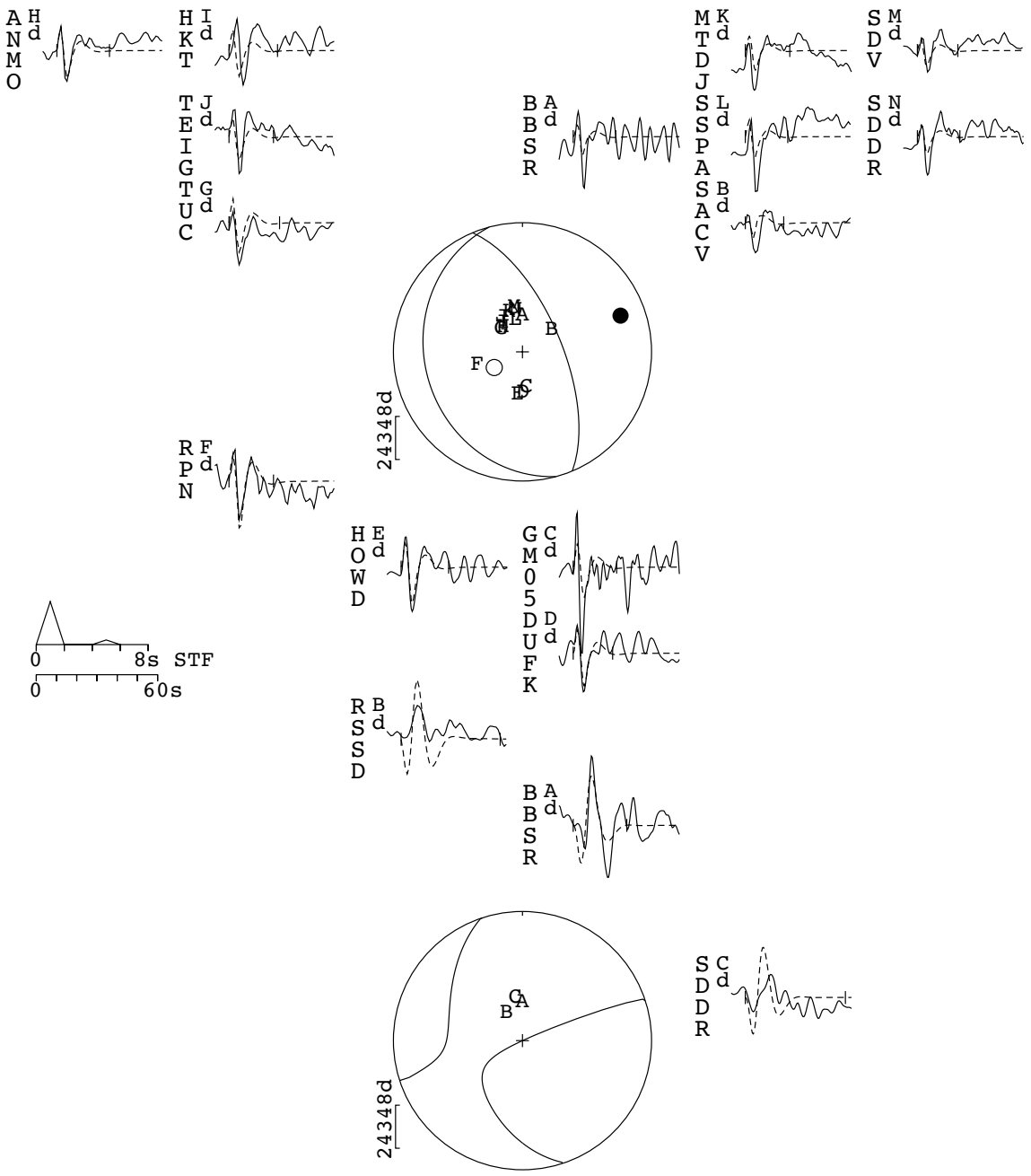

Figure B.4 Minimum-misfit teleseismic body-waveform model for the 27th February 2010 earthquake near Salta, Argentina (also studied by Scott et al. [2014]). The mechanism was fixed to the gCMT best double-couple solution, and I performed the inversion for moment, source-time function and depth only. I found centroid depths <20 km generally provide a reasonable fit to the waveforms. A M_w 8.8 earthquake on the subduction interface offshore Chile and a M_w 7.7 outer-rise normal-faulting earthquake preceded this event by 9 and 7 hours, respectively. Long-period noise in the seismograms is probably coda from these preceding events, and leads to a non-zero mean and a low signal-to-noise ratio of the observed waveforms, limiting further analysis.

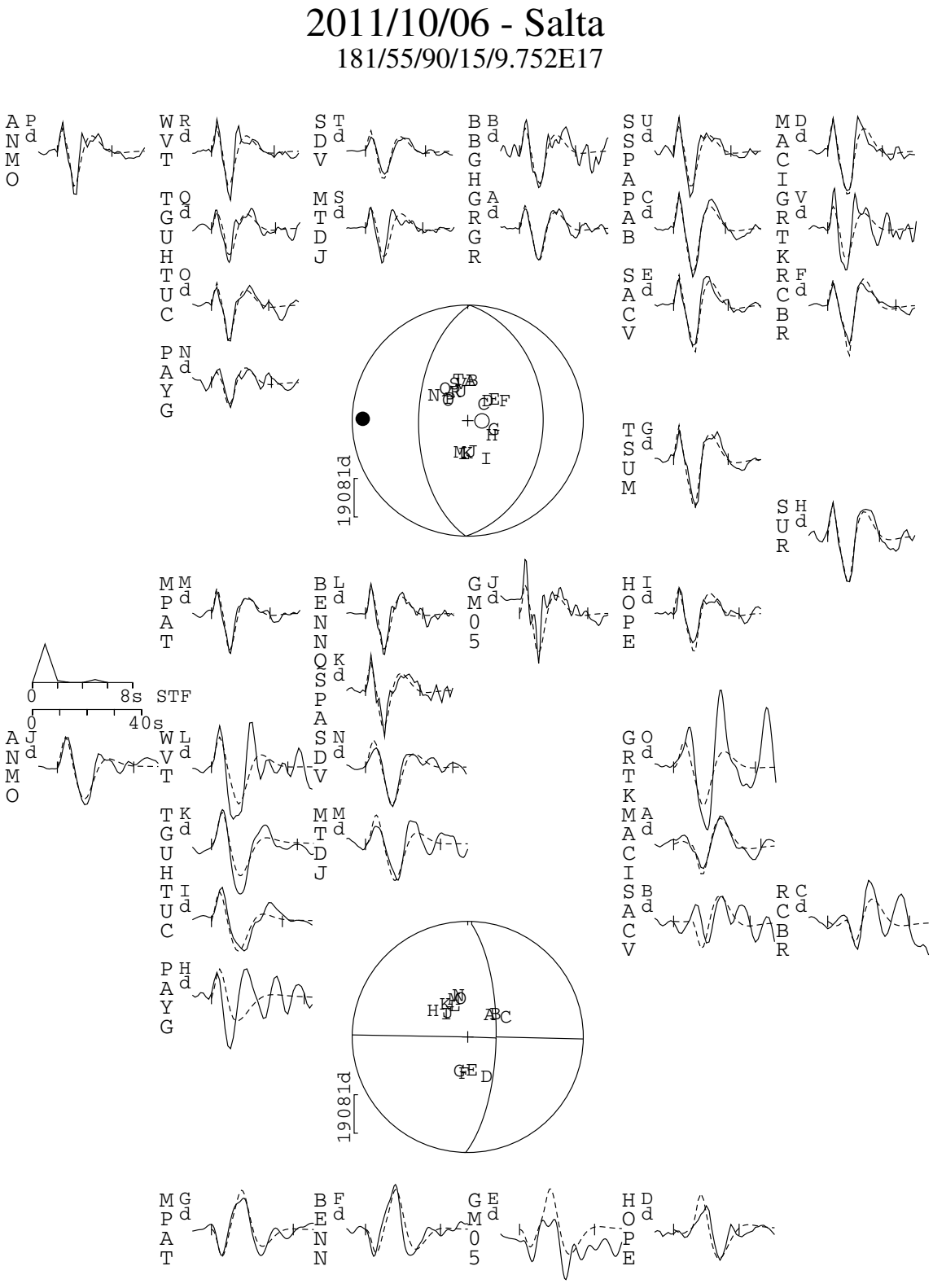

Figure B.5 Minimum-misfit teleseismic body-waveform model for the 6th October 2011 earthquake in Salta Province, Argentina. The uncertainties in the fault parameters are: strike = $\pm 15^o$, dip = $\pm 5^o$, rake = $\pm 15^o$ and centroid depth = $^{+3}_{-10}$ km. The extended lower bound for the centroid depth is due to a significant trade-off between the source-time function and centroid depth when the earthquake is shallow, as the direct and depth-phase arrivals overlap in the long-period waveforms.

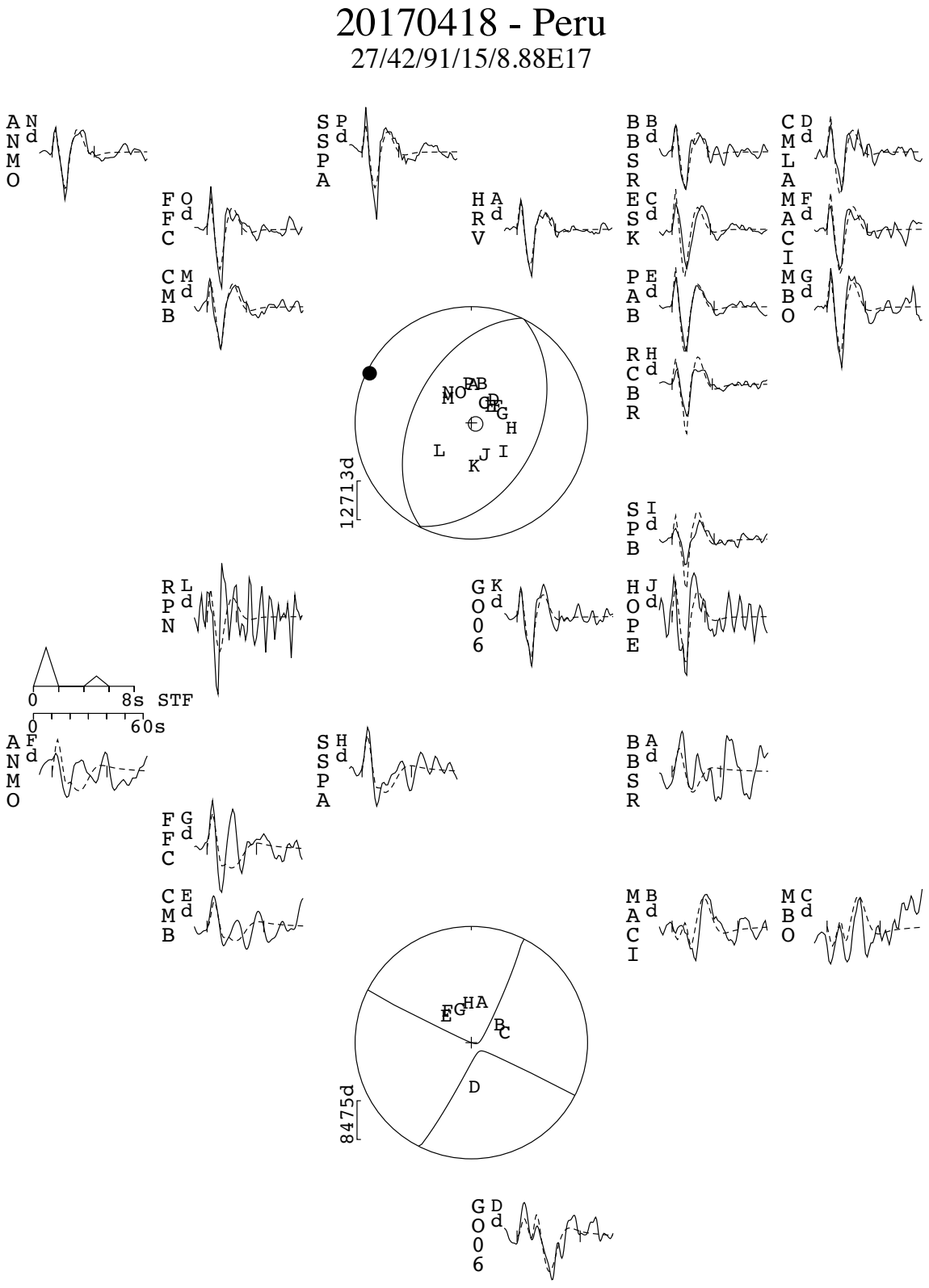

Figure B.6 Minimum-misfit teleseismic body-waveform model for the 18th May 2017 earthquake within the Oriente foreland of northern Peru. The source mechanism was fixed at the best double-couple gCMT solution, and I solved for the depth and source-time function only. The gCMT mechanism provides a reasonable fit to the observed waveforms, with acceptable centroid depths in the range 5-22 km.

B.3 Earthquake Depths from Forward Modelling

A number of M_w 5-5.7 earthquakes in the high Andes and South American forelands were too small to generate usable signals at teleseismic distances in the period band needed for full body-waveform modelling as described in Section 3.2.2. However, these events often have clear direct (P) and depth-phase (pP, sP) arrivals on vertical-component seismograms recorded at teleseismic distances. In this section, I present models of the broadband vertical-component seismograms for a number of smaller-magnitude earthquakes, using synthetic seismograms to estimate their hypocentre depths [e.g. Maggi et al., 2000b].

To generate the synthetic seismograms, I calculated the impulse response of the direct P phase and depth phases pP, sP for each event, using its gCMT source mechanism [Dziewonski et al., 1981; Ekström et al., 2012] and NEIC catalogue epicentral location, by ray tracing through the ak135 velocity model [Kennett et al., 1995] using the WKBJ3 algorithm [Chapman, 1978]. The velocity model was adapted to have a crustal thickness of 65-80 km in the Andes, or 40-45 km in the forelands. Due to the small magnitude of these earthquakes, it is reasonable to assume that their source-time function approximates an impulse when measured at teleseismic distances and in the period band studied (1-100 s). The impulse response was then convolved with the relevant station instrument response and a Futterman attenuation operator to account for anelasticity and geometrical spreading effects on the waveform amplitude ($t^* = 1$). The synthetic waveforms were then aligned on the first peak or trough following the direct P arrival on the broadband vertical-component seismograms to avoid uncertainties in picking non-impulsive first arrivals. Finally, I normalised the amplitude of the modelled waveform to the observed waveform over a 30-50 second window using the root-mean-square amplitude of the waveforms.

For earthquakes with particularly small magnitudes ($M_w \lesssim 5.0$), I used recordings from small-aperture seismic arrays in North America and Northern Europe to study the depth-phase signals using the method of Heyburn and Bowers [2008] and Craig et al. [2012]. This technique uses the NEIC earthquake location to calculate the back azimuth and slowness of the body-wave arrivals, and, assuming that the wavefront is planar as it passes over the array, the seismograms are time-migrated and linearly stacked into what is referred to as the 'beam'. Subsequently, I applied a 4-pole Butterworth filter to extract the high-frequency body-wave signals in the beam, and the same filter was applied to the synthetics.

An additional quality control that I used for identifying the depth-phase arrivals at the small-aperture array sites is the F-statistic. The F-statistic is a measure of the coherency of the energy within the beam, and is defined as the power of the beam divided by the difference between each seismogram in the array and the beam averaged over a window [Heyburn and Bowers, 2008]:

$$F(t) = (N-1)\frac{\sum_{t=1}^{M} \hat{u}(t)^2}{\left(\frac{1}{N}\sum_{i=1}^{N}\sum_{t=1}^{M} u_i(t)^2 - \sum_{t=1}^{M} \hat{u}(t)^2\right)}, \tag{B.1}$$

where u_i is the amplitude of trace i at time t, $\hat{u}$ is the amplitude of the beam, N is the number of traces in each beam and M is the width of the window used for averaging. Therefore, if $F(t)$ is large, then signals are coherent as the numerator in Equation B.1 (the beam amplitude) is larger than the denominator (the difference between the beam amplitude and the individual traces).

To determine the hypocentre depth of each event, I systematically varied the source depth used to calculate the synthetics, starting from the EHB or NEIC catalogue estimate, until I found the best-fit between the relative amplitudes and arrival times of the depth phases on the observed and synthetic waveforms. I also varied the source mechanism, which controls the relative amplitudes of the direct and depth phase arrivals, to test the effect on the depth estimates. However, I generally found that it is difficult to differentiate between the effects of noise and source mechanism on the relative amplitudes of the depth phases. In addition, the same depth does not always provide the best fit to all the seismograms, probably because there is significant azimuthal heterogeneity in the velocity structure beneath the Andes that is not accounted for in the 1-D velocity model. Nonetheless, I found that the depths of earthquakes in which the depth phases are separated from the direct arrivals (typically those >10 km depth) are constrained to within ±3 km using this technique, which is roughly equivalent to half a cycle in the depth-phase waveforms.

For shallower events (<7-8 km) the depth phases often overlap with the direct P arrival, so there is a trade-off between the finite length of the source-time function, or changes in the earthquake mechanism, and the earthquake depth. Therefore, I do not attempt to remodel the earthquake mechanisms based upon the vertical-component seismograms for these shallow events, and only interpret the depth of the earthquakes as being shallower than ∼7-8 km.

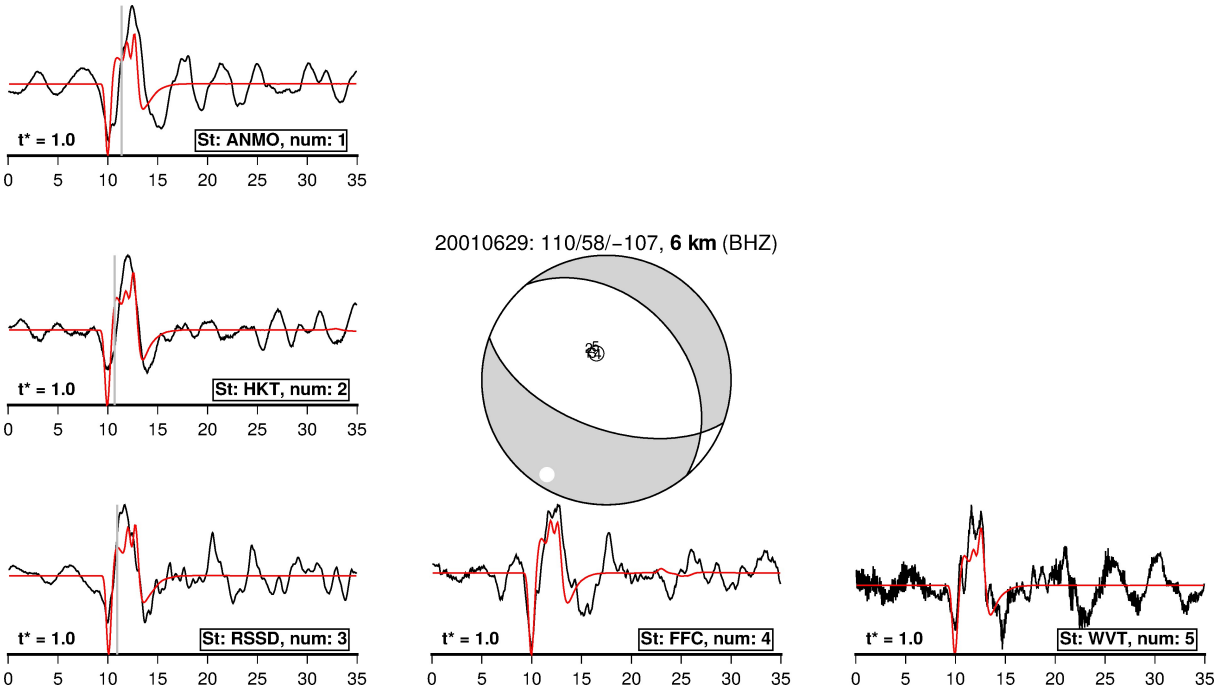

Figure B.7 Synthetic depth-phase modelling for the 29th June 2001 M_w 5.4 earthquake in the high Andes of south Peru. Observed broadband seismograms are shown in black, with the modelled seismograms in red. The station code is shown in the bottom right of each seismogram, along with the station number that is also plotted on the focal sphere. The value of the Futterman attenuation operator t^* is shown in the bottom left. The focal mechanism is the best double-couple gCMT solution for the event used to generate the synthetic seismograms. P and T axes of the mechanism are shown as black and white circles, respectively. The timescale shown below the seismograms is in seconds. The date, source parameters and best-fit hypocentre depth of the earthquake are shown above the focal mechanism. Grey vertical lines are the predicted P arrival using the NEIC epicentre and the ak135 velocity model. All subsequent images follow the same format.

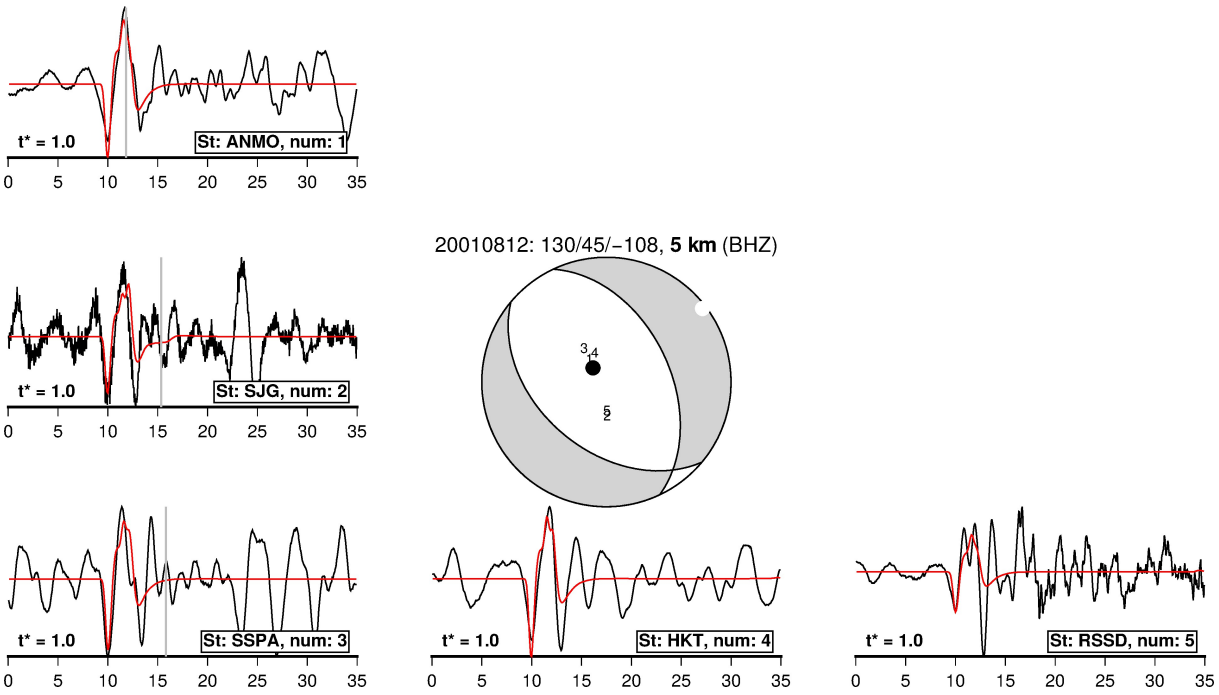

Figure B.8 Synthetic depth-phase modelling for the 12th August 2001 M_w 5.1 earthquake in the high Andes of south Peru.

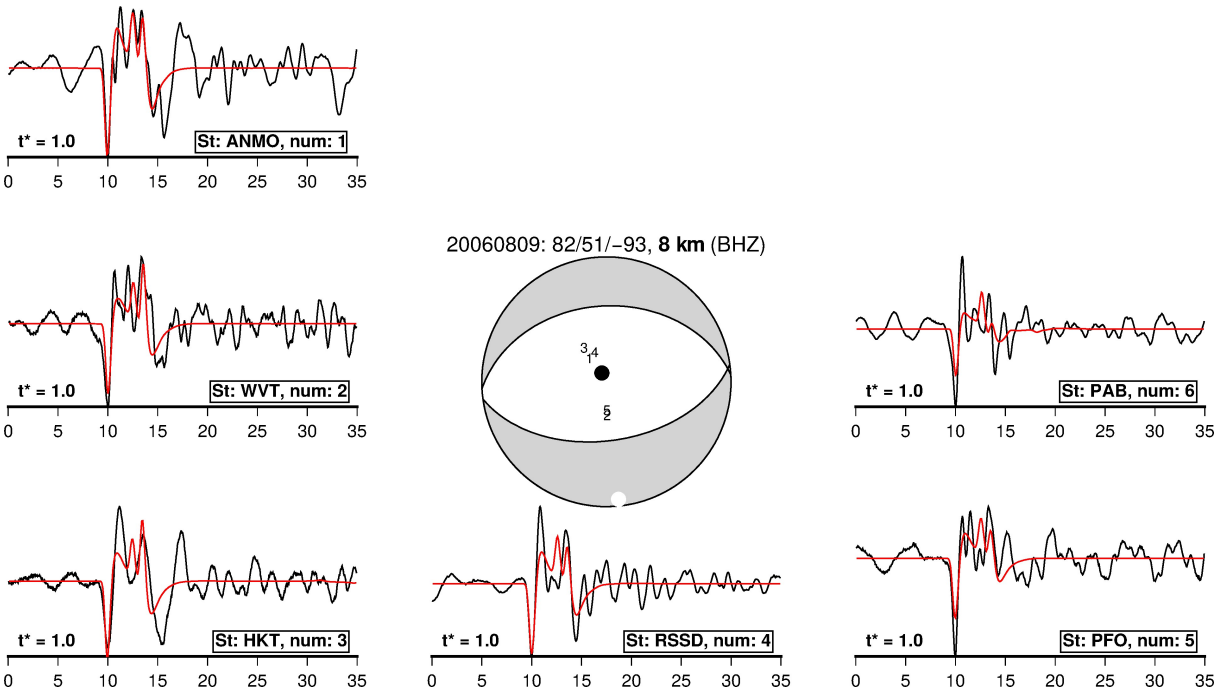

Figure B.9 Synthetic depth-phase modelling for the 9th August 2006 M_w 5.2 earthquake in the high Andes of south Peru.

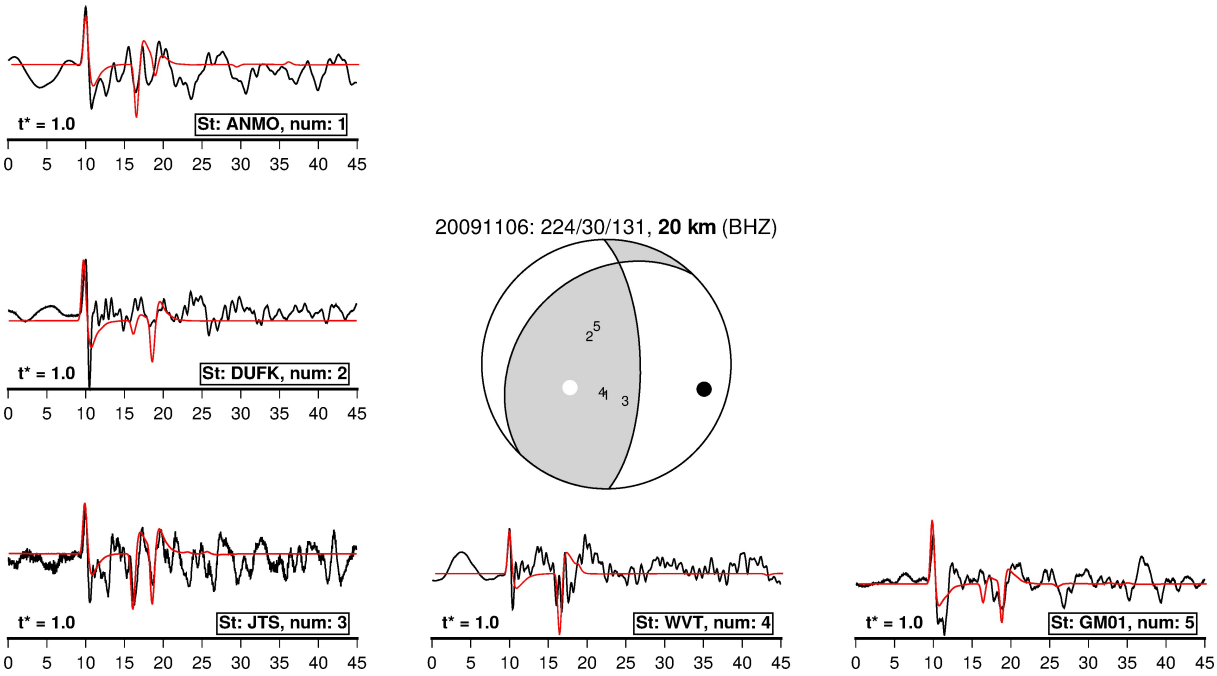

Figure B.10 Synthetic depth-phase modelling for the 6th November 2009 M_w 5.4 earthquake in the Argentinian foreland.

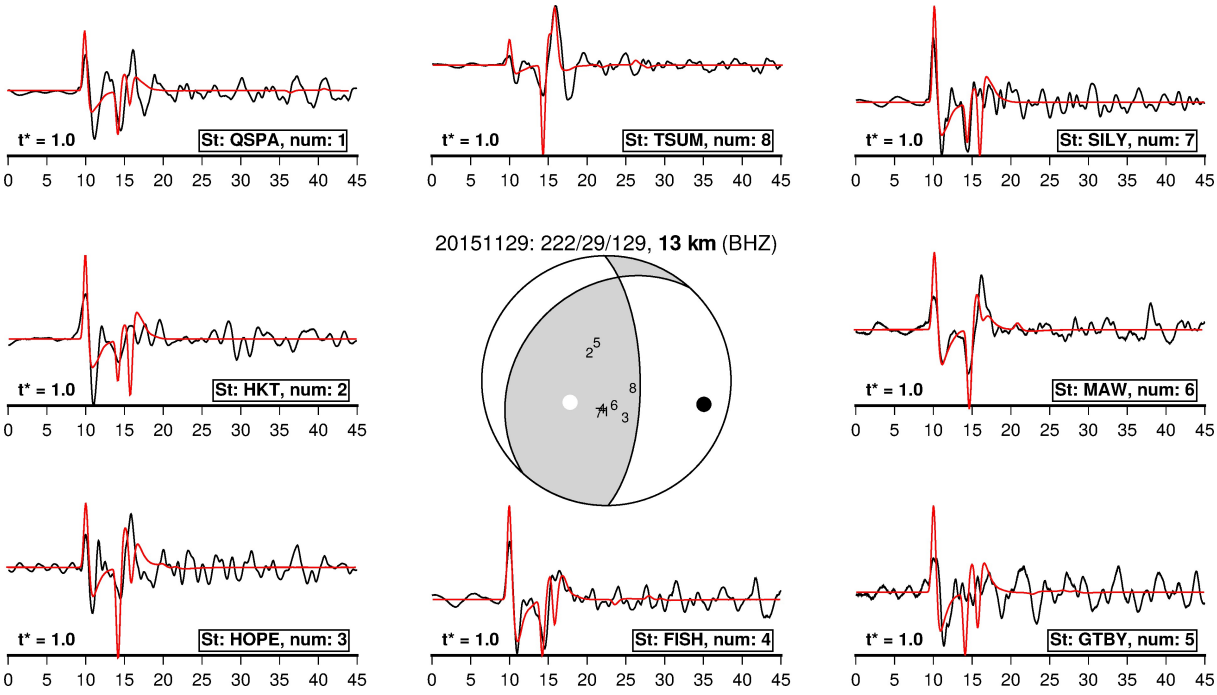

Figure B.11 Synthetic depth-phase modelling for the 29th Novemeber 2015 M_w 5.7 earthquake in the Argentinian foreland.

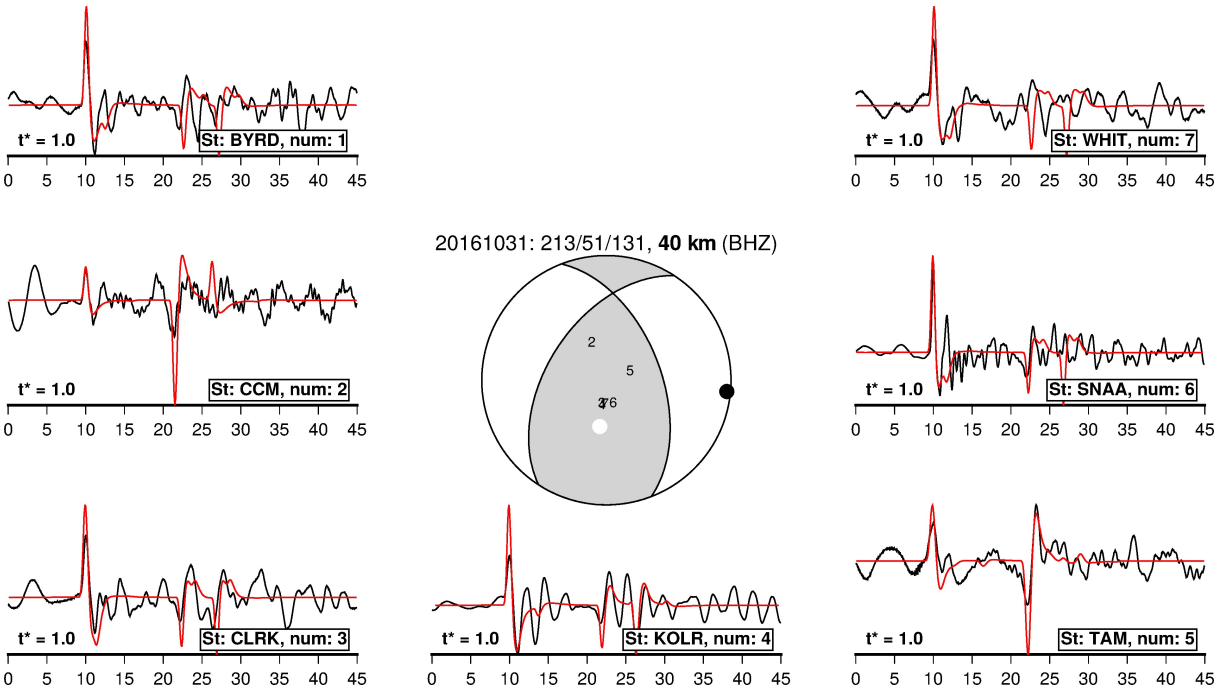

Figure B.12 Synthetic depth-phase modelling for the 31st October 2016 M_w 5.6 earthquake in the foreland of the Colombian Andes.

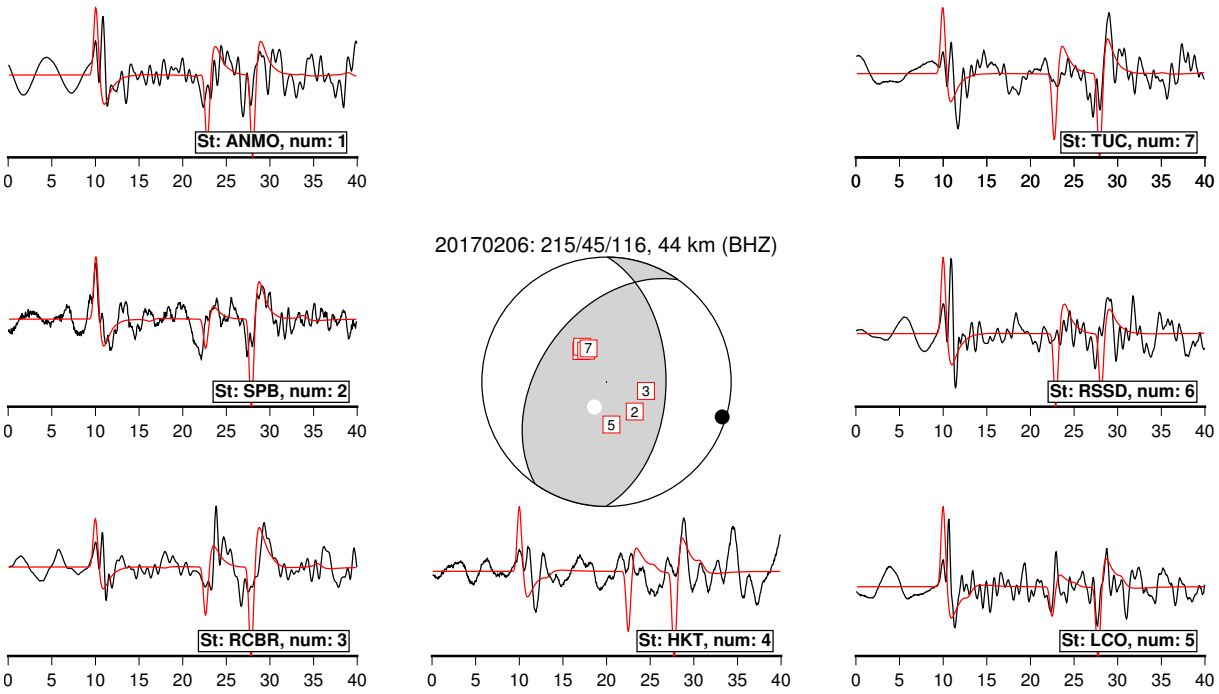

Figure B.13 Synthetic depth-phase modelling for the 6th February 2017 M_w 5.5 earthquake in the foreland of the Colombian Andes.

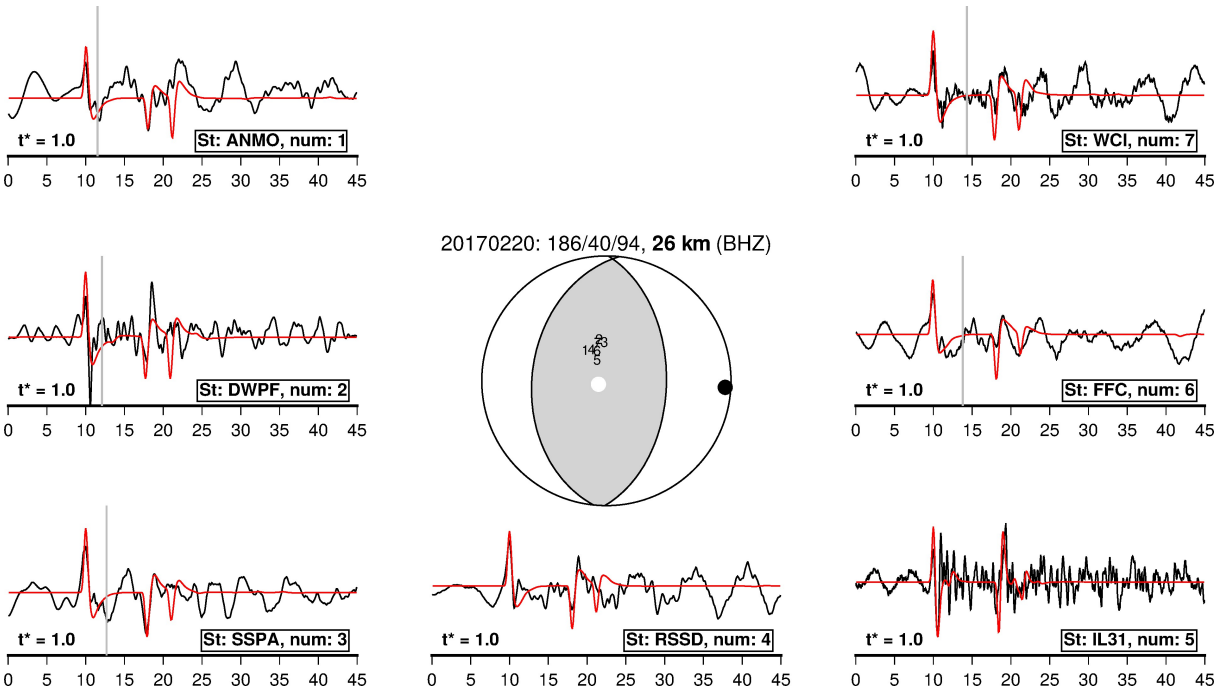

Figure B.14 Synthetic depth-phase modelling for the 20th February 2017 M_w 5.4 earthquake in the foreland of the Peruvian Andes.

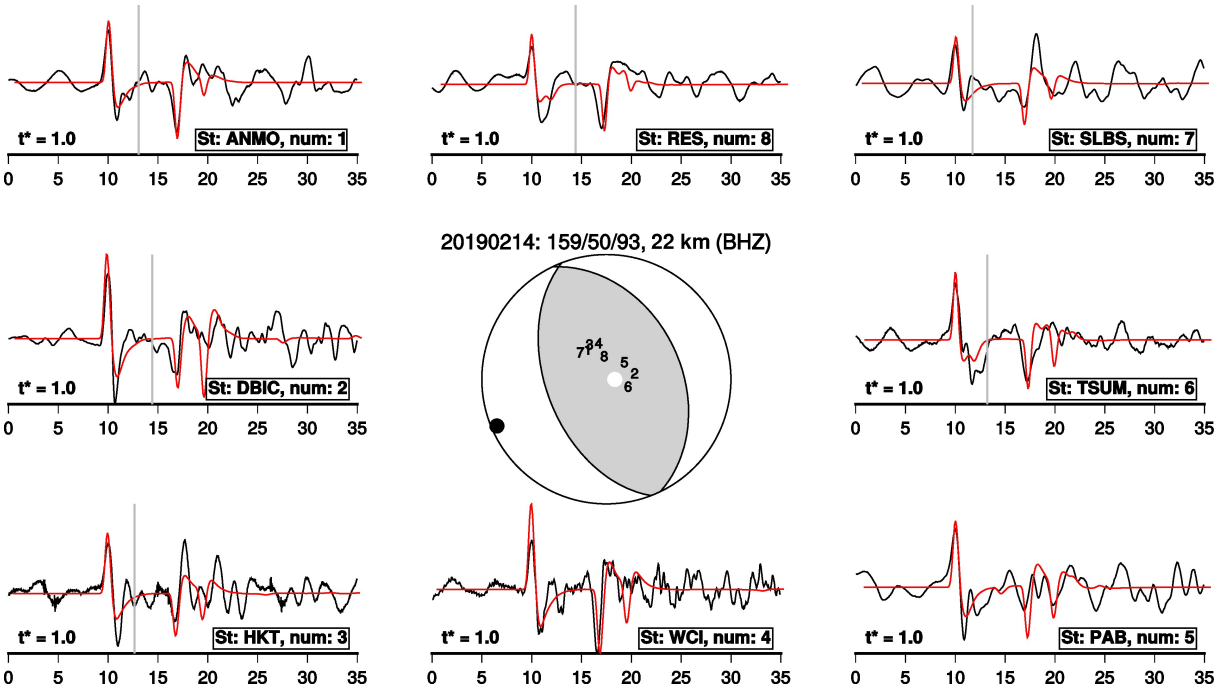

Figure B.15 Synthetic depth-phase modelling for the 14th February 2019 M_w 5.4 reverse-faulting earthquake beneath the Shira Uplift in central Peru.

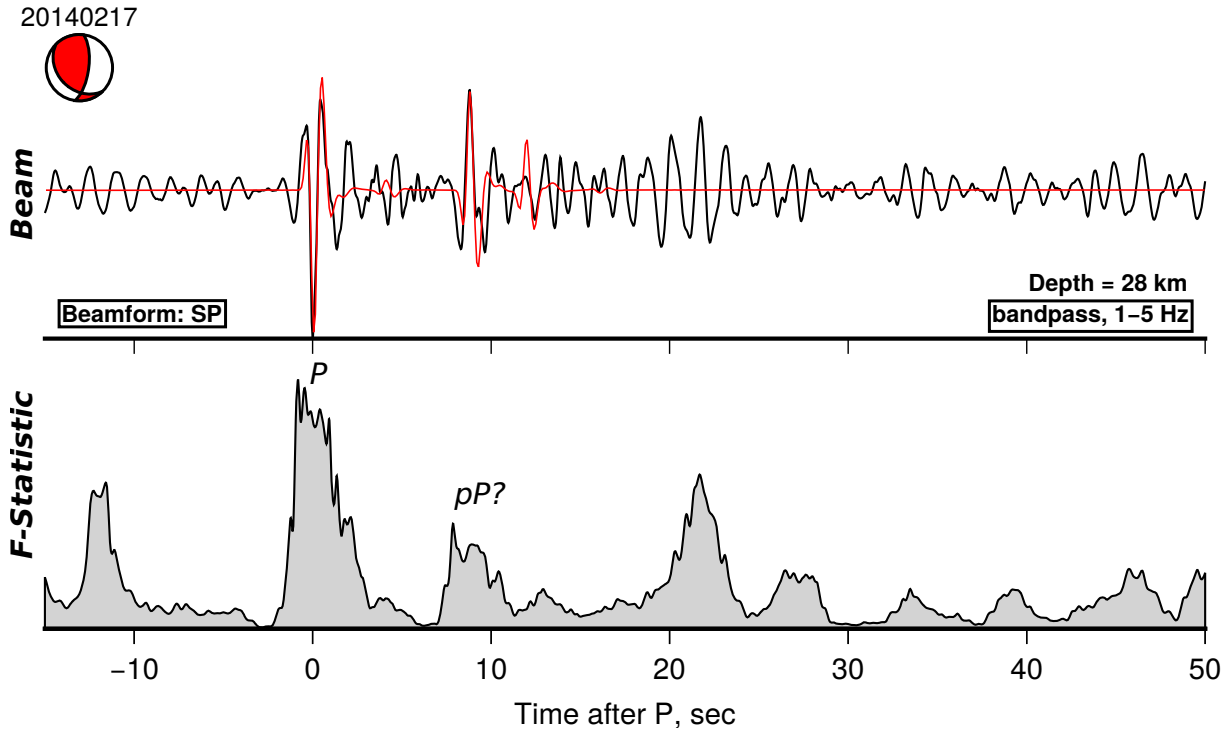

Figure B.16 Beamformed vertical-component seismogram from the Spitsbergen small-aperture array for the 17th February 2014 reverse-faulting earthquake in the Llanos Basin of Colombia. The beam has been bandpass filtered using a four-pole Butterworth filter between 1-5 Hz. Below is the F-statistic [Heyburn and Bowers, 2008], which is a measure of the coherency of the energy in the beam across the array. The beam shows a clear direct P arrival at 15 s, followed by a second arrival at 24 s, which I interpret as the surface-reflected pP phase. This interpretation is consistent with the relative amplitudes of the pP and sP phases from the gCMT focal mechanism. No later arriving sP phase is evident, suggesting its amplitude is less than the noise in the seismogram. Synthetic depth-phase models of a reverse-faulting earthquake at a hypocentre depth of 28 km beneath the Llanos Basin can reproduce the relative amplitudes of the P and pP arrivals, and their relative arrival times, and the low-amplitude sP arrival. By varying the hypocentre depth, I find the waveforms begin to misfit the observed arrivals at ∼26 km and 30 km. If the energy arriving after 10 s were in fact the sP, then the hypocentre depth would be shallower.

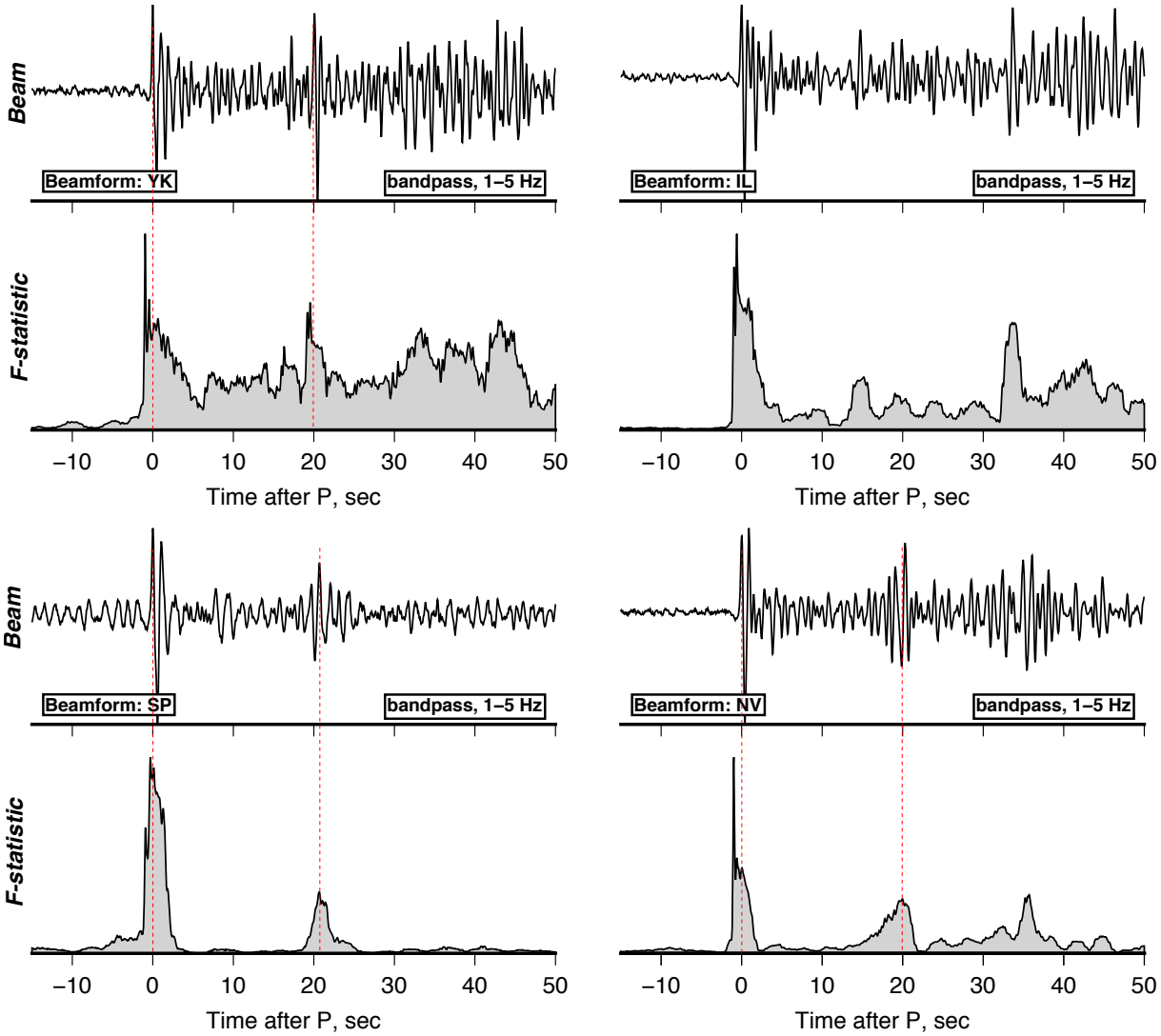

Figure B.17 Normalised F-statistic and beamformed vertical-component seismograms for the 19th July 2018 M_w 5.0 earthquake in the Colombian foreland. The F-statistic is shown beneath each array beam (YK = Yellowknife, Canada; IL = ILAR, USA; NV = NVAR, USA; SP = Spitsbergen, Norway). In both the beam and the F-statistic for NV, SP and YK there is coherent energy arriving ∼20 s after the direct P arrival. In Fig. B.18 I assume the signal at ∼20 s is the sP arrival to yield the shallowest-possible depth estimate for the event.

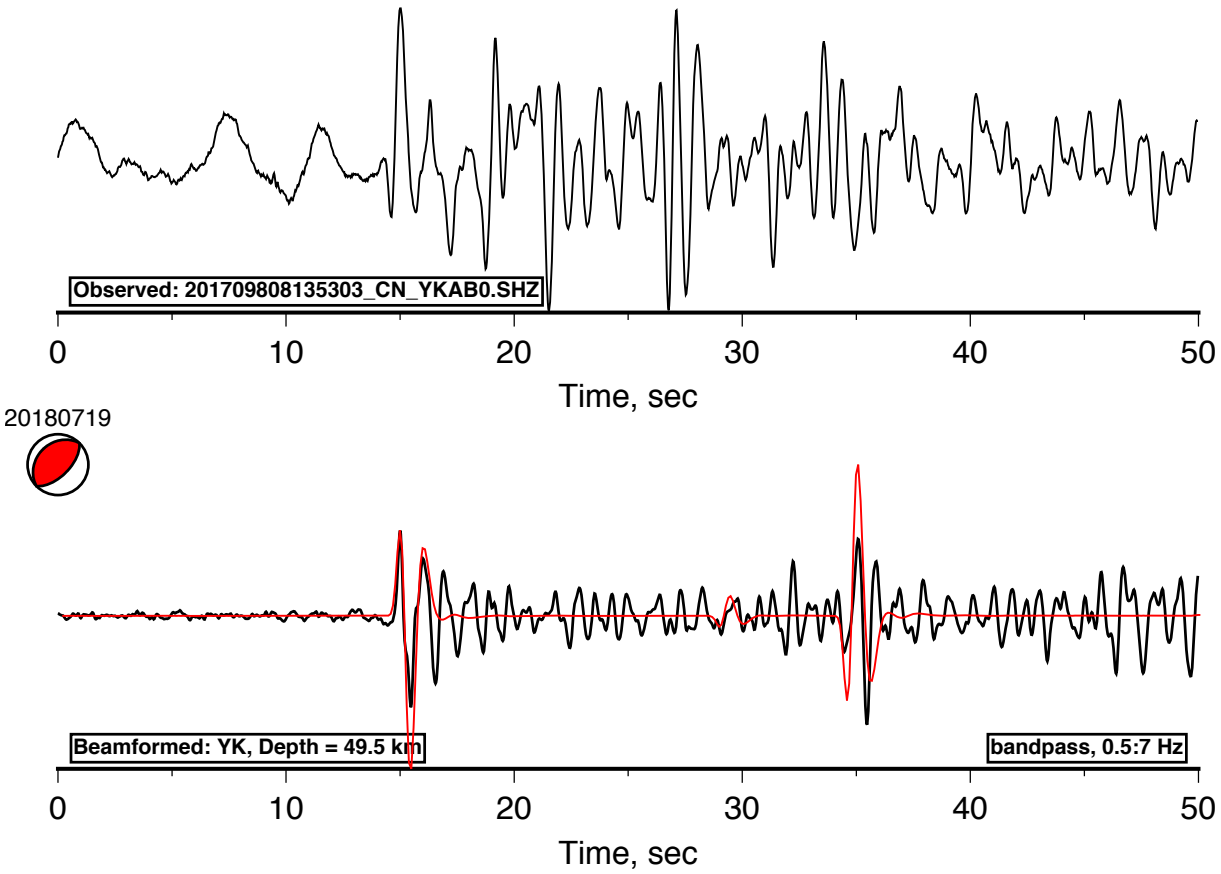

Figure B.18 Example single-station seismogram (top) and beamformed vertical-component seismogram (bottom) of the 19th July 2018 M_w 5.0 earthquake in the Colombian foreland from the short-period instruments in the Yellowknife array in Canada. The beam was filtered between 0.5-7 Hz using a four-pole Butterworth filter and the synthetic (red) was generated using the ak135 velocity model adapted to have a 45 km thick crust. The arrival at 35 s is taken to be the sP depth-phase and would be consistent with an earthquake at ∼49-50 km hypocentre depth. The uncertainty in the hypocentre depth estimate is 47-55 km. The extended upper bound is due to the non-impulsive shape of the later-arriving energy. If this arrival at ∼35 s were in fact the pP depth phase, the earthquake hypocentre depth would be deeper.

B.4 Deep Earthquakes in the Colombian Andes

Three of the earthquakes modelled in Section B.3 have estimated hypocentre depths close to the Moho in the South American forelands (i.e. $\gtrsim$40 km [Poveda et al., 2015]; see Fig. B.12, B.13, B.18). All of these deep events occur along the margin of the Colombian Eastern Cordillera (labelled DE-1,2 and 3 in Fig. B.19). Earthquakes with hypocentre depths close to, or within, the upper mantle are rare, and have significant implications for the study of continental rheology [e.g. Jackson, 2002; Sloan and Jackson, 2012]. Therefore, I discuss the evidence for these deep earthquakes further in this appendix. In Appendix B.5, I discuss evidence for the along-strike variability in the depth of earthquakes in the Andes foreland based on the earthquake catalogue in Table B.1, and relate the seismicity to the shortening style at the surface.

The first deep earthquake occurred on the 31st October 2016 near the Colombia-Venezuela border, with an epicentre beneath the range front of the Eastern Cordillera (Fig. B.19; DE-1). The Moho depth near the epicentre has been inferred from receiver functions to be 42 ± 6 km [Poveda et al., 2015]. The best constraint on the source depth of this earthquake comes from the vertical-component seismogram at station TAM, where a clear depth-phase arrival can be seen at ∼12-13 s after the direct P arrival (Fig. B.12). I generated synthetic seismograms for this event using the ak135 velocity model [Kennett et al., 1995] adapted to have a crustal thickness of 42 km. The synthetic seismograms calculated with the gCMT mechanism predict that the pP should be much larger in amplitude than both the direct P and the sP arrival, suggesting the energy arriving at ∼12-13 s may be the pP depth phase. The synthetics fit the observed seismogram at TAM best when the earthquake hypocentre depth is ∼40 km, which is slightly shallower than the crustal thickness in the region (Fig. B.12). A depth of 40 km also provides a reasonable fit to the other vertical-component waveforms shown in Fig. B.12. Varying the hypocentre depth suggested the waveforms could still be fit reasonably well in the depth range 40^{+3}_{-2} km, placing the event at the base of the lower crust.

The second deep earthquake occurred on the 6th February 2017 with an epicentre around ∼20-30 km west of the range front in the Colombian Eastern Cordillera (Fig. B.19; DE-2). There are no estimates of the crustal thickness within this region, but ∼100 km to the north the foreland crustal thickness is estimated to be 31 ± 3 km, whilst within the range interior the crustal thickness is 55-70 km [Poveda et al., 2015]. The vertical-component seismograms for this event recorded at stations ANMO, SPB, RCBR, LCO and TUC all show two clear arrivals at ∼12-13 s and ∼17-18 s following the direct P phase (Fig. B.13). Unusually, the direct arrival is double-peaked at almost all of the stations, independent of back azimuth or epicentral distance. One possible explanation for the double peak is that the earthquake source mechanism involved a double rupture less than a few seconds apart, either on a single fault or two closely-spaced faults. A complex double rupture mechanism could also account for the unusually broad peaks of the depth-phase arrivals for an earthquake of M_w 5.5, if the individual depth phases for each sub-event have interfered (for example, compare the signal at TAM in Fig. B.12 with the signal at RCBR in Fig. B.13). The broad depth-phase peaks contributes additional uncertainty to the depth estimate, as the synthetics and the depth-phases overlap over a wider region. Synthetic seismograms using a Moho depth of 45 km (based on the spatial averaging of the Moho depth between distant measurements around the epicentre) suggest the best-fit hypocentre depth is ∼44 km, though

hypocentre depths in the range 40-49 km fit the observed waveforms well. Due to the uncertainty in the Moho depth, this earthquake may have occurred at the base of the lower crust, or in the upper mantle.

The final deep earthquake occurred on the 19th July 2018 with an epicentre 25 km west of the range front in the Colombian Eastern Cordillera, close to event DE-2 (Fig. B.19; DE-3). The 19th July 2018 earthquake was too small to study using broadband vertical-component seismograms, therefore I used recordings from small-aperture arrays in North American and Europe to extract the depth-phase signals for this event [e.g. Craig et al., 2012]. Beamformed and filtered seismograms and the F-statistic from three North American array sites (ILAR, NVAR and YK) and one European array site (SP) are shown in Fig. B.17. Highlighted on Fig. B.17 are coherent signals arriving ∼20 s after the direct P arrival, which correspond to parts of the trace that have a large F-statistic. As the arrays in Fig. B.17 have different back azimuths and epicentral distances, then it is unlikely the coherent energy in the beam is coming from another earthquake with a significantly different epicentral location.

It is most likely that the energy arriving at ∼20 s is the pP or sP depth phase. To yield the shallowest-possible depth estimate, I assume the arrival is the sP depth phase. Synthetic seismograms calculated using a crustal thickness of 45 km are shown in Fig. B.18 for the Yellowknife short-period array. The best-fit between the observed and synthetic waveforms is found for earthquake hypocentre depths between 47 and 55 km. Such large uncertainties are due to the non-impulsive nature of the depth-phase arrivals on the filtered beam. As with the previous event, the uncertainty associated with the Moho depth in the area [Poveda et al., 2015] means it is not possible to determine whether this earthquake occurred in the upper mantle or the lower crust. This is the deepest earthquake recorded in South America that is unrelated to the subducting oceanic crust.

The earthquake hypocentre depth estimates discussed above indicate that the base of the lower crust on the margin of Colombian Andes is brittle and seismogenic. However, there is no robust evidence that any of these earthquakes occurred within the continental lithospheric mantle, mainly because there are steep and poorly-constrained gradients in the Moho depth near the epicentres of earthquakes DE-2 and DE-3. Lower crustal earthquakes are typically considered to be a sign of strong, cold and anyhdrous lower crust commonly associated with Proterozoic and Archean shields [e.g. Maggi et al., 2000a; Sloan et al., 2011; Craig et al., 2011]. Given that the Guiana Shield outcrops ∼300 km east of the Colombian Eastern Cordillera, and may extend beneath the Llanos Basin, it is possible that the earthquakes on the margin of the Colombian Andes adhere to this pattern and result from faulting on the western margin of the Guiana Shield.

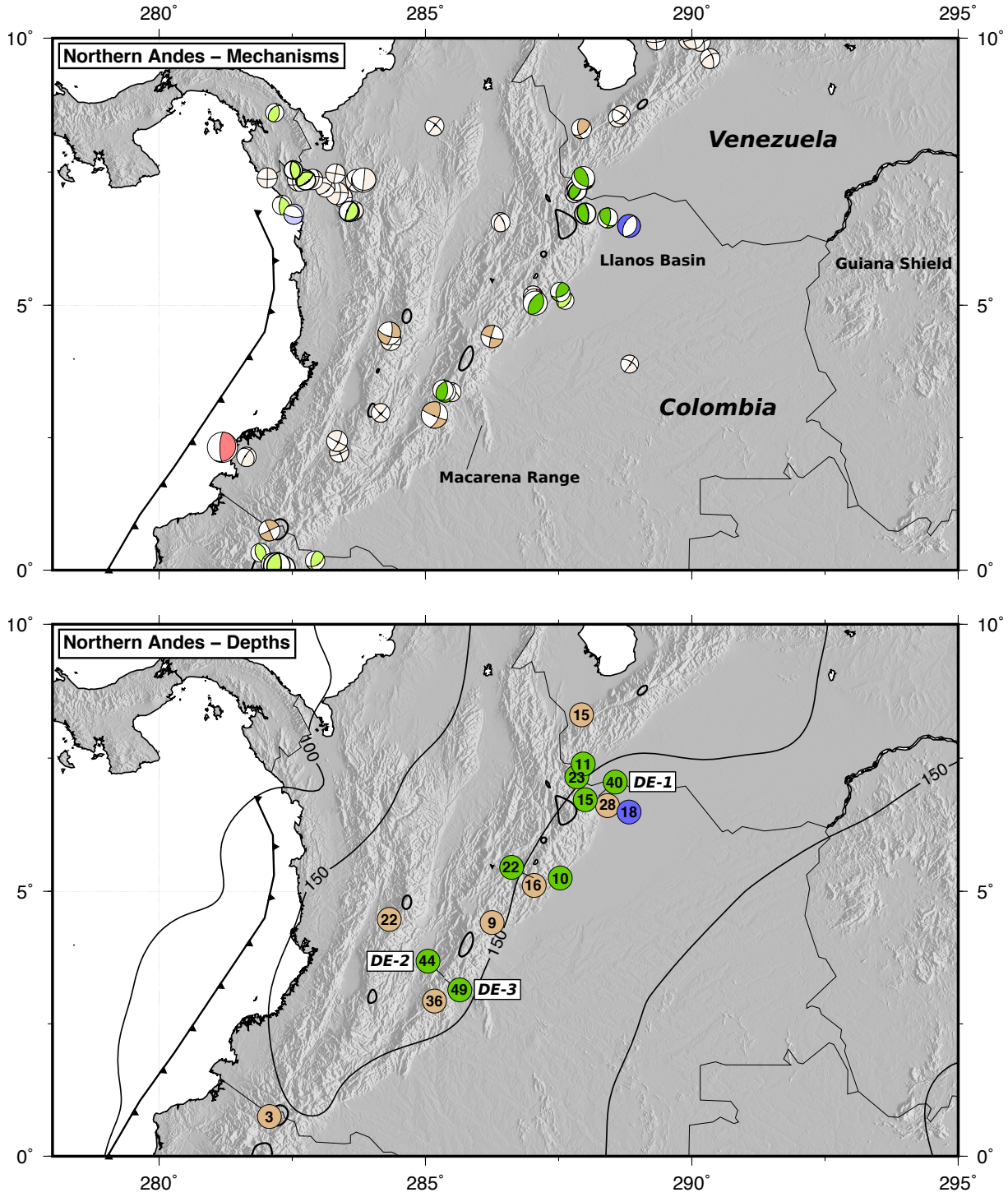

Figure B.19 Earthquake mechanisms and centroid/hypocentre depths in Colombia derived from teleseismic body-waveform modelling (events in Table B.1). The colour scheme for the earthquake mechanisms is the same as that used in Fig. 3.1 in the main text. Contours in the bottom panel are the lithospheric thickness in kilometres taken from Priestley and McKenzie [2013].

B.5 Controls on the Shortening Style in the Eastern Andes

There are significant along-strike variations in the structural style of the shortening in the eastern Andes [e.g. Kley et al., 1999]. In Colombia, the high mountains form a narrow, linear range that is bounded by a steep range front on both sides. Much of the range front consists of exposed Paleozoic and Precambrian high-grade metamorphic basement rocks, and there are locally regions of block-like topography consisting of uplifted Paleozoic basement that step out from the range front into the foreland [Ordóñez-Carmona et al., 2006] (e.g. Sierra da la Macarena; Fig. B.19). This style of shortening, in which basement is exposed at the surface, I shall refer to as 'thick-skinned'. In contrast, the Central Andes between south Peru and Bolivia consists of a wide, low-relief plateau that is bound by the low-gradient topography of the sub-Andean lowlands. In the sub-Andes, the surface morphology is dominated by short-wavelength anticlinal ridges consisting of Mesozoic and Cenozoic sediments [e.g. Gubbels et al., 1993; Perez et al., 2016b]. Regions like the sub-Andes, where there are trains of closely-spaced (<10 km) anticlines formed of sedimentary rocks and no crystalline basement exposed at the surface, I will refer to as 'thin-skinned'. In Argentina the foreland deformation is different yet again, with a ∼200 km-wide region of basin-and-range style topography (the Sierra Pampeanas) formed of 10-20 km-wide blocks of Precambrian and Paleozoic metamorphic basement separated by undeformed sedimentary basins [Jordan et al., 1983] (Fig. B.20). As basement is exposed at the surface, I categorise the deformation in the Sierra Pampeanas as 'thick-skinned'.

What controls these along-strike differences in the style of shortening in the eastern Andes remains unclear. Both Kley et al. [1999] and Watts et al. [1995] suggested that in regions where the lower crust and crystalline basement is being underthrust beneath the Andes whilst the sedimentary veneer is being shortened, then the foreland lower crust and lithospheric mantle is probably too strong to deform significantly. However, there is little agreement on how and why the lower crust is shortening in regions such as the Colombian Eastern Cordillera and the Sierra Pampeanas. Kley et al. [1999] argued that the correlation between areas that underwent pre-Andean rifting and the regions currently undergoing thick-skinned deformation indicates that weak normal faults in the lower crust may have been reactivated during the recent shortening. In contrast, Watts et al. [1995] and Mouthereau et al. [2013] argued that the thick-skinned deformation occurs where there is a warm lower crust and thin lithospheric mantle that can deform through grain-scale creep on compression. Both agree that the lower crust in thick-skinned forelands must be weaker than in thin-skinned forelands.

The key difference between these two models is the mechanism they invoke to reduce the strength of the lower crust and lithospheric mantle relative to regions of thin-skinned faulting, allowing it to become deformable. Either the lower crust is cool enough that it remains brittle, but can deform because of weak faults that are re-activated [Kley et al., 1999], or the lower crust is hot and hydrous enough that grain-scale creep can occur [Mouthereau et al., 2013]. One way to differentiate between these two alternatives is to study the along-strike variation in the earthquake mechanisms and centroid/hypocentre depths in the region.

B.5.1 Earthquake Centroid and Hypocentre Depths

A compilation of body-waveform modelled earthquakes in the Eastern Andes is shown in Fig. B.20 and the events are listed in Table B.1. In the Colombian and Argentinian forelands, where the deformation is thick-skinned, the seismicity is characterised by a large number of reverse-faulting earthquakes throughout the upper and lower crust. In contrast, in the foreland of the Central Andes and parts of central Peru, where there are thin-skinned fold-thrust belts at the surface, there is little seismicity in the lower crust and a number of the earthquakes have low-angle thrust faulting mechanisms. There is also a factor of ∼3-4 times more moment release per distance along-strike the range from earthquakes in the regions of thick-skinned shortening than in the thin-skinned Central Andes [Gutscher et al., 2000].

B.5.2 Gravity Anomalies

Normalised profiles of the free-air gravity anomalies in the eastern Andes provide information regards the along-strike changes in the integrated strength of the lithosphere (Fig. B.21). In particular, the half-wavelength of the gravity anomalies produced by a flexed plate under a line load should be proportional to $T_e^{3/4}$ [Turcotte and Schubert, 2002]. From Fig. B.21 there is no resolvable along-strike change in the wavelength of the gravity anomalies associated with flexure, apart from one profile in the northern Bolivian sub-Andes where the half-wavelength is ∼40 km (∼30-40%) longer than elsewhere. As the same wavelength gravity anomalies are not present in south Bolivia, it seems unlikely there is foreland lithosphere beneath the whole thin-skinned Central Andes with a T_e ∼2-3 times larger than elsewhere along-strike [contrary to Watts et al., 1995]. The simplest interpretation is that any along-strike changes in the foreland strength are small enough that they have no resolvable affect on gravity anomalies generated by flexure.

B.5.3 Conclusions

Earthquakes throughout the crust of the thick-skinned forelands are a sign that the lower crust is cool ($<600^oC$), anydrous [McKenzie et al., 2005; Jackson et al., 2008] and supports stresses by frictional resistance along faults [contrary to Mouthereau et al., 2013]. Beneath the Sierra Pampeanas and central Peru, the deep seismicity has been linked to the cooling of the base of the crust as a result of flat-slab subduction [e.g. Smalley and Isacks, 1987; Gutscher et al., 2000; Emmerson, 2007]. In the Northern Andes of Colombia, the cause of the presumably cool lower crust is not clear, as there is a poorly-defined Wadati-Benioff zone associated with the subducting Nazca slab. There is evidence, however, that the lithosphere is locally thick in parts of the Colombian Andes directly beneath the Sierra de la Macarena, where the earthquakes are also deep (Fig. B.20c).

The simplest interpretation of these observations is that thick-skinned faulting can occur where pre-existing faults within the brittle lower crust are re-activated on shortening. These pre-existing faults weaken the lower crust relative to sections of the foreland where there is thin-skinned deformation. Differences in the integrated strength between forelands with thick- and thin-skinned faulting must be small in order not to significantly change the gravity anomalies associated with lithospheric flexure, or the elevations of the mountain belt that can be supported.

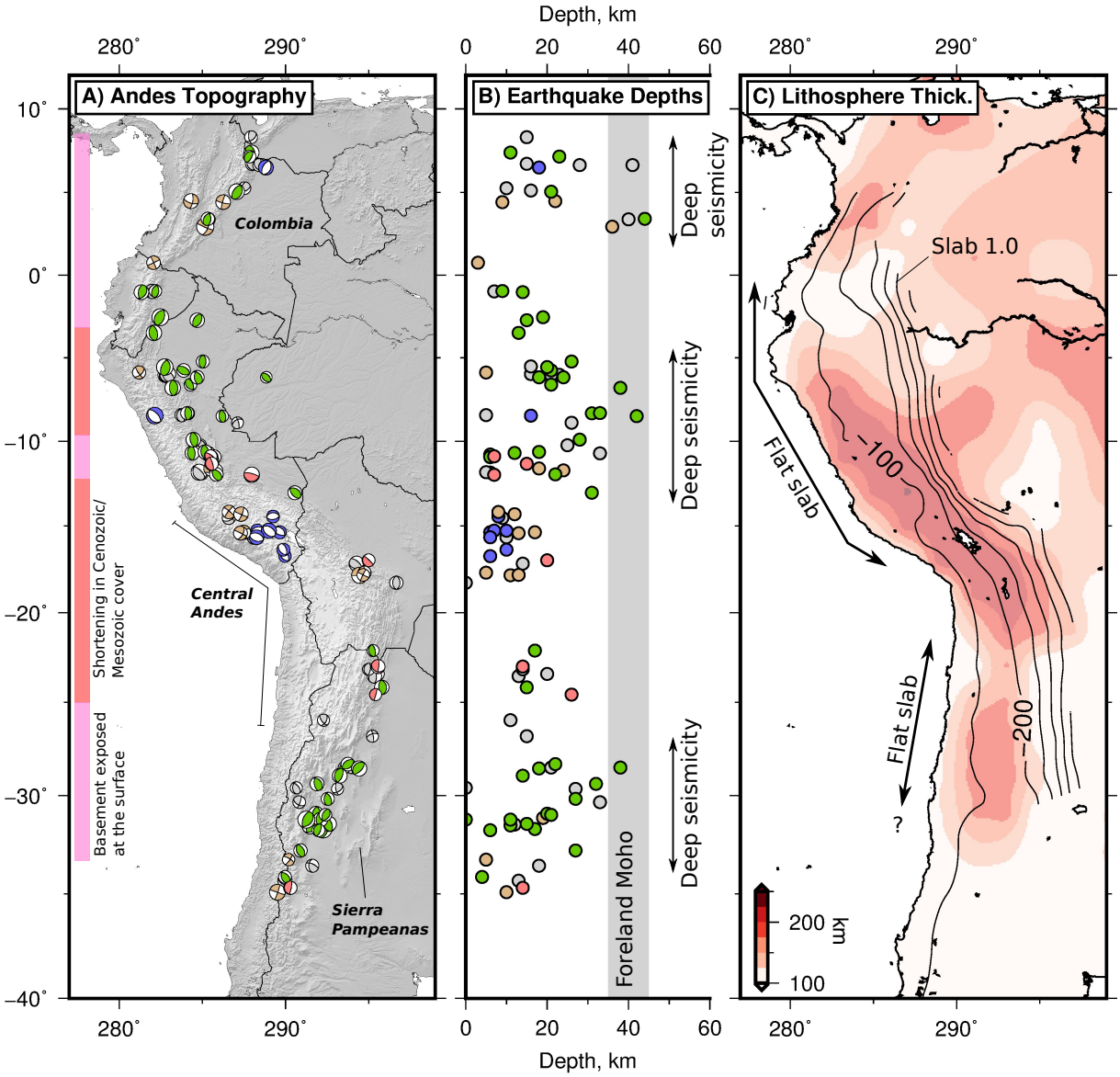

Figure B.20 Along-strike variability in earthquake centroid/hypocentre depths in the overriding South American lithosphere (i.e. not associated with the Wadati-Benioff zone of the Nazca Slab). (a) Earthquake focal mechanisms coloured by mechanism type. The colour scheme is the same as used in Fig. 3.1, but light red events are now low-angle thrusts. Grey mechanisms are those with a strongly oblique component of slip, or a poorly-constrained mechanism. The coloured bar on the left highlights the along-strike changes in the foreland deformation style, characterised by whether crystalline basement is exposed at the surface in the foreland or not [Kley, 1996]. (b) Earthquake centroid/hypocentre depths, with colours corresponding to the mechanism type. The Moho depth is taken by averaging the estimates from the compilation of Assumpção et al. [2013] throughout the South American continent, plus 1 standard deviation (37-45 km). (c) Lithospheric thickness from the model of Priestley and McKenzie [2013] with the depth contours of the Nazca slab surface from Slab 1.0 overlain [Hayes et al., 2012].

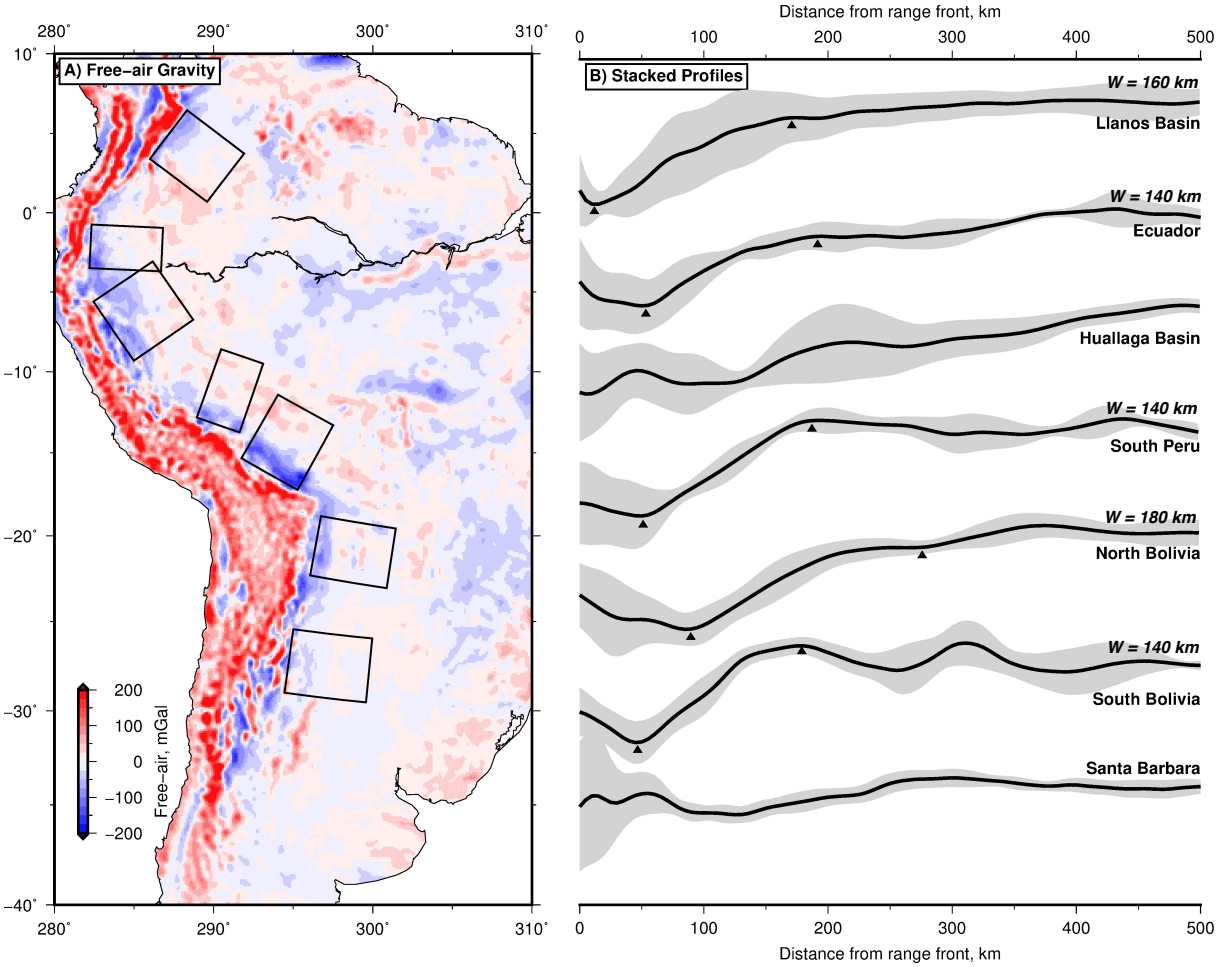

Figure B.21 Stacked free-air gravity profiles along-strike the eastern Andes. (a) Eigen-6C free-air gravity anomalies [Shako et al., 2014] plotted at $0.1^o \times 0.1^o$ resolution filtered with an elliptical filter using a lowpass of 0.5^o to remove short-wavelength signals unrelated to flexure. Black boxes represent regions where profiles have been extracted and stacked in (b). (b) Normalised, stacked profiles of the free-air gravity anomalies. The mean is shown as a black line with 1 standard deviation bounds in grey. Profiles are ordered from north to south. Black inverted triangles demarcate the regions with free-air gravity signals associated with flexure. Locations of the black triangles have been picked from the inflexion points along the gravity profiles. The width of the flexure signal W is given on the right of each profile where measurable.

Appendix C

C.1 Moraine Age Compilation

Many of the faults in the high Andes cross-cut fresh lateral moraines and drift sheets. A key development in estimating the age of the fault offsets, and therefore fault throw rates, is the recent proliferation in studies using cosmogenic exposure dating to constrain the timing of moraine deposition in the Central Andes [e.g. Smith et al., 2005b; Rodbell et al., 2009; Jomelli et al., 2014; Ward et al., 2015; D'Arcy et al., 2019, and references therein]. A compilation of the ages of boulders from the surfaces of moraines is shown in Fig. C.1.

The following patterns can be observed from the moraines in south Peru and northern Bolivia: (1) extensive moraine formation took place between ∼10 and 45 ka in regions >3500 m elevation, and (2) few moraines are dated from >45 ka (Fig. C.1). The lack of older moraines may partly reflect a sampling bias. The few moraines older than the LGM that have been identified are characterised by rounded crests and are often positioned down-valley of a fresher set of LGM and Late Glacial (<10 ka) moraines [Smith et al., 2005a]. Therefore it is possible the older glacial deposits can be distinguished from those dating to the LGM based on their morphology. In this thesis, I assume that moraines in the Central Andes that outcrop at >3000 m elevation, and which appear to be the youngest moraines in the region, probably formed in the last 10-45 ka.

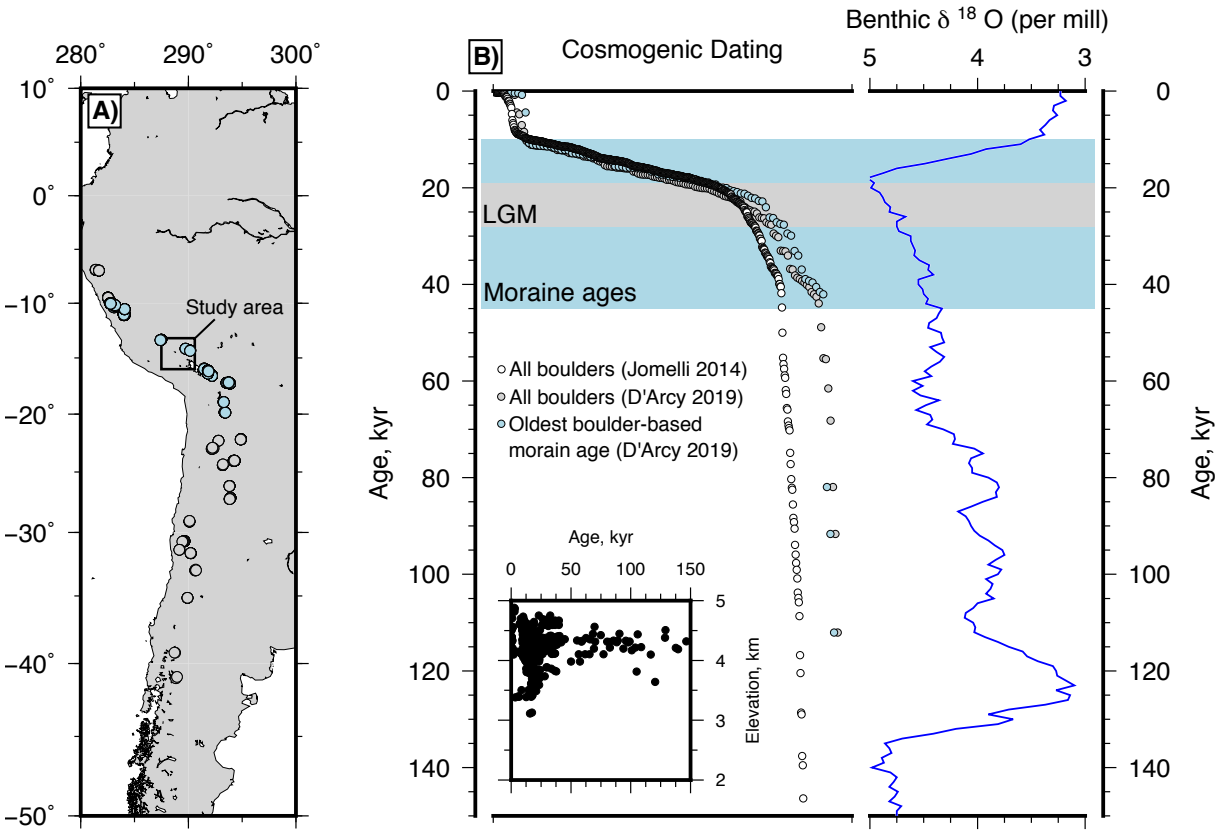

Figure C.1 A compilation of moraine and boulder ages from the Andes. (a) Spatial distribution of dated moraines from the high Andes. Dots in light blue are a subset of the most well-constrained moraine ages from the Central Andes and the grey dots are all the dated moraines. (b) Cumulative density function plot of moraine ages against time. The steepest part of the curve corresponds to the time with the most dated moraines. Also shown is the LR04 benthic δ^{18}O stack of Lisiecki and Raymo [2005], which is a proxy for global sea temperatures. The grey bar represents the timing of the global Last Glacial Maximum from Clark et al. [2009], whilst the blue bar covers the full range of well-dated moraines from D'Arcy et al. [2019]. Inset is the distribution of moraine ages as a function of their elevation, showing that most moraines occur >3500 m. The older moraines are restricted to >4000 m.

C.2 Garmin Watch Barometer: Benchmark

Barometric altimeter data in this section were collected by Alex Copley. The comparison between the Pleiades DEM and the theory developed below are my own.

Changes in barometric pressure can be used to estimate height changes. Therefore, in regions where differential GPS is not permissible for surveying, watches or hand-held GPS equipped with a barometric altimeter can be used to measure the height changes across fault scarps. In this section, I test the accuracy of a Garmin watch-based barometric altimeter by benchmarking a profile across the Sangarara Fault against a digital elevation model (DEM) derived from bistereo Pleiades imagery with a 1 m pixel resolution (see Section 4.2.2 for discussion about the DEM). I begin by developing a theoretical understanding of how the altimeter works below, before using this theory to interpret the benchmark results.

Relative elevation changes measured by a barometric altimeter Δh_G are a function of the air pressure $P(h_1)$ at some reference height h_1 and the air pressure at some new height $P(h_2)$. The air pressure changes are related to elevation changes by:

$$dP = -\rho g \, dh, \tag{C.1}$$

where g is the acceleration due to gravity. The density of air ρ depends on factors such as its composition (molar weight M), the absolute temperature T and the absolute air pressure P. An equation of state is required to link these variables, and account for the variation of air density with height. I use the Modified Ideal Gas Law:

$$\rho = Z\frac{PM}{RT}, \tag{C.2}$$

where R is the universal gas constant and Z is the compressibility factor.

I assume that T is constant, as the temperature lapse-rate dT/dh is small $\sim 6.5^oC/\text{km}$, so has a negligible affect on the air density for the small elevation changes associated with scarp surveys. Similarly, I assume that the atmosphere has a constant molar mass M over the small time-span of a normal profile measurement. Under these assumptions, the density of the air varies only due to the changing air pressure with height. Substituting Equation C.2 into Equation C.1 and integrating yields:

$$\ln(P/P_0) = -h/\alpha, \tag{C.3}$$

where $\alpha = RT/MgZ$ is a constant and P_0 is the air pressure at $h = 0$. The difference in air pressure at two different heights that would be measured by a barometric altimeter would therefore be:

$$\Delta h_G = \alpha \ln\left(\frac{P(h_1)}{P(h_2)}\right) \tag{C.4}$$

A positive Δh_G corresponds to an increase in elevation.

Assuming the barometric altimeter can measure air pressure perfectly (i.e. there is no error in P), then any difference between the inferred and true height changes across a fault scarp would result from

inaccuracies in the scaling parameter α, which deviates from its true value α_t. Errors in Δh_G will scale linearly with the true height change $h_1 - h_2$, with the constant of proportionality being α/α_t.

Figure C.2 shows the Pleiades measured heights h_P against $h_P - h_G$, the difference between the Pleiades and barometric altimeter measured heights, with a constant offset removed. The constant offset is to account for errors in the reference height used in the construction of the DEM. The root-mean-square deviation between the two data sets is 5.5 m over a profile with ∼100 m elevation change (∼5 %). There is a clear linear correlation between h_P and h_G with a gradient of 0.15. From the mathematical analysis developed above, the linear errors in the baromertic altimeter measurements would result if α was in error by ∼15%. Not recalibrating the barometer to the height at which the profile was taken may contribute to some of the error in α. Nonetheless, the relative height error (5%) is small compared to the typical age uncertainty for offset features encountered in fault slip rate studies. Therefore, barometric altimeters are a viable option for estimating scarp offsets in the field when no other methods are available.

Removing the linear trend that may result from calibration issues (red line, Fig. C.2) shows there is still residual noise between the Pleiades and barometric altimeter data sets. This noise is not Gaussian, and varies systematically at the largest elevations (on the right of Fig. C.2). These data points with systematic errors were collected at the start of measuring the profile, suggesting that accurate barometric altimeter readings require some 'burn-in' period to allow for the barometer to equilibrate with its surroundings. At the end of the survey, the scatter appears reduced and shows no systematic errors. The root-mean-square deviation of the difference between height changes measured by the barometric altimeter versus the Pleiades DEM once the linear trend is removed are ∼1.3 m, but could be lower if a 5 minute equilibration period for the barometer is allowed before data collection.

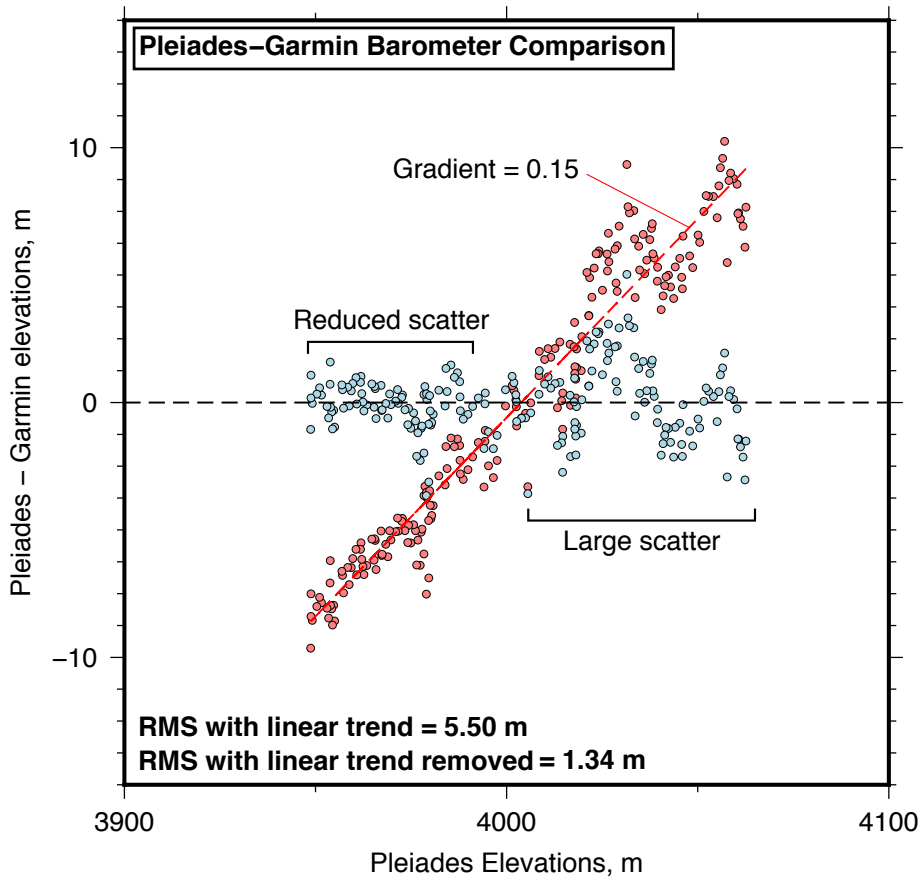

Figure C.2 Benchmark test for the height changes measured by a watch-based barometric altimeter. Red dots have had a constant offset removed, blue dots have had a linear ramp removed.

C.3 Derivation of Equation 4.3

Following the method of Lamb [2006] the average shear stresses on a planar detachment fault dipping at an angle θ from the horizontal, overlain by a triangular wedge of crust (sub-Andes) that has a horizontal force on its back F_f is given by (Fig. 4.18):

$$\tau = \frac{L}{2(L-h)}\left[\frac{F_f}{L} - \frac{\rho g(L-h)}{2}\right]\sin 2\theta, \tag{C.5}$$

where h is the height of the back of the wedge above the horizontal, $L-h$ is the depth of the back of the wedge below the horizontal and ρ is the average wedge density (see Fig. 4.18b). I include the $L/(L-h)$ term at the front of this expression that is assumed negligible by Lamb [2006], as it makes a difference of $\sim$4% relative to the exact solution in the case of high mountains with a low detachment dip. A perturbation to the average shear stresses on the detachment $\delta\tau$ in Equation C.5 will lead to a change in the horizontal force on the back of the sub-Andean wedge δF_f:

$$\delta\tau = \frac{L}{2(L-h)}\frac{\delta F_f}{L}\sin 2\theta \tag{C.6}$$

The term $\delta F_f/L$ is equivalent to the change in the differential stress $\Delta\sigma$ on the back of the sub-Andes due to a change in the average shear stress on the detachment fault $\delta\tau$. If there were no differential stresses on the back of the sub-Andes prior to the change in τ, then $\Delta\sigma$ is the absolute value of the differential stresses driving deformation in the high plateau behind the sub-Andes.

It is more informative to express the shear stress perturbation in terms of the down-dip width of the detachment W, its dip θ and the height of the mountains h. Using the geometry of the model wedge shown in Fig. 4.18b I can re-write Equation C.6 as:

$$\delta\tau = \Delta\sigma\cos\theta\left(\sin\theta + \frac{h}{W}\right) \tag{C.7}$$